Frequency modulation of spin torque nano-oscillators (STNOs) for wireless communication applications

Anike Purbawati

To cite this version:

Anike Purbawati. Frequency modulation of spin torque nano-oscillators (STNOs) for wireless communication applications. Networking and Internet Architecture [cs.NI]. Université Grenoble Alpes, 2017. English. NNT : 2017GREAY023 . tel-01663773

HAL Id: tel-01663773
https://theses.hal.science/tel-01663773

Submitted on 14 Dec 2017

Communauté
UNIVERSITÉ Grenoble Alpes

THÈSE

Pour obtenir le grade de

DOCTEUR DE LA COMMUNAUTÉ UNIVERSITÉ GRENOBLE ALPES

Spécialité : **NANOPHYSIQUE**

Arrêté ministériel : 25 mai 2016

Présentée par

Anike PURBAWATI

Thèse dirigée par **Ursula EBELS, Ingénieur-Chercheur, CEA**,
et codirigée par **Liliana BUDA-PREJBEANU, Enseignent-Chercheur, Grenoble-INP**

préparée au sein du **Laboratoire Spintronique et Technologie des Composants**
dans **l'École Doctorale Physique**

Modulation de la fréquence d'un oscillateur spintronique (STNO) pour des applications de communication sans fil

Frequency modulation of Spin Torque Nano-Oscillators (STNOs) for wireless communication applications

Thèse soutenue publiquement le **17 juillet 2017,**
devant le jury composé de :

Monsieur OLIVIER FRUCHART
DIRECTEUR DE RECHERCHE, CNRS DELEGATION ALPES,
Président du Jury
Monsieur MATHIAS KLAUI
PROFESSEUR, UNIVERSITE J.G. DE MAYENCE - ALLEMAGNE,
Rapporteur
Monsieur JEAN-PHILIPPE ANSERMET
PROFESSEUR, ECOLE POLYTECH. FEDERALE LAUSANNE SUISSE,
Rapporteur
Monsieur GREGOIRE DE LOUBENS
INGENIEUR DE RECHERCHE, CEA SACLAY,
Examinateur

ACKNOWLEDGMENT

This work would not have been possible without the help and support of a number of people. I would like to take this chance to acknowledge all people who have supported and contributed to this work. First of all, I would like to thank my supervisor, Ursula Ebels, for giving me the opportunity to perform my PhD Thesis in her group and the trust in me. I am deeply grateful for all her guidance, support, and important advice during the work. She has always been available whenever I needed her advice and help. She has also helped me in improving my writing and presentation skills. Her creativity, academic diligence, and profound knowledge make her an excellent role model for me to follow. Also, the efforts of my co-supervisor, Liliana Prejbeanu Buda, are greatly appreciated. I would like to express my appreciation for all of her help and guidance, in particular for the simulation and theoretical part achieved in this work. I thank her a lot for valuable discussions, support and her hospitality.

I gratefully acknowledge CNRS for funding my research. A huge thank for nanooscillator group. Jerome, thanks for being such a nice office mate and also for your help whenever I had any problems with the measurements and the data extraction program. I would also thank Karla, Erika, and Chandra, who have fabricated the nanooscillators devices so that the experimental part of this work can be realized. I am very grateful to Ana Ruiz Calaforra who has helped me a lot in the device characterizations and measurements. Thanks for nice discussions and advice during the work. Mathiew and Michael, thanks for the fruitful discussions and the jokes during the group meeting. I would also like to thank intern students, Hiteshika and Fanjian Du, for helping me in the device characterization and sharing their experience with me. Finally, I would also like to thank other previous nanooscillator group members, Christopher, Elmer, Marina, and Miguel, for training me on how to do the measurements and how to interpret and analyze the data measurements at the beginning of my thesis. Thanks also for helping me in understanding the scientific concept of nanooscillators.

I would also like to thank Mosaic partner, Rui Ma and Martin Kreissig, from Technische Universität Dresden (TUD) who were responsible for the design and the realization of nanooscillator emitter-receiver electronic cards. In particular, I gratefully appreciate Rui Ma for performing together the measurements. He is really hard working and never gives up before getting satisfying results. I have been lucky to collaborate with him and sharing experiences during his stay in Grenoble.

I thank Hieu Tan Nguyen for the nice time inside and outside the lab. I also thank Claire, Lamprini, Safeer for fruitful discussion and amazing road trip in California. It was unforgettable moment. I thank to all PhD students in Spintec for sharing their experiences and for the joy in the lab. I greatly thank Caterine Broisin and Rachel Mauduit for their help in administration issues. Finally I would like to thank all Spintec members for their help and support during these years.

I am thankful to Indonesian student community in Grenoble. Thanks for being my second family and great moments we have spent together. I thank to my best friend, Ria. We got France together and travelling together. Thanks for supporting and caring me during these years. Thanks to BFF (Best Friend Forever) community for supporting me even though we are apart.

My special and huge thank, go to my fiancé, Anthony Naddeo, for caring, encouraging and powering me every moment. You make my days colorful and full of happiness. I also thank to his family who gives the support and encouragement these days.

Ultimately, I would like to express my deepest thanks to my family, my parents and my brother, who has encouraged and supported me with their unconditional love. Though they are on the other side of the earth, I know that they never stop caring about me for even a single minute. Thanks very much for standing behind me with your endless love and support.

Thank you all!

Anike Purbawati

17 July 2017, Grenoble

To my mother, my father,
and my brother

ABSTRACT

Spin Transfer Nano-Oscillators (STNOs) are a novel type of Radio Frequency (RF) oscillators that make use of the Spin Transfer Torque (STT) effect in a magnetic tunnel junction (MTJ) device to produce high-frequency auto-oscillations. STNOs provide compact solutions for wireless communication used in wireless sensor networks (WSNs) since their frequency can be tuned via the DC current. This frequency tuning permits to encode the information via frequency shift keying (FSK) by digital modulation of the current between two discrete values without the need of an external RF mixer, leading to potentially less complex RF components. In this thesis, the feasibility of the FSK scheme by current modulation has been studied for in-plane magnetized MTJ STNOs in view of wireless communications used in WSNs. The parameters addressed in this study are the achievable frequency shift and the maximum modulation rate, up to which the frequency can be shifted between two discrete values.

To characterize the maximum data rate, macrospin simulation and experimental studies have been performed. The simulations reveal that the maximum data rate for FSK by current is limited by the relaxation frequency f_p of the STNO, which is on the order of a few hundred MHz for standard in-plane magnetized STNOs. This means that the data rate is limited to a few hundred Mbps which is targeted here for moderate data rate wireless communication as used in WSNs. Experimental studies of the FSK by digital current modulation in STNOs have been performed for standalone STNO devices and for integrated STNOs within microwave systems. The FSK on standalone STNO devices shows a frequency shift around 200MHz (the frequency shift between ≈8.9 GHz and ≈9.1 GHz) at the modulation rate of 10Mbps. This modulation rate is less than the upper limit given by the relaxation frequency f_p of the STNO as predicted in the numerical simulation due to the relatively high phase noise of the device measured. In order to test the feasibility of the STNO within microwave systems, the FSK modulation of STNOs was performed on a printed circuit board (PCB) emitter. The PCB emitter was realized and developed by the partner of the Mosaic FP7 project, TUD University. The analysis confirms that a frequency shift around 300MHz (the frequency shift between ≈9 GHz and ≈9.3 GHz) was observed with a modulation rate of 20 Mbps. The data rate is limited by characteristics of the PCB emitter and not intrinsic to the STNO. The simulation and experiment studies of frequency modulation of STNOs demonstrate that the data rate is adequate for wireless communication used in WSN. However, further improvements in materials and nanofabrication of STNOs are required to enhance the output power and improve the spectral characteristics of the oscillations to push the data rates to higher values with large frequency shift.

Keywords: spin transfer nano-oscillators, magnetic tunnel junction, relaxation frequency, frequency shift keying, data rate.

Table of Contents

General Introduction

A. Research Background

A wireless sensor network (WSN), as part of the internet of things, has attracted a lot of interest in the industry and research community due to its huge potential to control and monitor wirelessly physical or environmental conditions such as temperature, pressure, and pollution [1-3]. A critical issue on WSNs is that the sensor nodes employ batteries whose lifetime is limited and it is difficult to change or recharge batteries since the sensor nodes is deployed unattended and in large numbers. Therefore, it is important to design low-power sensor nodes. The most power consuming part of a sensor node is the wireless communication. This is driving research on wireless communication that needs to be compact, low cost, and low power consumption.

Here, spintronic oscillators or so-called Spin Torque Nano-Oscillators (STNOs) can provide compact solutions for wireless communication compatible with the needs of WSNs. STNOs, consisting of ferromagnetic material heterostructures, have the capability to convert a DC current of a few mA into an RF output voltage signal at a frequency that can range from 100MHz to several tens of GHz. This conversion makes use of two fundamental spintronic effects which are the Spin Transfer Torque (STT) and the magnetoresistance effect. The STT effect induces periodic oscillations of the magnetization via spin angular momentum transfer from conduction electrons to the local magnetization [4-6]. These magnetization oscillations are converted into an RF output voltage signal [7] through the Giant Magnetoresistance (GMR) [7] or Tunneling Magnetoresistance (TMR) effect [8]. An STNO with GMR is a spin valve STNO and an STNO with TMR is a Magnetic Tunnel Junction (MTJ) STNO. MTJ STNOs offer a larger output power than spin valve STNOs which is of importance for RF applications.

STNOs allow for compact wireless communication since their frequency can be tuned via the DC current. This permits transmission on different base frequencies (different channels) with the same device and circuit, whereas in current wireless communication schemes, different base frequencies require different circuits. Furthermore, the frequency tunability permits to encode information via frequency shift keying (FSK) onto the carrier signal without the need of an external RF mixer, leading to potentially less complex RF components. Therefore, it is of great interest to demonstrate the FSK scheme by current modulation in STNOs for wireless communication used in WSNs.

B. State of the Art

Research on STNOs and their associated microwave properties has made major advances in the past years towards the understanding of the non-linear magnetization dynamics under STT, understanding of excitation modes and their frequency tuning characteristics, enhancing output power and reducing phase noise through the synchronization of STNOs [9-14] as well as a large variety of different magnetic stack compositions and nanofabrication optimizations [15-21]. This permitted to improve the microwave performances (output power, spectral coherence, frequency tunability) and to define new operational principles other than the often highlighted microwave signal generation. The agility of STNOs has also been studied theoretically [22] and experimentally [23,24] through the modulation of STNO properties via the application of sinusoidal RF currents, in terms of investigating the maximum achievable data rate for communication applications. Based on these achievements and considering the fascinating potentialities in terms of microwave excitation properties, frequency tuning, miniaturization and modulation data rate, studies are currently focusing on the implementation of STNOs for wireless communication applications.

FSK modulation using vortex MTJ-based STNOs, that emit in the 0.1-2 GHz range, has been first reported by Manfrini et al. in 2011 by modulating the DC current between two values at modulation frequencies up to 10MHz [25]. In 2014, the first ever complete wireless communication scheme using homogeneous MTJ-based STNOs has been recently demonstrated by Choi et al. [26], adopting non-coherent wireless communication systems based on digital On-Off Keying (OOK) modulation and envelope detection technique. They reported wireless communication with a decent data rate, 0.2Mbps, and a signal to noise ratio (SNR) of 12.5 dBm at a distance between the transmitter and receiver of 100cm. One year later, using the same wireless communication concept, R. Sharma et al. [27] were able to improve the data rate up to 4Mbps at the same communication distance as demonstrated by Choi et al. The SNR is however 6dB smaller due to the larger STNO noise. Further demonstration of a homogeneous MTJ-based STNO modulation using OOK concept on a printed board card (PCB) level has been first reported by Oh et al. in 2014 [28], resulting in communication over 10mm with the data rate of 0.4Mbps. This data rate is slightly less compared to Choi et al. and R. Sharma et al. The data rates achieved in the mentioned demonstrations above are all limited by the rising time and falling time of the electronic components in the measurement system, i.e. the bias-T, and not to the intrinsic of STNOs as mentioned in Ref. 22-24.

Another FSK concept using STNOs has been recently demonstrated by the Toshiba group [29-33] for dynamic read head applications, i.e. to read the data bit orientations in the media field. In this concept, the FSK is achieved by digital modulation of the applied field instead of the DC current as reported by Manfrini et al. This results in an enhancement of the modulation rate up to Gbps. This FSK concept would be of interest for wireless communication used in WSNs when data rates up to Gbps and more are needed. However, this additionally requires a microstructured antenna to generate the magnetic field pattern from a current pattern injected into the antenna. As a consequence, the integrated chip size for wireless communication system becomes larger and potentially consumes more power. The power consumption and the data rate trade-off thus needs to be evaluated when employing the FSK field modulation for WSN applications or wireless applications in general. .

For compact and low power WSNs, the FSK by current is more suited and will be explored in this thesis. For this, the maximum achievable data rate will be limited by the relaxation frequency of STNOs, as investigated in Ref. 22-24, which for the homogeneous MTJ-based STNO devices is on the order of a few hundred MHz and means that the maximum data rate is on the order of a few hundred Mbps. This limit remains suitable for the data rates targeted here for WSN applications which is up to 100Mbps.

The FSK modulation is better than OOK modulation in terms of noise immunity, distortion, and propagation conditions [34]. The FSK concept is thus a good strategy for STNO-based wireless communication used in WSNs. As for the demodulation, a non-coherent demodulation technique (delay detection technique) proposed by Toshiba [29,30,33] provides solutions for the poor phase noise characteristics of MTJ-based STNOs.

C. Thesis Objectives and Contributions

The objective of this thesis is to characterize the RF performances of STNOs and to study the FSK by current in STNOs for wireless communication used in WSNs. The parameters that need to be addressed are the maximum data rate (up to which the STNO frequency can follow the modulating signal), achievable frequency shift, achievable emission power and signal to noise ratio that will determine the distance of communication. In this thesis, we only address the maximum data rate and the achievable frequency shift. The STNO devices explored in this thesis for FSK-based wireless communication are homogeneous in-plane magnetized MTJ-based STNOs. For these devices, the wireless communication is targeted to achieve data rates of 10-100 Mbps with the frequency ranging from 5-10 GHz.

This thesis is part of a collaborative project on STNO technology realized within the FP7 Mosaic project. Within Mosaic, the STNO materials were deposited by the International Iberian Nanotechnology (INL) laboratory, Portugal. The nanofabrication was carried out by Leti and Spintec at the Technological Platform (PTA), Grenoble. The author’s contribution was to characterize and evaluate the RF performances of the realized STNO devices to give feedback for further development and optimization of the material deposition and nanofabrication processes, and to identify devices with good RF performances to be used for FSK measurements. Moreover, the author has carried out the macrospin simulation to investigate and characterize the maximum modulation rate of STNOs for different frequency modulation configurations, i.e. under the application of sinusoidal RF current and RF field. This suggests an important strategy for the design of wireless communication used in WSNs and how to achieve high data rate wireless communication. The author has also realized the FSK measurements for standalone STNO devices and in parallel performed the numerical simulations of the FSK scheme by digital current modulation in STNOs. In order to test the feasibility of STNOs within microwave system (RF emitter), the author has also characterized the FSK modulation of STNOs integrated within an RF emitter, in collaboration with the partner of the Mosaic FP7 project, the Technische Universität Dresden (TUD). In this work, TUD was responsible for the design and the realization of the RF emitter. The author was responsible to select STNO devices of suitable RF performances and realized the RF characterization together with Rui Ma from TUD. .

D. Thesis Organization

The thesis is organized into five chapters as follows:

- **Chapter 1** provides the theoretical background needed to understand the presented work in this thesis. The chapter starts with an introduction to STNOs, including the operating principle and their microwave properties. Next, a theoretical approach of understanding the magnetization dynamics in presence of STT is reviewed based on the direct approach of the Landau-Lifshitz-Gilbert-Slonczewki (LLGS) equation and the analytic approach of the nonlinear oscillator model described in the Kim-Tiberkvich-Slavin (KTS) model. The latter describes the power and frequency of the generated microwave signal of STNOs in the free running state (no external signals) and under the influence of external signals, i.e frequency modulation. The noise extraction method as well as the noise properties of STNOs is also described. Finally, the basic concept of modulation and the state of the art of frequency modulation of STNO are reviewed.

- **Chapter 2** is dedicated to the characterization of RF performances of STNO devices realized by different groups: Mosaic devices (realized within Mosaic project) and Hitachi devices (realized by HGST Inc., San Jose, USA). They differ by their magnetic stacks and compositions. This chapter starts with the description of the experimental setup and measurement techniques used to characterize the RF performances of STNO devices. Subsequently, STNO devices measured within this thesis will be introduced. The discussion will be then specialized for the Mosaic devices, including their nanofabrication process and optimization. Next, the RF performances of Mosaic devices and Hitachi devices are evaluated and compared in terms of their microwave excitation (single or multimode), their linewidth, their output power, and their signal stability (phase noise). The results are used to give feedback for further development and optimization of materials deposition and nanofabrication processes, and to identify devices with good RF performances to be used for FSK measurements.

- **Chapter 3** is dedicated to macrospin simulations of frequency modulation in STNOs under the application of a sinusoidal RF current (current modulation) and RF field (field modulation). The aim is to investigate and characterize the maximum achievable modulation rate for different frequency modulation configurations. As the maximum achievable data rate for current modulation in STNO has been investigated in Ref. 24, this chapter highlights the maximum data rate achievable with field modulation in STNO at different RF field orientations with respect to the static field (in-plane direction), i.e. longitudinal and transverse field modulation. First, an analytic approach based on the KTS model of current and longitudinal field modulation in STNOs is described for further understanding on different mechanisms of frequency modulation in both configurations. Next, numerical simulations of field modulation in STNOs are presented. This starts with the description of the simulation parameters which are chosen in order to stay close to situations of experiments and applications and also to stay within the validity range of the analytical model. Next, the extraction method of the maximum achievable data rate from numerical simulation is presented. The results are discussed and compared with the analytical model. As additional studies, the maximum achievable data rate as a function of applied RF field angle and the dependence of the modulation peaks as a function of the modulation strength are also presented and discussed.

- **Chapter 4** presents the studies of FSK by digital current modulation in STNOs for wireless communication used in WSNs. This starts with the introduction of the FSK communication scheme using STNOs. In this part, the FSK concept and the delay detection technique proposed by Toshiba are described. The study of FSK modulation in STNOs is divided into three parts. The first part is dedicated to numerical simulation of FSK by digital current modulation in STNOs. The second part is the experimental demonstration of FSK current modulation on standalone STNOs. The STNOs with different types of nanofabrication are measured and compared in terms of the modulation capabilities, i.e. frequency shift and modulation rate. The calculation of delay detection of the modulated signal is also presented to read back the digital input. The last part is the FSK measurements of STNOs within microwave system, i.e. RF emitter card. The same analysis is done as mentioned for FSK measurements on standalone STNOs. The measurements are done using STNOs from different types of nanofabrication. The frequency shift performance and the corresponding modulation rate are characterized. The demodulation is done numerically using the delay detection to read back the digital input signal.

- **Chapter 5** summarizes the simulation and experimental results of this thesis and gives an outlook on potential future investigations and perspectives.

Chapter I
Literature Review

This chapter gives fundamental aspects of Spin Torque Nano-Oscillators (STNOs) which are important for the understanding of the results of this thesis. This starts by a brief introduction to spintronics, with emphasis on magneto-resistance (MR) and the spin transfer torque (STT) effect. It will be shown how these concepts are used to define the STNO capable of generating a high frequency voltage signal. The understanding of the magnetization dynamics of STNOs described by the Landau-Lifshitz Gilbert equation including the STT term (LLGS) will also be discussed. In order to understand the nonlinear dynamical processes taking place in STNOs, the analytical model derived from the transformation of LLGS equation to complex c-variables will be reviewed. In particular, the model describes the power and frequency of STNO as a function of DC current and DC field, predict the magnitude and properties of the generation linewidth, and also explain the STNO behavior under the influence of periodic and stochastic external signals. This provides the understanding of basic analytic model for STNO that can be developed for any different cases, i.e. STNO behavior under the influence of RF field that will be investigated in Chapter 3. Finally, the research advance of STNO-based applications will be discussed to better understand the motivation and objective of this thesis.

1.1 Introduction to Spintronics

The advent of improved thin-film deposition and nano-structuration systems have led to an emerging field of nanoelectronics called spin electronics or also called Spintronics. Spintronics exploits the spin degree of freedom of conduction electrons and their interaction with magnetization to control the flow of electrons and magnetization state of nanoelectronic devices, which are made from magnetic thin film heterostructures. Spintronics research following the discovery of the giant magnetoresistance (GMR) effect in the late 1980s [35,36], which exhibits magnetic field dependent changes in resistance of magnetic thin film heterostructures, composed of two ferromagnetic layers separated by a non-magnetic spacer (a normal metal layer). This discovery was followed, in 1997, by the commercial introduction by IBM (Stuart Parkin and his colleagues) of novel magnetic field sensors in hard disk drive (HDD) read heads. The GMR head enabled HDD to read smaller data bits, which boosted the areal density of HDD with 16.8 GB of storage. For this reason, the discovery of GMR was honored with the Nobel Prize in Physics in 2007 to Albert Fert and Peter Grünberg and with the Millennium Technology Prize to Stuart Parkin in 2014 [37].

A few years later, due to the advances in the thin film growth and device fabrication, an even more significant effect, called the tunneling magnetoresistance (TMR) effect, i.e. a phenomenon where electrons tunnel through a thin insulating layer, was observed at room temperature in magnetic tunneling junctions (MTJs) [38,39]. In MTJ-devices, the non-magnetic spacer layer in a GMR-device is replaced by this insulating layer. Because of their huge variation in the electrical resistance (high TMR), which is almost 100 times larger than that from a GMR-device, MTJs promise attractive applications in magnetic field sensor and magnetic random access memory (MRAM) in very small scale. The read heads with MTJs in HDD has been commercially available with the areal density up to terabytes and more of storage. MRAMs based on MTJs were first commercialized by Everspin in 2006 [40,41], which uses the magnetic moments for storing data. As the magnetic bit will not lose its magnetization over time, it can retain information without consuming any power (it is “non-volatile”). The reading and writing of data are done electrically (unlike the mechanical reading and writing in hard drives), which allows a high sensitivity with a reduced energy consumption and fast operation speed.

Another important breakthrough of spintronics is the discovery of spin transfer torque (STT) effect by Slonczewski [4] and Berger [5] twenty years ago. The STT effect has received much attention since its theoretical prediction was experimentally verified in 2000 [42-44]. Slonczewski and Berger predicted independently a way to control the magnetization state of magnetic thin film heterostructures based on the spin-transfer-torque (STT) effect from a spin-polarized current instead of an applied field, leading to several possible applications. The angular momentum carried by the spin-polarized current exerts a torque on the local magnetization inducing either magnetization reversal or steady state magnetization precession. The current-induced switching (reversal) is of interest for future MRAMs (STT-MRAM) since commutation between the two states of the memory can be directly driven by an electrical current, thanks to the spin transfer torque effect. Hence, this could improve the scalability of MRAM. There are significant progress and many ongoing efforts to realize STT-MRAM [45-49]. They are seen as high impact applications either as standalone memories to replace other random access memories or embedded in complementary metal-oxide-semiconductor (CMOS) logic.

Another important consequence of STT effect is the large angle steady state magnetization oscillations of the thin magnetic heterostructures. By using the magnetoresistance (MR) effect, these oscillations are converted into an oscillatory output signal at high-frequency, ranging from 100MHz to several tens of GHz. This STT effect and MR effect together enables new type of high-frequency tuneable nanoscale oscillators, namely spin-torque nano-oscillators (STNOs). The first steady-state precession of the magnetization in thin magnetic heterostructures, at frequencies of a few GHz, were detected by Tsoi et al. [7] in a point-contact geometry and then it was directly observed in nanoscale device structures by Kiselev et al. [6] and Rippard et al. [15]. After these experimental demonstrations, it has rapidly become clear that the steady state oscillations in the microwave range were generated, whose frequency depends on the applied current or external magnetic field. This frequency tuning properties is desirable for RF applications. Therefore, STNOs are seen as promising technologies that propose solutions for low power, high frequency tunability, cost effective, and compact RF components and systems. Many research efforts are currently being devoted to improve the RF performances of STNOs (output power and phase noise) and to test their feasibility in the microwave system.

In this thesis, the study is focused on the STNO spintronics devices for wireless communication application. The STNO devices studied in this thesis are nanopillar MTJ devices. In the following, the basic concepts of spintronics for an overall understanding of the STNOs will be discussed. It starts with the origin of ferromagnetism in materials composed by 3d elements which is used in spintronics devices. This will be followed by an introduction to spin dependent transport phenomena, with a focus on tunneling transport and the corresponding tunnel transport models. Afterwards, the spin transfer torque effect which is responsible for the steady state oscillations in STNOs will be discussed.

1.1.1 Ferromagnetism in 3d transition metals

The macroscopic magnetic properties of materials are a consequence of magnetic moments associated with individual electrons [50]. In addition to mass m_e and charge e, an electron has an additional degree of freedom, the electron spin. Each electron in an atom has magnetic moment $\boldsymbol{\mu}$ originates from the orbital motion and the spin of the electron. The orbital motion of the electron around the nucleus having a magnetic moment $\boldsymbol{\mu_0}$ along the axis of rotation, given by:

$$\boldsymbol{\mu_0} = -\frac{\mu_B}{\hbar}\boldsymbol{L} \tag{1.1}$$

Where μ_B is the Bohr magneton given by $\mu_B = \frac{e\hbar}{2m_e}$ and $\boldsymbol{L}$ is the angular momentum of the orbital electron which is antiparallel (opposite direction) to the orbital magnetic moment, $\boldsymbol{\mu_0}$. In quantum mechanics, the orbital angular momentum $\boldsymbol{L}$ is quantized in units of $\hbar$ (reduced Planck constant). By analogy with orbital magnetic moment, the magnetic moment originating from the electron spin, $\boldsymbol{\mu_s}$, which is directed along the spin axis, is given by the formula:

$$\boldsymbol{\mu_s} = -\mathrm{g}\frac{\mu_B}{\hbar}\boldsymbol{S} \tag{1.2}$$

With g is the the Lande-factor and $\boldsymbol{S}$ is the spin angular momentum or simply spin, characterized by a spin quantum number $\boldsymbol{s} = \pm 1/2$, i.e. $\boldsymbol{S} = \hbar\boldsymbol{s}$. Due to its quantum nature, the spin of the electron can only point up (spin-up) or down (spin-down).

The spin of the electrons in atoms is the main source of ferromagnetism. In ferromagnetic materials, the magnetic moment of adjacent atoms tends to align spontaneously due to a quantum mechanical effect called exchange interaction which arises from the Coulomb interaction between electrons and Pauli's exclusion principle. The alignment of spin magnetic moments in a system gives rise to a spontaneous magnetization, even when in the absence of a magnetic field. The magnetization $\boldsymbol{M}$ in a material of volume V is expressed in terms of density of net magnetic moments, $\boldsymbol{\mu}$.

$$\boldsymbol{M} = \frac{1}{V}\int_{v} \boldsymbol{\mu} dV \tag{1.3}$$

In ferromagnetic metals like Co, Fe, and Ni, magnetization is better described with band theory, also known as the free electron model, which was initially developed by Stoner and Slater [51]. In this model, the exchange interaction results in a spitting of energy band ΔE. As a consequence, the numbers of filled spin-up (↑) and spin-down (↓) are unequal, as illustrated in Fig. 1.1. This leads to the asymmetry in density of states (DOS) for the majority (spin-up (↑)) and minority spin (spin-down (↓)) at Fermi energy, E_F, and gives rise to a spin polarized current: electrons are less scattered when their spin moment is parallel to the local spin than when it is antiparallel.

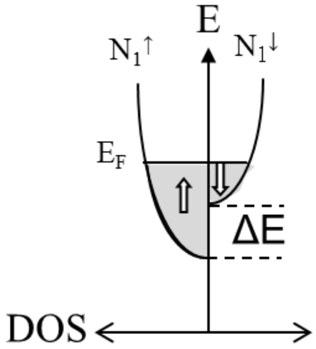

Fig. 1.1-Schematic of DOS in a ferromagnetic 3d transition metal

The degree of spin polarization P in ferromagnets is defined as:

$$P = \frac{N^{\uparrow} - N^{\downarrow}}{N^{\uparrow} + N^{\downarrow}} \tag{1.4}$$

where $N^{\uparrow}$ and $N^{\downarrow}$ is the density of states (DOS) of majority spin and minority spin at the Fermi level. The quantity of spin polarization in ferromagnets is important for the efficiency of spin-dependent effects such as magnetoresistance effects or the spin-transfer torque in MTJs.

1.1.2 Tunneling magnetoresistance (TMR)

A magnetic tunnel junction (MTJ) consists of two ferromagnetic (FM) layers, called electrodes, separated by a very thin insulating layer (IL), called tunnel barrier. The thickness of the barrier ranges from a few angstroms to a few nanometers, allowing electrons to tunnel through the dielectric layer. The concept of tunnel transport or spin dependent tunnelling was introduced by Tedrow and Mersevey in 1971 [52] and four years later Julliere [53] measured the tunnel magnetoresistance (TMR) in Fe-Ge-Pb and Fe-Ge-Co structures at 4.2K. A change in the resistance of 14% as a function of the external magnetic field was found by Julliere. Julliere proposed a phenomenological model, where the spin is conserved during the tunneling process. As a consequence, the spin up(down) electrons from one electrode, FM_1, must tunnel into the up(down) states available in the other electrode, FM_2, as illustrated in In Fig. 1.2. The tunneling probability for a single electron of the first electrode is proportional to the DOS of available empty states at the second electrode. In the parallel state (Fig. 1.2a), the electrodes present the same DOS for their majority and their minority band, respectively. The majority(minority) electrons of the first electrode (FM_1) tunnel to the majority(minority) electrons of the second electrode (FM_2). In this configuration, the tunnel conductance, G_P, is dominated by the majority electrons. Since there is large number of states available in the majority electrons, the tunnel conductance in parallel configuration is large and thus, the resistance, R_P, is low. In the antiparallel state (Fig. 1.2b), the majority(minority) band electrons can only tunnel to the minority(majority) band electrons of the second electrode. In this case the conductance, G_{AP}, is dominated by a mix between minority and majority band electrons. Due to the reduced number of states available for the antiparallel configuration, the conductance is low and the resistance, R_{AP}, is large. Hence, the tunneling conductance and thus the resistance of MTJs depend on the relative orientation of the magnetization of the electrodes with respect to each other, as expressed as follow:

$$G_P = N_1^{\uparrow} N_2^{\uparrow} + N_1^{\downarrow} N_2^{\downarrow} \tag{1.5a}$$
$$G_{AP} = N_1^{\uparrow} N_2^{\downarrow} + N_1^{\downarrow} N_2^{\uparrow} \tag{1.5b}$$

where N_i^{σ} is the density of states (DOS) at the ferromagnetic layers i for the spin direction σ at the Fermi level. The corresponding tunneling magnetoresistance ratio (TMR) is defined as:

$$TMR = \frac{G_P - G_{AP}}{G_{AP}} = \frac{R_{AP} - R_P}{R_P} \tag{1.6}$$

The relation between the TMR ratio and the spin polarization P of both electrodes is described by the Julliere model:

$$TMR = \frac{2P_1 P_2}{1 - P_1 P_2} \tag{1.7}$$

where P_1 and P_2 and are the spin polarization factors (given by Eq. 1.4) for the two electrodes, respectively. Therefore, the higher the spin polarization of the electrodes the larger the effect and if $P_1 = P_2 = 1$, the TMR ratio is infinitely high.

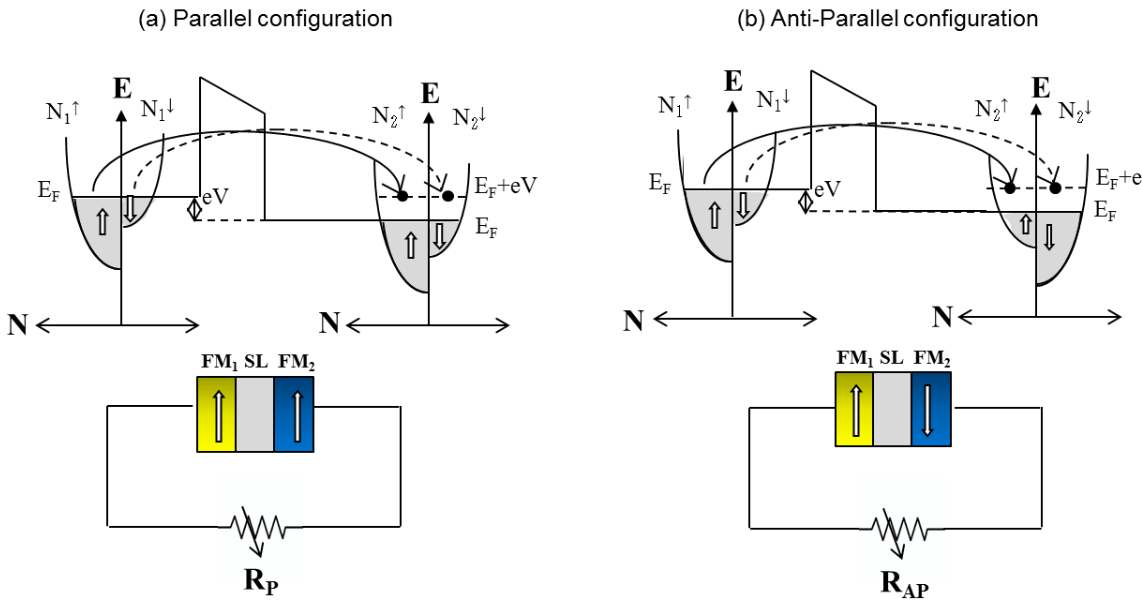
(a) Parallel configuration

(b) Anti-Parallel configuration

Fig. 1.2-Schematic representation of the tunneling process in (a) the parallel configuration and (b) the anti-parallel configuration of the two electrodes. These two band models supposes the existence of an effective barrier potential, eV. FM_1, SL, FM_2 correspond to first ferromagnetic layer, insulating spacer layer (a tunnel barrier), and second ferromagnetic layer, respectively.

In reality, the Julliere model is a simplification and the magnitude of the TMR ratio depends additionally upon the effective polarization of the electrode surfaces, the quality of the interfaces between the electrodes and the barrier, and the properties of the barrier itself. A more realistic model was proposed by Slonczewski [54], which takes into account these factors. Slonczewski expressed Eq. 1.7 by writing the transmission coefficient for each spin when taking into account the effective polarization of the DOS at each ferromagnetic/insulator interface:

$$P_i = \frac{(k_\uparrow - k_\downarrow)(\kappa^2 - k_\uparrow k_\downarrow)}{(k_\uparrow + k_\downarrow)(\kappa^2 + k_\uparrow k_\downarrow)} \qquad (1.8)$$

Where $k_\uparrow$ and $k_\downarrow$ depends on the Stoner energy, $\kappa^2 = 2m_e(U_0 - E_F)/\hbar$ is the effective barrier height and U_0 is the total barrier height. Using this formalism, the angular dependence of the conductance G through an insulating barrier of width d, is given by:

$$G(\theta) = G_0[1 + P_1 P_2 cos\theta)] \text{ with } G_0 \propto e^{-2\kappa d} \qquad (1.9)$$

When κ is large, the Slonczewski model (Eq. 1.8) is equivalent to the Juliere model for infinite barrier height, U_0 is large.

The improvement of deposition techniques since the first experience of Tedrow and Julliere, has allowed the fabrication of MTJ structures showing large TMR at room temperature. A reproducible large TMR (~18%) at room temperature was achieved in MTJs with an amorphous Al_2O_3 [55,56]. Ever since then, many researches in spin dependent tunneling have focused on MTJs with an Al_2O_3 as a tunnel barrier [57-59]. Although intensive efforts in such MTJs showed that the maximum TMR only reached about 70% [60,61]. Meanwhile, extensive theoretical and experimental work has been carried out to increase the TMR by studying crystalline tunneling barriers [62,63].

Butler *et al.* carried out first calculations of a TMR ratio higher than 1000% in Fe(001)/ MgO/ Fe(001) crystalline junctions [62]. This enhanced TMR is due to the coherent tunneling process in MgO barrier. In Fe(001)/ MgO/ Fe(001) crystalline tunnel junctions, the electrons propagate or tunnel within specific electronic Bloch state (Δ_1 for majority electrons, Δ_2 and Δ_5 for the minority electrons), as illustrated in Figs. 1.3a,b. Its tunneling conductance depends strongly on the symmetry of the Bloch states in the electrodes and of the evanescent states in the barrier. Thus Bloch states of different symmetry decay at different rates within the barrier. The Δ_1 state decays slowest among all the states and can make a significant contribution to the tunneling conductance.

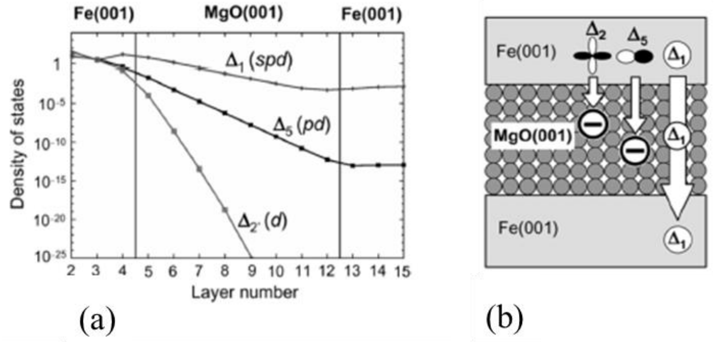

(a) (b)

Fig. 1.3-(a) Evolution of the density of states as a function of the numbers of MgO layers. Adapted from [62]. (b) Schematics of the electrons tunneling through (a) amorphous Al-O barrier and (b) crystalline MgO (001) barrier. Adapted from Yuasa [64]

The discovery of a high TMR in MTJ due to MgO produced the reorientation of research towards the improvement in the MgO deposition with a good texture with adjacent ferromagnetic layers. The most successful MTJs to date have used (001) MgO barriers with recrystallized body centered cubic (bcc) CoFeB electrodes, which have MR ratios of 200%–600% at room temperature and over 1000% at 4.2K [65-67]. The advantage of CoFeB electrodes is that after deposition, the CoFeB/MgO/CoFeB stack is amorphous. In order to generate a lattice matching i.e crystallize the two CoFeB electrodes in the bcc MgO(001) structure, it is necessary to anneal the devices. In a MTJ device with very low resistance area (RA), studied in this thesis, the annealing is fundamental to obtain high TMR but it gives rise to several problems such as the degradation of the MgO barrier (pinholes) due to the Boron diffusion to the grain boundaries [67,68]. In order to protect the MgO barrier against Boron diffusion, the CoFeB can be replaced by CoFeB/CoFe and CoFe/CoFeB bilayers respectively, using a thin CoFe layer (≈0.5nm) at the interface to MgO. As shown in Ref. 69 this can increase the TMR from 105% to 192%.

1.1.3 Spin transfer torque (STT)

The previous section describes the TMR effect in MTJs which can be considered as a control of current flow via the magnetization state. The reverse effect, called the *spin transfer torque (STT) effect*, is the control of magnetization state through a spin polarized current. In other words, in a thin magnetic heterostructure device, there are two spintronics effects, MR effect and STT effect, leading to various applications, i.e. magnetic sensor in HDD read head, MRAM, STT-MRAM, STNOs, etc. Hence in order to observe the STT effect, it requires the same magnetic heterostructure as MR effect, i.e. two ferromagnetic layers FM_1 and FM_2, separated by a thin spacer SL (either a metallic layer or a tunnel barrier). The physic origin (in the macrospin approach) and the effect of STT in the magnetization state of such thin magnetic heterostructure are shown in Fig. 1.4. A microscopic picture of spin transfer torque can be found in [70-72].

Consider a thin magnetic heterostructure, illustrated in Fig. 1.4a, with the magnetizations of both ferromagnetic layers, $\boldsymbol{M}_1$ and $\boldsymbol{M}_2$, are misaligned at angle θ. An electrical current passes through the structure, perpendicularly to the interfaces, with electrons flowing from the left (ferromagnetic layer FM_1) to the right (ferromagnetic layer FM_2). Electrons flowing in FM_1 are spin polarized along the direction of the magnetization $\boldsymbol{M}_1$ and carry a magnetic moment $\boldsymbol{\mu}_1$ ($\boldsymbol{\mu}_1$ parallel to $\boldsymbol{M}_1$), once they have passed through FM_2 their magnetic moment rotates to align with the direction of the magnetization $\boldsymbol{M}_2$. The outgoing magnetic moment is now $\boldsymbol{\mu}_2$.

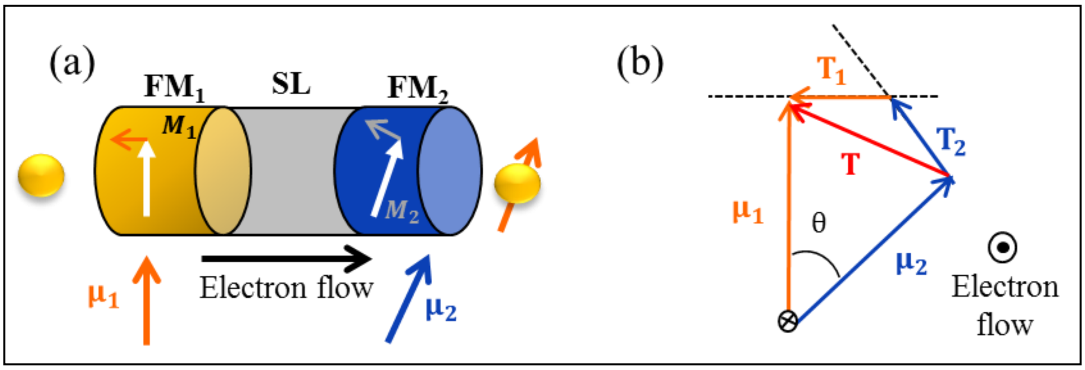

Fig. 1.4-(a) Illustration of spin transfer torque in magnetic heterostructures, consisting of two ferromagnetic layers, FM_1 and FM_2, (their magnetization is aligned by an angle θ) separated with a

NM layer as spacer layer SL. (b) Schematic of the transferred angular momentum ($\boldsymbol{T}$) in the magnetization of the ferromagnetic layer FM$_2$ which is then decomposed in two parts $\boldsymbol{T}_1$ and $\boldsymbol{T}_2$ respectively acts on the magnetization of the first ferromagnetic layer $\boldsymbol{M}_1$ and the second ferromagnetic layer $\boldsymbol{M}_2$. Adapted from [72].

The rotation of the conduction electron moments, $\boldsymbol{\mu}_1$ and $\boldsymbol{\mu}_2$, is due to a torque applied by the local magnetizations FM$_1$ and FM$_2$ respectively. Hence, the local magnetizations feel an equal and opposite torque. The transverse component of the conduction electron moment $\boldsymbol{T}_1$ and $\boldsymbol{T}_2$ (see Fig. 1.4b) is transferred to the local magnetizations. This spin-transfer torque on the magnetization leads to the change in spin momentum of the localized moment per second. However the length of the magnetization vectors, $\boldsymbol{M}_1$ and $\boldsymbol{M}_2$, are conserved:

$$\frac{d|\boldsymbol{M}|^2}{dt} = 2\boldsymbol{M}.\frac{d\boldsymbol{M}}{dt} = 0 \tag{1.10}$$

It results that any variation of magnetization $\frac{d\boldsymbol{M}}{dt}$ is necessarily transverse to the magnetization. The total transferred angular momentum $\boldsymbol{T}$ in the system is a sum of two moments $\boldsymbol{T}_1$ and $\boldsymbol{T}_2$, where $\boldsymbol{T}_1$ is a torque transferred to $\boldsymbol{M}_1$ and $\boldsymbol{T}_2$ is a torque transferred to $\boldsymbol{M}_2$. In practice, the magnetization of FM$_1$ is designed to be fixed (polarizing layer PL) for example by using a Synthetic Anti-Ferromagnetic (SAF) structure [73-75] or a thick electrode FM$_1$, in order to make FM$_1$ less susceptible to spin torque and mainly serves as a polarizer to provide spin polarization. Whereas, the magnetization of FM$_2$ is usually thin and can be excited by spin torque, called as free layer FL. In this case, the spin torque acting on the free-layer magnetization $\boldsymbol{m}$ due to the misalignment with the polarizing layer magnetization $\boldsymbol{p}$ is given by two terms. The first term, called the 'spin transfer torque STT term $\boldsymbol{T}_{\parallel}$', corresponds to a transfer of the transverse component of the spin momentum that lies in the plane of $\boldsymbol{m}$ and $\boldsymbol{p}$, while the second term, called field-like term $\boldsymbol{T}_{\perp}$, corresponds to a transfer of the transverse component that is perpendicular to the plane of $\boldsymbol{m}$ and $\boldsymbol{p}$. The spin torque $\boldsymbol{T}_s$ including two terms is described as follow:

$$\boldsymbol{T}_s = \boldsymbol{T}_{\parallel} + \boldsymbol{T}_{\perp} = \gamma_0 a_j \boldsymbol{m} \times (\boldsymbol{m} \times \boldsymbol{p}) + \gamma_0 b_j (\boldsymbol{m} \times \boldsymbol{p}) \tag{1.11}$$

Here, $\boldsymbol{m}$ is the unitary magnetization vector of the free layer given by $\boldsymbol{m} = \frac{\boldsymbol{M}}{M_s}$ with M_s is the spontaneous magnetization. γ_0 is the gyromagnetic factor, a_j is the spin torque amplitude proportional to the applied current, and b_j is the prefactor of the field-like term depending on the net current charge. In this thesis, the contribution from b_j will be neglected, as it is assumed that b_j does not have strong impact on the dynamics of MTJ-based STNOs, $\frac{a_j}{b_j} \ll 1$. This assumption is justified by the maximal value encountered in MTJ for b_j, which is 30% the value of a_j [74].

1.2 Magnetization Dynamics

It has been introduced the physic origin of spin transfer torque STT in thin magnetic heterostructures. In this section the effect of STT on magnetization dynamics of STNOs in the macrospin approximation will be discussed. This Section starts with the introduction of Landau-Lifsthitz-Gilbert-Slonczewski (LLGS) equation. The constant energy trajectory obtained by solving the LLGS equation will be discussed. The evolution of magnetization dynamics under external control parameters, applied field and applied current density, will be shown for the case of zero temperature and finite temperature.

1.2.1 Introduction to LLGS equation

The magnetization dynamics is described by the Landau-Lifshitz-Gilbert equation, that includes the conservative precession of the magnetization and the damping torques (first two terms of eq. 1.12). In order to take the effect of spin transfer into account, the longitudinal spin torque $\boldsymbol{T}_{\parallel}$ is included to the LLG equation (third term of eq. 1.12), thus leading to the Landau-Lifsthitz-Gilbert-Slonczewski (LLGS) equation as given by eq. 1.12, i.e. The b_j term is neglected, two magnetization dynamical modes occur under the influence of STT in its simplest form ($a_j \propto J_{app}$).

$$\frac{d\boldsymbol{m}}{dt} = -\gamma_0\left(\boldsymbol{m} \times \boldsymbol{H_{eff}}\right) + \alpha\left(\boldsymbol{m} \times \frac{d\boldsymbol{m}}{dt}\right) - \gamma_0 a_j \boldsymbol{m} \times (\boldsymbol{m} \times \boldsymbol{p}) \tag{1.12}$$

Here γ_0 is the gyromagnetic factor given by $\gamma_0 = \mu_0\gamma = 2.21x10^5\ \frac{m}{As}$ with μ_0 is vacuum permeability. α is the natural damping constant, M_s is the saturation magnetization and a_j is the spin torque amplitude proportional to the applied current density J_{app} given by the general expression:

$$a_j = \frac{\hbar}{2e}\frac{J_{app}}{\mu_0 M_s t}\eta \tag{1.13}$$

Where, t is the thickness of the STNO device and η is the spin polarization value.

$\boldsymbol{H_{eff}}$ is the effective field given by the negative gradient of the free energy density E with respect to the unitary magnetization vector $\boldsymbol{m}$, $\boldsymbol{H_{eff}} = -\frac{1}{\mu_0 M_s V}\frac{\delta E}{\delta \boldsymbol{m}}$. It is important to note that the free energy density E is the sum of all potential energies E_i resulting from any fields $\boldsymbol{H}_i$ acting on $\boldsymbol{m}$. For STNO devices the most important energy E terms are (i) the Zeeman energy, $E_{app} = -\mu_0 M_s V \boldsymbol{m}\boldsymbol{H_{app}}$, due to an external applied bias field $\boldsymbol{H_{app}}$, (ii) the demagnetization energy due to geometry of the sample, E_d, (iii) the anisotropy energy due to crystalline or interfacial energies E_u, and (iv) the exchange energy due to spin-dependent quantum mechanical interactions E_{ex}. Detail of each contribution fields can be found for instance in [71]. In the case of single domain or macrospin model, the exchange interaction is assumed to be sufficiently strong so that all of the magnetic moments in a device layer are aligned and move together. In this model the magnitude of the moment is constant in time. Since the exchange energy is negligible $\boldsymbol{H_{ex}} = 0$, the effective field can be described as follow:

$$\boldsymbol{H_{eff}} = \boldsymbol{H_{app}} + \boldsymbol{H_d} + \boldsymbol{H_u} \tag{1.14}$$

Due to the demagnetization and anisotropy contributions to the effective field $\boldsymbol{H_{eff}}$, the equilibrium orientation of the magnetization $\boldsymbol{m}$ will be different from the direction of the applied field $\boldsymbol{H_{app}}$.

A simple illustration of the evolution of the magnetization dynamic under the LLGS equation is given in Fig. 1.5. The magnetization dynamic under the torque $\boldsymbol{T}$ exerted by a magnetic field $\boldsymbol{H_{eff}}$ is given by the first term in the right-hand side of eq. 1.12 (conservative term). The term says simply that the magnetization $\boldsymbol{m}$ precesses around the effective magnetic field $\boldsymbol{H_{eff}}$ at a constant energy trajectory (constant magnitude), i.e. closed loop trajectory, as illustrated in Fig. 1.5a (red curve). The second term is a relaxation term and describes the energy losses (energy dissipation) due to interaction of the magnetization with its environment. The parameter that characterizes the losses is the Gilbert damping constant α. It should be noted that α is rather small, α ~ 0.01 in typical magnetic materials used for spin torque experiments. The damping torque itself is, usually, comparable in magnitude with the spin transfer torque and much smaller than the conservative precessional torque $-\gamma_0[\boldsymbol{m} \times \boldsymbol{H_{eff}}]$. Hence, the damping term can be considered as a small perturbation to the precessional term. From any initial position, the damping torque will relax the magnetization towards its energy minimum (low energy state), i.e. realigned with the local effective field, on a timescale given by αM_s (few nanoseconds). The effect of damping on the overall trajectory is shown in Fig. 1.5b. As the magnetic moment relaxes, it will sample a family of nearly constant energy orbits. To first approximation, these are the orbits that are stabilized by the transfer of spin, STT, from the applied current. This STT, i.e. described by the last term of eq. 1.12, can be either as an energy source or an additional dissipative (or damping) contribution for the system, depending on the current sign. In the case of an energy source or gain, the STT cancels and compensates the damping torque and thus brings the magnetization into the steady state precession (closed loop trajectory), as illustrated in Fig. 1.5c. In contrast to this, in the case of an additional dissipation, the STT enhances the damping torque and relaxes the magnetization towards the energy minimum.

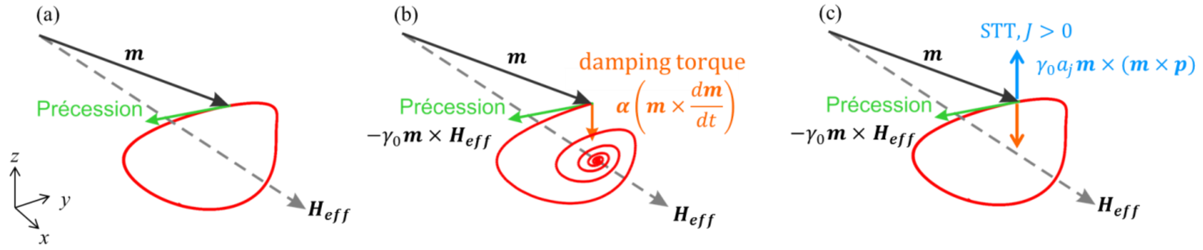

Fig. 1.5-Illustration of the evolution of the magnetization dynamic (red curve): (a) conservative precession term (b) negative damping (dissipative term) (c) STT term, i.e. STT cancels the negative damping torque. Adapted from [76].

The illustration above is a very general picture of magnetization dynamic in the presence and the absence of damping term and spin transfer torque term. In the next Subsection, the solution of LLGS equation within the macrosin approach will be discussed in order to get a more intuitive macrospin description of the magnetization dynamic for magnetic thin film geometry, by considering special trajectories and their frequencies. Here the simplest magnetic thin film geometry, i.e. an in-plane magnetized MTJ configuration, where the free layer and polarizing layer are in-plane magnetized, is considered which corresponds to the devices studied in this thesis (Fig. 1.6). In coordinate system, the free magnetic layer lies in the x-y plane, axis z is normal to the thin film plane, and the easy axis of the in-plane anisotropy is along the x axis. The in plane rotation is characterized by the spherical angle φ and the out plane rotation is characterized by the spherical angle θ.

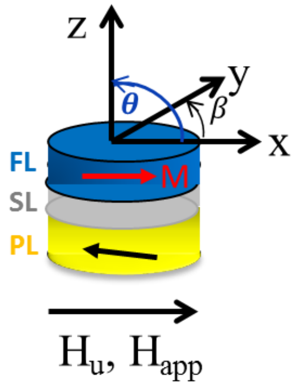

Fig. 1.6-Left: definition of the (x, y, z) coordinate system and the spherical angles φ, θ. Right: the free layer considered is an in-plane magnetized thin film.

A uniaxial magnetocrystalline (MCA) anisotropy field $\boldsymbol{H_u}$ along x-axis direction is considered of amplitude K_u (K_u>0), $\boldsymbol{H_u} = \frac{2K_u}{\mu_0 M_s}(m_x \quad 0 \quad 0)$. The demagnetizing effect are included by the demagnetizing tensor $\overleftrightarrow{\boldsymbol{N}} = (N_{X,}N_Y, N_Z)$. For a nanopillar geometry, $\boldsymbol{H_d}$ is assumed in the z-axis direction, $\boldsymbol{H_d} = -M_s(0 \quad 0 \quad N_Z m_Z)$. The external applied field, $\boldsymbol{H_{app}}$, is applied parallel to the easy axis of the in-plane anisotropy (in the x-direction) so that $\boldsymbol{H_{app}} = (H_{app,x} \quad 0 \quad 0)$. The magnetic energy density E of this system can be written as the sum of the anisotropy, demagnetizating (magneto-dipolar), and applied field energies:

$$E = K_u[1 - m_x^2]V + \frac{1}{2}\mu_0 M_s^2(N_z m_z^2)V + -\mu_0 M_s H_{app} m_x V \tag{1.15}$$

With $(m_x, m_y, m_z) = (cos\theta cos\varphi, cos\theta sin\varphi, sin\theta)$

1.2.2 Constant energy trajectories

Since the damping torque and the spin torque are small as compared to the precession (conservative) torque, a first approximation to the magnetization precession trajectories at constant energy trajectories (eigenmodes of the undamped system) can be made. In a macrospin description, the constant energy trajectories of the magnetization dynamics are determined by the conservative precession term (first term) of LLGS eq. 1.12, (i.e. for α=0 and a_j=0). The solution of the precession term for a given initial energy density E_0 (eq. 1.15) yields the static and periodic solutions which are shown in Fig. 1.7. There are three static states, see Figs. 1.7a,b, (defined by $\frac{\partial \boldsymbol{m}}{\partial t} = 0$) which are the in-plane energy minimum (along the in-plane easy axis), the out of-plane energy maximum (representing the demagnetization energy cost when rotating M perpendicular to the film plane) and the saddle point (in-plane hard axis). Preparing the system initially in one of these three static states, the system does not change and remain in its initial state (constant energy). When perturbing the system, the magnetization will follow period orbits around either the energy minimum or the energy maximum as indicated by the colored lines in Figs. 1.7a,b. The precession around the energy minimum (m_x=±1) is generally called in-plane precession (IPP) since the energy minimum of a thin magnetic film is in-plane (Fig. 1.7a) and the precession around the out-of-plane energy maximum is called out-of-plane precession (OPP) (Fig. 1.7b) [70-72,77]. The IPP magnetization trajectories are described by a windscreen wiper motion in a counter-clockwise oscillation sense. The in-plane excursion angle φ of IPP mode trajectories increase with increasing initial energy E_o. When the trajectories pass through the energy saddle points (in-plane hard axis), the trajectories bifurcate into two energetically equivalent OPP modes (one for positive m_z and one for negative m_z). These OPP modes trajectories are described by a circular motion, or a tilted circular motion in a clockwise rotation sense around the energy maximum.

Due to the non-linearity of the equation of motion, $\boldsymbol{H_{eff}}\ (\boldsymbol{m})$, there is a strong dependence of the precession frequency on the precession amplitude, which is different for the IPP and OPP mode, as given in Fig. 1.7c. They are plotted as a function of the initial energy E_o, expressed by the maximum m_z^+ value on the trajectory. For IPP mode, the frequency decreases with increasing amplitude of initial energy (redshift) since the length of the orbit increases faster than the local velocity. Close to the saddle point, the local velocity goes to zero, explaining the zero frequency at the transition from IPP to OPP. For the OPP mode the frequency increases with increasing amplitude (blueshift). The frequency value is given by the out-of-plane demagnetization field which is proportional to the out-of-plane magnetization component m_z.

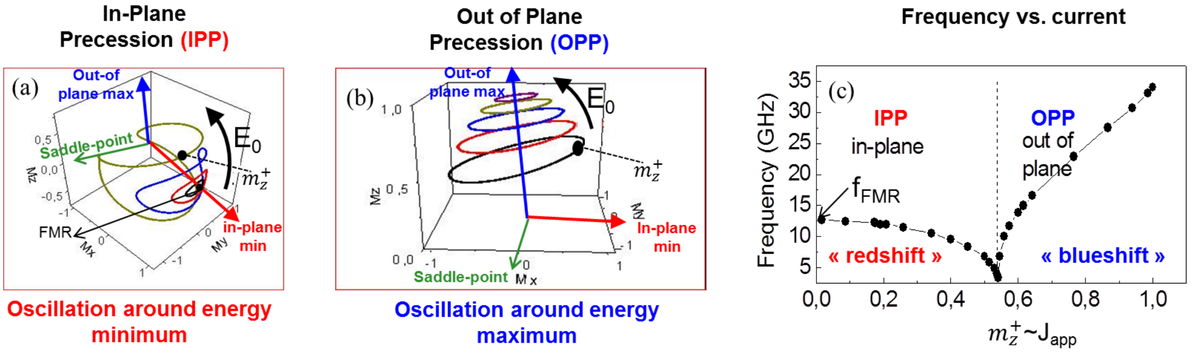

Fig. 1.7-(a) Conservative IPP and (b) OPP oscillations as a function of the initial energy E_o. (c) Precession frequency for conservative IPP and OPP oscillations as a function of the initial energy E_o, expressed by the maximum m_z^+ value on the trajectory. Adapted from [72].

Adding damping in the system, the magnetization dynamics are determined by the conservative precession term (first term) and the damping term (second term) of LLGS eq. 1.12, (i.e. for α=0.01-0.02 depending of the materials and a_j=0). The precession term will change the stability of the three static solutions. Now, only the energy minimum is stable, leading to IPP oscillations at small precession angles around the energy minimum. This means that the energy maximum and saddle point are not stable against small perturbations (the damping term can be considered as a small perturbation to the precessional term), which will relax the magnetization on a spiral orbit away from the energy maximum or the saddle point towards the stable energy minimum. These small IPP precession angles correspond to the FMR excitations and are indicated for comparison in Fig. 1.7a.

Including the STT in the system, i.e. full LLGS equation, their contribution can be either, an energy source for the system if the spin-torque opposes the damping torque, or an additional dissipation (or damping) contribution if the spin-torque torque has the same direction as the damping torque. In the case of an additional dissipation, the motion is damped and thus the static state in the energy minimum is stable, i.e. in the in-plane magnetized MTJ configuration, the spin polarization $\boldsymbol{p}$ is collinear to the effective field $\boldsymbol{H_{eff}}$ of the free layer energy minimum. In contrast to this, for the case of an energy source, the motion is excited away from the static state and thus the static state is unstable. Upon increasing the current density from zero, an initially stable state can become unstable. The current value for which this occurs is called the critical current J_{th}. When the initial static state become unstable, the magnetization can either transit into another static state or into a dynamic state, depending on the current amplitude. It is important to note that the STT does not change the energy surface, the STT moves the magnetization along the energy surface until the magnetization stabilizes on a periodic orbit defined by the precession term (see Figs. 1.7a,b). For further understanding on the transition from the static state to a dynamic state, the illustration of the general features of the dynamic state for the case of in-plane magnetized magnetic thin film will be discussed in the following.

1.2.3 State diagram of an in plane magnetoresistive device (0K)

State diagram defines the different static and dynamic states in the current-field plane. As already mentioned, for in plane magnetoresistive devices, the spin torque is more or less collinear with the damping torque and the free layer has a uniaxial anisotropy (given by an anisotropy field $\boldsymbol{H_u}$) in the same direction as the applied field, $\boldsymbol{H_{app}}$. For this configuration the state diagram has been predicted from macrospin simulations at T=0K as shown in Fig. 1.8. This diagram is asymmetric as a function of the sign of current J_{app} (normalized) and field, $\boldsymbol{H_{app}}$, which is normalized by anisotropy field $\boldsymbol{H_u}$. At zero applied field and no current, there are two energy minima (stable states) which are given by the parallel (P) and antiparallel (AP) alignment of the free layer magnetization with respect to the polarizer magnetization direction. The initial state defines the evolution of the magnetization with applied current. This magnetization dynamic evolution is summarized as follows:

(i) In the sub-critical regime ($J_{app}<J_{th1}$) the spin torque acts such that for one sign of the current, it enhances the natural damping and stabilizes the initial state, while for the opposite current direction it will counteract damping and destabilize the initial state.

(ii) Above the critical regime ($J_{app}>J_{th1}$), for the correct sign, the magnetization goes into steady state oscillations of the type IPP, which are around the initial stable state (energy minimum).

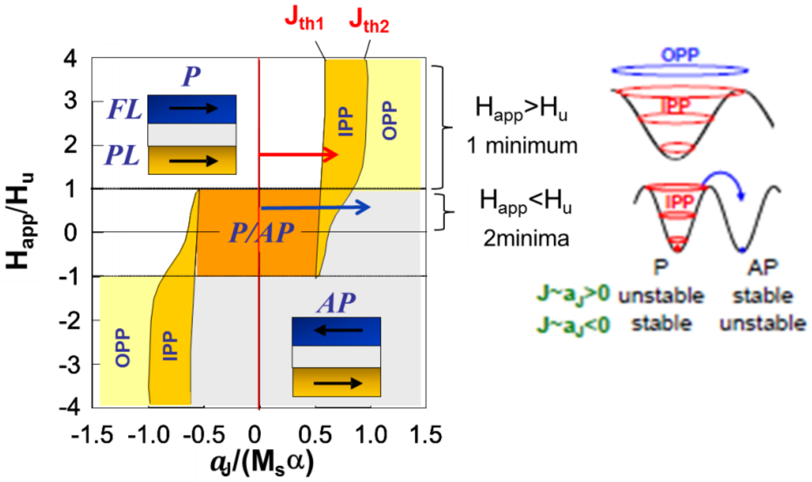

Fig. 1.8-Left: State diagram of the magnetization state in In-plane magnetized structures. Right, IPP and OPP trajectories in the energy landscape as a function of in-plane angle φ. Adapted from [72].

(iii) Upon increasing the current further, the oscillation amplitude increases and the magnetization transits into steady state OPP oscillations when the current is larger than a second threshold current ($J_{th1}>J_{app}>J_{th2}$). This transition occurs however only when the bias field is larger than the anisotropy field ($H_{app}>H_u$). For $H_{app}<H_u$, the magnetization transits from the IPP steady state oscillations into the reversed static state. This transition into the OPP state or the reverse static state occurs, when the IPP trajectories are pushed up on the energy landscape such that they pass through the energy saddle point.

According to the state diagram shown in Fig. 1.8, it is possible to induce the steady state oscillation in the parallel and antiparallel state depending on the direction of the field and current. For example, at positive field and positive current the steady state oscillation around the antiparallel energy minimum exists and at negative field and negative current the steady state oscillation around the parallel energy minimum can be excited. However, in reality, only the steady state oscillations at antiparallel state can be induced. This is because in the antiparallel state, the resistance is higher than in the parallel state, such that higher amplitude or voltage oscillation can be achieved. However, only IPP mode can be excited for in-plane magnetized MTJ device whereas the OPP steady state oscillations seem to be difficult to realize experimentally for this geometry due to the breakdown voltage limitation. There is experimental confirmation of this excitation for the standard in plane magnetic structures (spin valve) [78]. The OPP excitation in standard in plane magnetic structures however requires either relatively large current amplitudes or relatively large out of plane bias fields, which is not suitable for RF applications. In contrast, for out of plane polarizer combined with an in-plane magnetized free layer, it has been shown experimentally [79] and theoretically [72,80-82] that the OPP mode can be induced at relatively small current close to the critical current J_{th} as well as in zero external field. The state diagram for perpendicular polarizer will not be shown here (since this thesis will be focused on in-plane magnetized STNO) and can be found in Ref. 72.

1.2.4 State diagram of an in plane magnetoresistive device with temperature

The state diagram presented in Fig. 1.8 can be different from what is observed experimentally since it does not take into account the effect of temperature. The state diagram obtained from direct integration of eq. 1.12 when taking into account a fluctuating thermal noise field to the effective field $\boldsymbol{H_{eff}}$, given by eq. 1.16 [83], is shown in Fig. 1.10.

$$\langle \mathbf{H}^{\mathbf{i}}_{\mathbf{th}}(t)\mathbf{H}^{\mathbf{j}}_{\mathbf{th}}(t')\rangle = \frac{2\alpha k_B T}{\gamma_0 V \mu_0 M_s}\delta_{\mathrm{i,j}}\delta(t-t') \qquad (1.16)$$

The i,j representing Cartesian coordinates and k_B is the Boltzmann constant. The $\mathbf{H_{th}}$ is a magnetic random field with zero mean and its autocorrelation function is given by eq. 1.17, which corresponds to a white Gaussian noise with a variance proportional to the temperature T, the damping factor $\boldsymbol{\alpha}$, and it is inversely proportional to the magnetic volume V. In Fig. 1.9, the state diagrams were deduced from macrospin simulation by taking into account the thermal noise in the system for different temperatures, from left to right: T=3K, T=300K, T=3000K [84].

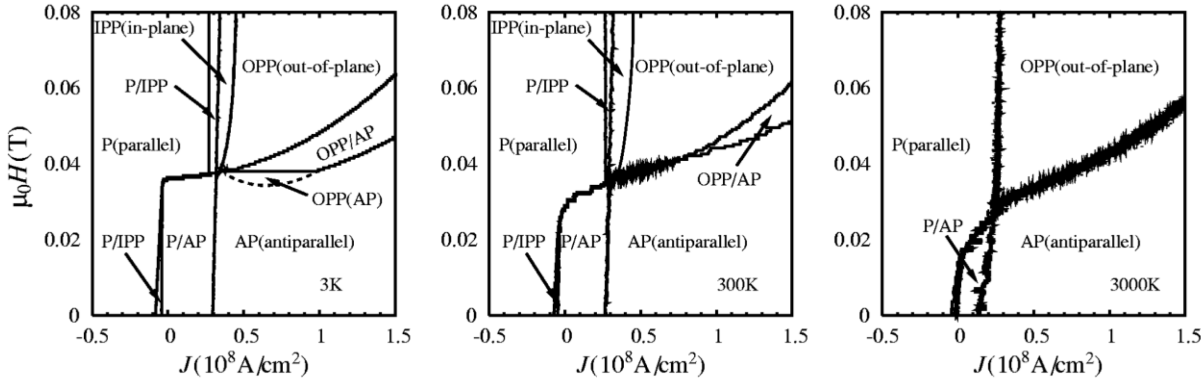

Fig. 1.9-State diagrams from numerical integration of LLGS with thermal fluctuations (from left to right: 3 K, 300 K, 3000 K). Adapted from [84].

As can be seen in Fig. 1.9, at low temperature (3K and 300K), the state diagrams are close to the one deduced at zero temperature (see Fig. 1.8, for $\mathbf{H}_{\mathbf{app}}>\mathbf{H}_{\mathbf{u}}$) where the two static states, P (parallel) and AP (antiparallel), and two dynamic modes, IPP and OPP mode, are observed. Upon increasing the temperature, the bi-stable region denoted “P/AP” is reduced due to thermal activation whereby the magnetization $\boldsymbol{M}$ can overcome the energy barrier between the two minima “P” and “AP”. It leads to a non-trivial dependence of the critical lines (switching from AP to P or P to AP) with temperature. The dynamic state corresponds to the case in which IPP trajectories first grow in amplitude until switching occurs. The stable dynamic states of the magnetization exists whose critical lines (stable state to dynamical state or dynamical to stable state) are temperature independent (especially when $\mathbf{H}_{\mathbf{app}}>\mathbf{H}_{\mathbf{u}}$). Particularly, the bifurcation between a static state and IPP is temperature independent in LLGS, since temperature does not affect damping and STT terms (when thermal fluctuations are considered in the form of eq. 1.16. However, material parameters (Ms, α) and a_j are temperature dependent and will induce a temperature dependence of critical or threshold lines J_{th1} experimentally.

Since the resistance of TMR structure depends on the relative angle between the magnetization of the free layer and the polarizing layer, state diagrams can be deduced from the measurement of the resistance. For the static state, it can be realized by monitoring the resistance and for dynamic states, one can monitor the alternating dynamic resistance induced in the gigahertz (GHz) range. For that reason, direct comparison between experiments and expected state diagrams can be performed.

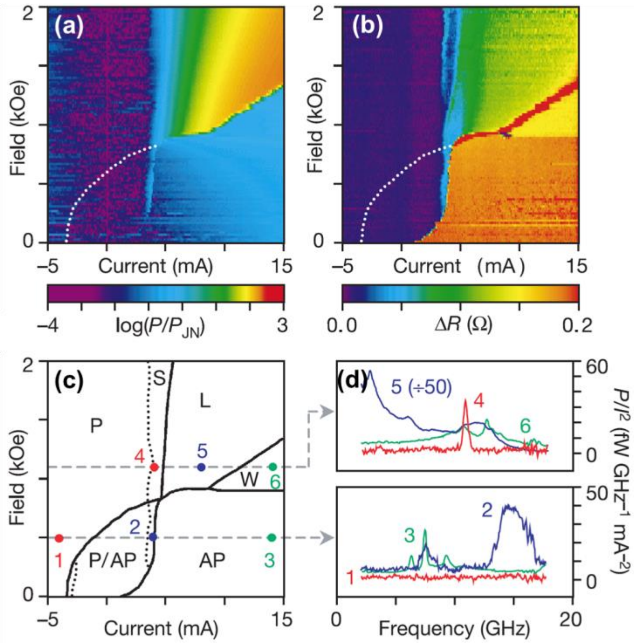

Fig. 1.10-Experimental measurements of the dynamic state: (a) H-I diagram of the output power measured on a Co/Cu/Co nanopillar. (b) Differential resistance plotted in colors for the same (H-I) region. (c) Deduced state diagram. S and L refer respectively to small and high amplitude IPP modes. W refers to chaotic modes. (d) Output Spectra for different operating points. Adapted from [6].

Fig. 1.10 shows the first experimental measurement of the dynamic state diagram by Kiselev et al. [6] with corresponding voltage output in the GHz range. The measured state diagram shows that only IPP mode can be excited, i.e. it is difficult to excite the OPP mode in an in-plane magnetized magnetic structures even though it is predicted in the simulation (Fig. 1.8 and Fig. 1.9). The information extracted from both output power (Fig. 1.10a) and differential resistance measurement (Fig. 1.10b) indicates a good agreement with numerical integration of LLGS taking into account the thermal noise fluctuations (Fig. 1.9). In Fig. 1.10d, the linewidth broadening present in the emitted spectra of those structures under a current/voltage bias is observed. This broadening is considered to be a consequence of the fluctuations of the trajectory due to the fluctuating field defined by Eq. 2.16.

In Fig. 1.11, the macrospin trajectory (inset figure) is given without (Fig. 1.11a) and with considering the fluctuating field (Fig. 1.11b) [85]. The calculated power spectral density (PSD) of the signal emitted from a MTJ is also given. It is clear that the noise broadens the linewidth of the microwave emission (Fig. 1.11b). Doing the inverse Fast Fourier transform (FFT) for these PSD, one can obtain the corresponding output voltage of the STNO oscillations in time $V(t)$. For Fig. 1.11a, when thermal noise fluctuation is absent, the output voltage can be expressed as in the eq. 1.17a. This corresponds to an ideal noiseless oscillator whose output voltage $V(t)$ oscillates in time at constant amplitude V_0 and constant angular frequency given by $\omega_0 = 2\pi f_0$. However, noise is inevitable in the system, thus the output voltage in the presence of the fluctuating field (noise) is given by eq. 1.16b. This corresponds to the output voltage $V(t)$ oscillations in time whose amplitude δa and angular frequency (phase) φ fluctuates around its average value V_0 and ω_0, respectively. As a result of these fluctuations, the PSD of $V(t)$ (Fig. 1.11b) shows the oscillation power which is spread around the main central frequency, f_0.

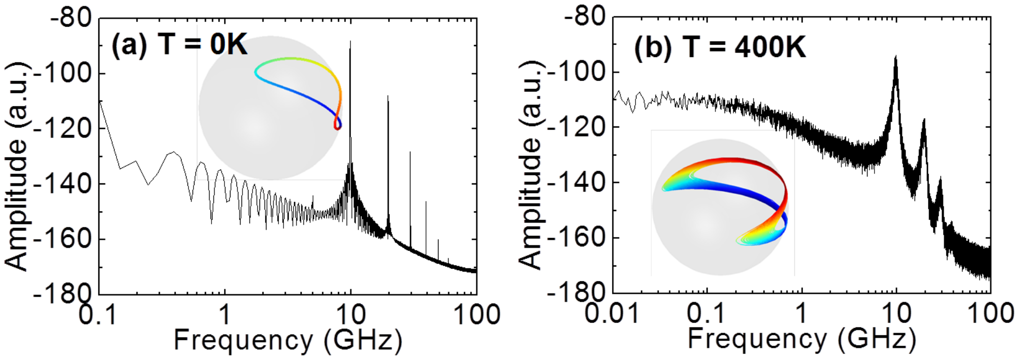

Fig. 1.11-PSD of the M_x component in double logarithmic plot for a typical IPP mode for (a) T=0K and (b) T=400K. The broadening of the trajectory (b) implies the broadening of the emission linewidth. Adapted from [85].

$$V(t) = V_0 \cos(\omega_0 t) \tag{1.17a}$$

$$V = V_0[1 + \delta a(t)] cos[\omega_0 t + \varphi(t)] \tag{1.17b}$$

An analytical study of the impact of the noise on the system is difficult from the LLGS equation. A simple analytic theory of current-induced microwave generation in magnetic nano-structures based on complex c-variables, which is developed by Joo-von Kim [86] and Slavin and Tiberkevich [87], provides a powerful tool to predict linewidth broadening of oscillation. In particular, it allows one to directly link the noise source to the oscillator output. In order to understand this, Section 1.3 summarizes the analytical model and is meant to give an insight into underlying concepts. Before coming to the discussion of the analytical model of STNOs, it is important to summarize the STNO's basic principle which is based on the previous discussion on spintronics effects (magnetoresistance and STT effect) and its magnetization dynamics (LLGS equation). Hence, a clear understanding of the physical concepts of STNOs can be achieved. An analogy between the STNO and the conventional oscillator (LC-VCO) will be also reviewed to introduce the general model of auto-oscillatory systems (complex c-variables).

1.2.5 Summary: Magnetization dynamics

To conclude, the magnetization dynamic is generally described by the LLGS equation, including a precession term, a damping term, and an additional term that represents the torque from spin momentum transfer. The LLGS equation can be solved in a macrospin or micromagnetic approach. This gives the understanding of qualitative pictures of the magnetization dynamics under the presence of spin transfer torque effect in the system, such as the stable solution, precession mode, state diagram: evolution of magnetization dynamic as a function of effective field and current, etc. This Section is important to understand the results that are shown in Chapter 2 (characterization of STNOs). In this chapter, the microwave excitations of STNOs are characterized under external control parameters, i.e. applied field and current, to observe the microwave excitation properties, i.e. excitation mode, frequency dependence on the applied field and current, the threshold current, transition to steady state, etc. However, as already mentioned, the LLGS equation does not provide an intuitive understanding of the effect of the noise to the dynamics of STNOs, i.e. amplitude and phase noise properties and the linewidth broadening and the extraction of its nonlinear parameters. The transformation of LLGS equation into complex c-variables oscillator equation is thus required to provide intuitive understanding of the STNO dynamics that contains the nonlinear parameters. This analytical model will be discussed in the next Section.

1.3 Kim-Tyberkevych-Slavin (KTS) Model

An analytical model for STNO based on the general model approach of an auto-oscillator (complex c-variables) was first described within the KTS model that refers to scientists J.-V. Kim (IEF Orsay), V. Tyberkevych and A.N. Slavin (Oakland University). Details of this model have been summarized in a tutorial [86,87] for perpendicular polarizer (circular/symmetric trajectory) STNO configuration. This thesis is mainly focused on the in-plane magnetized free layer and in-plane magnetized polarizer STNO (see Fig. 1.6). In the following the analytical model for this STNO configuration will be discussed. The model was developed by L. Buda Prejbeanu [74,75], following the model derivation procedures as discussed in the Refs. 86,87. The essential features of this model will be summarized to get insight on how the nonlinear oscillator model can be derived for STNO, i.e. from the LLGS equation to KTS model. Its stationary solution and stability for the case of the absence of the driving force will be discussed, i.e. the KTS model for autonomous or free running STNO. The model is then expanded for the specific case when a driving force is present, i.e. thermal fluctuations (linewidth broadening), phase locking to external signals (synchronization), and frequency modulation. Understanding the basic derivation from LLGS equation to KTS model is of importance for this thesis for further model derivation of different cases, i.e. frequency modulation of STNO under external RF field (see Chapter 3).

1.3.1 Introduction to complex c-variables model

The general model of auto-oscillatory systems with three key elements (resonator, dissipative element, and the active element), regardless of a particular physical realization, can be described by [87]:

$$\frac{dc}{dt} + j\omega(|c|^2)c + \Gamma_+(|c|^2)c - \Gamma_-(|c|^2)c = f(t) \tag{1.18}$$

Here $c(t)$ is the complex amplitude of auto-oscillations which measures both the power $p = |c|^2$ and phase $\phi = \arg(c)$ of the oscillations. $\omega(p)$ is the frequency of auto-oscillations due to the resonator or equivalent to the precession term. $\Gamma_+(p)$ is the positive damping which is responsible for the energy dissipation or equivalent to the damping term, $\Gamma_-(p)$ is the negative damping which acts as an energy source or an active element, and $f(t)$ is the driving force, i.e. influence of external signals or/and thermal fluctuations to the auto-oscillations. The resonance frequency $\omega(p)$ and both damping rates $\Gamma_\pm(p)$, in general, are functions of the auto-oscillation power $p = |c|^2$, which makes the auto-oscillator is a nonlinear dynamical system. In the following, the analytical model of STNO for specific configuration, in-plane magnetized free layer and in-plane magnetized polarizer, which is based on this general model approach, will be discussed. It will be shown that STNO is a nonlinear oscillator and it is possible to extract these nonlinear parameters from the analytical model.

1.3.2 From the LLGS equation to complex c-variables (KTS model)

The derivation of the nonlinear oscillator model for the STNO is deduced from the LLGS equation given by eq. 1.12. It has been noted, that the Gilbert damping constant, $\alpha \sim 0.01$, is rather small (in typical magnetic materials used for spin torque experiments). Therefore, the damping torque in the second term of eq. 1.12 itself is small compared to the conservative precessional torque (the first term in eq. 1.12). The spin-transfer torque described in the third term of eq. 1.12 is, usually, comparable in magnitude with the damping torque. Thus, both nonconservative torques (damping torque and spin transfer torque) in eq. 1.12 are much smaller than the conservative one. This allows one to substitute in the second term of eq. 1.12 the exact time derivative $\frac{d\boldsymbol{m}}{dt}$ by its “conservative” value, $-\gamma_0\big(\boldsymbol{m} \times \boldsymbol{H_{eff}}\big)$. This substitution, $\frac{d\boldsymbol{m}}{dt} \rightarrow -\gamma_0\big(\boldsymbol{m} \times \boldsymbol{H_{eff}}\big)$, leads to the extended Landau-Lifsthitz equation [87].

$$\frac{d\boldsymbol{m}}{dt} = -\gamma_0'\big(\boldsymbol{m} \times \boldsymbol{H_{eff}}\big) - \alpha\gamma_0'\big[\boldsymbol{m} \times \big(\boldsymbol{m} \times \boldsymbol{H_{eff}}\big)\big] - \gamma_0' a_j[\boldsymbol{m} \times (\boldsymbol{m} \times \boldsymbol{p})] \tag{1.19}$$

As can be seen in eq. 1.19, the damping torque (second term) now has the Landau-Lifshitz form instead of Gilbert form, where $\gamma_0' = \frac{\gamma_0}{1+\alpha}$. The extended Landau-Lifsthitz equation has a clear advantage compared to the LLGS form in eq. 1.12, as the equation of magnetization dynamics with the Landau-Lifshitz form of the damping torque becomes an explicit differential equation for $\boldsymbol{m}$. Therefore, the extended Landau-Lifsthitz equation is more convenient to perform reduction to the general oscillator model and also to perform the numerical simulation.

In this Section, the reduction from the Landau-Lifsthitz equation to the general oscillator model (eq. 1.18) is considered for the in-plane magnetized STNO (see Section 1.2.1). Following the Holstein-Primakoff transformation [88], the extended Landau-Lifsthitz equation is rewritten in canonical coordinates. Through this transformation, the components of the magnetization vector (m_x, m_y, m_z) are transformed to an equation in “complex c-variable”. Assuming that the magnetization inside the free layer is uniform (only one mode or oscillation type is excited) and keeping only potential resonant terms, (weakly nonconservative system) and also neglecting higher order terms in $|c|^2$ for simplicity, one can obtain complex c-variable model for STNO:

$$\frac{dc}{dt} = -j[\omega_0 + N|c|^2]c - \Gamma_0[(1 + Q|c|^2)]c - \Gamma_j P_x[1 - |c|^2]c \tag{1.20}$$

The first term in the right-hand side of Eq. 1.20 corresponds to precession term, $\omega(|c^2|)$, the second term is the positive damping, $\Gamma_+(|c^2|)$, which is responsible for the energy dissipation, and the last term is the negative damping, $\Gamma_-(|c^2|)$, which acts as an energy source or active element provided by the STT. The expressions for the coefficients are the following:

$$N = -[3\omega_M uv(u^2 + v^2) + (2\omega_A + \omega_M)(u^4 + v^4 + 4u^2v^2)]\frac{\omega_0}{A}$$

$$\Gamma_0 = \alpha A$$

$$Q = -\left[3uv\omega_M + (u^2 + v^2)\left(\omega_H + 3\omega_A + \frac{3}{2}\omega_M\right)\right]\frac{\omega_0}{A^2}$$

$$\Gamma_j = \gamma_0' a_j$$

The notations are similar to that of Ref. 85:

$$\omega_A = \gamma_0' H_u, \qquad \omega_H = \gamma_0' H_{app}, \qquad \omega_M = \gamma_0' M_s,$$

$$A = \omega_A + \omega_H + \frac{\omega_M}{2}, \qquad u = \sqrt{\frac{A+\omega_0}{2\omega_0}}, \qquad v = -\sqrt{\frac{A-\omega_0}{2\omega_0}}$$

with $\omega_0 = \sqrt{A^2 - B^2}$ and $B = -\frac{\omega_M}{2}$. Here, ω_0 is the ferromagnetic resonance (FMR) frequency of the in-plane magnetized STNO, ω_A is the frequency due to anisotropy field H_u, ω_H is the frequency given by the a static magnetic field H_{app}, and ω_M is the frequency due to the demagnetization field. P_x in eq. 1.20 is the magnetization of polarizing layer in the plane x-direction.

The analytical model of STNO in eq. 1.20 contains nonlinear parameters N and Q. The extraction of these nonlinear parameters is of important for the STNO to predict the general STNO behavior. Since $|c|^2 = p$, the precession term, the positive and the negative damping terms in eq. 1.20 can be expressed as follows:

$$\omega(p) \approx \omega_0 + Np \tag{1.21a}$$
$$\Gamma_+(p) \approx \Gamma_0(1 + Q_1 p) \tag{1.21b}$$
$$\Gamma_-(p) \approx \Gamma_j P_x(1 - p) \tag{1.21c}$$

From eq. 1.21a, one can see that the frequency of an STNO, $\omega(p)$, strongly depends on the power p. The STNOs are thus characterized as "nonlinear" auto-oscillators.

1.3.3 Autonomous dynamics of STNO

The nonlinear oscillators model (eq. 1.18) has a general solution which can be easily found in the form of $c(t) = |c(t)|e^{-j\phi(t)}$, where $|c(t)| = \sqrt{p}$ corresponds to dimensionless power and $\phi(t)$ corresponds to the phase, $\phi(t) = \arg(c)$. This form permits to rewrite eq. 1.20 as a system of two real equations for the power p and the phase ϕ:

$$\frac{dp}{dt} = -2[\Gamma_+(p) + \Gamma_-(p)]p \tag{1.22a}$$

$$\frac{d\phi}{dt} = \omega_0 + Np \tag{1.22b}$$

The first equation determines the dynamics of the oscillation power p in an autonomous auto-oscillator, whereas the second one describes the dynamics of the oscillation phase ϕ or defines the instantaneous frequency, $f_i(t) = \frac{1}{2\pi}\frac{d\phi}{dt}$.

The static solution $p = 0$ is trivial and corresponds to the absence of any oscillations. Linearizing (1.22a) near this zero-power solution $p \to 0$, one obtains the equation:

$$\frac{dp}{dt} = -2[\Gamma_+(0) - \Gamma_-(0)]p \tag{1.23}$$

From the linearized equation, it is shown that the zero-power solution is stable when the positive damping is larger than the negative one, $\Gamma_+(0) > \Gamma_-(0)$. The generation frequency at zero power solution corresponds to ω_0 (ferromagnetic resonance frequency). When the positive and negative damping are equal, $\Gamma_+(0) = \Gamma_-(0)$, the oscillation of the system has a nonzero power. This corresponds to the threshold of dynamic oscillation in STNO, above which the dynamic steady state oscillation occurs. At this point, the free running power p_0 and the amplitude relaxation rate Γ_p can be derived from eq. 1.21b and 1.21c:

$$p_0 = -\frac{\Gamma_0 + \mathrm{P}_x\Gamma_J}{\Gamma_0 Q_1 - \mathrm{P}_x\Gamma_J} \tag{1.24a}$$

$$\Gamma_p = (\Gamma_0 Q_1 - \mathrm{P}_x\Gamma_J)p_0 \tag{1.24b}$$

For dynamic solution, the oscillation has a nonzero power $p = p_0$ where p_0 is determined from the condition of $[\Gamma_+(p_0) = \Gamma_-(p_0)]$, see Fig. 1.12a. This means that the energy losses due to positive damping $\Gamma_+(p_0)$ should be exactly compensated by the energy supply from the external energy source (spin transfer torque) $\Gamma_-(p_0)$, and the total effective damping should be exactly equal to zero $[\Gamma_+(p_0) - \Gamma_-(p_0) = 0]$.

The stability of dynamic solutions $p = p_0$ above the threshold current I_{th} can be obtained by doing the linearization of eq. 1.22a for small perturbations δp around the power p_0, such that $p(t) = p_0 + \delta p$. Thus the eq. 1.22 has a form as follow:

$$\frac{d\delta p}{dt} = -2\Gamma_p \delta p \tag{1.25a}$$

$$\frac{d\phi}{dt} = \omega_g + N\delta p \tag{1.25b}$$

Where $\omega_g = \omega_0 + Np_0$ is the free running frequency. The output power of the autonomous STNO (eq. 1.25a) is characterized by the nonlinear parameter Γ_p. This parameter corresponds to the amplitude relaxation rate (or also called effective damping rate) of small power perturbations δp around the power p_0 (see eq. 1.29b). In autonomous (free running) oscillators, Γ_p relates to the timescale required to recover from an external perturbation such as noise, or it also relates to the timescale or the rate at which the frequency can be effectively tuned (by the applied current density through the STNO device for instance). Large Γ_p (fast time response) is desired in most RF applications, in particular, as will be shown in the next Subsection, this Γ_p limits the modulation data rate of the STNO when an external RF current is applied to STNO, i.e. frequency modulation.

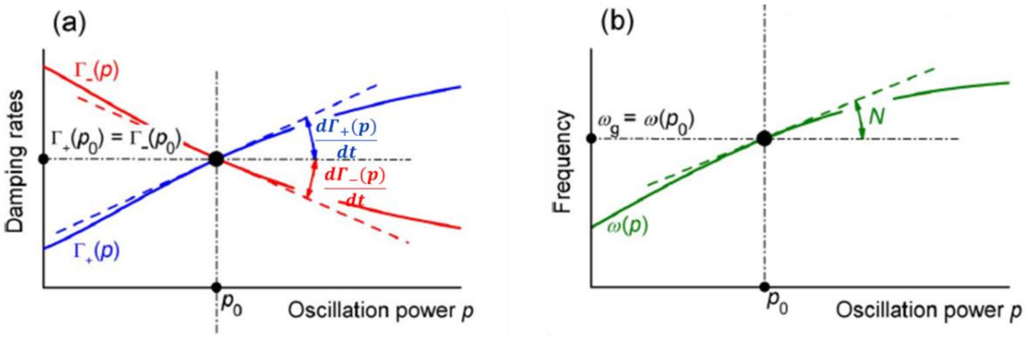

Fig. 1.12-Dependences of the damping rates $\Gamma_\pm(p)$ (a) and oscillation frequency $\omega(p)$ (b) on the oscillation power p. Intersection of the curves $\Gamma_+(p)$ and $\Gamma_-(p)$ determines the free-running operation point of the oscillator with the power p_0 and free-running generation frequency $\omega_g = \omega(p_0)$.

Eq. 1.25b shows the dynamic of the oscillation phase or frequency of the STNO. From the equation, it is clear that the phase or frequency of the STNO is coupled nonlinearly, via *N*, with the output power $p(t)$. Hence, any change in the output power will induce changes in the output frequency, leading to a large slope frequency-power tunability. The corresponding slope is related to the nonlinear frequency shift coefficient, *N*. The larger N, the larger the slope frequency-power (Fig. 1.12b). Large slope frequency-power is of interest for RF application such as in wireless communication system where large frequency shift is needed to achieve large signal to noise ratio. This large frequency-power tuning is difficult to achieve in conventional oscillator as their frequency does not depend on the output power. The nonlinear frequency shift coefficient, *N*, can be negative or positive depending on the mode excitations as already discussed. For positive *N*, the frequency increase with the increase of the current, i.e. blueshift behavior, and this corresponds to the out of plane precession (OPP) mode excitations. Whereas, for negative *N*, the frequency decreases as the current increases, i.e. redshift behavior, and this corresponds to in-plane precession (IPP) mode excitations. However, large nonlinearity N of STNO is also disadvantage for RF application because this nonlinearity enhances the phase noise of the STNO through the coupling with the power noise (see Section 1.3.5). In contrast to this, weak nonlinearity of the frequency to the power in conventional oscillators makes their phase noise better than the one of STNO.

To conclude, the analytical solution (KTS model) for the case of autonomous (free running) STNO provides direct analysis on their output power and frequency under the external control parameters such as DC current. Furthermore the analytical model predicts a frequency dependence on the generated power in STNOs. Thus, STNOs are characterized as nonlinear oscillators. The predictions coincide with the experimental and numerical results of STNOs of various configurations. For the practical applications of STNOs, it is important to understand how these auto-oscillators will behave under the influence of external periodic signals which can lead to a synchronization or frequency modulation. The KTS model for the case of synchronization can be found in literature [86,87]. In the following, the KTS model for frequency modulation of STNO will be summarized since this thesis is focused on frequency modulation of STNOs.

1.3.4 Frequency modulation of STNO via current modulation

In this section the dynamic behaviors of STNO under the influence of external periodic signals will be discussed. The external signal considered here is an RF oscillating current, given by $I_{RF}\cos(\omega_m t)$, where I_{RF} and $\omega_m = 2\pi f_m$ correspond to the amplitude and the angular frequency of RF current, respectively (f_m is the frequency of the RF current). Depending on the f_m value, on can distinguish different two operational regimes:

(a) f_m is much less than the free running STNO frequency, f_g, induced by the DC current. This is the case of frequency modulation, $f_m < f_g$.

(b) f_m is on the same order magnitude as the free running STNO frequency, f_g, induced by the DC current. This leads to synchronization, $f_m \approx f_g$ (or nf_g) .

As already mentioned, the frequency modulation of the STNO is of interest of this thesis. Hence the discussion will be focused on the case of frequency modulation. A detail discussion of the synchronization can be found in the literature [87].

For practical applications, the frequency modulation of STNOs can be easily or directly achieved by modulating the current, I_{DC}.

$$I(t) = [1 + \varepsilon\cos(\omega_m t)]I_{DC} \tag{1.26}$$

Where $I(t)$ is the modulated DC current and ε is the modulation depth ($\varepsilon = I_{RF}/I_{DC}$). In this modulation, the negative damping (spin transfer torque), $\Gamma_-(p)$, is considered to be modulated, since it depends on the bias current, $I_{DC} \sim a_j$. The modulated negative damping, $\Gamma_-^{DC+RF}(t,p)$, is given by:

$$\Gamma_-^{DC+RF}(t,p) = [1 + \varepsilon\cos(\omega_m t)]\Gamma_-(p) \tag{1.27}$$

Assuming that the modulation depth ε is small ($\varepsilon \ll 1$) the oscillation power $p(t)$ can be represented as $p(t) = p_0 + \delta p(t)$, where p_0 is the free running power (unmodulated oscillator, $\varepsilon = 0$), and $\delta p(t)$ is a small modulation around the free running power, $\delta p(t) \sim \varepsilon$. Doing the linearization of eq. 1.22 for small ε (small modulation around the free running power), one can obtain a system of equations for the power modulation δp and the phase $\phi = \arg(c)$ of the modulated STNO:

$$\frac{d\delta p}{dt} = -2\Gamma_p \delta p + 2\varepsilon\Gamma_-(p_0)p_0 \cos(\omega_m t) \tag{1.28a}$$

$$\frac{d\phi}{dt} = \omega_g + N\delta p(t) \tag{1.28b}$$

In comparison with eq. 1.25a, the power fluctuations (modulation) δp of free running STNOs has an additional nonhomogeneous term proportional to the modulation depth ε. A stationary solution of eq. 1.28 has the form:

$$\delta p(t) = \varepsilon \frac{2\Gamma_-(p_0)p_0}{\sqrt{\omega_m^2 + 4\Gamma_p^2}} \cos(\omega_m t + \psi) \tag{1.29a}$$

$$\frac{d\phi}{dt} = 2\pi f_i(t) = \omega_g + N\delta p(t) \tag{1.29b}$$

$$\phi(t) = \omega_g t + N\Delta\phi \sin(\omega_m t + \psi) + \phi_0 \tag{1.29c}$$

Where $\Delta\phi = \varepsilon \frac{2\Gamma_-(p_0)p_0}{\omega_M \sqrt{\omega_m^2 + 4\Gamma_p^2}}$ is the amplitude of the induced phase modulation N is the nonlinear frequency shift coefficient, $\psi = -\arctan(\omega_m / 2\Gamma_p)$, and Γ_p is the amplitude relaxation rate. The final output signal of an STNO modulated through its DC current has thus both a sinusoidal varying amplitude and phase (frequency). As given in eqs. 1.29b,c, the modulation of the phase (frequency) of the STNO occurs due to nonlinear coupling N with its modulated power $\delta p(t)$. The spectrum of the frequency-modulated oscillations can be obtained by writing the solution for the complex amplitude $c(t) = \sqrt{p(t)} e^{-j\phi(t)}$ and developing the solution in a Fourier series:

$$c(t) = \sqrt{p(t)} e^{-j\omega_g t + j\phi_0} \sum_{n=-\infty}^{\infty} J_n(\Delta\phi) e^{jn(\omega_m t + \psi)} \tag{1.30}$$

where $J_n(x)$ is the Bessel function of the *n*th order. The spectrum (eq. 1.30) consists of a central peak at the frequency ω_g with an infinite number of sidebands at the frequencies $\omega_g + n\omega_m$ having relative amplitudes $J_n(\Delta\phi)$. This predicts a dependence of the intensity of the spectrum sidebands on the modulation frequency.

The equation for $\delta p(t)$, eq. 1.29a, predicts that the modulated power cuts off at the relaxation frequency $f_p = \Gamma_p / \pi$, and, therefore, f_p determines the maximum modulation rate of the amplitude (power) modulation. Due to the nonlinear coupling N between frequency and amplitude, the same cut-off appears for frequency modulation. Hence, the modulation data rate of the frequency modulation is also given by the relaxation frequency f_p. This becomes evidence when taking the Fast Fourier Transform (FFT) of eq. 1.29a:

$$PSD_{\delta p}(f) \propto \varepsilon^2 \frac{(2N\Gamma_-(p_0)p_0)^2}{4\pi^2} \times \frac{1}{f_m^2 + f_p^2} \tag{1.31}$$

For slow modulation frequencies, $f_m \ll f_p$, the contribution of f_m in eq. 1.31 can be neglected such that the response of $A(f_m)$ is constant. For this case, the amplitude in the frequency response is modulated in white Gaussian manner, i.e. the same strength at all frequencies below the f_p at the same time. This means that under slow modulation frequencies (slow perturbation) compared to the STNO precession period, the STNO has time to follow the perturbation such that the STNO can respond and follow the modulating RF current. In contrast, for faster modulation frequencies, $f_m \gg f_p$, the amplitude response $A(f_m)$ is inversely proportional to the square of f_m. This means that under a faster perturbation (faster than its relaxation rate f_p), the STNO does not has enough time to follow the modulating RF current and will result in an amplitude attenuation. Hence, the larger f_m (as compared to to f_p), the larger the attenuation of the amplitude $A(f_m)$. This analytical model, hence, predicts the behavior of the amplitude and frequency modulation of the STNO via current modulation and it is shown that the maximum achievable data rate of amplitude and frequency modulation of the STNO are given by its relaxation frequency f_p. This has been confirmed experimentally in Ref. 89 by using a noise spectroscopy technique, i.e the extraction of the amplitude and frequency noise. This technique provides a very simple method to extract the amplitude relaxation frequency f_p and to characterize the modulation data rate of STNO. Hence, this technique is of importance of this thesis since it will be used for further investigation of the modulation data rate of STNO for different modulation configuration that will be discussed in Chapter 3.

To summarize, the KTS model is able to explain the behavior of STNOs under an external periodic signal and the importance of the extraction of the most important parameter of STNO, Γ_p. In addition, the experimental results qualitatively coincide with the prediction of the KTS model, i.e. the nonlinear dependence on the modulating signal parameters (amplitude and frequency) and most importantly the extraction of the Γ_p from frequency modulation experimental studies. Another major achievement of the model involves providing a full description of the STNO dynamics in the presence of thermal noise, as discussed in the following.

1.3.5 Thermal noise in the KTS theory: Amplitude and phase noise

It has been discussed in detail the deterministic component of the system, i.e. the stable trajectory, and how the system returns to it after a single perturbation around the free running power p_0, i.e. the returning time is characterized by the amplitude relaxation rate, $t_p \sim 1/\Gamma_p$. This Section describes the analytical model of an STNO in the presence of thermal noise and its influence on the STNO dynamical systems. When a stochastic force $f_n(t)$ acts on the system, eq. 1.18 can be rewritten as follow:

$$\frac{dc}{dt} + j\omega(p)c + \Gamma_+(p)c - \Gamma_-(p)c = f_n(t) \text{ with } |c|^2 = p \tag{1.32}$$

The statistical solution of eq. 1.32 requires some assumptions: (i) the noise does not perturb the system too much so that the eq 1.32 can be linearized, (ii) stochastic force $f_n(t)$ in eq. 1.32 is considered as a phenomenological term describing action of thermal fluctuations. Hence, its expression should verify a proper thermodynamical behavior of the STNO in the state of thermal equilibrium (i.e. the Boltzmann distribution of the system state when $\Gamma_-(p) = 0$) [87]. This is obtained by considering $f_n(t)$ to be a white Gaussian noise with the zero mean value and second-order correlator given by [87,89]:

$$\langle f_n(t) f_n(t') \rangle = 0, \quad \langle f_n(t) f_n^*(t') \rangle = 2D_n \delta(t - t') \tag{1.33}$$

Where D_n is the diffusion coefficient that characterizes the noise amplitude. For a nonlinear oscillator (STNO), i.e. the strong dependences of the frequency $\omega(p)$ and damping $\Gamma_\pm(p)$ on the oscillation power, this diffusion coefficient also depends on the oscillation power p [87,89].

$$D_n(p) = \Gamma_+(p)\eta(p) = \Gamma_+(p)\frac{k_B T}{\lambda\omega(p)} \tag{1.34}$$

where $\eta(p) = \frac{k_B T}{\lambda\omega(p)}$ is the effective noise power in the nonlinear regime. k_B is the Boltzmann constant, T the temperature and factor λ is a scale factor that relates the energy of the oscillation to the oscillation power p.

With the definition of the diffusion constant D_n and using $f_n(t) = \tilde{f}_n(t)e^{-j\phi(t)}$, the solution of eq. 1.32 has forms:

$$\frac{d\delta p}{dt} + 2\Gamma_p\delta p = 2\sqrt{p_0}Re\left[\tilde{f}_n(t)\right] \tag{1.35a}$$

$$\frac{d\phi}{dt} + \omega_g + N\delta p = \frac{1}{\sqrt{p_0}}Im\left[\tilde{f}_n(t)\right] \tag{1.35b}$$

Eq. 1.35 is of main importance for this thesis, because it allows a simple expression for both amplitude (power) and phase of the STNO in the presence of white Gaussian noise. Let us first consider the amplitude (power) noise given by the eq. 1.35a. The autocorrelation function of power fluctuations, leads to the direct extraction of the amplitude relaxation rate, Γ_p [87], i.e. the power fluctuations can be directly extracted from the Hilbert transformation (see Chapter 2 Section 2.1.3.1).

$$\langle\delta p(t)\delta p(t-\tau)\rangle = \mathrm{K}_{\delta\mathrm{p}}(\tau) = \frac{\pi\Delta f_0}{\Gamma_p}e^{-2\Gamma_p\tau} \tag{1.36}$$

Where Δf_0 is the linear linewidth of the STNO, i.e. $\Delta f_0 = D_n(p)$. The autocorrelation function of the power fluctuations (eq. 1.36) is an exponential decaying function with the time constant τ_c, given by the inverse of Γ_p, $\tau_c = 1/2\Gamma_p$. This time constant describes the relaxation time needed for the STNO to drive the magnetization back to its stable limit cycle (constant trajectory) after perturbations.

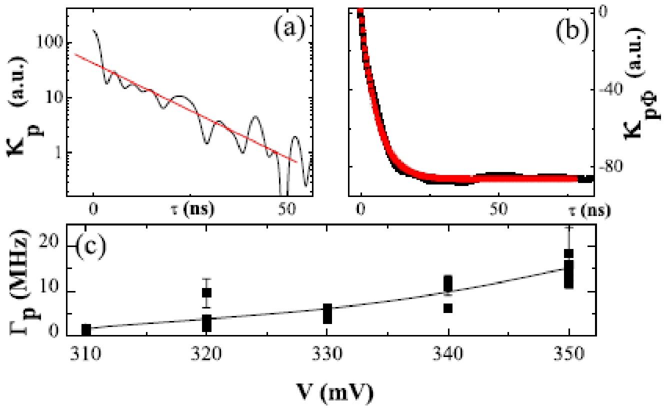

Fig. 1.13-(a) The power fluctuation autocorrelation function K_p for a MTJ-STO. (b) The power-phase cross correlation function K_Φ from the same set of data. The red curve is an exponentially decay fit with a time constant τ_c equal to $1/2\Gamma_p$. (c) The Γ_p as a function of the applied current or voltage. Adapted from [90].

The first experimental extraction of Γ_p through the power autocorrelation function was performed by Bianchini et. al [90]. The Γ_p was extracted from single shot time domain measurements of the output voltage of an MTJ based STO, by using the Hilbert transformation to obtain the power (amplitude) fluctuations. The autocorrelation function of power fluctuations gives the value of $\tau_c = 1/2\Gamma_p$ by fitting the response with the exponential decaying function. The results are given in Fig. 1.13, showing that Γ_p lies in the range of tens of MHz (Fig. 1.13c).

It is more convenient to express the solution of power fluctuations (1.35a) through its Fast Fourier Transform (FFT), to form power spectral densities (PSD) of the power fluctuations as given by eq. 1.44. From this the occurrence and interpretation of the roll-off frequency $f_p = 1/\pi\Gamma_p$ in the amplitude (power) noise plots becomes clear.

$$PSD_{\delta p}(f) = \frac{\Delta f_0}{2\pi}\frac{1}{f^2+f_p^2} \tag{1.37}$$

In addition, it is possible to extract the linear linewidth Δf_0 through the PSD of the power fluctuations. Considering two limiting behaviors of the system amplitude in presence of noise: low frequency $(f \ll f_p)$ and high frequency perturbations $(f \gg f_p)$. For low frequency perturbations $(f \ll f_p)$, the eq. 1.37 can be written:

$$PSD_{\delta p}(f) = \frac{\Delta f_0}{2\pi f_p^2} \tag{1.38a}$$

This means that the system responds the perturbations in the white Gaussian manner, $1/f^0$, (the same nature as the excitation force). For this case, there is a restoring torque (given by the balance between spin transfer and damping torque) that drives the magnetization back to its initial stable trajectory. For high frequency perturbations $(f \gg f_p)$, it becomes:

$$PSD_{\delta p}(f) = \frac{\Delta f_0}{2\pi f^2} \tag{1.38b}$$

This results in a random walk behavior $1/f^2$, i.e. power fluctuations are adding up, meaning that the STNO does not have time to relax to its stable trajectory. The prediction of the system response for these two limiting cases has been experimentally demonstrated by Quinsat. et. al [85,91] as shown in Fig 1.14. The experimental results (red plots in Figs. 1.14b,c,d) were compared with the ones obtain from the macrospin simulation (red plots in Figs. 1.14a), and both showed good agreement to the analytical model. In experiment [85,91] the cut-off frequency is on the order of few hundred MHz which is slightly larger with the one measured in [90].

To summarize for the case of amplitude (power) fluctuations, there are two methods of the extraction of Γ_p: direct from power autocorrelation function (extracting the time constant τ_c) and from the amplitude noise response (extracting the roll of frequency f_p). The latter will be discussed in detail in Chapter 2 since this technique will be used for the data analysis in this thesis. Furthermore, this analysis technique can also be used to determine the upper limit of the modulation frequency for the case of modulated STNO as confirmed in Ref. [91].

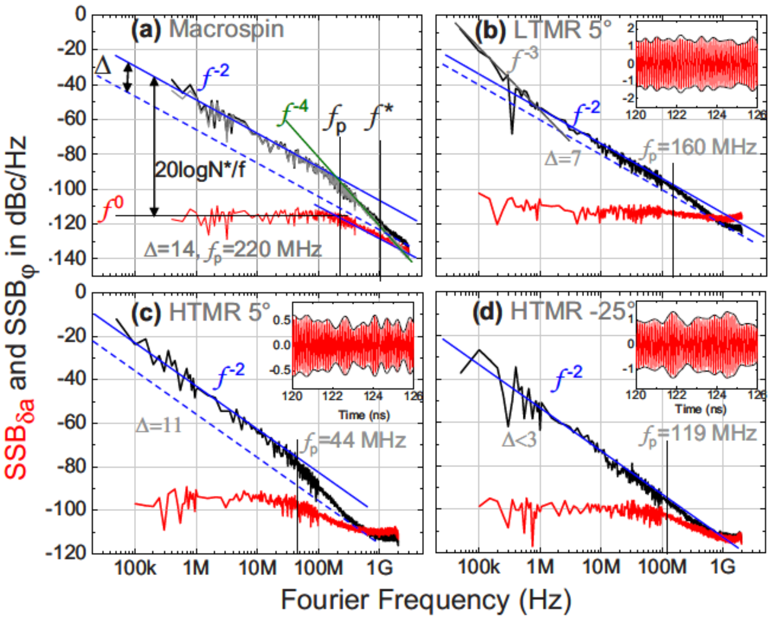

Fig. 1.14-The amplitude (red curve) and phase noise plots (blue curve) obtained from (a) macrospin simulation (b-d) experimental measurements of different STNO devices: high tunneling magnetoresistance (HTMR) and low tunneling magnetoresistance (LTMR). Adapted from [91].

It has been discussed in detail all information that can be obtained from the study of amplitude/power fluctuations. This part is focused on the information that can be obtained from the study of the phase fluctuations. In the phase equation of eq. 1.35b, it is shown that the phase has a direct contribution from power fluctuations $N\delta p$, i.e. power-phase coupling. To investigate the power fluctuations on the phase noise, it is convenient to express the eq. 1.35b through its Fast Fourier Transform (FFT), to form power spectral densities (PSD) of the phase fluctuations as given by eq. 1.39.

$$PSD_\phi(f) = \frac{\Delta f_0}{\pi f^2} + \frac{\Delta f_0}{\pi f^2}\frac{v^2 f_p^2}{f_p^2+f^2} \tag{1.39}$$

With $v = N/\Gamma_p p_0$ is the dimensionless nonlinear amplitude phase coupling. The first term (right hand side) corresponds to the linear contribution to the phase noise, while the second term is the nonlinear contribution to the phase noise. The linear contribution is the direct effect of noise on the phase term, the nonlinear contribution is the noise on the phase term originating from the amplitude fluctuations. Since the frequency depends on the amplitude of the auto-oscillation (i.e. STOs are non-linear oscillators), it naturally induces this nonlinear contribution. Two limiting cases can be also made for $PSD_\phi(f)$, as mentioned previously for the analysis of amplitude fluctuations: low frequency $(f \ll f_p)$ and high frequency perturbations $(f \gg f_p)$, see eq. 1.40. For low frequency perturbations $(f \ll f_p)$, the phase noise is indeed given by the nonlinear contribution from amplitude fluctuations. This amplitude noise enhances the phase noise level by a factor $1 + v^2$. In this case, there is no restoring force for the phase and the phase is free. This is why the phase accumulates all fluctuations, resulting in a random walk behavior, 1/f^2. For high frequency perturbations $(f \gg f_p)$, the phase noise is linear and mainly given by the direct effect of noise on the phase. This also results in random walk behavior. The phase noise plots are thus a means to extract the non-linear parameter v.

$$PSD_{\phi}(f) \approx \begin{cases} \frac{\Delta f_0}{\pi f^2}(1+v^2), & for\ f \ll f_p \\ \frac{\Delta f_0}{\pi f^2}, & for\ f \gg f_p \end{cases} \tag{1.40}$$

1.3.6 Summary: KTS model

In conclusion, the KTS model provides a means to transform the LLGS equation into a general oscillator model, from which the basic behavior in the autonomous regime and in the non-autonomous regime (under the influence of periodic and stochastic external signals) can be derived. This model permits to extract the nonlinear parameters N, Γ_p, and v. N (nonlinear frequency shifts) represents the strong dependence of the generated frequency on the power of the generated signal. Depending on $N \sim \frac{df}{dI}$, positive or negative, the frequency dependence on the power can be redshift (IPP mode) or blueshift (OPP mode). In one hand, strong N induces large slope of frequency current tunability $\frac{df}{dI}$ which is of interest for many applications such as for digital wireless communication application where large frequency shift is desired to achieve high signal to noise ratio. On the other hand, strong N leads to enhance a phase noise due to nonlinear contribution from amplitude fluctuations. This makes the phase noise of STNOs poorer compared to conventional oscillators whose frequency weakly depend on the power. Study the noise properties of STNOs provide a means to extract the most important parameter of STNO, Γ_p, which gives the timescale or the rate of STNO to drive the magnetization back to its stable trajectory after perturbations. This is possible by doing the autocorrelation function of the amplitude fluctuation or forming the power spectral density of the amplitude fluctuations (amplitude noise). While the phase noise provides a tool for the extraction of the nonlinear amplitude-phase coupling parameter v and to study the linewidth broadening that is also relevant for applications.

Under the influence of periodic signals, the KTS model is also able to explain the dynamics behavior of STNO for example for the case of frequency modulation. It is predicted that Γ_p limits the upper modulation frequency for the case of modulation current and hence it characterizes the modulation bandwidth up to which the modulation is effective. To finish, this Section is important since it is rich of information for the understanding the results achieved in this thesis.

1.4 State of the Art of Experimental and Theoretical of Frequency Modulation

This thesis subject is to demonstrate the use of STNOs for wireless communication applications. In such applications, modulation is an important signal processing concept. Modulation processes have been successfully employed in the case of microwave STNO [26-28]. Some recent experiments have already demonstrated great potential of STNOs to be used as modulators in wireless communication systems. It has also been demonstrated that STNOs can be employed to develop novel high-data-transfer-rate readers for hard disk drives (HDDs). This Section aims to give a brief review of state-of-art of STNO modulation to highlight the motivation of this thesis. Before coming to the review, the fundamental of modulation in signal theory will be first present to understand the mechanism behind the STNO modulation and to follow easily the discussion of the review.

1.4.1 Fundamental of modulation: amplitude and frequency modulation

Modulation is the process of varying the characteristic parameters of a periodic high-frequency wave ("carrier"), in accordance with a low-frequency information signal ("modulating"), to obtain a "modulated" signal. The carrier wave is generally a sinusoidal waveform characterized by modifiable parameters: amplitude and frequency or phase. The corresponding analog modulation processes are referred to as amplitude modulation (AM), frequency modulation (FM), respectively [92,93], as illustrated in Fig. 1.15.

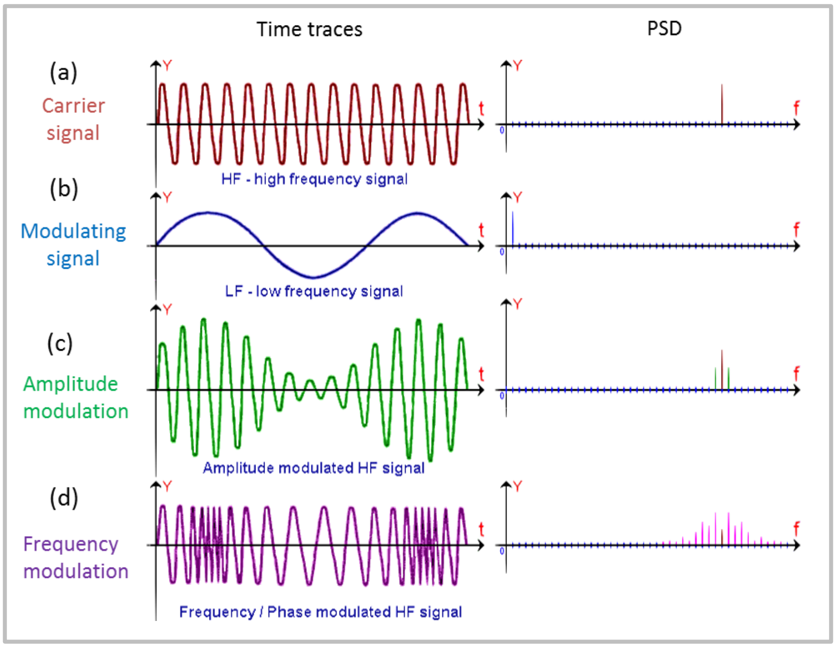

Fig. 1.15-Figures (a), (b), (c), (d) correspond to carrier signal, modulating signal, amplitude modulation signal and frequency modulation signal, respectively. The left figure shows the waveform signal, while the right figure presents the corresponding power spectral density (PSD), leading to the sidebands generation around the carrier frequency. Adapted from [93].

- **Amplitude modulation**

Amplitude modulation is the simplest form of modulation, which results in a variation of the carrier amplitude that is proportional to the amplitude of the modulating signal as shown in Fig. 1.15c. The amplitude modulation of the carrier wave S(t) is created by multiplying the carrier wave with a modulating signal m(t):

$$S(t) = A_c[1 + k_a m(t)\cos(2\pi f_c t)] \tag{1.41a}$$

$$S(t) = A_c \cos\omega_c t + \frac{\beta A_c}{2}\cos(\omega_c + \omega_m)t + \frac{\beta A_c}{2}\cos(\omega_c - \omega_m)t \tag{1.41b}$$

Where, A_c and f_c corresponds to amplitude and frequency of the carrier wave, k_a is the amplitude sensibility of modulator responsible for the generation of the modulated signal. $m(t) = A_m\cos(2\pi f_m t)$ is the modulating signal having a sinusoidal form. Substituting $m(t)$ in relation 1.41a and defining β as the modulation index, given by $\beta = A_m/A_c$, one can obtain relation 1.41b. This relation shows that the amplitude modulation results in a sum of three sinusoids of different frequencies. One of these sinusoids has the same frequency f_c and amplitude A_c as the un-modulated carrier. The second sinusoid is at a frequency equal to the sum of the carrier frequency and the modulation frequency (f_c+f_m); this component is the *upper sideband*.

The third sinusoid is at a frequency equal to the carrier frequency minus the modulation frequency (f_c-f_m); this component is the *lower sideband*. The two sideband components have equal amplitudes (symmetric sideband), which are proportional to the amplitude of the modulating signal A_m. The frequency domain of an amplitude-modulated carrier, Fig. 1.15c (right), shows the modulated spectrum consisting of carrier and sideband components of equal amplitude (symmetric sideband). The bandwidth of amplitude modulation is twice the frequency of the modulating signal, BW=2f_m.

- **Frequency modulation**

In frequency modulation (FM), the carrier frequency is modulated by a modulating signal, while the amplitude is constant (see Fig. 1.15d, left). And ideal FM signal has a form:

$$S(t) = A_c\cos[\phi_i(t)] \tag{1.42}$$

where A_c is the constant carrier amplitude and $\phi_i(t)$ is the instantaneous phase of the modulated signal, related to the instantaneous frequency by $f_i(t) = \frac{1}{2\pi}\frac{d\phi_i(t)}{dt}$. In a typical FM system [92,93], the instantaneous frequency varies *linearly* with the modulating signal $f_i(t) = f_c + k_f m(t)$, where k_f is called frequency sensitivity (Hz/Volt). According to the previous definitions, (1.42), the FM signal may be rewritten as:

$$S(t) = A_c\cos\left[2\pi f_c t + 2\pi k_f \int_0^t m(t)dt\right] \tag{1.43}$$

The modulated signal defined by relation 1.43 is a nonlinear function of the modulating signal $S(t)$, which makes FM an intrinsic *nonlinear* modulation process. Nevertheless, because of the linearity between $f_i(t)$ and $m(t)$, this phenomenon is referred to a *linear* modulation process. Assuming now that the modulating signal has a cosine form, $m(t) = A_m\cos(2\pi f_m t)$, relation 1.43 becomes:

$$S(t) = A_c\cos[(2\pi f_c)t + \beta\sin(2\pi f_m)t] \tag{1.44}$$

With $\beta = \frac{k_f A_m}{f_m} = \frac{\Delta f}{f_m}$

Here, β corresponds to the modulation index (unitless), indicating by how much the modulated variable varies around its unmodulated level. f_m is the highest frequency in the modulating signal (Hz), and $\Delta f_{peak} = k_f A_m$ corresponds to the frequency deviation of the peak (Hz) which represents the maximum shift away from f_c in one direction. Relation 1.44 can be written in the Fourier transform form by using the formalism of complex envelopes [92,93]:

$$S(t) = A_c Re \sum_{n=-\infty}^{\infty} J_n(\beta) \exp[j2\pi(f_c + nf_m)t] \tag{1.45}$$

With, $J_n(\beta) = \frac{1}{2\pi} \exp[j(\beta \sin x - nx)]dx$

where $J_n(\beta)$ is the nth-order Bessel function showing the relation between the carrier and sideband amplitudes of the modulated wave as a function of the modulation index β. From (1.45), it can be seen that the spectrum of wideband FM signal consists of the carrier frequency f_c and an infinite number of sidebands whose amplitudes are proportional to $J_n(\beta)$, although in practice the spectrum of an FM signal is not infinite. Their sideband amplitudes decrease and become negligibly small beyond a certain frequency offset from the carrier, depending on the magnitude of β. The bandwidth required for low distortion transmission can be now determined by counting the number of significant sidebands. For high fidelity, significant sidebands are those sidebands that have a voltage at least 1 percent (–40 dB) of the voltage of the unmodulated carrier for any β between 0 and maximum. Fig. 1.16 shows the spectral behavior of an FM signal for different values of modulation index $\beta = \frac{k_f A_m}{f_m} = \frac{\Delta f_{peak}}{f_m}$. In Fig. 1.16A, the spectra of a signal for β =0.2, 1, 5, and 10 are shown. The sinusoidal modulating signal has the constant frequency, f_m, so β is proportional to its amplitude, $k_f A_m$. In Fig. 2.16B, the amplitude of the modulating signal $k_f A_m$ is held constant and, therefore, β is varied by changing the modulating frequency, f_m. In Figs. 1.16B-a,b,c, individual spectral components are shown, whereas in Fig. 1.16B-d, the components are not resolved, but the envelope is correct.

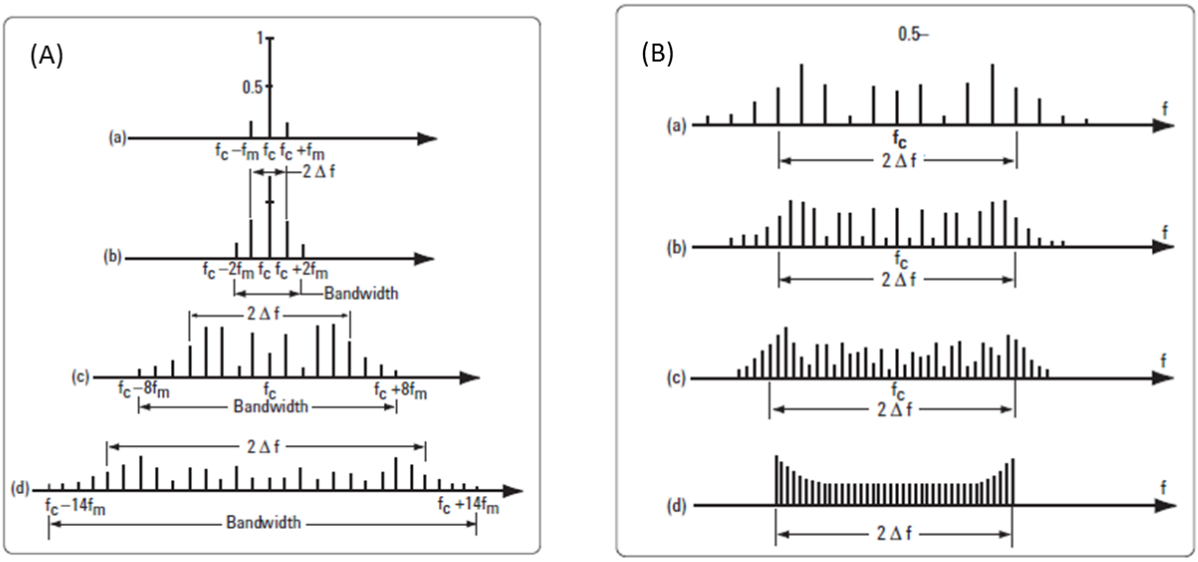

Fig. 1.16-(a) Amplitude-frequency spectrum of an FM signal (the modulation frequency f_m is *fixed*, the modulation amplitude A_m is *varying*) for (a), β = 0.2, (a) β = 1, (c) β = 5, (d) β = 10. (b) Amplitude-frequency spectrum of an FM signal (the modulation frequency f_m is *varying*, the modulation amplitude A_m is *fixed*) for (a) β = 5, (b) β = 10, (c) β = 15, (d) $\beta \to \infty$. Adapted from [93].

Two important facts emerge from Figs. 1.16A and 1.16B [93]:

(1) For very low modulation index (β less than 0.2), only one significant pair of sidebands is obtained. The required transmission bandwidth in this case is approximately $2f_m$, as for Amplitude Modulation (AM). This corresponds to narrowband FM (see Fig. 1.16A-a).

(2) For very high modulation index (β more than 100), the transmission bandwidth is $2\Delta f_{peak}$. This corresponds to wideband FM. While wideband FM uses more bandwidth, it can improve the signal to noise ratio significantly (see Figs. 1.16A-b,c,d) where the value of Δf_{peak} is varied, while keeping f_m constant.

For values of β between these extremes we have to count the significant sidebands to calculate the required transmission bandwidth (BW) or it can be calculated using the approximation:

$$BW = 2f_m + 2\Delta f_{peak}$$

or

$$BW = 2f_m(1+\beta)$$

So far the discussion of FM sidebands and bandwidth has been based on having a single sine wave as the modulating signal. Extending this to complex and more realistic modulating signals is difficult. We can, however, look at an example of single-tone modulation for some useful information. An FM broadcast station has a maximum frequency deviation (determined by the maximum amplitude of the modulating signal) of Δf_{peak} =75kHz. The highest modulation frequency f_m is 15 kHz. This combination yields a modulation index of β=5, and the resulting signal has eight significant sideband pairs. Thus the required bandwidth can be calculated as 2 x 8 x 15 kHz = 240kHz. For modulation frequencies below 15 kHz (with the same amplitude assumed), the modulation index increases above 5 and the bandwidth eventually approaches $2\Delta f_{peak}$ =150kHz for very low modulation frequencies. We can, therefore, calculate the required transmission bandwidth using the highest modulation frequency f_m and the maximum frequency deviation Δf_{peak}.

Conclusion

An important thing to note from the spectrum of an *linear* FM signal shows in Fig. 1.16 is that the carrier frequency does not change with the modulating signal parameters (A_m and f_m) and also the sidebands in the left and right side of the carrier signal have an equal amplitude (symmetric sidebands amplitude). It will be shown in the next Section, that this not the case for STNOs. Due to the STNO nonlinearity, the carrier frequency is shifted as a function of the modulating amplitude and the sidebands amplitude are asymmetric [94,95].

1.4.2 Experimental and theoretical studies of frequency modulation of STNO

It has been discussed, the spectrum of "pure" (linear) FM signals as a function of modulating signal parameters, i.e. the modulation frequency f_m and the modulation amplitude A_m. The term "pure or linear" FM signal refers to the FM signal whose amplitude is constant during the frequency modulation. So that it does not affect the carrier frequency while varying the amplitude of the modulating signal A_m and leads to symmetric sidebands amplitudes around the carrier signal (see Fig. 1.16). However, this is not the case for STNOs. As already discussed previously, STNOs are characterized as a non-linear oscillator which means that the precession frequency strongly depends on the precession amplitude or power, i.e. power-phase nonlinear coupling. In the modulation case, modulating the amplitude or power of the STNO will also induce frequency modulation due to such nonlinear coupling. The term of "pure or linear" FM modulation is not valid anymore for the case of amplitude-induced frequency modulation in STNOs. This has been confirmed experimentally by Pufall et al. [94] and Akerman et. al [95]. The experiments were performed at a fixed modulation frequency f_m and varying the modulation amplitude A_m. In the pioneering frequency modulation experiment [94], the authors took advantage of the strong phase-power coupling of GMR-based STNOs to obtain a frequency modulation. The modulation was performed at a single operating point of the free running STNO, which is in the curve region of frequency versus DC current (nonlinear region). Although the gross features of frequency modulation were present, significant discrepancies from the "pure or linear" FM model were observed: (i) an unexpected carrier frequency shift as a function of modulation amplitude A_m (or ΔI in Ref. [94]) (Figs. 1.17a,b), and (ii) asymmetric sideband amplitudes in contrast to the expected *n*th order Bessel functions (Figs. 1.17a,c,d).

The attempt to justify these results was carried out by nonlinear FM (NFM) theory which takes into account the nonlinear change in the intrinsic operating frequency during modulation and performing numerical macrospin calculations. This theory is able to accurately describe the frequency shifts during modulation. However, the amplitude asymmetry of the modulated sidebands only agrees with calculations based on a theory of combined nonlinear frequency and amplitude modulation (NFAM) developed by Consolo et. [96], see Fig. 1.18. In this theory, the temporal signal eq. 1.42 was defined to be both amplitude-modulated and frequency-modulated:

$$S(t) = A_c[m(t)]\cos(\phi_i[m(t)]) \tag{1.46}$$

where the amplitude A_c and instantaneous frequency $f_i(t) = \frac{1}{2\pi}\frac{d\phi_i(m(t))}{dt}$ are polynomial expansions of a modulating signal $m(t)$.

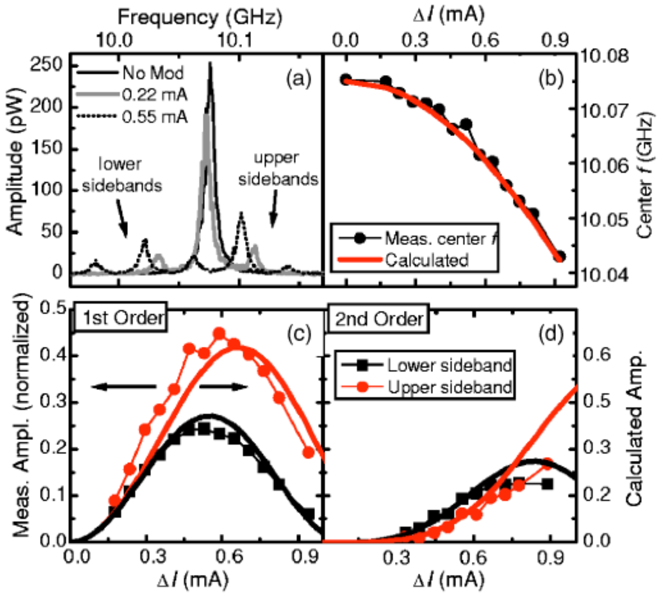

Fig. 1.17-(a) PSD of the STO output (for a nanocontact) with and without modulation current. (b) Shift of the center frequency versus modulation amplitude ΔI. Measured normalized sideband amplitude (squares) and calculated one (full lines) from a nonlinear frequency modulation NFM model using first order sidebands (c) and second-order side-bands (d). A linear modulation model is unable to explain the frequency-shift versus ΔI, and the asymmetry between the upper and lower sideband amplitude which should be equal in a linear modulation model. Adapted from [94].

By using the formalism of complex envelopes [92,93], the relation (1.46) can be written in the Fourier transform. As can be seen in Fig. 1.18, the derived analytical solution shows remarkable agreement with the micromagnetic calculations of the carrier frequency shift (Fig. 1.18a) and asymmetry amplitude of the modulated sidebands (Figs. 1.18b,c, blue line). In contrast to this the NFM theory failed to explain the asymmetry amplitude of the modulated sidebands (Figs. 1.18b,c, red dashed line).

In experiment [95], the author investigated the impact of different levels of frequency nonlinearity ($\frac{df^2}{dI^2}$ being zero, positive, and negative), on the frequency modulation of nanocontact STNO. The same modulation features as in Ref. 94, i.e. a shift of the center frequency and asymmetric sideband amplitudes with modulation amplitude A_m, are observed for the case of a nonlinear frequency dependence (positive and negative $\frac{df^2}{dI^2}$). In contrast to this, for the linear frequency dependence case ($\frac{df^2}{dI^2} = 0$), the carrier and sideband frequencies are entirely independent of the modulation amplitude, A_m. However, the asymmetry of sideband amplitudes was still observed.

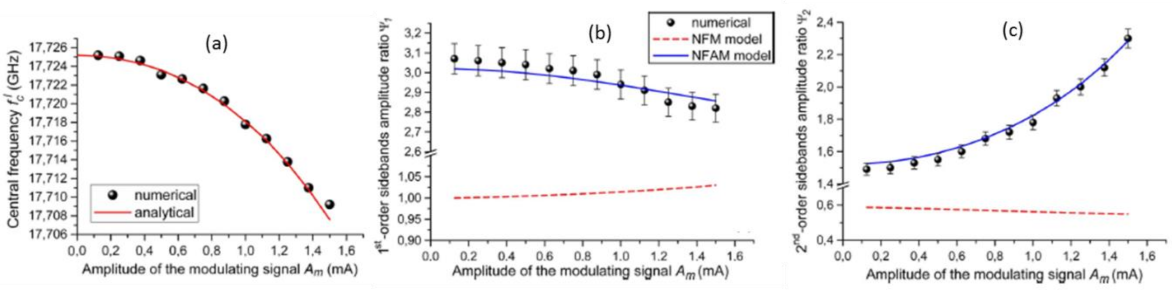

Fig. 1.18-(a) Dependence of the carrier frequency f_c on the amplitude of the modulating signal A_m. Dependence of first-order (b) and second-order (c) sidebands amplitude ratio on the amplitude of the modulating signal A_m. Symbols, together with error bars, are representative of numerical results, whereas the analytical ones are denoted by lines (dotted lines for NFM and solid lines for NFAM). Error bars associated to numerical results are representative of a computational error of about 2.5%. Adapted from [96].

This case of linear frequency modulation provides strong experimental evidence, that amplitude modulation is also taking place. Using the analytical model of NFAM proposed by Consolo et.al [96] remarkable agreement between the experimental data and calculations were shown. Moreover, it was possible to fit the modulation data with very good accuracy with a polynomial expansion up to the third order. However, the information acquired from these coefficients does not reflect the intrinsic mechanism of NFAM in STNOs, nor its consequences for a specific choice of experimental conditions and device characteristics. To investigate the origin of NFAM in STNOs, Ref. [97] derived the modulation spectrum as a function of the intrinsic STNO parameters as suggested by Slavin et. al (KTS model) (eq. 1.30). The Fourier coefficients obtained by this method give quantitative information, such as the carrier frequency shift, the modulation index, and the modulation bandwidth (MBW) of the STNO. The MBW is measured from the peak frequency deviation Δf_{peak} (a function of the modulation index) dependence on the modulation frequency as shown in Fig. 1.19.

A common criterion of the 3 dB power attenuation that is usually used to characterize filters was used to determine the cutoff frequency which is given by $2\Gamma_p$. This modulation bandwidth (MBW) gives a measure of the frequency range in which an oscillator has optimal modulation properties. This means that above the cutoff frequency, the modulation properties such as a full frequency deviation Δf_{peak}, cannot be achieved. i.e the frequency deviation Δf_{peak} is attenuated. This leads to a degradation of the modulation bandwidth.

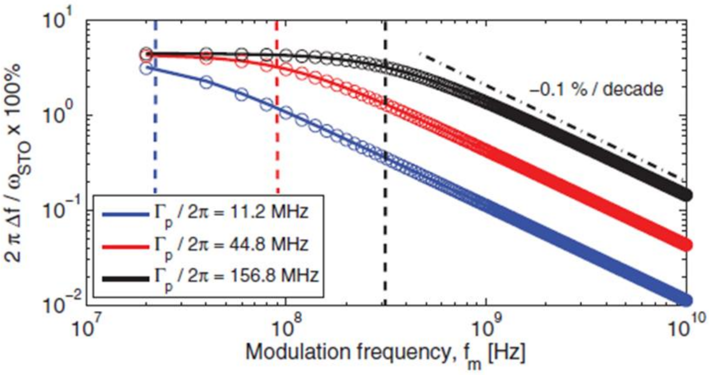

Fig. 1.19-Peak frequency deviation Δf dependence on the modulation frequency for different operating points of free running STNO (different DC currents) obtained via numerical simulation. The plots have a low-pass filter behavior with a cutoff frequency given by $f_p \sim \Gamma_p/\pi$. Adapted from [97]

A more straightforward modulation analysis technique on the determination of the modulation bandwidth of an STNO was reported by Quinsat et. al [24]. This technique is based on the extraction of the amplitude and phase noise from single-shot time traces as has been discussed in Section 1.3.5 (see Fig. 1.14). Extracting the amplitude and frequency noise plots of the modulated output voltage traces will provide the same plots as shown in Fig. 1.14, with the addition of a well-defined peak appearing above the noise level (red plot) at the modulation frequency, see Fig. 1.20. Varying the modulation frequency f_m of the modulating signal (from 1MHz up to 1GHz) for a constant modulation amplitude and superpose the responses, one can see that its amplitude envelope (peaks above the noise level) has the same cut-off as the noise spectra (red plot), this for amplitude (Figs. 1.20a,c) and frequency noise plots (Figs. 1.20b,d), in simulation and experiment.

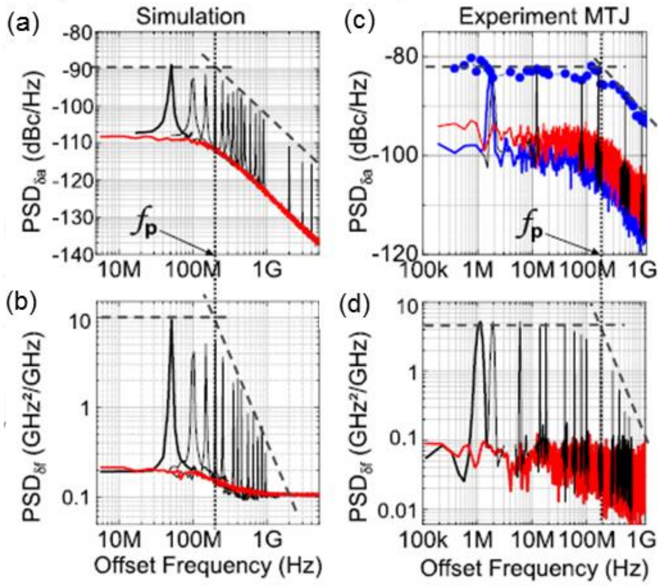

Fig. 1.20-The amplitude $PSD_{\delta a}$ (a,c) and frequency noise $PSD_{\delta f}$ plots (b,d) of modulated output voltage STNO obtained from numerical simulation and experimental measurements. As a guide to the eye, the envelope of these peaks is given in (a)-(d) by the dashed lines indicating the roll-off at f_p estimated by the vertical dotted lines. For the simulation, a ratio of I_m/I_{DC}=0.1 was used. For the experiments on the MTJ devices, a modulation power of -30 dBm was used, which corresponds to I_m/I_{DC}=0.03 with I_{DC}=0.5 mA. Adapted from [24].

For current modulation this is understandable, since the current modulation will in a first place modulate the power of the STNO. As discussed previously in Section 1.3.5, this cut off frequency f_p determines the maximum modulation frequency where the amplitude can follow an external modulation signal. Hence the bandwidth for amplitude modulation via current modulation is given by f_p. Due to the nonlinear coupling between frequency and amplitude, the same cutoff appears for frequency modulation via current modulation. Its modulation bandwidth is thus given by $f_p \sim \Gamma_p/\pi$. This coincides with the prediction of the KTS model (eq. 1.30) and the numerical results obtained by Akerman et al by analyzing the frequency deviation Δf dependence on the modulation frequency (see Fig. 1.19). Another technique of the extraction of Γ_p was reported in [23,25], in the context of characterizing the agility of STNOs as frequency synthesizers, i.e. the shortest time it takes for the STNO to hop and stabilize from one frequency to another. However this leads to complex measurement setup and the determination of Γ_p was obtained from a complex fit of the data from the frequency domain experiments (for different modulation frequencies). For this thesis, the technique presented by Quinsat et. al. [24] will be used to analyze the frequency modulation simulation results in Chapter 3.

Besides understanding the physical concept behind the frequency modulation of STNO and the method for the extraction of the modulation bandwidth of STNO, recent studies of frequency modulation of STNOs have demonstrated the use of STNO for wireless communication applications. FSK digital modulation has been first reported by Manfrini et al. [23,25] using vortex MTJ-based STNOs that emit in the 0.1-2 GHz range by modulating the current between two discrete values at frequencies up to 10MHz. The first ever complete wireless communication scheme using homogeneous MTJ-based STNOs has been recently demonstrated by Choi et al. [26], adopting non-coherent wireless communication systems based on digital On-Off Keying (OOK) modulation and envelope detection technique. They reported wireless communication with a decent data rate, 0.2Mbps, and SNR of 12.5 dB at a distance between the transmitter and receiver of 100cm. Using the same wireless communication concept, R. Sharma et al. [27] were able to improve the data rate up to 4Mbps at the same communication distance as demonstrated by Choi et al. The signal to noise (SNR) ratio is however 6dB smaller. Further demonstration of a homogeneous MTJ-based STNO modulation using OOK concept on a printed board card (PCB) level has been first reported by Oh et al. [28], resulting communication over 10mm with the data rate of 0.4Mbps. This data rate is slightly less compared to Choi et al. and R. Sharma et al. The data rates achieved in the mentioned demonstrations above are all limited by the rising time and falling time of the electronic components in the measurement system, i.e. the bias-T, and not to the intrinsic (agility) of STNOs as mentioned in Ref. 22-24.

A recent application of STNOs that has been proposed by Toshiba is to use them as dynamic read heads in hard disk drives [29-33]. In this concept, the STNO frequency is modulated by the dipolar stray field from the bit “0” and “1”, leading to a frequency shift into two discrete values which refer to FSK digital modulation. For the read out, this frequency shift can be converted into a voltage signal level using non-coherent demodulation technique (delay detection technique). In order to increase the bit data rate, the STNO has to respond fast to the changing bit stray field. The challenge is to define the STNOs with modulation bandwidths that achieve high bit data rate. This means also that the investigations presented previously for current modulation need to be extended to field modulation, to see whether the modulation bandwidth is controlled by the same parameter. The investigation of field modulation in STNO is thus essential for read head applications. This is the aim of Chapter 3, where the field modulation in STNO will be carried out numerically within macrospin approach. The upper limit of modulation bandwidth for the field modulation will be investigated for different field configurations and compared with the one for current modulation that has been intensively studied.

1.5 General Summary

To conclude, an overview of fundamental aspects of STNOs has been discussed starting from the physical concepts underlying the STNOs, its magnetization dynamics, and the analytical model that explains the dynamic behavior of STNOs in the autonomous and non-autonomous regime. The STNO's operating principle is based on two spintronics effects: spin transfer torque effect to set the magnetization dynamic into steady state oscillation, and the magnetoresistance effect to produce an output voltage. The effect of spin transfer torque on the magnetization dynamics is described by the LLGS equation. The LLGS equation solution predicts the evolution of magnetization dynamics under the external control parameters which permits to acquire important information such as the threshold current, the excitation modes (IPP and OPP), the frequency dependence on the external control parameters, influence of the noise on the magnetization dynamics, etc. The LLGS equation does not show direct insight into most pertinent nonlinear parameters. The transformation of LLGS equation to universal oscillator model (KTS model) gives a clear and simple physical picture of the nonlinear dynamical occurs in STNOs, both in the autonomous auto-oscillation regime and under the influence of periodic/stochastic external signals. In particular, the model suggests a direct way of extracting the most important parameters of STNOs, which is the amplitude relaxation rate Γ_p, and predicts that this parameter determines the agility of STNOs, i.e. the rate of STNO to drive the magnetization back to its equilibrium trajectory after perturbations. Moreover, it has been shown by many studies that this parameter also limits the modulation frequency of STNOs and hence the modulation bandwidth of STNO is given by Γ_p under current modulation. Finally, recent studies of frequency modulation of STNO have been summarized, which took advantage of the strong frequency-power coupling of STNO to obtain the frequency modulation. It demonstrated the use of STNOs for non-coherent wireless communication system, i.e ASK modulation. The maximum data rate is however still lower than the expectation due to setup limitations. This motivates the study which is carried out in Chapter 4, where the FSK concepts will be applied to investigate the maximum data rate of STNOs. For some other applications such as the use of STNOs for dynamic read heads in hard disk drive technologies, the frequency modulation studies of STNO need to be extended to field modulation, in particular for the determination of the maximum achievable data bit rate and to see whether an upper limit exists and whether it is controlled by the same parameter as in current modulation. This is the main aim of Chapter 3 where the investigation is performed via numerical simulation. The amplitude and phase noise technique will be used to analyze the maximum achievable data bit rate. To confirm the simulation results the analytical model (KTS model) needs to be developed for the case of field modulation.

Chapter II
STNO realization and characterization

To demonstrate the feasibility of STNOs in the radio frequency (RF) application level, one has first to optimize the RF performances of STNO devices. For such applications, the STNOs have to emit high frequency oscillation with good spectral purity, low linewidth, high output power, wide frequency tuning, good signal stability (good phase noise), good barrier stability and low threshold current. For this, one has to define appropriate magnetic nanostructures and nano-fabrication processes and to characterize their RF performances. Prior to the start of my thesis the RF performances of STNO devices, Hitachi GST (HGST), have been studied. These studies permitted to acquire the basic knowledge of the RF performances of STNO. Within Mosaic project, the state of the art of STNO devices has been realized by International Iberian Nanotechnology (INL) laboratory for material (MTJ stack) deposition and Spintec for nanofabrication processes and RF characterization. Here, the author's contribution was to characterize and evaluate the RF performances of STNO devices. The results are used to give feedback for further development and optimization of the material deposition and nanofabrication processes, and to identify devices with good RF performances to be used for further studies, i.e. FSK measurements.

In this chapter, the RF performances of STNO devices realized in this thesis (Mosaic devices) will be investigated, evaluated, and compared with the RF performances of other STNO devices, such as Hitachi devices, which have different magnetic stack compositions. To characterize the RF performances of STNOs, two measurement techniques are considered, i.e. frequency domain technique and time domain technique. The measurement setup for this characterization is discussed in Section 2.1. Afterwards, in Section 2.2, the discussion is continued on the introduction of STNO devices investigated in this thesis, i.e. Mosaic devices and Hitachi devices. The advancement and the optimization of Mosaic devices and its challenge during the realization, magnetic stack development and nanofabrication process, are also discussed in this Section. In Section 2.3, the statistical analysis of STNOs from different nanofabrication processes and different magnetic stacks will be evaluated. The dynamic characterization of STNOs will finally be evaluated in Section 2.4. The results are compared in terms of their microwave excitation (single or multimode), their linewidth, their output power, and their signal stability (phase noise). This defines important strategies for further improvement and optimization of STNO devices, especially for STNO devices realized within Mosaic.

2.1 Experimental Setup and Measurement Technique

This section is devoted to the measurement techniques and experimental setup for RF characterization of STNOs. Prior to the start of my thesis, appropriate RF measurement techniques for the characterization of STNOs have been developed, i.e. frequency domain [76] and time domain measurement techniques [85]. The frequency domain measurements provide direct extraction of the microwave emission peaks of the STNO which leads to an easy way to analyze the evolution of frequency, linewidth, and output power of the STNO as a function of external control parameters, i.e. DC current and applied field. For characterization of the microwave signal stability, the time domain technique is needed, showing the voltage variation (amplitude oscillations) over a period of time. The main advantage of using time domain techniques is the possibility to extract the amplitude and phase (frequency) noise characteristics of the STNO. This provides direct access to deduce the important nonlinear parameters of the STNO: the dimensionless non-linear amplitude-phase coupling parameter, ν, and the amplitude relaxation rate, Γ_p (see Chapter 1, Section 1.3.5), which are the relevant technological parameters. In this thesis, both techniques are used to investigate the RF performances of STNOs which is the major importance for the optimization of device performances. In the first part, the experimental setup for RF measurements and the problem of the extraction of the actual signal emitted by the STNO will be discussed. The basic issues of the power transmission in RF circuits, i.e. impedance mismatches, will be introduced in the second part to give an idea on the correction of the signal measurement. In the last part, the analysis method of the extraction of amplitude and phase noise of the STNO will be discussed.

2.1.1 Experimental setup

The frequency and time domain measurement can be achieved at the same time using the experimental setup shown in Fig. 2.1. For the frequency domain technique, the measurements are done using a spectrum analyzer, while the time domain technique uses a real time oscilloscope to register the time traces of the output voltage signal.

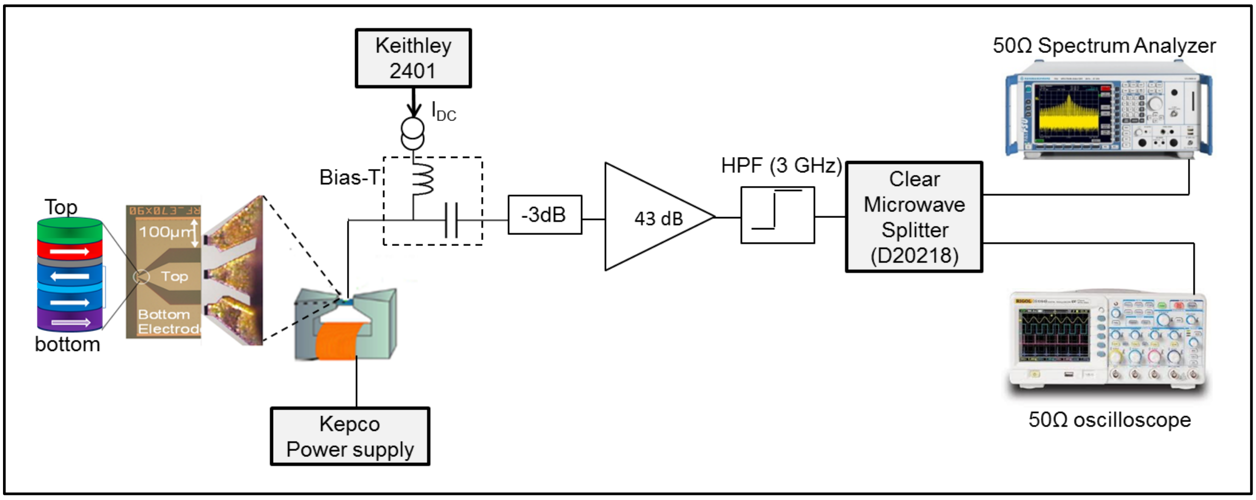

Fig. 2.1-Experimental setup for STNOs characterization

The STNO devices generate a microwave signal in high frequency in the range of GHz. This requires special components, RF components, to guide the microwave signal from an input port to the output port. The RF components needed in these measurements, from left to the right (Fig. 3.1), are a pico probe, a bias-T (Marki Microwave BTN-0040), an attenuator, a power splitter (Clear Microwave D20218 with an insertion loss of 0.9dB over 2GHz to

18GHz), an amplifier (Miteq AMF-5D with a 43 dB gain over 100 MHz to 12 GHz), a 3GHz high pass filter (HPF), a spectrum analyser (Agilent PNAE8363B with a bandwidth of 1 MHz to 40 GHz) and a real time oscilloscope (Textronix DPO72004). Besides RF component, a source meter (Keithley 2401), a Kepco power supply, and an inductive circuit are needed. The measurement procedure is as follow:

1. The STNO device is placed in the middle of the cones of an electromagnet, so that the magnetic field felt by the STNO is homogeneous.
2. An in-plane magnetic field with maximum strength of ±1500Oe is generated by the electromagnet which is controlled by a Kepco power supply with a Labview interface. The magnetic field orientation can be adjusted in the in-plane direction.
3. A Ground-Signal-Ground (GSG) pico-probe is used to make an electrical contact with the STNO devices.
4. A DC current is injected to the STNO devices through the DC part of the bias-T. Injecting a small current of 0.05mA and sweeping the magnetic field from 1500Oe to -1500Oe, one obtains the magnetoresistance (MR) curve of the STNO, i.e. the evolution of the resistance as a function of magnetic field. From the magnetoresistance curve, the static properties such as the device resistance and the corresponding resistance area (RA) product and TMR value can be obtained. The maximum DC current can be applied to the STNO nanopillar is determined by the degradation or breakdown voltage divided by the antiparallel resistance, $I_{max}=V_b/R_{AP}$.
5. In order to observe the dynamic microwave signal induced by the STNO, the DC current is increased to the maximum value and the magnetic field is swept while adjusting its orientation with respect to the easy axis direction of the STNO.
6. The oscillating microwave signal is separated from I_{DC} by a bias-T.
7. A 3dB attenuator is positioned after the bias-T to reduce the standing wave due to the impedance mismatch between the high STNO resistance, $R_{STNO}\geq 100\Omega$, and the 50Ω RF components.
8. Since the output power emitted by the STNO is very low, on the order of nWatt, the output signal is amplified by a 43dB amplifier over 100MHz to 12GHz.
9. The amplified signal is filtered using a 3GHz High Pass Filter (HPF) to reject the low frequency noises that arise from the RF components.
10. The filtered signal is split into two outputs by a power divider (splitter). One output is connected to a spectrum analyzer (frequency domain technique), showing a peak in voltage as a function of the frequency, and the other output is connected to an oscilloscope (time domain technique), showing a signal oscillation in voltage as a function of the time.

The signal received by the spectrum analyzer and oscilloscope is not the actual signal emitted by the MTJ-based STNOs. In order to extract the correct signal (power) emitted by the MTJ-based STNO, one has to take into account the power transmission issues and the impedance mismatches that occur in a RF measurement. The impedance mismatch between each interface of two elements of the measurement chain, i.e. the STNO (≈100Ω) and the 50Ω measurement chain, leads to a reflected wave (and thus power), that decreases the transmitted power to the RF measurement chain. In addition, the signal amplification by the amplifier is not ideal because the amplifier gain is varying with the frequency, as shown in Fig. 2.2. The measured signal will be thus a modulation of the real signal by the amplifier gain. This will modify the form of the spectra observed in the spectrum analyzer. To conclude, it is indispensable to correct the measured spectra. For this, two steps are considered:

- The evaluation of the impact of the STNO’s electrodes and the impedance mismatch between the STNO and the RF component on the power transmission transmitted to the measurement chain.

- The calibration of the RF chain by measuring the S-matrix obtained via a vector network analysis (VNA) in order to correct measured spectra, i.e the actual output power emitted by the STNO.

These steps will be discussed in the next section.

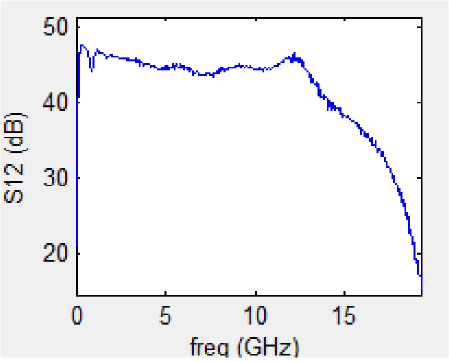

Fig. 2.2-Characteristic of RF amplifier measured via a vector network analysis (VNA). The gain (dB) is varied with the frequency with cutoff frequency is about 12GHz.

2.1.2 Specifics of RF measurements: Frequency domain technique

Before showing the evaluation of the impedance mismatches of the STNO and the gain correction from the RF chain, it is important to introduce first the basic issues of the power transmission in RF measurements, i.e. theory of transmission line, to understand the origin of the impedance matching and its effect on the power transmission.

2.1.2.1 Transmission line theory

The equivalent circuit of the RF measurement chain (Fig. 2.1) is shown in Fig. 2.3. The Device Under Test (DUT), in this case is the STNO, is measured at one end of the measurement chain (characterized by a load Z_M = 50). Since the signal generated by the STNO is in high frequency, GHz range, their wave nature must be taken into account. For instance, if a 10 GHz signal is considered, the wavelength is about 3 cm that is a similar length to most of the components found in Fig. 2.1. When the wave length of the signal is comparable to the length of the RF components, the quasi-static approximation that allows the use of Kirchhoff's law is not suitable. Here the microwave signal is considered as a power quantity (a wave) that propagates into a certain direction. Most of the RF components are waveguides that guide the microwave from their input port to their output port. The description of the propagation of the power through the different components makes use of continuity equations given by Maxwell's equations and transmission line theory.

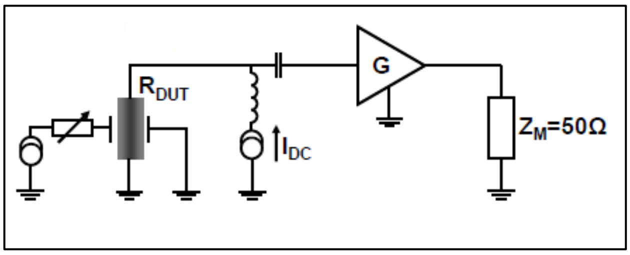

Fig. 2.3-Equivalent circuit of the measurement chain given in Fig. 3.1. The measurement is done on a 50Ω load (spectrum analyzer or oscilloscope) after the gain amplification of the chain G. R_{DUT} is the resistance of the STNO which is more complex than only a resistance (see section on de-embedding). Adapted from [85].

To take into account the spatial variation along a waveguide, the telegraph model is used as given in Fig. 2.4. In the circuit, the letter C corresponds to the capacitance and L to the inductance. In the transmission line the signal is propagated in the +x direction. In the telegrapher model, the wave will be propagated in an infinite medium, separated infinitesimal parts of size *dx* where Kirchhoff's law is valid. If the transmission line is lossless, only a linear capacitance *C* and linear inductance *L* is needed to define the propagation of the wave described by (*u, i*). Here u and i represent the voltage and current wave amplitudes. The wave propagation for the case of a lossless transmission line is called as telegraph equation, given by:

$$\frac{\partial^2 u}{\partial^2 x^2} - \frac{1}{LC}\frac{\partial^2 u}{\partial t^2} = 0 \tag{2.1a}$$

$$\frac{\partial^2 i}{\partial^2 x^2} - \frac{1}{LC}\frac{\partial^2 i}{\partial t^2} = 0 \tag{2.1b}$$

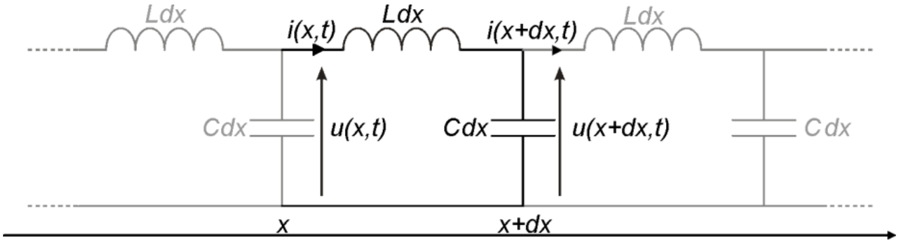

Fig. 2.4-Telegraph model of ideal (lossless) transmission line. Adapted from [88].

Solving the telegraph equation (eq. 2.1), one can obtain a general expression for the characteristic impedance of a lossless transmission line, $Z_c = \sqrt{L/C}$. This characteristic impedance Z_c indicates the ratio of inductive/capacitive ratio of a line. In a real case of transmission lines, the resistance R and the conductance G will introduce losses in the system. The real circuit of the transmission line is shown in Fig. 2.5. In this case the characteristic impedance is a complex quantity that explicitly depends on the frequency, $Z_c = \sqrt{\frac{R+j\omega L}{G+j\omega C}}$. The real impedance of transmission lines depends on its geometry and electrical properties that could be for example the size of the cables or the dielectric media inside them.

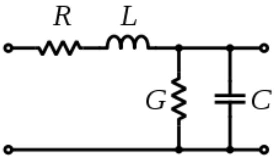

Fig. 2.5-An equivalent circuit of finite (non-losses) transmission line. Adapted from [88].

The common value of the characteristic impedance used for components in the RF range is 50Ω. It is important to remember that the characteristic impedance is related with the wave propagation energy in the transmission line and is not to be confused with the ohmic resistance representing the energy dissipation.

2.1.2.2 Impedance matching

Impedance matching means that the impedance between the interfaces of two different media should match to minimize the reflection and maximize the power transmission. The different impedance between two media leads to a reflected wave (and thus power) that decreases the transmitted power. Fig. 2.6a shows the different impedance (impedance mismatch), Z_{c1} and Z_{c2}, between the interfaces of two different transmission lines. Considering an incoming wave (u_1^+, i_1^+) is traveling through the transmission line from 1 to 2. When this wave reaches the interface, one part of this wave is transmitted (u_2^+, i_2^+) and the other part is reflected (u_1^- , i_1^-). Hence the transmission and reflection coefficients are described as follow:

$$\Gamma_{trans} = \frac{u_2^+}{u_1^+}, \qquad \Gamma_{reflex} = \frac{u_1^-}{u_1^+} \tag{2.2}$$

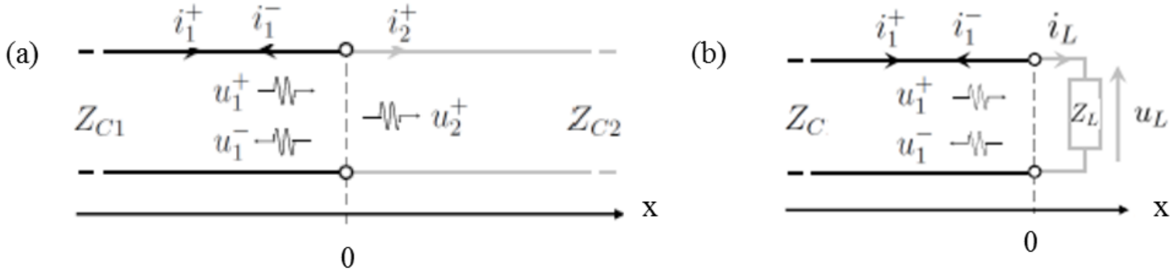

Fig. 2.6-(a) Two infinite media linked at $x = 0$ with two different characteristic impedances Z_{C1} and Z_{C2}. (b) Transmission line terminated by a load of impedance Z_L. Adapted from [88].

From the continuity conditions $i_1^+ = i_1^- + i_2^+$, the above equations can be written as follows:

$$\Gamma_{trans} = \frac{2Z_{c2}}{Z_{c1}+Z_{c2}}, \qquad \Gamma_{reflex} = \frac{Z_{c1}- Z_{c2}}{Z_{c1}+Z_{c2}} \tag{2.3}$$

For the case of a load terminated line as shown in Fig. 2.6b, with a load of impedance Z_L, the Z_{C2} is replaced by Z_L. The reflection coefficient is thus:

$$\Gamma_{reflex} = \frac{Z_{c1}- Z_L}{Z_{c1}+Z_L} \tag{2.4}$$

It is clear now that an impedance mismatch between the transmission lines will lead to a reflection of the incident wave. The reflection creates a standing wave if there is reflection at both ends of the transmission line, which leads to further power waste and may cause frequency-dependent loss. Therefore, impedance matching is desirable. In the case of a terminated transmission line shown in Fig. 2.6b, the reflection can be minimized by matching the impedances Z_{c1} and Z_L so that they are equal (Γ=0).

2.1.2.3 Measurement of the voltage power spectral density (PSD)

We focus now on the last components of the RF chain that is the Spectrum Analyzer (SA). This instrument is used to analyze the signals in the frequency domain, i.e. the signal's amplitude as a function of frequency. The basic theory of operation of a spectrum analyzer, the heterodyne method, can be found in [98]. In this section, important measurement parameters using the SA will be highlighted to obtain accurate RF measurements.

(a) Resolution Bandwidth (RBW)

RBW determines how close two signals can be resolved by the analyzer into two separate peaks. The RBW setting must thus be considered when concerned with separating spectral components. Using a narrow RBW is necessary to get accurate and correct signal measurements, i.e. to resolve peaks and obtain the correct linewidth and output power estimation. When using a narrow RBW, the displayed average noise level of the spectrum analyzer is lowered, increasing the dynamic range and improving the sensitivity of the spectrum analyzer. However narrower RBW translates to longer sweep times, which translates to a tradeoff between sweep speed and sensitivity. For efficient measurement but still to get correct information of the signal, the RBW should be set at least four times smaller than the signal linewidth Δf as can be seen in Fig. 2.7. In the example given in Figs. 2.7a,b, the correct evaluation of the linewidth of a Lorentzian signal of Δf=6MHz and power P=-30.5dBm (parameters are set in the signal generator menu) is obtained when the RBW<Δf. In this thesis, an RBW of 1 MHz is applied during the measurement, for a minimum linewidth of the measured devices around 15MHz.

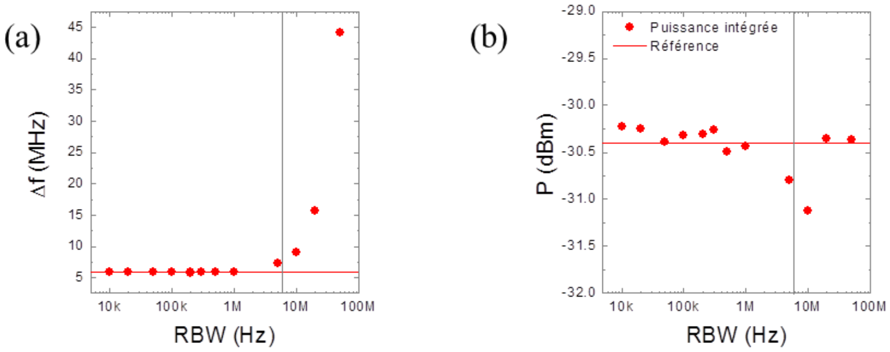

Fig. 2.7-Signal characteristic of a Lorentzian signal of Δf=6 MHz and P=-30.5 dBm generated by signal generator with different RBW used for the measurement with the SA: (a) Δf versus RBW and (b) power versus RBW. Adapted from [76].

(b) Sweep time

Sweep time is the time to sweep the frequency across the displayed frequency span. Sweeping an analyzer too fast causes a drop in the displayed amplitude and a shift in the indicated frequency. The sweep time must be selected to be compatible with the RBW. Sweep time of a spectrum analyzer is approximated by the span divided by the square of the resolution bandwidth (RBW). For example, the sweep time for an 18 GHz frequency span and 1 MHz RBW is 18ms.

(c) Trace averaging

From the basic principle of spin torque driven excitations, stating that the spin momentum transfer cancels natural damping, one would expect that the linewidth is zero (perfect Diract peak). However, noise in the system is inevitable. In particular STNO are nanoscale devices which are very sensitive to noise. It is evident that the linewidth of the emission peak of STNOs is not zero. This means that the frequency oscillation is not stable but fluctuating, leading to a noisy emission peak or spectrum. The noisy spectrum measured on a spectrum analyzer can be improved by repeating the experiment several times and averaging, allowing noise to be averaged out and yielding more accurate power measurements. In a spectrum analyzer, the trace averaging is accomplished over two or more sweeps on a point-by-point basis. At each display point, the new value is averaged with the previously averaged data. The display gradually converges to an average over a number of sweeps. The trace averaging is done by setting the number of sweeps over which the averaging occurs. Figure 2.8 shows trace averaging for different numbers of sweeps. As the number of sweeps increases, the spectrum is smoothened and well-defined. However, the large the number of sweeps, the longer the measurement time. In this thesis, the trace averaging of 15 is used to improve the spectrum of the measured STNOs.

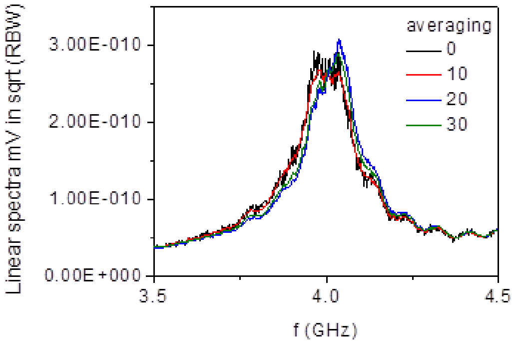

Fig. 2.8-Spectrum of the measured STNO (non-corrected spectrum) as a function of the trace averaging. When the number of sweeps is increased to 20 (blue curve) or 30 (green curve), the spectrum is better (one single peak instead of two peaks).

To conclude, the parameters of the spectrum analyser discussed above are applied during the RF measurement of the STNOs in this thesis in order to have an accurate and better sensitivity of the measured signal. The spectrum of the STNO measured with the spectrum analyser is not corrected yet. In order to correct the spectrum, i.e. to have a correct output power extraction, the correction of the signal measurement is necessary. The procedure of the signal correction will be discussed in the following.

2.1.2.4 Correction of the signal measurement

The Section 2.1.2.2 highlights the importance of a good matching between the elements in the RF measurement setup. This condition is not always accomplished, generating losses in the STNO emitted signal. In order to extract the real output power emitted by the STNO, two types of signal corrections are taken into account. The first is the de-embedding, which corresponds to finding the equivalent electric circuit of the electrode layout of the MTJ inserted in between a top and bottom electrode. Second is the correction of the gain of the measurement chain (i.e. from the picoprobes to the spectrum analyzer) by using a vector network analysis (VNA) and measuring the transmitted power.

2.1.2.4.1 De-embedding

Detail studies of the de-embedding of the STNO on reflection devices have been done by Houssameddine [76] and M. Quinsat [88]. The goal of the de-embedding is to extract the actual RF power generated by the MTJ pillar. Since a MTJ-based STNO has a load impedance of about 100Ω to 1kΩ, the signal generated in the STNO is not fully transmitted to the measurement chain because of the impedance mismatch problem discussed in Section 2.1.2.2. Moreover, the STNO pillar is embedded in coplanar waveguide electrodes, i.e. a top and bottom electrode. Since the top and bottom electrodes overlap, it implies a capacitance effect between these electrodes, as illustrated in Fig. 2.9a with a zoom at the position of the MTJ device. This Section discusses the extraction of the actual power generated by the STNO from the measurement of reflected power with a vectorial network analyzer (VNA).

Two different geometries of coplanar waveguide exist, called transmission and reflection device. In the transmission device, the central line is split into two parts to contact the MTJ. The reflection device is presented in Fig 2.9a with a zoom at the position of the MTJ device. The reflection device is used in this thesis. Taking into account the specific of the electrode geometry of the STNO reflection device, an equivalent circuit can be modeled by a basic RLC circuit as shown in Fig. 2.9b. This model consists of the resistance of MTJ (R_{MTJ}), capacitance C (formed by the overlap of the upper and lower electrode), inductance component L, and the resistance of the electrodes r_l. The equivalent impedance Z_{eq} calculated from the equivalent circuit model is defined as follow:

$$Z_{eq} = \left(r_l + \frac{R_{MTJ}}{1+\left(R_{MTJ}C\omega\right)^2}\right) + j\left(L\omega - \frac{R_{MTJ}^2 C\omega}{1+\left(R_{MTJ}C\omega\right)^2}\right) \tag{2.5}$$

By measuring the characteristic impedance of the STNO via a VNA and fitting the measured curve (impedance versus frequency) using the eq. 2.5 (Fig. 2.10a), the electrode parameters r_l, L and C can be extracted. The corresponding value of r_l, L and C from the fitting is r_l≈6Ω, L≈12pH, and C≈54f (see Fig. 2.9b).

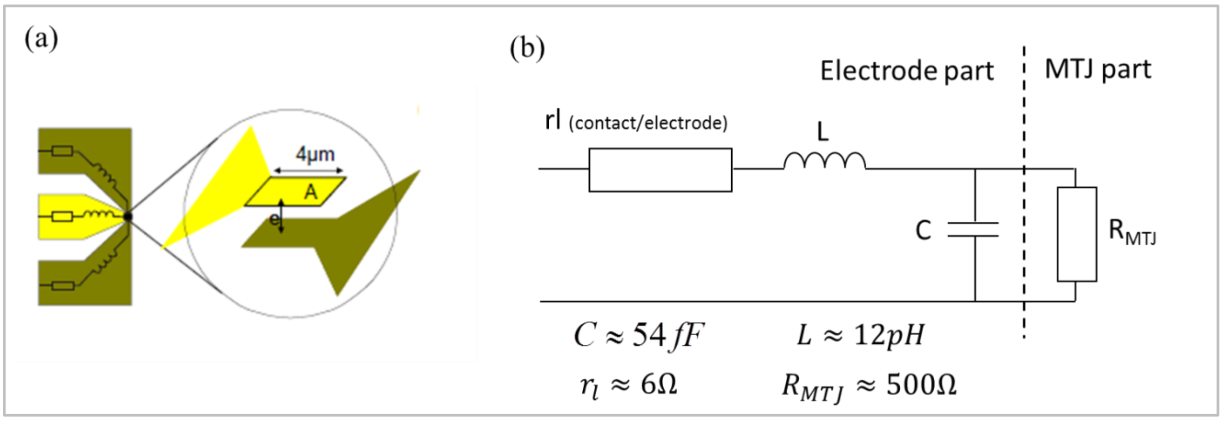

Fig. 2.9-(a) Schematic view of the STNO geometry encapsulated in its electrodes. (b) Block diagram of the equivalent electrical circuit for each component. Adapted from [88].

In this example, the resistance of the MTJ pillars is close to 500Ω (Hitachi device). The value of the gain, the ratio of the voltage/power measured at the 50Ω load to the actual voltage/power emitted by the MTJ pillar, can be deduced from this expression:

$$G = \frac{1}{1+\frac{1}{Z_C}\left(r_l+R_{MTJ}(1-CL\omega)\right)+j\omega\left(R_{MTJ}C+\frac{L}{Z_C}+\frac{R_{MTJ}}{Z_C}r_l C\omega\right)} \tag{2.6}$$

with Z_c is the load impedance.

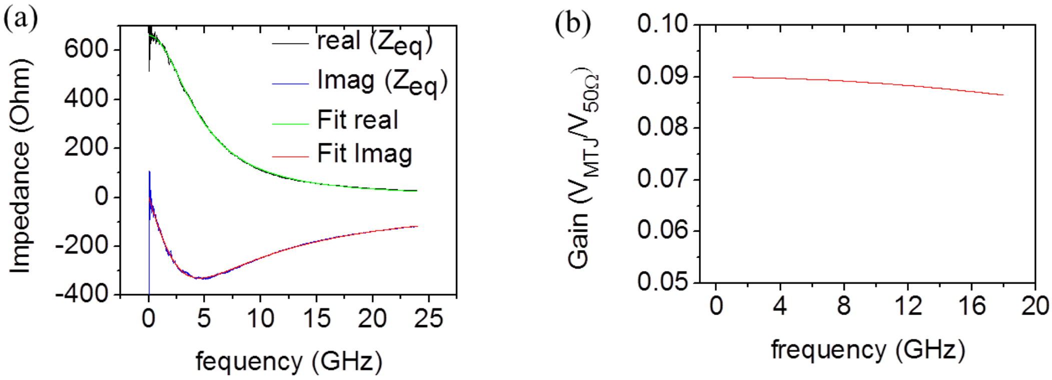

Fig. 2.10-(a) Real and imaginary part of the characteristic impedance of the STNO embedded in its electrodes, measured by the VNA. The fitted curves correspond to the model eq. 2.5 (b) The transmitted voltage/power generated at the MTJ pillar (500Ω) to a 50Ω load. Adapted from [88].

The curve of the gain as a function of the frequency (eq. 2.6) for $Z_c = 50\Omega$ is given in Fig. 2.10b. The curve shows that the high resistance value of the MTJ pillar reduces the transmitted voltage/power to the 50Ω chain that is around 0.09 times lower than its actual value for a given frequency range (1GHz to 17GHz). Moreover, the curve shows small variation of the gain over the frequency range. This small variation is due to the small capacitance value (C=54fF), such that the capacitance effect on the voltage/power transmission can be neglected [88]. The voltage/power transmission from the MTJ to the 50Ω chain is thus mainly affected by the high impedance mismatch between the high resistance MTJ pillar and the 50Ω chain. Therefore, in order to obtain the actual voltage/power emitted by the MTJ pillar, it is necessary to multiply the measured voltage/power by a constant value around 11.

To conclude, the characteristic impedance model (eq. 2.5) of the STNO embedded in its electrodes can be used to estimate the actual power generated by the STNO. In particular, this model will be of use when injecting high frequency signals to the STNO, i.e. modulation experiment.

2.1.2.4.2 Gain correction of the RF measurement chain

The RF measurement chain plays an important role for the extraction of the actual power generated by the STNO. As an example, the signal amplification by the amplifier in the RF chain is not ideal. The amplifier gain is varying with the frequency, as shown in Fig. 2.2. The measured signal will be thus a modulation of the real signal by the amplifier gain and will modify the form of the spectra observed in the spectrum analyzer. Moreover, the other RF components, such as attenuator, power divider, bias-T, etc, have their own characteristics that can attenuate the power generated by the STNO. Therefore, the correction of the RF measurement chain is needed to extract the actual power generated by the STNO.

A VNA is used to measure the characteristic (scattering matrix) of the RF measurement chain. Here, the input of the RF measurement chain (without STNO) is linked with the output of the chain via a VNA. From VNA measurements, the scattering matrix [76,88] is obtained, as shown in Figs. 2.11. The scattering matrix formalism has a very direct use for the physical interpretation of its elements. For instance, S_{12}, i.e. the ratio of output voltage to the input voltage, is actually the (voltage) gain of the component.

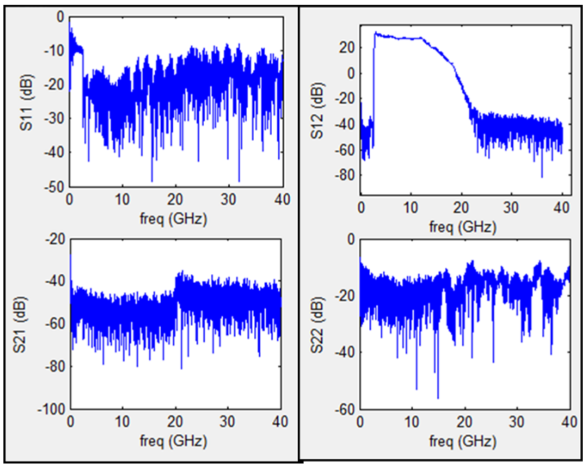

Fig. 2.11-The scattering matrix of the measurement chain measured via VNA.

As shown in Fig. 2.11, the total gain of the RF measurement chain, S_{12}, varies with frequency. The gain drops at the cut-off frequency of 12GHz which is mainly given by the characteristic of the amplifier. The cut-off frequency at low frequency, 3GHz, is given by the high pass filter (HPF). As mentioned previously, the HPF of 3GHz is used to reject the low frequency noises that arise from the RF components. Due to the power transmission losses in a RF measurement chain, i.e. the use of attenuator, the RF cables, and other RF components, the total gain of the chain is reduced by 10dB compared to the initial gain of the standalone amplifier, see Fig. 2.2. The transfer function of the total gain of RF measurement chain, S_{12}, measured by the VNA provides thus an accurate tool to extract the real output signal (spectra and power) emitted by the STNO, $V_{measured} = G(f).V_{STNO}$. The procedures of the correction of signal measurement obtained from frequency domain measurements are summarized in the following:

(a) Baseline correction

The spectrum of the STNO is measured with a spectrum analyser, as shown in Fig. 2.12a. A 3GHz HPF (vertical red line) was applied in the RF chain to reject the noise at low frequency. The RBW and trace averaging of spectrum analyser were set to 1MHz and 15 sweeps, respectively. The spectrum contains the intrinsic noise of the RF measurement chain, i.e a baseline. Its amplitude is amplified by the gain of the RF chain. In order to obtain the real spectrum emitted by the STNO, the baseline noise level and the total gain of the RF chain have to be taken into account. The baseline of the RF chain is measured at zero DC current and zero applied field, shown in Fig. 2.12b. The baseline profile is mainly determined by the amplifier profile whose amplitude rolls off at 12GHz, see Fig. 2.2. The following is the baseline correction procedure:

Step. 1- Normalization of the baseline (BL) in V^2/Hz: $BL_{norm} = \frac{(BL)^2}{RBW}$

Step. 2- Baseline correction from the RF chain gain. The total gain of the RF chain is given by scattering matrix, S_{12}, in Fig. 2.11.

$$BL_{cor} = BL_{norm} * 10^{-gain_{dB}(S_{12})/10}$$

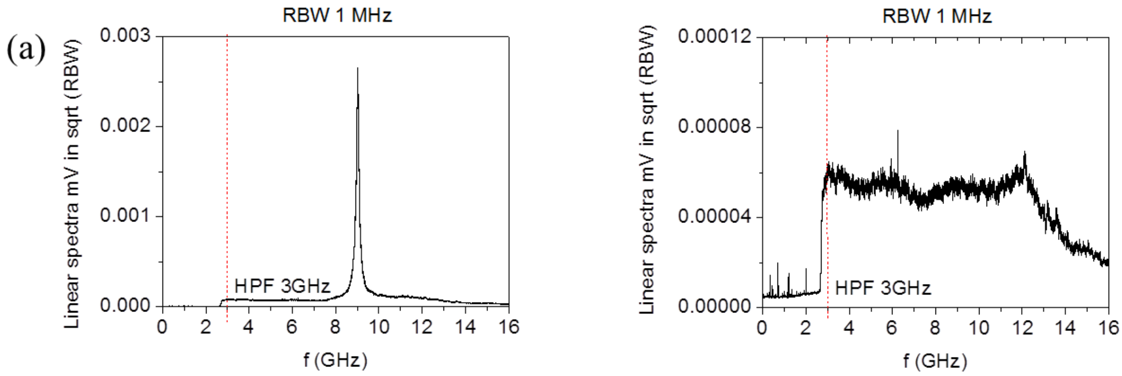

Fig. 2.12-(a) non-corrected spectrum of the STNO (b) the baseline profile of the RF chain. The vertical red dashed line corresponds to the cut-off frequency of high pass filter, HPF.

(b) Spectrum correction

The same step as the baseline, the correction procedure of the spectrum of STNO is given as follow:

Step.1 – Normalization of the spectrum of STNO in V^2/Hz to obtain a power spectral density PSD: $PSD_{norm} = \frac{(PSD_{non-cor})^2}{RBW}$

Step.2 – PSD correction from the RF chain: $PSD_{cor} = PSD_{norm} * 10^{-gain_{dB}(S_{12})/10}$. Gain, dB, here, is given by the scattering matrix S_{12}.

Step.3. – PSD correction from the baseline: $PSD_{final} = PSD_{cor} - BL_{cor}$. The corrected PSD of the STNO is now in units V^2/Hz, shown in Fig. 2.13.

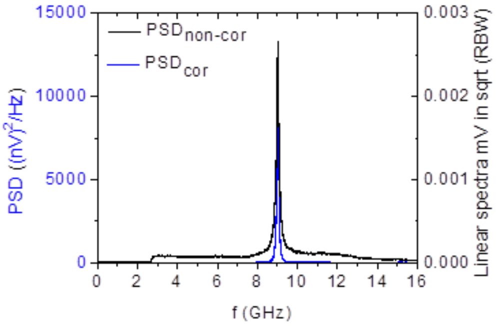

Fig. 2.13-Corrected PSD (blue curve) and non-corrected PSD (black curve) of the STNO. The non-corrected PSD has been shown previously in Fig. 2.12a.

(c) Power measurement of the corrected PSD

In this step, the corrected PSD shown in the blue curve of Fig. 2.13 is fitted with a Lorentzian function. As can be seen in Fig. 2.14, the Lorentzian fits well with the PSD. From this fitting, the centre frequency f_c, and the linewidth Δf and the integrated peak V^2 (over the frequency interval) are obtained. The output power is then calculated by dividing the integrated peak V^2 by 50Ω impedance, i.e. P (Watt)=V^2/50.

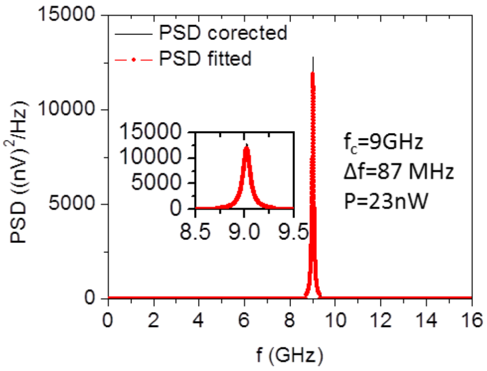

Fig. 2.14-Extraction of RF properties of the corrected PSD with Lorentzian fitting: frequency f_c, linewidth Δf, and output power P.

In order to facilitate the data measurement analysis, the aforementioned procedures, i.e. the baseline subtraction, the gain correction and the lorentzian fitting of the corrected PSD, were integrated into matlab program, such that the data analysis can be done automatically. In this way, the STNO parameters extraction such as the frequency, the linewidth, and the output power can be performed correctly and efficiently.

While measurements with the SA provide linewidth Δf, they do not provide a deeper insight into its origin, in particular, as to amplitude and phase fluctuations. The next section describes a time domain technique that allows one to analyze the amplitude and phase of STNOs, by using signal analysis techniques.

2.1.3 Time domain measurement technique

The time domain measurement technique is performed using a high speed real time oscilloscope (Textronix DPO72004). The detail information about this instrument can be found in Ref. 99. Important parameters needed to adjust using this instrument for STNO characterization are the sampling rate, the record length, and the bandwidth. For instance, this instrument has the capability to measure with fast sampling rate up to 50G samples/s which corresponds to a time resolution of 20ps/point. Record length is the number of points in a complete waveform record. Textronix DPO72004 has a maximum record length (memory) of 5 x10^6 points which corresponds to a time traces of 0.1ms at the highest sampling rate. The longer the time traces, the more accurate the measurement is, i.e. high frequency resolution. In this thesis, the record length is set to 2x10^6 points, which gives rise to the time traces of 40μs (2x10^6 points/50G samples/s). This corresponds to a frequency resolution of 25kHz which is small enough for STNO devices measured in this thesis, compared with its minimum linewidth (around 20MHz). Apart from the sampling rate, the bandwidth (the maximum frequency range that the oscilloscope can accurately measure) of Textronix DPO72004 is up to 20GHz, enabling high frequency measurements.

Using oscilloscope's parameters mentioned above, the time domain signal of STNOs registered on a single shot oscilloscope is given in Figs. 2.15a,b, where the voltage V oscillation over time can be clearly seen. The voltage oscillation reveals that the amplitude fluctuates in time and so does the phase via the nonlinear coupling of amplitude-phase. These fluctuations are due to noise in the system such as thermal fluctuations. The corresponding voltage signal is therefore written as:

$$\mathrm{V} = \mathrm{V}_0[1 + \delta\mathrm{a}(\mathrm{t})]\sin[\omega_0 \mathrm{t} + \varphi(\mathrm{t})]$$

Where V_0 is the mean amplitude, δa is the relative amplitude fluctuation, ω_0 is the precession frequency, and $\varphi(\mathrm{t})$ is the phase fluctuation. Evidently, taking the Fourier transform (FFT) of the voltage signal V (40μs long), does not result in a Dirac peak, but in a peak of finite linewidth (given in Fig. 2.15c) as also measured on the spectrum analyzer.

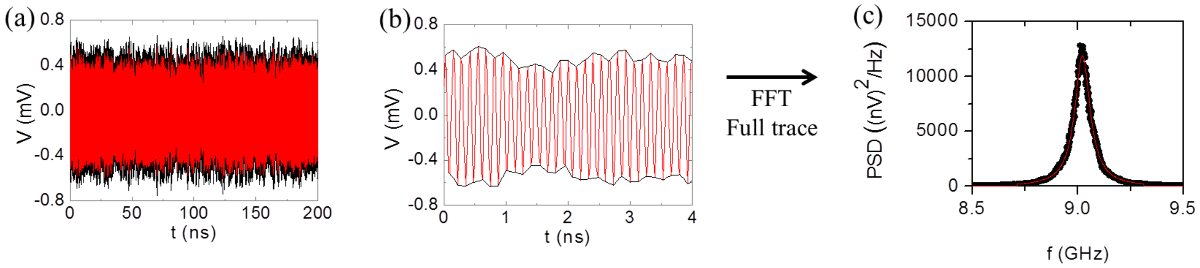

Fig. 2.15-(a) 200 ns long segment of time domain trace of the amplified voltage signal (total length is 40μs) (b) a zoom of 4ns, showing clearly the voltage oscillations. The envelope is outlined by the black curve. (c) The PSD of the full trace, 40 μs.

In the past years, many studies have been subjected to understand the origin of the linewidth broadening of STNOs. From theoretical models developed for STNOs [22], phase noise (fluctuation) is a major contribution to linewidth broadening. The phase and frequency are directly related by $2\pi f = d\varphi/dt$, so phase and frequency noise are as well. Hence if the frequency fluctuates, evidently the linewidth will be enlarged. The existence of frequency fluctuations in a STNO device has been first demonstrated in Ref. 100 by taking the FFT of the signal voltage over only a short window size and then gliding the window along the trace.

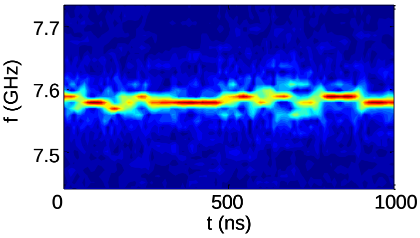

Fig. 2.16-Spectrogram shows the frequency fluctuation in time. Adapted from [100].

This will result on the evolution of the frequency as a function of time, called frequency-time spectrogram as shown in Fig. 2.16. However, this spectrogram technique does not provide good quantitative information of frequency fluctuations and it is related to time window. In fact frequency fluctuations exist on all timescale and are better described by white noise. This becomes evident when extracting amplitude and phase noise [85,91]. This technique is more appropriate to investigate the frequency fluctuations and the corresponding time scales for STNOs, $\tau_c \approx 1/\Gamma_p$. In the following, the extraction of amplitude and phase noise of STNOs via the Hilbert transform method will be reviewed.

Amplitude and phase noise extraction

An appropriate method for the extraction of amplitude and phase noise of the voltage signal V(t) has been achieved by constructing the analytical signal using a Hilbert transform of the measured signal [90,91]. This method allows one to directly extract the instantaneous amplitude and phase (frequency) of a time domain signal V(t). In this method, the analytic signal is a complex signal S(t) whose real part is the measured signal V(t) and imaginary part is the Hilbert transform of V(t), H(t). H(t) is obtained from the convolution of the real part $V(t)$ with the Hilbert transform kernel $1/\pi t$.

$$S(t) = V(t) + jH(t) = A(t)e^{j\Phi(t)} \tag{2.7}$$

The modulus and the argument of the complex signal S(t) are the instantaneous amplitude A(t) and the instantaneous phase $\Phi(t)$, respectively. The relative amplitude fluctuation (noise) $\delta\mathrm{a}(\mathrm{t})$ around the average amplitude $\langle A(t)\rangle$ is expressed in eq. 2.8a. The $\delta\mathrm{a}(\mathrm{t})$ has a zero mean distribution:

$$\delta\mathrm{a}(\mathrm{t}) = \frac{A(t)-\langle A(t)\rangle}{\langle A(t)\rangle} \tag{2.8a}$$

The phase fluctuation (noise) $\varphi(\mathrm{t})$ is obtained by subtracting the instantaneous phase $\Phi(t)$ with the mean angular frequency $2\pi f_0$:

$$\varphi(t) = \Phi(t) - 2\pi f_0 t \tag{2.8b}$$

The mean angular frequency $2\pi f_0$ is extracted from the linear regression of the instantaneous phase $\Phi(t)$ and the slope of the linear regression gives the value of the mean angular frequency (for simulation and experimental phase noise extraction). In terms of data presentation, i.e. frequency modulation (discussed in Chapter 3), the frequency noise is also important to extract. The frequency noise $\delta f(t)$ is defined as the time derivative of the phase noise, $\delta f(t) = \frac{1}{2\pi}\frac{d\varphi(t)}{dt}$. Normalizing the $\delta f(t)$ by the mean frequency of f_0 gives the relative frequency noise which is also used to compare the quality of an oscillator of different carrier frequency.

In order to qualify and evaluate the performances of an oscillator, it is more convenient to express the amplitude and the phase (frequency) noise discussed above through its squared FFT transforms to form the PSD of amplitude, $PSD_{\delta a}(f) = |FFT(\delta a(t))|^2$, and phase (frequency) noise, $PSD_{\varphi}(f) = |FFT(\varphi(t))|^2$. The PSD of amplitude and phase noise is then plotted on a double logarithmic scale and typically expressed in units of dBc/Hz, as shown in Fig. 2.17. It represents the noise power relative to the carrier contained in a 1 Hz bandwidth centered at a certain offset from the carrier. For example, the phase noise (black curve) of the simulated STNO is -50dBc/Hz at an offset of 1 MHz and -70dBc/Hz at an offset of 10 MHz. This is a general way to characterize the performances of an oscillator.

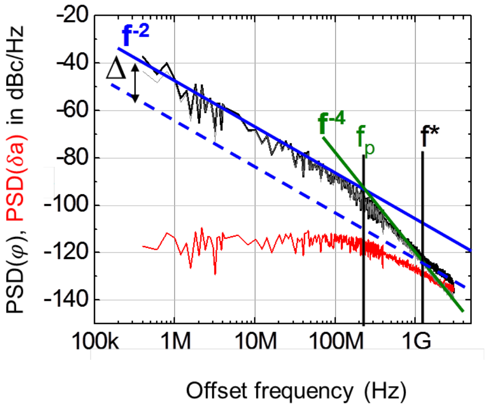

Fig. 2.17-Double log plot of the amplitude (red curve) and phase noise (black curve) of STNOs for IPP modes of planar devices obtained from simulated time traces (macrospin simulations). Adapted from [85].

From the inverse power law dependence of the PSD on the Fourier frequency PSD~$1/f^x$, one can conclude on the type of noise that governs the phase fluctuations (Fig. 2.18), i.e. x=0 corresponds to white noise, x=1 corresponds to 1/f noise, x=2 $1/f^2$ corresponds to random walk noise [85].

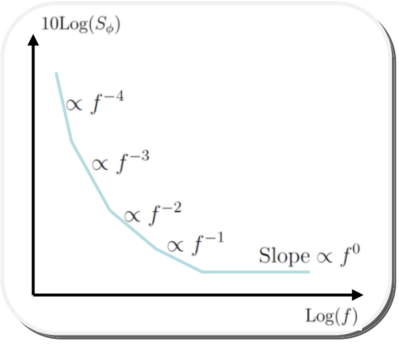

Fig. 2.18-Model of phase noise in power laws. On a log-log plot, noise PSD has different slopes depending on typical noise contributions. Adapted from [85]

As has been discussed in Chapter 1 Section 1.3.5, the amplitude noise (Fig. 2.17-red curve) provides an important tool to extract the amplitude relaxation frequency f_p. The amplitude relaxation frequency f_p is extracted at the frequency when the noise power PSD drops by 3dB (half-power attenuation). This cut-off frequency f_p determines the frequency up to which the amplitude fluctuations are damped out. For low noise frequencies $f<f_p$ (slow perturbation), the system relaxes to its equilibrium amplitude. The amplitude responds and follows the external perturbation in a white noise manner, i.e. the perturbation is white noise. For noise frequencies $f>f_p$ (fast perturbation), the amplitude does not have time to relax to its equilibrium amplitude and the fluctuations add up. This results in random walk behavior with $1/f^2$ characteristics.

The phase noise (black curve) shown in Fig. 2.17 behaves mostly as $1/f^2$ (random walk), changes over to $1/f^4$ above f_p, and then returns to $1/f^2$ dependence above a frequency f*. The high frequency $1/f^2$ random walk dependence results from white noise frequency fluctuations ($2\pi f = d\Phi/dt$) where the noise influences directly the phase. Below the f*, this random walk noise in phase is enhanced by the amplitude noise due to the nonlinear coupling between these two parameters. This coupling results in a $1/f^4$ dependence for $f_p<f<f^*$ and in a $1/f^2$ dependence for $f<f_p$ with a noise level that is enhanced as compared to the intrinsic noise level (compare full and dashed blue lines in Fig. 2.17-back curve). If one neglects the transition region from intrinsic phase noise (at higher frequency) to amplitude-dominated phase noise at lower frequency, then this means that white noise frequency fluctuations exist for a large range of excitation frequencies (<100kHz up to >1GHz). In other word, white noise frequency fluctuations exist for time scales going from miliseconds to nanoseconds. Phase noise plots are therefore the adequate method to characterize the time scales of fluctuations. In addition, the difference Δ in the two noise levels (at low frequency) of phase noise provides direct access to the dimensionless non-linear amplitude-phase coupling parameter υ, i.e. $\Delta = 10log(1+\upsilon^2)$. Hence phase noise plots provide an important tool to extract the amplitude and phase coupling parameter υ.

In this chapter, the extraction of amplitude and phase noise using Hilbert transform method will be used to characterize the noise properties of STNOs studied in this thesis. In chapter 3, the amplitude and phase noise technique will be used for determination and characterization of the modulation data rate of STNOs for different modulation configurations. Since it is also possible to extract the instantaneous frequency from the Hilbert transform, this will also be of great importance for frequency modulation analysis that will be discussed in Chapter 4.

2.1.4 Summary

The measurement techniques used to characterize the STNOs, i.e. frequency domain and time domain measurement technique, have been discussed. Frequency domain technique provides information on the microwave excitation spectra and direct analysis on the frequency, linewidth, and the output power of STNOs as a function of external control parameters, i.e. DC current and applied field. The signal stability and the noise properties of STNOs are characterized by using time domain technique. The following sections are dedicated to the characterization of MTJ STNOs realized within Mosaic to be compared to the other MTJs STNO devices realized outside Mosaic as well as to the state of the art. The characterizations are carried out using frequency domain and time domain techniques. Before coming to the characterization results, general properties of STNOs based in plane-magnetized MTJ STOs, i.e. Mosaic devices and non-European devices, will be presented in the next Section.

2.2 Description and Realization of STNO Devices

This Section discussed the STNO devices measured in this thesis, i.e. Mosaic and Hitachi devices. In the first part, the STNO configuration and the magnetic stack compositions of different STNO devices will be described. In the second part, the realization of Mosaic devices as well as its challenges will be discussed.

2.2.1 Description of STNO Devices

The STNO devices studied in this thesis are homogeneous (uniform magnetization system) STNOs based on Magnetic Tunnel Junction (MTJ). Such STNOs operate at the frequencies in the range of 1GHz to 20GHz which is compatible for FSK-based wireless communication schemes. The magnetic stack consists of an in-plane magnetized free layer (FL) and an in-plane pinned layer (PL), separated by very thin MgO barrier, as illustrated in Fig. 2.19. The FL is capped by capping layer (CL). The PL is a Synthetic Antiferromagnetic (SAF) consisting of two ferromagnetic layers exchanged coupled via a metallic NM spacer Ruthenium (Ru) so that the magnetization of the ferromagnetic layers is antiparallel. The bottom layer of the SAF is pinned (exchange biased) by a strong Antiferromagnetic (AF) layer (IrMn or PtMn) so that both layers stay stable up to relatively higher magnetic field [73,75]. With this a standard MTJ structure is AF/SAF-PL/MgO/FL/CL. The MTJs are nanopatterned into a pillar form with nominal diameters as given in Table 2.1. The shapes are circles and ellipses.

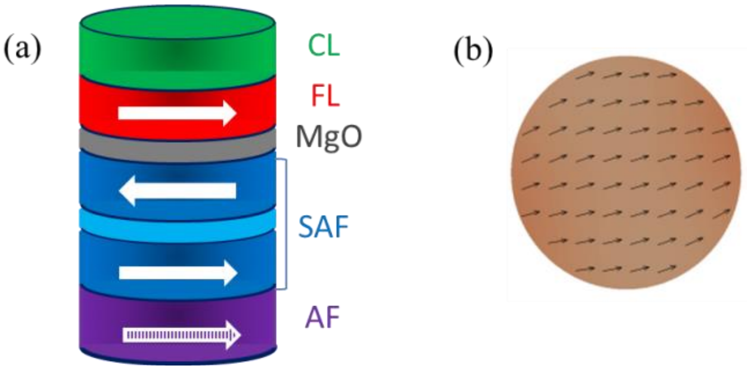

Fig. 2.19-(a) Magnetic structure of MTJ devices. The arrows correspond to the magnetization direction. (b) The free layer magnetization is uniformly magnetized in-plane, i.e. homogeneous MTJ devices.

<u>Two types of STNO devices from different nanofabrication are investigated</u>:

(a) The STNO devices that are fabricated within Mosaic, i.e. <u>Mosaic devices</u>:
MTJ stack deposition from the Mosaic project partner, International Iberian Nanotechnology Laboratory (INL) at Braga Portugal, using a Timaris-Singulus deposition tool and nanofabrication at Leti and Spintec at Upstream Technological Platform (PTA), Grenoble. The MTJ properties are shown in Table 2.1, the thickness of MTJ stack in the bracket is in nm. The shape of these devices is mostly circular. The devices correspond to two sets with different Resistance Area (RA) product, i.e. RA=1Ωμm^2 and RA=1.5Ωμm^2. These devices have also variations, with different top layer of the SAF (CoFe), and Free Layer FL composition (insertion of composite layer FeNi).

(b) The STNO devices that are fabricated by other laboratories:
- <u>Hitachi</u>: MTJ stack deposition and nanofabrication from Hitachi GST, USA,

- AIST-LETI: MTJ stack deposition from AIST, Japan and nanofabrication at Leti and Spintec at Upstream Technological Platform (PTA), Grenoble, and;
- Seagate: MTJ stack deposition and nanofabrication from Seagate

The MTJ properties are given in Table 2.2. The devices have the same RA value ($1\Omega\mu m^2$) with different magnetic stack composition and thickness: the use of IrMn instead of PtMn (Mosaic devices) as antiferromagnetic AF layer, Ta insertion in SAF, SAF composition, and FL composition.

Table 2.1-The summary of the properties of STNO devices from Mosaic with deposition from INL and nanofabrication at LETI.

Mosaic Devices	AF/SAF	MgO/FL/capping layer	RA $(\Omega.\ \mu m^2)$	Nominal diameter (nm)
INL-LETI RFHR046	PtMn(20)/CoFe(2)/Ru(0.85)/CoFeB(2.2)/ CoFe(0.5)/	MgO/CoFe(0.5)/CoFeB(1.5)/Ta(5)/Ru(7)	1	Circle/ 100
INL-LETI RFL733	PtMn(20)/CoFe(2)/Ru(0.85)/CoFeB(2.2)/ CoFe(0.5)/	MgO/CoFe(0.5)/CoFeB(1.5)/Ta(5)/Ru(7)	1	Circle/ 100
INL-LETI RFL731	PtMn(20)/CoFe(2)/Ru(0.85)/CoFeB(2.2)/ CoFe(0.5)/	MgO/CoFe(0.5)/CoFeB(1.5)/Ta(5)/Ru(7)	1.5	Circle/ 100
INL-LETI RFL742	PtMn(20)/CoFe(2)/Ru(0.85)/CoFeB(2.2)/ CoFe(0.5)/	MgO/CoFe(0.5)/CoFeB(1.5)/Ta(5)/Ru(7)	1.5	Circle/ 60-140
INL-LETI RFL741	PtMn(20)/CoFe(2)/Ru(0.85)/CoFeB(2.2)/	MgO/ CoFeB(1.5)/Ta(0.2)/FeNi(2)/Ta(5)/Ru(7)	1.5	Circle/ 50-300

Table 2.2-The summary of the properties of STNO devices from other laboratories (realized outside the Mosaic project)

Other Devices	AF/SAF	MgO/FL/capping layer	RA $(\Omega.\ \mu m^2)$	Nominal diameter (nm)
AIST-LETI 7366D	IrMn(7)/CoFe(2.5)/Ru(0.85)/CoFeB(1.2)/ Ta(0.2)/CoFeB(1.2)/CoFe(0.4)/	MgO/CoFe(0.2)/CoFeB(1.5)/Ta(7)/ Ru(7)	1	Circle/ 100
Hitachi	IrMn(6)/CoFe(1.8)/Ru(0.4)/CoFe(2)/	MgO/CoFe(0.5)/CoFeB(3.4)/Ru(6)/ Ta(3)/Ru(4)	1	Circle and ellipse/ 50-150
Seagate	IrMn(7)/CoFe(2.6)/Ru(0.86)/CoFeB(1.6)/ Ta(0.13)/CoFeB(1.4)/	MgO/CoFeB(2)/ Ta(1)/Ru(7)	1	unknown

2.2.2 Realization of Mosaic devices and its challenges

The RF performances of STNO devices will depend on the influence of all layers composing the magnetic stack. Besides the magnetic layer structures, the magnetic layer deposition and nanofabrication processes also play an important role in the RF performances. Hence, it is important to go through the device realization process and its challenge to understand the outcome measurement results. In the following, issues on the realization of Mosaic STNO devices will be summarized.

The MTJ layers including the MgO barrier are deposited on a high resistivity silicon (Si/SiO2) substrate by sputtering. The development of the MTJ stack using industry compatible sputter deposition techniques is one of the most crucial points to obtain magneto-resistive stacks of high tunneling magnetoresistance (TMR) and low resistance area (RA) product. Low RA values require thin MgO barrier close to 1 nm for injecting the minimum current density in the MTJ nanopillars to induce the magnetic excitations without degrading or breaking the thin tunnel barrier. An ideal thin MgO barrier has a homogeneous structure and no pinholes or local defects as illustrated in Fig. 2.20a, which exhibits “pure” tunneling transport R_{TMR} [101]. The total resistance can be described as a sum of two resistors connected in serial between nanopillar resistance R_{TMR} and contact resistance R_{ct} (small defects in contact electrodes) as illustrated in Fig. 2.20b. This results in a high resistance and thus high TMR (HTMR). However, deposition of such thin MgO barriers is quite challenging. Low RA risks in the presence of the pinholes (Fig. 2.20-c) or local defects and the inhomogenities of the structure or topography (Fig. 2.20d) inside the MgO tunnel barrier that can degrade the TMR [66,102]. The presence of pinholes makes a direct metallic contact between two ferromagnetic layers. Thus the pinholes behave like an ohmic conductor. This means that the electron transport is no longer a pure tunnel process but a mixing between tunnel R_{TMR} and ohmic transport $R_{pinholes}$. It can be described as a sum of two resistors connected in parallel, i.e. parallel resistance (Fig. 2.20e). One resistor represents the pinholes and the other is the reminder of the tunnel junction. As a consequence, the overall resistance decreases which results in low TMR (LTMR). The possible cause for the formation of pinholes is the incomplete oxidation of deposited Mg to obtain MgO and also diffusion of Boron into the grain boundaries. In order to minimize the Boron diffusion into MgO barrier, a CoFe free is inserted between the MgO and CoFeB layer and also the use of Ta and Ru capping layer which have Boron affinity (Table 2.1), therefore can act as a Boron sink. Another challenge is to deposit a homogeneous MgO barrier. When the tunnel barrier is too rough, the irregular surface may lead to the barrier inhomogeneity. These inhomogenities also lead to a mixed conduction regime. Furthermore, the inhomogeneus barrier induces a non-homogeneous current density flowing through the barrier which can influence the dynamic excitation of the STNO. Hence, it is a real engineering challenge to produce ultra-low RA MTJs with high TMR ratios. Further efforts to improve barrier homogeneity and stability are by growing the MgO layer at low power deposition conditions to control the barrier thickness distribution and using ultra smooth buffer layers (the substrate and the bottom electrode). The buffer layers roughness might play an important role in the view of the very thin MgO barrier impacting its homogeneity.

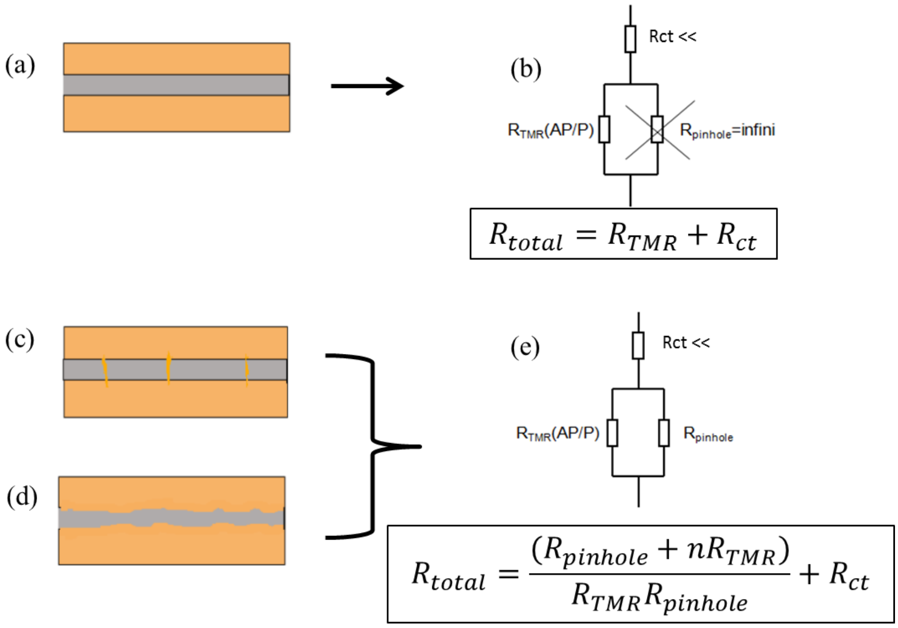

Fig. 2.20-(a) MgO barrier with homogeneous structure/ topology and no pinholes (b) The equivalent circuit model corresponding to the Fig. a. (c) The pinholes creation in the barrier and (d) the inhomogenious barrier, leading to a parallel resistance between tunnel R_{TMR} and ohmic transport $R_{pinholes}$. The contact (electrodes) resistance is assumed to be small enough so that its influence to the overall output resistance can be neglected. Adapted from [76].

Besides the materials development aspect, the nanofabrication process is also crucial for good RF performances, where the definition of straight pillar sidewalls and re-deposition of material during physical etching on the MTJ are major issues. This can lead to variations of the quality of the realized devices from one wafer to the other and again from one device to the other. To understand the reasons behind the different characteristic features (discussed later) shown by different devices taken from different stacks, it is necessary to go through the nanofabrication process. The nanofabrication process was carried out by member of RF group: Karla, Erika, and Chandra. The author contributed to the RF measurement and characterization. As shown in Fig. 2.21, the nanofabrication process of Mosaic devices (realized at PTA) is summarized in 16 steps:

(1) MTJ Stack is deposited on to Si/ SiO2/ bottom layer (Ta5nm/CuN30nm/Ta5nm) by sputtering. Bottom layer is multilayer with low resistance which is used to provide a good growth in the subsequently layers, avoid roughness and grains. The Tantalum (Ta) hard mask of 150nm was deposited after annealing (at 350°C)**.** The next step was the deposition of the resin polymethyl methacrylate (PMMA) on top of hardmask. A PMMA is a polymer that allows extremely high resolution (at nanoscale) at e-beam lithography. E-beam lithography was used to transfer the geometric pattern of the nanopillar to the PMMA and later by chemical process (development), the resist of the pattern was removed.
(2) Evaporation of Cr 20 nm for pattern transfer.
(3) Chemical process (lift-off) to remove the remaining unexposed PMMA and metallic residues on top of it.
(4) Dry etching of Ta hard mask using Reactive Ion etching (RIE). The hard mask etching leaves the MTJ surface with Ta dust (very dirty surface) and needs annealing to improve cleanliness of wafers surface post lift-off of the Cr.
(5) Etching of the MTJ stack using Ion Beam Etching (IBE).
(6) Definition of bottom contact: The deposition of photoresist AZ 1512 HS (optical lithography) to transfer the geometric pattern of bottom contact.
(7) Etching the bottom contact using IBE.
(8) Stripping the damaged photoresist using RIE and acetone ultrasonication.
(9) A polymer called Accuflo was spin coated to insulate the top and bottom electrodes.
(10) The definition of the mask using optical (UV) lithography.
(11) Dry etching of polymer-Accuflo using RIE.
(12) Chemical process (lift-off) to remove the photoresist.
(13) The top and bottom electrodes were opened using RIE by thinning down the Accuflo.
(14) Definition of top contact. The photoresist AZ 1512 HS (optical lithography) was deposited to transfer the geometric pattern of top contact.
(15) Top contact (Aluminium) deposition.
(16) Lift-off to remove the resist. Accuflo acts as an isolation layer between the top contact and bottom contact.

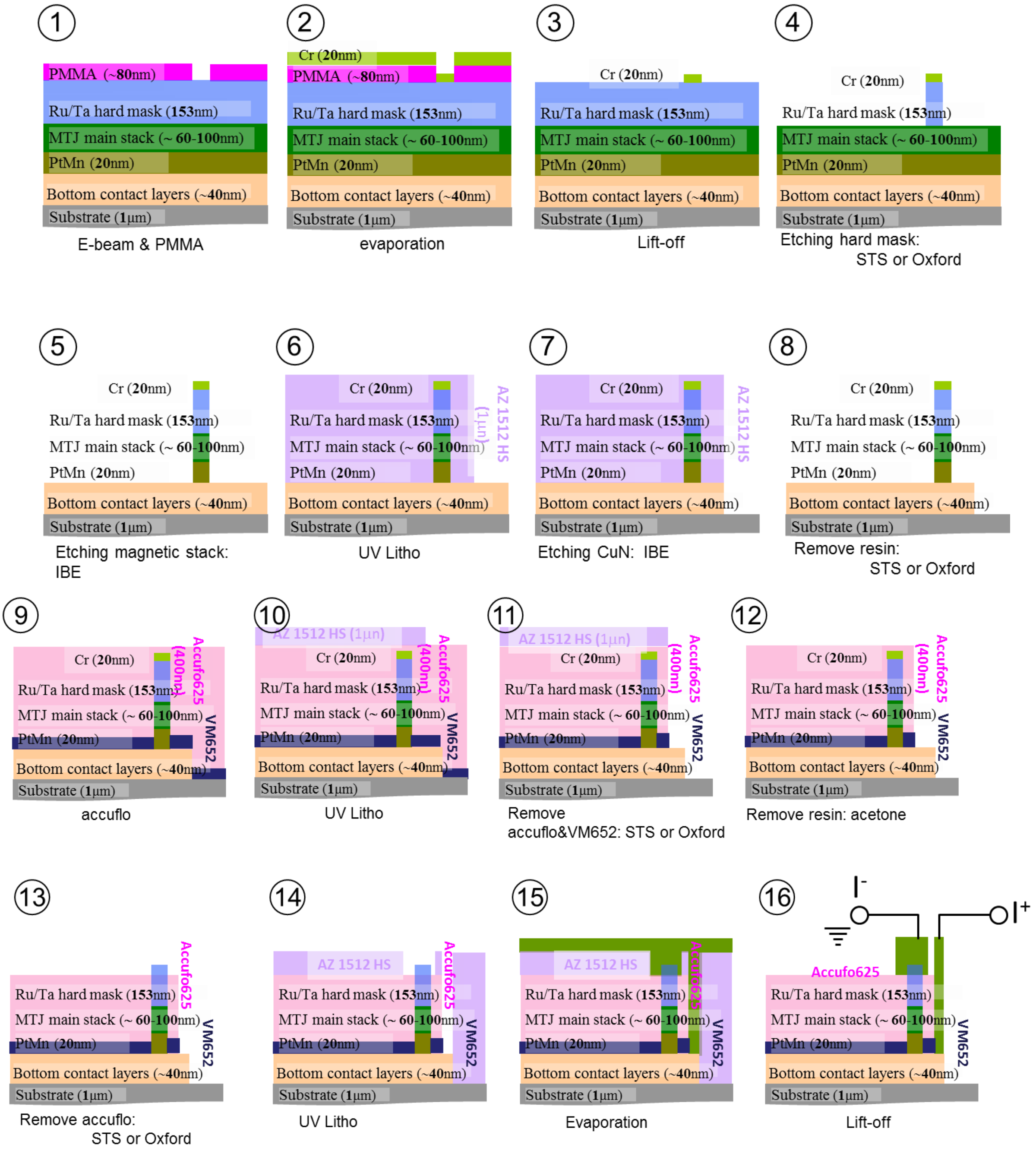

Fig. 2.21-Nanofabrication process of STNO devices

The process of etching the MTJ, step 5, is critical for high TMR and low RA, which are vital for good RF performances. The process used to define the pillars requires the use of IBE. IBE uses an Ar ion beam to etch the MTJ nanopillar at a certain angle. A part of the removed matter is re-deposited on the walls of the pillars. This re-deposition acts as a resistance in parallel to the MTJ and this decreases the overall resistance of the STNOs. Imperfect MgO deposition, i.e. the presence of the pinholes and inhomogeneity of the barrier, and the re-deposition of material during etching have thus a big contribution to the reduction of the TMR and influence the dynamics of microwave excitations. Output power of the oscillator scales according to the TMR. Hence, lower the TMR transfers into lower output power which is not suitable for shift keying applications. Another contribution that also degrades the TMR of the junction is the serial resistance, associated with top contacts. If contacts made during the fabrication are not good enough, the surface is rough and not clean. Moreover, bad lift-off during contacts development can cause contact issue. Only small part of injected current goes through to the pillar since the contacts become more resistive. Consequently, it is difficult to observe the STT effect and thus the dynamic excitations.

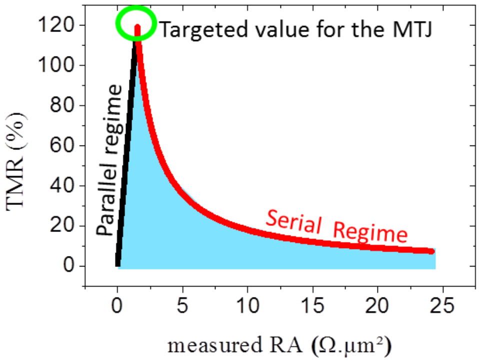

Fig. 2.22-TMR versus RA distribution characterized by the parallel and serial resistance

To conclude, the homogeneity and the roughness of each individual layer inside the MTJ stack plays a major role for the device performance and reliability. A very thin homogeneous MgO barrier as well as the optimized nanofabrication process is important to achieve high TMR and low RA and to improve the yield (working devices/per wafer as defined from static MR loops). The TMR versus RA distribution provides the first approach to investigate the STNOs quality. The parallel and serial resistance can be observed through the statistical analysis of TMR versus RA distribution as given in Fig 2.22. The TMR around 100% at low RA value (1Ωµm²-2Ωµm²) is the target which is crucial for good RF performances.

2.3 Static Characterizations

The realization of Mosaic devices is quite a challenging task and was performed in an iterative process. Different optimization aspects of the MTJ stack have been achieved and investigated, including the MgO barrier thickness, its stability and homogeneity, the free layer thickness and composition and the nanopillars size (Table 2.1). In parallel to this, an optimization of the nanofabrication process to further improve the yield of working device, the static properties, and the RF performances was undertaken.

In this Section, the statistical analysis of static measurements of Mosaic devices will be evaluated. For static experiments, working at low current is desirable, typically 0.05 mA to avoid dynamic excitation. The magneto-resistance (RH) curves on each device were measured using the automatic wafer tester, VEECO, at a fixed DC current 0.05mA and sweeping the magnetic field. From these loop the values for TMR% and RA for each device were extracted. This type of tester is used to characterize MTJ material properties and the nanofabrication process. Typical magneto-resistance MR curve (of RFHR046) is shown in Fig. 2.23.

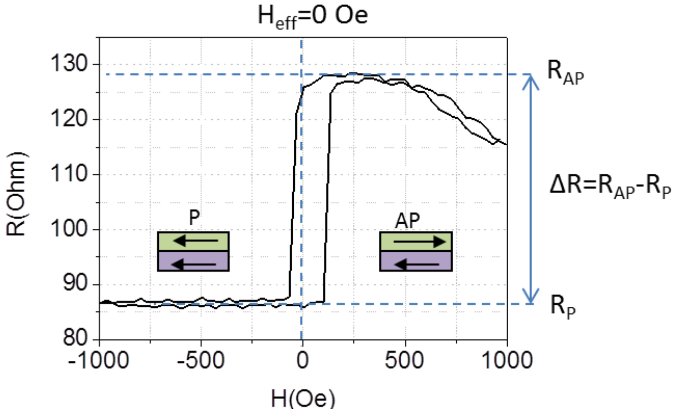

Fig. 2.23-Magnetorsistance curve of RFHR046 (Ø100nm) at low current 0.05mA

The magneto-resistance curve is almost centered at 0Oe (compensated SAF). The negative field stabilizes the parallel state, leading to low resistance R_p. At zero field, the magnetization reversal of the free layer is observed, then at positive field the magnetization of the free layer and SAF polarizing layer are antiparallel to each other, leading to high resistance R_{AP}. At high positive field (500Oe to 1000Oe), the plateau has a more or less steep slope, reducing the AP resistance. This is called spin flop which occurs when the magnetization of the top layer of the SAF is rotating with respect to the magnetization of the free layer. The presence of spin flop should be avoided in order to have a long plateau in the antiparallel state and thus to avoid the coupling between free layer excitation and SAF layer excitation. Hence, the optimization of the SAF layer is needed to achieve a rigid SAF. The TMR is calculated by the ratio between the difference of resistance and the parallel resistance, $TMR=100\%*(\Delta R/R_{AP})$ and the RA value is calculated by multiplying the resistance in parallel state to the devices area, $RA=R_{AP}x0.25\pi(Ø_{SEM})^2$. Here $Ø_{SEM}$ is the diameter measured in the SEM image. The measured diameter is larger, $Ø_{SEM}$110nm, than the nominal diameter, Ø100nm.

2.3.1 TMR versus RA distribution

The TMR versus RA distribution and the optimization of nanofabrication process of Mosaic devices will be discusses in this part and the results will be compared with Hitachi devices.

2.3.1.1 TMR versus RA distribution of Mosaic devices

At the beginning of this thesis, three wafers were realized and characterized. They had the same nanopillar size and magnetic stack composition with different free layer FL thickness, i.e. CoFeB 1.5nm (RFHR46), CoFeB 2nm (RFHR16), and CoFeB 2.5nm (RFHR19). The wafer with the thinnest free layer FL (RFHR46) showed better RF performances, characterized by the transition to steady state that are relatively robust (increased degradation voltage) compared to Hitachi devices. In contrast to this, the two other wafers did not show transition to steady state. Hence RFHR46, shown in the first lines of table 2.1, is used as the 'reference' MTJ for further materials optimization as well as nanofabrication process and will be discussed here.

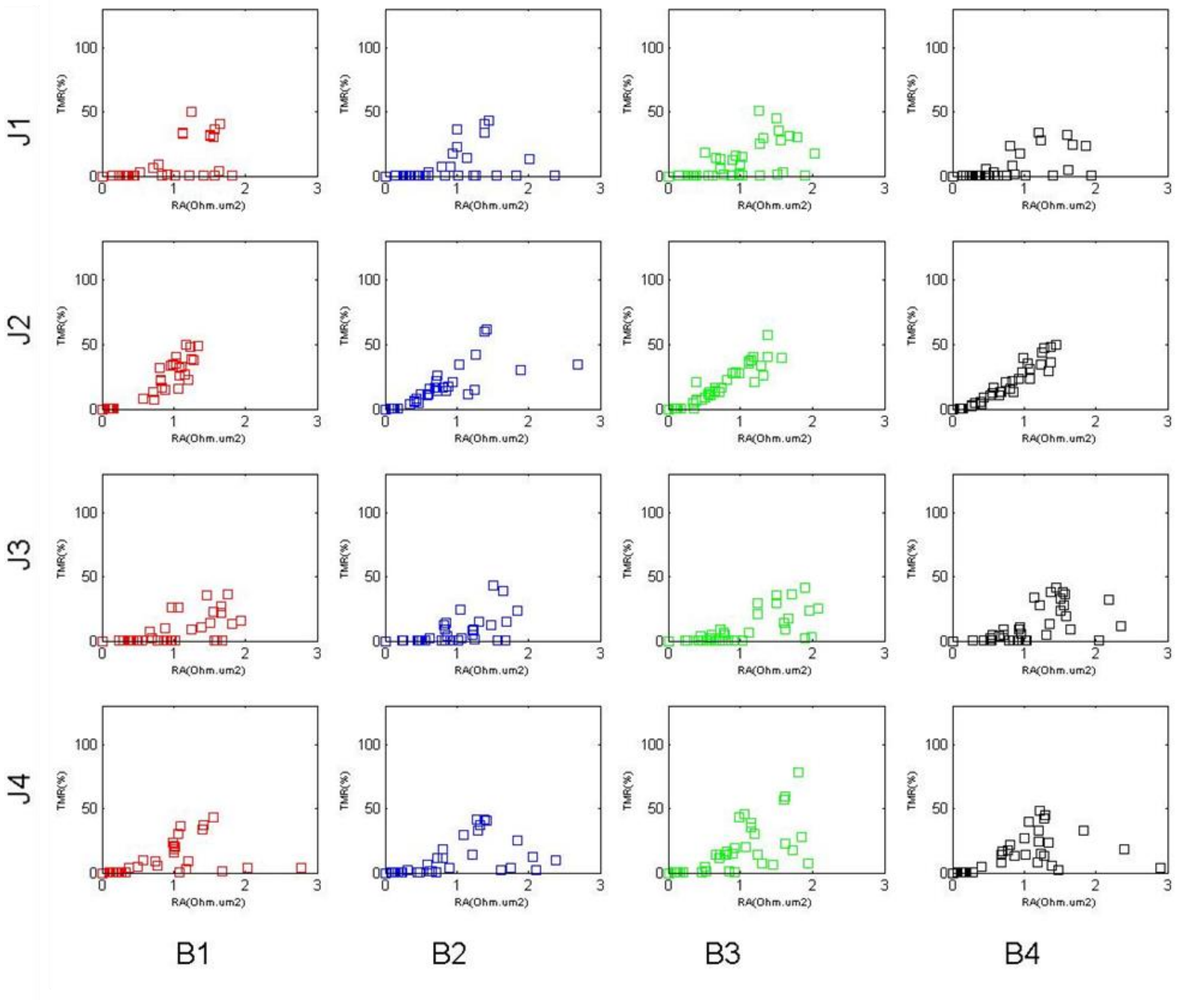

Fig. 2.24-TMR versus RA distribution of RFHR046 ($Ø_{SEM}$110nm).

Typical TMR versus RA distribution of RFHR046 is shown in Fig. 2.24. J1 and J3 correspond to the reflection devices, whereas J2 and J4 are the transmission devices (see Annexe A). The TMR versus RA shows low yield of working devices due to the bad lift-off during the nanofabrication process. The TMR versus RA is mostly characterized by the parallel resistance. This confirms the presence of the pinholes or local defects and the non-homogeneous topography inside the MgO tunnel barrier. As mentioned previously, the redeposition material during etching the MTJ stack also play role on the creation of parallel resistance. The maximum TMR achieved for this wafer is 50% (LTMR) with the corresponding RA varies from 1Ω.µm^2 to 2Ω.µm^2. HTMR at low RA devices are not achievable in this wafer. At low RA below 1 Ω.µm^2, the MTJ nanopillars are broken, leading to a low static and dynamic yield (working devices).

In order to improve the yield of the devices, new wafers were realized with MTJ stacks that were similar to RFHR46. The variations on the stack (Table 2.1) were (i) a slightly larger RA (RA=1.5 Ωµm^2) to obtain more robust and more homogeneous tunnel barriers and (ii) a slightly different free layer composition, i.e. the use of a CoFeB/Ta/NiFe composite free layer to reduce the threshold current and improve the dynamic properties. In parallel to this, the nanofabrication process has also been optimized to improve the straightness of the MTJ pillar. The detail of each wafer will be discussed in the following.

The magnetic stack and composition of RFL733 is exactly the same as the reference RFHR46. The nanofabrication was optimized to minimize the MTJ pillar sidewalls due to the re-deposition and to improve the pillar straightness. The nanofabrication optimization was done by etching the bottom electrode (BE), (see step 7 in Fig. 2.21), in two steps at different angles: first step at 20degree during 19:15minutes and the second step at 65 degree during 6:01minutes. Instead, the etching of bottom electrode for RFHR46 was done only in one step at angle 20 degree. The TMR versus RA distribution of reflection and transmission devices in RFL733 (using new statistic program to plot TMR vs RA) is shown in Fig. 2.25a. The TMR versus RA is characterized by the serial resistance. Good concentration of TMR (40%-80%) at RA around 2 Ωµm^2 was achieved due to the optimization of the BE etching. However the wafer mapping of RFL733 given in Fig. 2.25b shows a low static yield (working devices/per wafer), which is due to the crystal bonding in the nanofabrication process. The blue color means that the devices are broken, i.e. no magneto-resistance curve. Only 50% of devices in wafer can be measured for further RF studies.

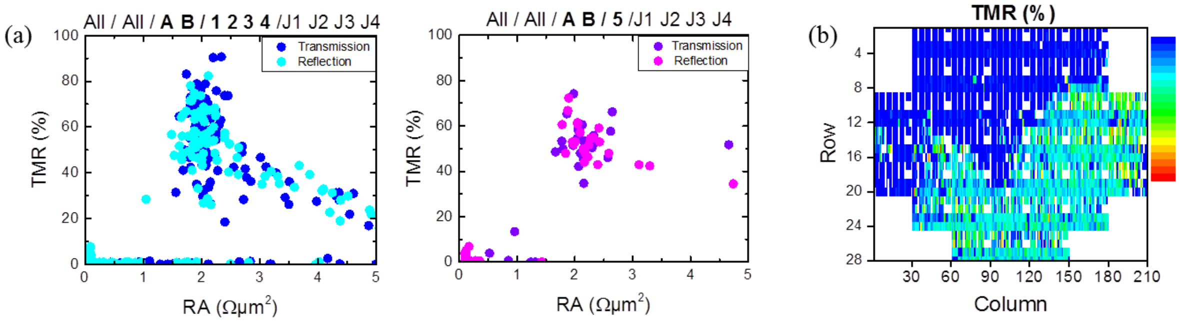

Fig. 2.25-(a) The TMR versus RA distribution and (b) the wafer mapping of RFL733 (Ø$_{\mathrm{SEM}}$130nm).

Wafer RFL731 has the same magnetic stack and composition as RFHR46, but the RA value is slightly larger, 1.5Ωµm^2. The aim is to obtain more robust and more homogeneous tunnel barriers. The nanofabrication steps were similar as for RFL733 with two steps etching of bottom electrode (BE), (see step 7 in Fig. 2.21) to improve the straightness of pillars. The TMR versus RA distribution given in Fig. 2.26 shows a lot of serial resistance in the reflection devices with TMR varies between 20%-70% at measured RA between 2Ωµm^2 to 4Ωµm^2 (the targeted RA is 1.5Ωµm^2). The static yield (working devices/per wafer) is still lower, <10% and the transmission devices are all broken.

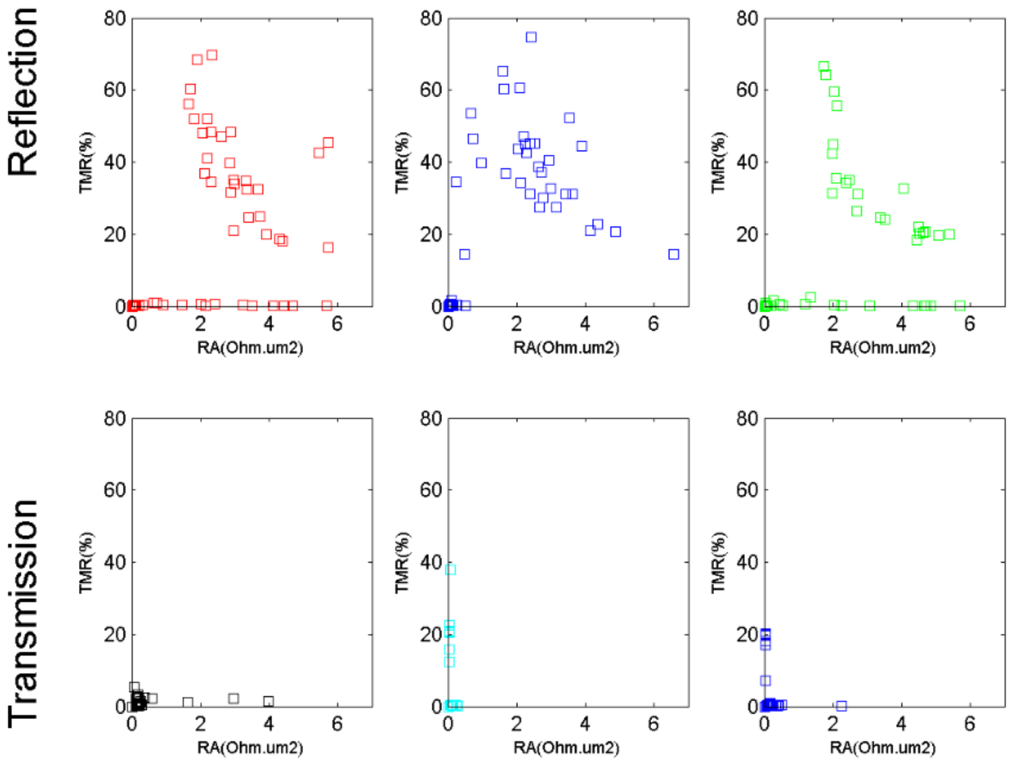

Fig. 2.26-TMR versus RA distribution of RFL731 ($Ø_{SEM}$130nm).

RFL742 has exactly the same magnetic stack and RA value as RFL731. Further change in nanofabrication process was done by etching the bottom electrode in two steps as previously and etching the MTJ in two steps (step 5, see Fig. 2.21) at different angle (45 and 65 degree, respectively) and duration (18:34 minutes and 3:26 minutes, respectively). This is a different process as previous mentioned wafers where etching of MTJ was done in one step at angle of 45degree with etching duration of 23:40 minutes.

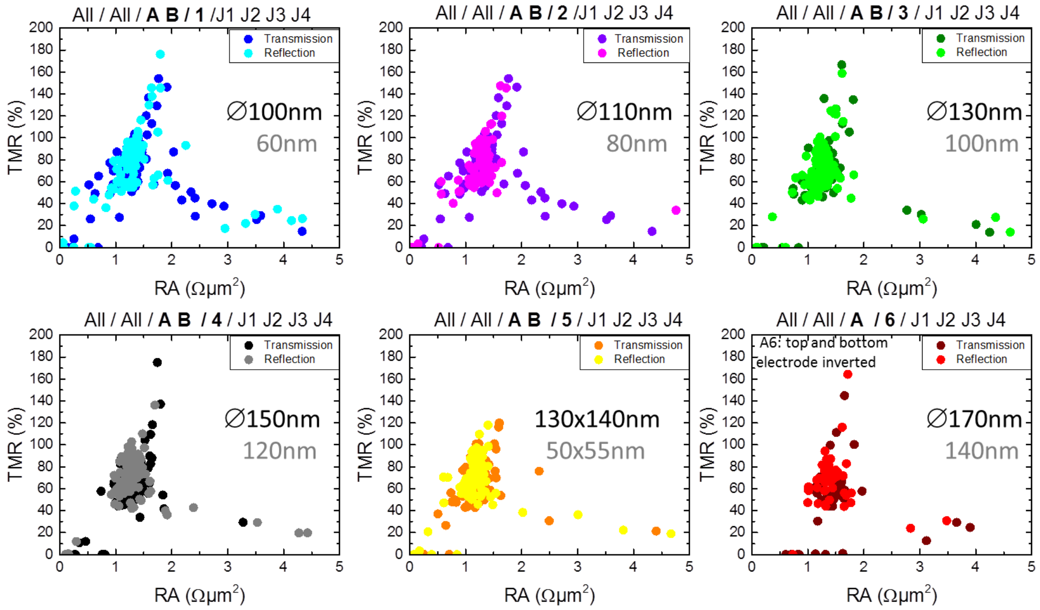

Fig. 2.27-TMR versus RA distribution of RFL742. The diameter of the devices in RFL742 is varied with the measured diameter, (shown in black) is larger than the nominal one (shown in grey).

In addition, the diameter of the nanopillar has been varied (previously it was constant at nominal 100nm), from 60nm to 140nm, and the use of a new mask allows one to fabricate a larger number of STNO devices in a wafer. Compared to the other wafers realized within Mosaic, RFL742 has the best TMR versus RA performance and yield. The TMR versus RA distribution shown in Fig. 2.27 is characterized by the parallel and serial resistance with a good concentration of TMR and RA value. The TMR varies from 50%-120% at RA value ranging from 1 Ωμm² to 1.5Ωμm², which is close to the targeted TMR and RA value. In addition, the wafer mapping given in Fig. 2.28a shows the increase of the yield of working devices compared with the previous wafers. This means that more devices can be tested for RF measurements. RFL742.

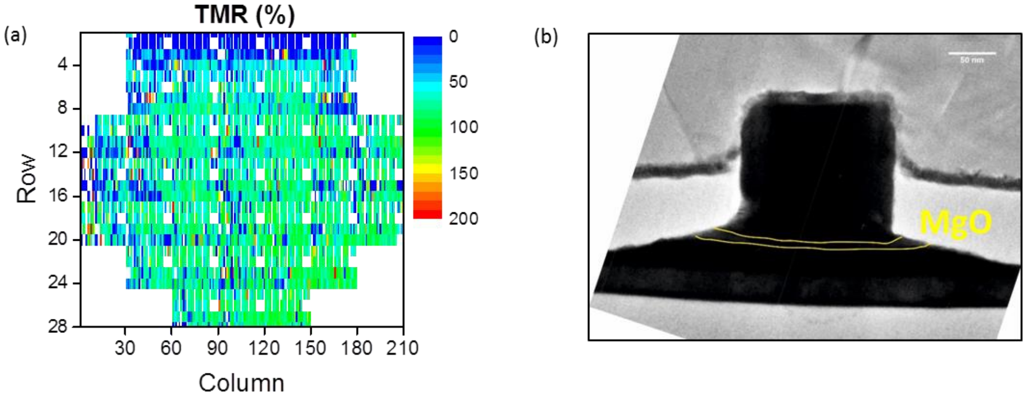

Fig. 2.28-(a) Wafer mapping and (b) TEM image of MTJ pillar of RFL742 by Eric Gautier.

Despite the improvements in the nanofabrication process, with higher yield of working devices and good improvement of TMR and RA value, the dynamic measurements (discussed in Section 2.4) did not show sufficiently good performances, i.e. no steady state dynamic excitations. This is due to the non-ideal nanofabrication as shown in Fig. 2.28b. The TEM image of MTJ pillar shows the pyramidal shape instead of the straight MTJ pillar.

The last Mosaic devices investigated in this work is RFL741. The nanopillars were patterned into circles form with measured diameter varies from 84nm-330nm. The RA value is 1.5 Ωμm², the same as RFL731 and RFL742. The variation of this wafer is the use of composite free layer CoFeB/Ta/FeNi. The Ta layer is used to decouple the growth of CoFeB and FeNi. From a magnetics point of view, FeNi is softer and has lower saturation magnetization (leading to lower critical current), so it should improve the dynamic properties. The nanofabrication process is similar as RFL742 with two steps of bottom electrode etching (angle 20 and 65 degree) and two steps of MTJ pillar etching (45 and 65 degree). In order to optimize the straightness of nanopillars (remember that RFL742 has pyramidal shape of pillars), the etching duration of MTJ pillars was changed to 22 minutes for the first step etching (angle 45 degree) and 16 minutes for the second step etching (angle 65degree).

The TMR vs RA distribution given in Fig. 2.29 is dominated by the serial resistance (TMR decreases as RA increases). Good TMR concentration (20% to 60%) at RA around 1Ωμm² to 2Ωμm² was achieved. The wafer mapping is shown in Fig. 2.30a, yielding more working devices that can be tested for RF properties. The use of composite free layer in RFL741 and the improved straightness of MTJ pillars result in good dynamics of RF performances (Section 2.4) and permit to perform FSK measurement on these devices (Chapter 4).

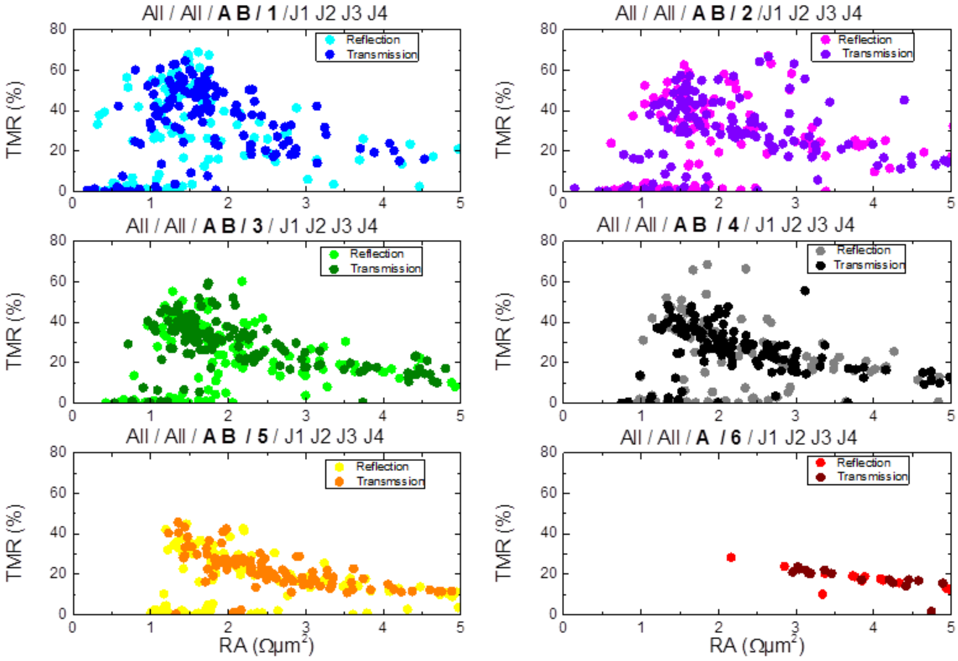

Fig. 2.29-TMR versus RA distribution of RFL741 ($Ø_{SEM}$84nm^2- $Ø_{SEM}$ 330nm^2)

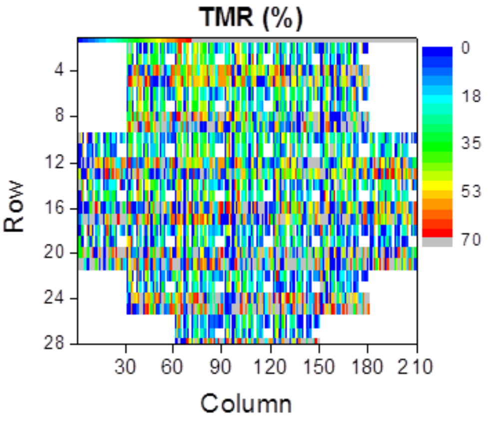

Fig. 2.30-Wafer mapping of RFL741

2.3.1.2 TMR versus RA distribution of Hitachi and other devices

Besides the Mosaic devices, the devices from other laboratories outside Mosaic were also measured: Hitachi, AIST-LETI 7366D, and Seagate. The statistical analysis of TMR versus RA distribution of AIST-LETI 7366D does not show a good concentration of TMR versus RA and it has low yield of working devices. Seagate devices were realized within the first Mosaic project period and they had not been characterized in detail. Instead, the statistical analysis of Hitachi devices as well as their dynamic excitations has been intensively studied by Houssameddine, Quinsat, and Dieudonne [21,24,76,85,91,100]. The studies show that the Hitachi devices have very good TMR contribution, yielding high static and dynamic yield. The TMR of Hitachi devices ranging from 50% to 100% with RA value spreads from 1Ωμm² to 1.5Ωμm². The studies of Hitachi devices permit to acquire the basic knowledge of the RF performances of STNOs. However, the breakdown voltage is limited to 300-400mV and the device finally breaks after several measurement runs. This makes further RF measurements (synchronization and modulation) difficult to perform. Hence, further effort was to realize STNO devices within Mosaic project with high barrier stability. In the following the barrier stability and the breakdown voltage of Mosaic devices will be discussed.

2.3.2 Degradation voltage of Mosaic devices

Magnetic tunnel junctions are very sensitive to degradation and breakdown, due to the ultrathin (few nm) tunnel barrier. When the junction is stressed with a constant current or voltage, a conductance change of the tunnel junction is observed. Sufficiently high stress will lead to breakdown of the junction that changes the properties of the barrier. Hence, the study of the degradation voltage of MTJ nanopillars is important for performing the dynamic measurements, i.e. to not break the device during dynamic measurements. The characterization of the degradation voltage of an MTJ nanopillar gives thus the knowledge about the maximum voltage that can be applied during dynamic measurements without change in its properties. In the following the procedure of the characterization of the degradation voltage of an MTJ pillar will be discussed. Afterwards, the comparison of the degradation voltage of Mosaic devices will be summarized.

2.3.2.1 Characterization of the degradation voltage of an MTJ pillar

In order to characterize the degradation (breakdown) voltage of MTJ nanopillars, a DC current was applied to the device with a certain increment, Δi, until the device degrades (no more magneto-resistance curve). After each increment, Δi, the magneto-resistance curve was measured at low current (0.05 mA) to check whether the magneto-resistance curve or magnetic properties are changed or not. For example Δi=0.1 mA, thus I_1= 0.05 mA, I_2=0.1 mA, I_3=0.05 mA, I_4=0.2 mA, I_5=0.05 mA, I_6= 0.3 mA … and so on (until the device breaks). The antiparallel resistance R_{AP} and parallel resistance R_P are extracted from the magneto-resistance curve measured at different DC currents, I_{DC}. The corresponding voltage at antiparallel state V_{AP} (R_{AP} x I_{DC}), parallel state V_P (R_{AP} x I_{DC}), the difference between antiparallel and parallel resistance ΔR, and the TMR are calculated and plotted as a function of the applied current. The results are given in Fig. 2.31.

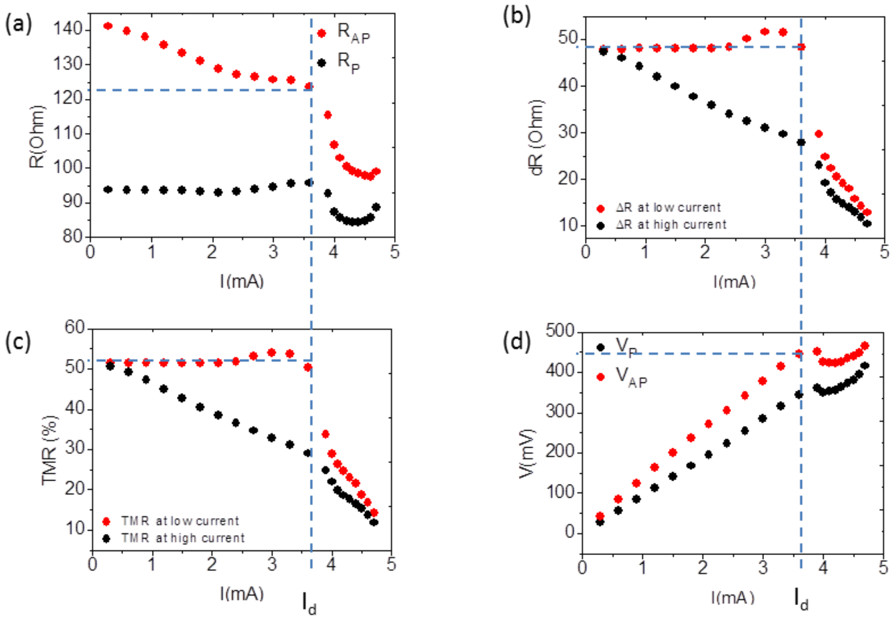

Fig. 2.31-(a) Resistance current dependence at high applied current. (b) Resistance difference versus applied current at high and low current. (c) TMR current dependence at high and low current. (d) Voltage current dependence at high applied current.

Normal behavior of resistance (R_{AP} and R_P), dR (R_{AP}-R_P), and TMR versus current for a tunnel barrier is observed, given in Fig. 2.31. Increasing DC current up to 3.6mA leads to a gradual reduction of R_{AP}, while R_P is constant (Fig. 2.31a). Above 3.6mA, both resistances, R_{AP} and R_P, decrease abruptly with the increase of current. This change in the resistance can be associated to a degradation or breakdown of the dielectric barrier due to the gradual increase in the pinholes size at high applied current. In order to confirm that the slight decrease in resistance is associated to barrier degradation, the dR and TMR as a function of applied current is plotted as shown in Fig. 2.31b and Fig. 2.31c, respectively. The black curve corresponds to the dR (TMR) extracted at high current (given in x-axis) while the red curve corresponds to the dR (TMR) extracted at low current (0.05mA) after applying high current. For low current (red curve in Figs. 2.31b,c) no change in the dR (Fig. 2.31b) and TMR (Fig. 2.31c) observed until 3.6mA. On the contrary for high current (black curve in Figs. 2.31b,c), the dR (Fig. 2.31b) and TMR (Fig. 2.31c) decrease gradually with increase of the current which is the normal behavior for a tunnel barrier. Upon further increasing the current (above 3.6mA) there occurs a sudden change in the dR and TMR (see for instance in the dR and TMR for low and high current (red and black curve)). The extraction of voltage was made by multiplying R_{AP} and R_P per the corresponding current, giving the voltage at antiparallel V_{AP} and voltage at the parallel current V_P (Fig. 2.31d). The voltage corresponding to the current, at which the abrupt decrease is observed, is termed to be the degradation or breakdown voltage. In the example given in Fig. 2.31, the degradation voltage is around 450mV. Using the same procedure, the degradation voltage of Mosaic devices was obtained and will be discussed in the following.

2.3.2.2 Comparison of the degradation voltage of Mosaic devices

The degradation voltage of Mosaic devices measured from several MTJ pillars is shown in Fig. 2.32. The scattering value of degradation voltage is due to imperfection in the magnetic stack deposition and nanofabrication process. RFHR46 has the lowest degradation voltage, 400mV-500mV (black dot in Fig. 2.32), compared to the other Mosaic devices because the RA value is smaller, 1Ωμm². For the same magnetic stack, size, and RA value as reference RFHR46, RFL733 has larger degradation voltage which is around 600mV-700mV (red dot in Fig. 2.32). However, as already mentioned, the static yield is still low due to the crystal bonding problem. For larger RA larger value, 1.5Ωμm², the degradation voltage of RFL731 (blue dot in Fig. 2.32) and RFL742 (green dot in Fig. 2.32) is slightly larger than RFHR46. This means that large RA value improves the barrier stability.

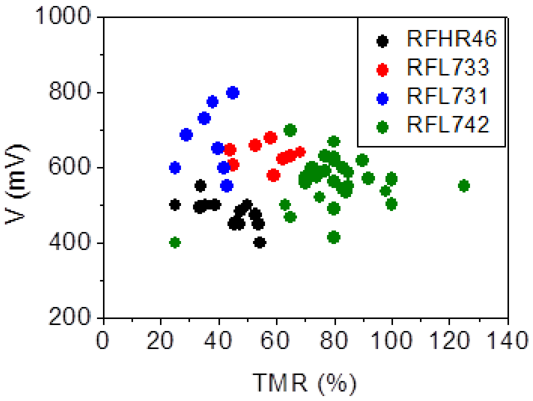

Fig. 2.32-The degradation voltage as a function of TMR value of Mosaic devices

Compared to Hitachi devices, Mosaic devices have higher degradation voltage. This is important achievement for tunnel junctions with insulating MgO barriers since high degradation voltage (robust barrier) improves the device stability under DC current and thus no degradation upon injection of current to induce microwave oscillations. However, the dynamic yield (working devices with good RF properties) of Mosaic devices is still low compared to Hitachi devices. Hence, further optimization of the MTJ deposition and nanofabrication process is needed to in order to compete with the Hitachi's RF performances.

2.3.3 Conclusion of statistical analysis of Mosaic devices

The magnetic stack and nanofabrication process of Mosaic devices have been optimized in order to achieve the targeted TMR (100%) and RA value (1Ωμm²-2Ωμm²) as well as to improve the yield (ratio of operational devices to non-operational devices). The results are summarized in Table 2.3.

Table 2.3 Statistical analysis and its optimization of investigated STNO devices

Mosaic Devices	Nominal diameter (nm)	Optimization		TMR vs RA distribution	Degradation Voltage (mV)	Static yield
		MTJ stack	Process			
INL-LETI RFHR046	Circle/ 100	RA: 1 $\Omega.\mu m^2$ Free Layer: CoFe(0.5)/CoFeB(1.5)	BE: 1 step etching (20deg) MJT: 1 step etching (45deg/23:40min)	Parallel resistance TMR_{max}:50% RA_{avg}:1.5 $\Omega.\mu m^2$	≈500mV	Low yield/ <10%
INL-LETI RFL733	Circle/ 100	RA: 1 $\Omega.\mu m^2$ Free Layer: CoFe(0.5)/CoFeB(1.5)	BE: 2 step etching (20deg/19:15min and 65deg/6:01min) MJT: 1 step etching (45deg/23:40min)	Concentrated/ TMR : 30%-80% concentrated at RA 2Ωμm²	≈600mV	Low yield/ 10%-30%
INL-LETI RFL731	Circle/ 100	RA: 1.5 $\Omega.\mu m^2$ Free Layer: CoFe(0.5)/CoFeB(1.5)	BE: 2 step etching (20deg/19:15min and 65deg/6:01min) MJT: 1 step etching	Serial resistance/ TMR: 20%-70% at RA: 2Ωμm² to 4Ωμm²	≈800mV	Low yield/ <10%
INL-LETI RFL742	Circle/ 60-140	RA: 1.5 $\Omega.\mu m^2$ Free Layer: CoFe(0.5)/CoFeB(1.5)	BE: 2 step etching (20deg/19:15min and 65deg/6:01min) MJT: 2 step etching (45deg/18:34min and 65deg/3:26min)	Concentrated/ TMR: 40%-120% RA: 1 Ωμm² to 1.5Ωμm²	≈600mV	High yield/ >50%
INL-LETI RFL741	Circle/ 50-300	RA: 1.5 $\Omega.\mu m^2$ Free Layer: CoFeB(1.5)/Ta(0.2)/FeNi(2)	BE: 2 step etching (20deg/19:15min and 65deg/6:01min) MJT: 2 step etching (45deg/22min and 65deg/16min)	Serial resistance/ TMR: 20% to 60% RA: 1Ωμm² to 2Ωμm²	≈600mV	High yield/ >50%
Other Labs	Nominal diameter (nm)	Optimization		TMR vs RA	Degradation Voltage (mV)	Yield
		MTJ stack	Process			
AIST-LETI 7366D	Circle/ 100	RA: 1 $\Omega.\mu m^2$ Free Layer: CoFe(0.2)/CoFeB(1.5) Ta insertion in the SAF	BE: 1 step etching MJT: 1 step etching	Serial resistance (Spread)/ TMR: up to 60% RA: 2 $\Omega.\mu m^2$ to 4 $\Omega.\mu m^2$	≈850mV	Low
Hitachi	Circle and ellipse/ 50-150	RA: 1 $\Omega.\mu m^2$ Thicker Free Layer: CoFe(0.5)/CoFeB(3.4)	unknown	Parallel resistance/ TMR: 50%-100% RA: 1Ωμm² to 1.5Ωμm²	≈300mV-400mV	High
Seagate	unknown	RA: 1 $\Omega.\mu m^2$ Free Layer: CoFeB(2) Ta insertion in the SAF	unknown	TMR: 40%-100%	≈300mV-600mV	unknown

The optimization was done by varying the etching process of the bottom electrode and MTJ pillar to improve the straightness of the pillar and to reduce the re-deposition materials at the bottom electrode and at the MTJ pillar. The best TMR and RA performance as well as the yield was achieved in RFL741. However, the dynamic properties did not show good RF performances (discussed in Section 2.4), i.e. no steady state dynamic excitations. This is due to non-ideal nanofabrication, i.e. non-straight of nanopillar shape as shown by TEM image. Hence, good controls and further optimization of the nanofabrication process are a crucial point to obtain good static and dynamic performances of the MTJ pillars.

An important result of Mosaic devices is that robust barriers can be realized with the enhanced degradation voltage (600mV-800mV) as compared to Hitachi devices (300mV-400mV) that were available at the start of the thesis. This is an important achievement for tunnel junctions with insulating MgO barriers. Higher degradation voltage and robust barrier improve the device stability under DC current and thus no degradation upon injection of current to induce oscillations.

Another aspect to be considered is the measured diameter of the pillars. A large offset of diameter around 10 nm-30 nm from nominal diameter after IBE is observed. Future efforts are to optimize the IBE recipes in order to reduce the diameters offset and strengthen the wall profiles of the pillar to produce straight walls (critical for the coherence of the dynamic oscillations).

2.4 Dynamic Characterizations

In this Section, the dynamic characterization of STNOs under external control parameters such as magnetic field H_{DC} and input current levels I_{DC} will be investigated, which is critical for RF applications. In the first part, the dynamic characterization obtained from the frequency domain measurements will be discussed. The second part focuses on the dynamic characterization obtained from time domain measurements.

2.4.1 Frequency domain characterizations

The details of frequency domain measurements have been discussed in Section 2.1. The characterizations were performed by taking into account the RF chain correction to extract the actual output power of STNOs. In the frequency domain characterization, the basic performance parameters are the oscillation modes (single or multimode), frequency oscillation range, the linewidth, and the output power (at minimum linewidth) as a function of external control parameters current and field (amplitude and orientation). Further parameters that need to be characterized are the frequency tuning via current (df/dI), which is of important for FSK measurements (Chapter 4), and the threshold current extraction at which the steady state oscillations start. Lower threshold current of STNOs is desirable for RF applications, leading to low power consumption.

In the frequency domain measurements, the standard procedure to characterize and evaluate the devices starts with the acquisition of the voltage PSD spectra as a function of external control parameters, current I_{DC} and field H_{DC} values. From this the following information is extracted:

(a) **The current-field state diagram**, i.e. the integrated PSD spectra as a function of current I_{DC} and field H_{DC}. The spin torque driven steady state excitations of the free layer occur in two quadrants of the current-field diagram, namely for fields stabilizing the antiparallel (parallel) state (with respect to the free layer and SAF top layer magnetizations) and for currents for which electrons flow from the SAF (free) layer towards the free (SAF) layer (see Chapter 1, Section 1.2.3). In practice only the antiparallel configuration leads to pronounced steady state excitations of the free layer and therefore the state diagram is usually measured and shown for one quadrant only.

(b) **The PSD spectra of frequency versus field**. The PSD spectra of frequency versus field is measured at a fixed DC current I_{DC}, larger than the threshold critical current $I>I_{th}$ and below the degradation voltage. These plots provide first information on the dynamic excitation modes (spectral purity), single or multimode and which mode goes into the steady state regime. From these plots, the mode which goes into steady state regime is fitted using Lorentzian fitting to extract the frequency and linewidth as a function of applied field H_{DC} at a fixed DC current I_{DC}. These plots are evaluated as discussed in (c).

(c) **Field dependence**: From the field dependence, the field values will be identified for which the linewidth is minimum. The current dependence at a fixed field value (minimum linewidth) is used to analyze the transition to steady state oscillations as discussed in (d).

(d) **Current dependence**: These plots are used to confirm that the excitations are really in steady state oscillation. The transition from damped mode into steady state mode can be observed clearly through these plots. For standard homogenous devices, the transition from damped mode into steady state mode is characterized by a more or less linear reduction of the linewidth until a minimum value close to the critical threshold current

I_{th} and a strong increase in power. From these plots the basic parameters of RF performances are extracted, i.e. the minimum linewidth, the corresponding output power and the frequency.

Following the aforementioned procedures, the RF performances of STNO devices studied in this thesis will be evaluated and discussed. The results are then compared to the RF performances of STNO devices from different nano-fabrications.

2.4.1.1 Dynamic performances of Mosaic devices

The representative results of dynamic characterizations of Mosaic devices are summarized in Table 2.4. In Table 2.4, Figs. 2.33, 2.34, 2.35, 2.36, and 2.37 correspond to the dynamic characterizations of RFHR46, RFL733, RFL731, RFL742, and RFL741, respectively. The description of figures (a)-(e) of each Fig. can be seen in Table 2.5.

RFHR46 has nominal RA value $1\Omega\mu m^2$, enhanced degradation threshold (450mV and above), and no degradation upon RF studies. Most of magneto-resistance curve of the devices are characterized by the presence of spin flop field around 600Oe – 1000Oe. In total there were not more than about 8 devices that showed steady state due to low static yield in RFHR46 (Section 2.3.1.1). Despite only 8 devices that showed the steady state, good RF performances in terms of low linewidth, Δf<50MHz, were achieved. Moreover, long plateau of low linewidth was achievable in RFHR46 (Table 2.4, Fig. 2.33d) which is an important parameter to perform frequency shift keying measurement.

In Fig. 2.33, an example of dynamic measurements of RFHR46 devices is shown. The investigated device has TMR of 32%. For this device, the best dynamic performance was found at an in-plane angle of 6 degree with respect to the easy axis direction. This angle is varied from one device to others in RFHR46. The PSD spectra plot of frequency versus field (Fig. 2.33a) reveals a multimode behavior instead of a clean single mode behavior. The multimode is characterized by the existence of several modes 1f and 1f' that are energetically close. The mode with the lowest damping (1f in this case) is driven into steady state with stronger amplitude than the others. Possible reasons for multimode behavior might result from a combination of non-ideal nanofabrication process (non-straight pillar shapes), non-homogeneous barrier and the in-plane magnetization configuration, that can give rise to excitation of spatially separated modes.

Table 2.4-The summary of dynamic characterization of Mosaic devices

<table>
<tr><th colspan="2">Dynamic characterization</th></tr>
<tr><th>RFHR46</th><th>RFL733</th></tr>
<tr><td>Angle =+6°, TMR=32%

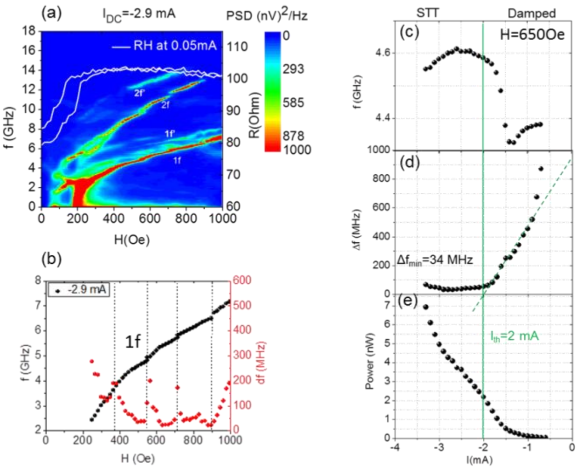

Fig. 2.33-see the description in table 3.5</td>
<td>Angle =8°, TMR=49%

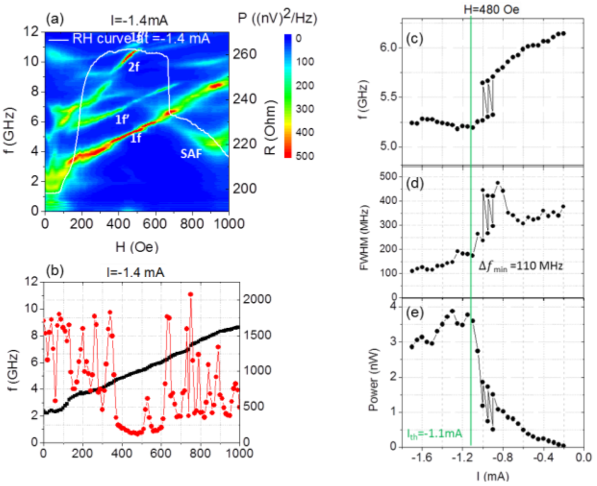

Fig. 2.34- see the description in table 3.5</td></tr>
<tr><th>RFL731</th><th>RFL742</th></tr>
<tr><td>Angle =+10°, TMR=43%

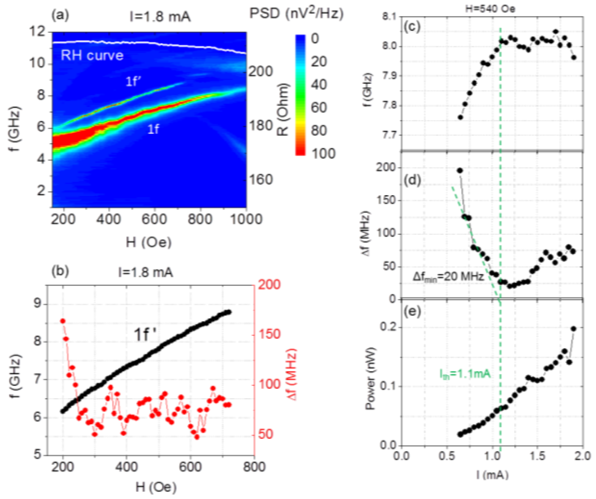

Fig. 2.35-see the description in table 3.5</td>
<td>Angle =-0°, TMR=55%

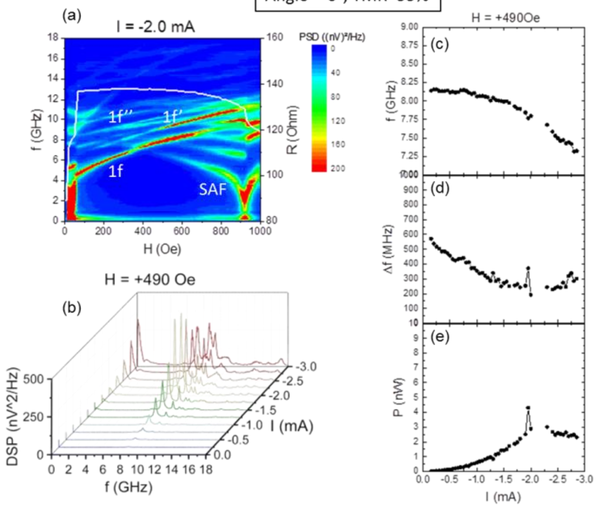

Fig. 2.36-see the description in table 3.5</td></tr>
<tr><th colspan="2">RFL741</th></tr>
<tr><td colspan="2">Angle =-7°, TMR=47%

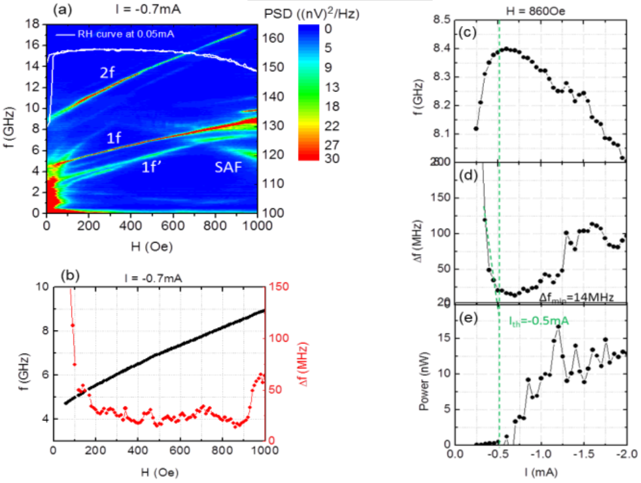

Fig. 2.37- see the description in table 2.5</td></tr>
</table>

Table 2.5-Description of the figures in Table 2.4

Figures	Description
(a)	The PSD spectra of frequency versus field, at a fixed current. 1f is the first mode, 2f is the second harmonic of 1f. 1f' is another mode, 2f' is the second harmonic of the other mode.
(b)	Field dependence (at a fixed current). The Lorentzian fitting of the PSD spectra versus field plot. Black curve is the field dependence of the center frequency and red curve is the field dependence of the linewidth. *Note:* In Fig. 2.36, figure b corresponds to PSD spectra (in 3D) as a function of the current
(c, d, e)	The current dependence (at a fixed field). The vertical line is the threshold current. (c) current dependence of the center frequency (f vs I), (d) current dependence of the linewidth (Δf vs I), and (e) current dependence of the output power (Power vs I).

At high field (900Oe-1000Oe), the SAF layer is weakly excited which corresponds to a weak spin flop observed in magneto-resistance curve (white curve). Focusing now on the 1f steady state mode, one can clearly observe that the mode is characterized by several branches, where at the intersection of two branches two modes can coexist over a small range of fields. This is more evident in the field dependence plot (Lorentzian fitting of PSD spectra) shown in Fig. 2.33b. In the field range of the experiment (0-1000 Oe), five branches of the frequencies (black curve) are observed. For each branch, the linewidth (red curve) goes to a minimum value and then increases at each transition (intersection of two branches). The increase is understood as a thermal activation between two modes, as a result of which the temporal coherency is reduced. Their origin is not well understood yet. However, from the studies on the influence of the coupling between the free layer and SAF reference layer on the free layer excitations [75,103], such branching can be attributed to the interaction between the FL steady state excitation and some other (damped) mode of the free layer (multimode interaction). Such interactions and the resulting branching influence the performances of the device and limit the operational range of field (tuning in frequency via field). The conditions to limit or suppress this branching still need to be further explored. Possible parameters to optimize are stack composition and barrier homogeneity, nanopillar size, form, and edge definition (straight or slanted pillar walls).

From the field dependence plot, one can find the field values where the linewidth is minimum, i.e. 500Oe, 650Oe, 800Oe, and 900Oe. Fixing the field at 650Oe, one can obtain the current dependence of frequency, linewidth, and the output power (Figs. 2.33c,d,e). From these plots, the transition from damped mode to steady mode can be observed clearly. This transition is characterized by an abrupt linear decrease in the linewidth until a minimum value (≈40MHz) close to the critical threshold current I_{th} (Fig. 2.33d) and followed by the strong increase in power (Fig. 2.33e). From this the critical threshold current is estimated around I_{th}=-2mA. Above the threshold current, the steady state frequency oscillation (Fig. 2.33a) decreases as the current increases with the frequency tuning of df/dI≈-50MHz/mA, showing a normal IPP mode behavior of standard homogenous MTJ. Doing the same analysis, the RF performances measured in 8 devices (low dynamic yield) in RFHR46 are summarized in Table 2.6. Only one device shows a clean single mode excitation. The mode which goes to steady state can be the main mode 1f or the other modes, 1f'. Most of measured devices are characterized by the presence of the branching behavior which is related to the multimode excitation. For instance, strong multimode leads to at least one branch. When the multimode is weak, i.e. the other mode 1f' has much lower amplitude than the main mode 1f, there was no branching behavior. The frequency range over the field can be varied depending on the excitation mode, i.e. 1f or 1f'. The threshold current varies from -1.5mA to -2mA (except the device in Chip 4.4 B2J3). The frequency current tuning is on the order of few MHz/mA, except the device (Chip 1.5 B1J1) whose linewidth goes to minimum value (long plateau) at large current range. The minimum linewidth can be achieved in RFHR46 is ≈20MHz which is comparable with the Hitachi devices. However the maximum output power, <10nW, is still much lower compared to the Hitachi devices, P≈100nW.

Table 2.6-The summary of RF performances of the devices in RFHR46

Device	TMR (%)	Angle	Multi mode	STT mode	Branching /number	f vs H range (GHz)	I_{th} (mA)	df/dI (MHz/mA)	Δf_{min} (MHz)	Power (nW)	at H(Oe)/ I(mA)
Chip1.5 A3J1	24	10°	strong	1f’	Yes/1	5.5 to 8.5	-2	-300/1.3	33	0.3	710/-2.2
Chip1.5 B1J1	26	-15°	Very weak	1f	No	4 to 8	-1.9	0 (flat)	24	7	880/ (-2mA to 2.6mA)
Chip1.5 B2J3	43	15°	strong	1f’	Yes/4	6 to 9	-1.5	-400/1.2	63	2	830/-1.7
Chip1.6 B2J3	32	6°	strong	1f	Yes/5	4 to 6.3	-2	-50/0.8	24	4.5	500/-2.9
Chip2.5 B4J1	41	20°	strong	1f	Yes/5	5 to 10	-1.7	-300/1.5	20	7	600/-2
Chip3.5 B4J3	58	0	Very strong	1f	Yes/4	5 to 9	-1.35	-20/0.4	33	0.35	415/-1.5
Chip4.4 B2J3	93	-11	Very strong	1f’	Yes/3	8.5 to 10	-0.55	-150/0.2	28	0.7	700/-0.75
Chip4.4 B4J3	45	5	strong	1f	Yes/4	4 to 7	-2.2	-100/0.8	37	18	680/-2.5

RFL733 has the same RA value as reference RFHR46 but different optimization in nanofabrication process to remove the pillar sidewalls re-deposition and improve the pillar straightness. The dynamic yield is lower compared to RFHR46, i.e. only three devices show steady state excitation. The results are summarized in Table 2.7. The PSD spectra plot of frequency vs field is again characterized by strong multimode and branching behavior. The minimum linewidths are slightly larger compared to RFHR46. An example of dynamic measurements of RFL733 (Chip 1.5 B2J3) can be seen in Table 2.5, Fig. 2.34. Strong multimode behavior, i.e. free layer excitation mode and SAF excitation mode, can be observed in Fig. 2.34a. The SAF excitation mode has an opposite direction with the free layer excitation mode. The SAF oscillation increases as the field decrease and vice versa the free layer excitation increases when the field increases. The crossing between SAF mode and the free layer mode and the interaction between the free layer excitation modes (1f and 1f’) lead to enhanced linewidth [75,103] as can be seen in Fig. 2.34b, red curve. A strong reduction of linewidth is observed in the field range of 400Oe-600Oe, just before the SAF mode crosses the main mode 1f. The analysis on current dependence was carried out at 420Oe where the linewidth goes to a minimum value, Δf≈100MHz. The current dependence as given in Figs. 2.34c,d,e confirms that the transition from damped mode to steady state mode occurs at threshold current I_{th}=-1.1mA. The minimum linewidth is however still large, 110MHz, and the frequency current dependence is characterized by the blueshift (increases with the current) instead of redshift (decreases with the current). Compared to RFHR46, the RF performance of RFL733 is worse and the dynamic yield is lower than in RFHR46.

Table 2.7-the summary of dynamic characterization of RFL733

Device	TMR (%)	Angle	Multi mode	STT mode	Branching/ number	f vs H range (GHz)	I_{th} (mA)	df/dI (MHz/mA)	Δf_{min} (MHz)	Power (nW)	at H(Oe)/ I(mA)
Chip3.6 B3J3	50	-32°	Very strong	1f’	Yes/3	5 to 10	-1.4	-300/0.5	75	6	250/-1.5
Chip3.7 B3J3	34	0°	strong	1f	Yes/3	3 to 9	-1.25	0 (flat)	50	12	420 /(-1.5mA to -1.7mA)
Chip1.5 B2J3	49	8°	Very strong	1f	Yes/3	4 to 9	-1.1	+100/0.5 (blueshift)	110	3	480/-1.7

RFL731 with slightly larger, 1.5Ωμm^2 was also characterized, expecting better dynamic performances since larger RA leads to more robust and more homogeneous tunnel barrier, i.e. potentially reduce the multimode and branching behavior as observed previously. The nanofabrication steps were similar as for RFL733 (see Section 2.3). The dynamic yield is however still lower, only 4 devices/44devices (two chips) go to steady state, as can be seen in Table 2.8. Multimodes remain an essential problem, and transition to the steady state could not be observed in all cases. Some devices are characterized by branching behavior with linewidth higher than 100MHz and some other devices are not characterized by branching behavior with lower linewitdh, below (or equal) to 50MHz. An example of dynamic measurements of RFL731 is given in Table 2.4, Fig. 2.35. The PSD spectra plot of frequency vs field shows clear multimodes, 1f and 1f', separated only by about 1 GHz (Fig. 2.35a). Both modes are parallel to each other. First mode 1f has much stronger amplitude but the peaks are more broadened. The analysis was done for the second mode 1f' since the linewidth is much narrower than the main mode 1f. The field dependence of 1f' mode is given in Fig. 2.35b. No branching behavior observed (black curve). However the linewidth as a function of field (red curve) fluctuates, i.e. no long plateau of minimum linewidth. From current dependence plot (Fig. 2.35c,d,e), the steady state oscillations occurs at I_{th}=1.1mA. The frequency-current tuning is difficult to extract since the frequency fluctuates around the average value. The minimum linewidth is 20MHz with the corresponding output power around 0.6nW (really small). For instance, the RA value does not seem to play a significant role, the devices show similar multimode and branching behavior.

Table 2.8-the summary of dynamic characterization of RFL731

Device	TMR (%)	Angle	Multimode	STT mode	Branching /number	f vs H range (GHz)	I_{th} (mA)	df/dI (MHz/mA)	Δf_{min} (MHz)	Power (nW)	at H(Oe)/ I(mA)
Chip6.2 B2L2	11	-74°	Strong	1f	Yes/1	3 to 8	1.5	-100/0.5	150	12	480/1.75
Chip6.2 C1L1	39	10°	Strong	1f'	No	6 to 9	1.1	0 (flat/fluctuates)	20	0.1	540/1.25
Chip6.2 C2L2*	27	54°	Strong	1f	Yes/4	3.5 to 5.7	-	-	150	-	500/2
Chip6.2 F2L2	23	3°	Strong	1f	No	3 to 7	1.2	-50/0.4	50	0.6	490/1.4

*No current dependence measurement. The device was broken during the measurement.

From the static characterization in Section 2.3, **RFL742** reveals the best static statistics and yield. Fast screening of dynamic measurements on devices in RFL742 has been done and surprisingly none of them revealed a transition to steady state. For curiosity, the MTJ pillars were observed under TEM and indeed it showed non-straight pillar shapes (Fig. 2.28b), due to non-ideal nanofabrication process, which influence the dynamic excitations. Such dynamic characterization is shown in Fig. 2.36. The PSD spectra plot of frequency vs field in Fig. 2.36a reveals a very strong multimode, including the first 1f and the other free layer excitation modes, 1f' and 1f''as well as the SAF excitation due to the presence of spin flop at high field (600Oe-1000Oe) in the magneto-resistance curve (white curve). This multimode is also observed in current dependence plot shown in Fig. 2.36b, i.e. PSD spectra as a function of applied current. The frequencies of multimodes are close to each other, separated only by few MHz. The frequency, linewidth and the output power as a function of the current at a fixed field (Figs. 2.36c,d,e) does not show the transition to steady state. The minimum linewidth is around 200MHz which is too broad.

RFL741 has RA 1.5Ωμm^2 and slightly different free layer composition which is a composite free layer CoFeB(1.5)/Ta(0.2)/ FeNi (2) instead of CoFeB(1.5)/CoFe(0.5). To note, using FeNi in conjunction with MgO MTJs is not usual since it does not promote the texture required for good TMR properties (note: the TMR of vortex devices with FeNi free layers is lower than for CoFeB free layers). However, from a magnetics point of view, FeNi is softer and has lower saturation magnetization (leading to lower critical current), so it should improve the dynamic properties. Combined with the optimization of nanofabrication process to have straight nanopillars, the dynamic characterization of RFL741 shows better performances than the previous measured devices. A representative dynamic characterization of RFL741 is shown in Fig. 2.37. This device is also used for FSK measurement given in Chapter 4. The PSD spectra of frequency vs field shown in Fig. 2.37a, reveal the presence of multimode and SAF excitations. The mode 1f' is crossing with the SAF mode. For instance, the SAF excitation does not cross the main mode 1f so that the branching behavior is less observed for this sample as shown in Fig. 2.37b (black curve). The linewdith vs field shows that minimum linewidths below 50MHz is observed over a large field range from 200Oe to 1000Oe (red curve) which is a great improvement of dynamic performances. The minimum linewidth is around 15MHz observed at 860Oe. At this field, the current dependence was measured as shown in Figs. 2.37c,d,e. From the current dependence, one can observe the dynamic transition from damped mode to steady state mode at threshold current of I_{th}=-0.5mA (vertical dashed line) which is much lower than the threshold current investigated in the previous devices. This can be attributed to the use of FeNi in the free layer which is softer and has lower saturation magnetization, leading to lower critical current. The use of FeNi also improves the frequency-current tunability, i.e. -400MHz/1.5mA, (Fig. 2.37c) which is larger than the one obtained from the previous devices. In addition, a long plateau of minimum linewidth below 50MHz is achieved from -0.5mA to -1.25mA. Above -1.25mA the linewidth increases to 100MHz. The output power is however still low compared with the power of Hitachi devices (discussed later).

Hence, it is of interest to study the FSK modulation on this device due to its large frequency current tunability and low linewidth below 50MHz (eigth times smaller than the frequency separation in two modulated states). In the following the dynamic performances of other devices (outside Mosaic project) will be investigated and compares with the Mosaic devices performances, at which point the Mosaic performances needs to improve.

2.4.1.2 Dynamic performances of other devices

For comparison, other devices from other laboratories with different magnetic stacks and different nanofabrication are also shown in this section. The results are given in Table 2.9. The reference are **Hitachi devices**, that were previously characterized with respect to synchronization and modulation, but it reveals low breakdown thresholds (300mV as compared to 500-800mV for Mosaic devices). This makes them very fragile and difficult to perform further measurements, such as FSK measurement and synchronization, since the device degrades and even breaks after several measurement runs. The main difference is that the spectra are very 'clean', i.e. it is single mode behavior, narrow linewidth below 50MHz, and high output power (0.01-0.1μW). This is similar to other reports in literature e.g. Toshiba with output power of 13nW, minimum linewidth of 44MHz @3-4GHz, TMR=44% [16]. An example of dynamic characterization of Hitachi devices is shown in Table 2.9, Fig. 2.38. It reveals a very clean single mode behavior (Fig. 2.38a). The field dependence does not show a branching behavior (Fig. 2.38b, black curve). Long plateau of narrow linewidth is achievable within the frequency range of 500Oe-900Oe (Fig. 2.38b, red curve). The threshold current (vertical dashed line) extracted from the current dependence (Figs. 2.38c,d,e) is comparable with Mosaic devices. A long plateau of narrow linewidth around 15MHz is observed above the threshold current as well as large output power up to 0.1μW. Best values for Mosaic devices (RFHR46 and RFL741) are close in terms of linewidth values, ≈20MHz, at somewhat less power (1-10nW).

Table 2.9-The summary of dynamic characterization of other devices (outside Mosaic project)

Dynamic characterization	
Hitachi GST	Seagate
Angle =-28°, TMR=54.5% 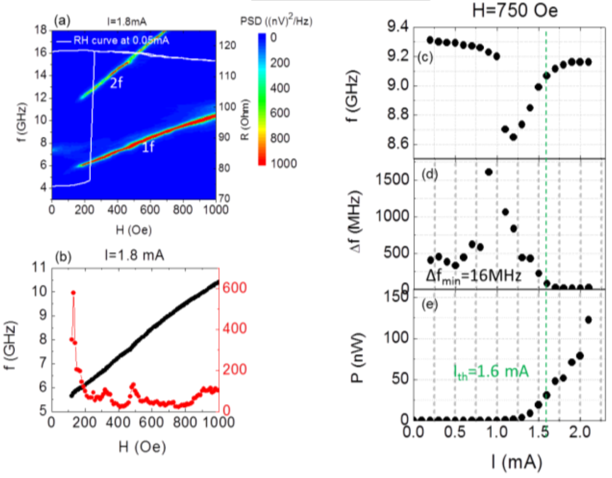 Fig. 2.38-see the description in table 2.5	Angle =0°, TMR=30% 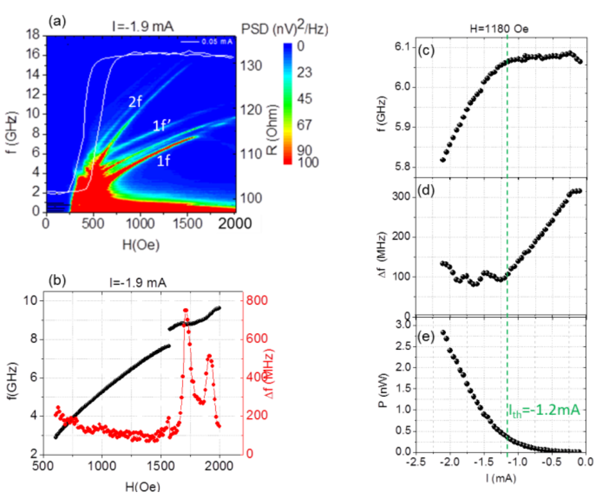 Fig. 2.39-see the description in table 2.5
AIST-LETI	
Angle =0°, TMR=45% 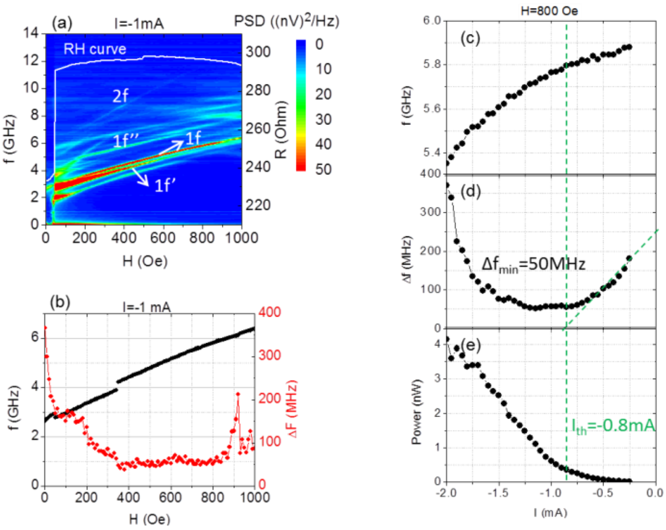 Fig. 2.40-see the description in table 2.5	

Only few devices of **Seagate** have been measured. A representative dynamic characteristic of a Seagate is shown in Fig. 2.39. The magnetoresistance curve (white curve in Fig. 2.39a) shows a strong loop shift around 500Oe and the SAF spin flop field is larger than 1000Oe (around 2000Oe as measured on three devices). The PSD spectra of frequency versus field show multimodes excitations. It is not clear whether the applied current is sufficient to reach the steady state. The lowest linewidth is 70-100 MHz (Fig. 2.39d).

The last device to compare is **AIST-LETI**. The materials deposition was done at AIST, Japan, and the nanofabrication process was done at Leti and Spintec at Upstream Technological Platform (PTA). The dynamic characterization of AIST-LETI shows a low dynamic yield. Many devices have been measured and all of them are characterized by the multimode and no clear STT, similar to RFHR46, RFL733, RFL731, and RFL742. The branching behavior is however less pronounced. Only one device in a wafer shows transition to steady state. The corresponding dynamic characterization is given in Fig. 2.40. The dynamic characteristic is again limited by the presence of multimodes (1f, 1f’, 1f’’) which are separated only by few GHz of frequency (Fig. 2.40a). Interestingly, in most AIST devices, the multimodes, 1f and 1f', is from the same mode (at low field, below 300Oe), which then splits in two modes at high field above 300Oe. The branching behavior observed in Fig. 2.40b (black curve) is actually the plot of two modes (1f' and 1f) whose frequency is close by few tens MHz, i.e. the automatic fitting will fit the peak that has stronger amplitude. Hence for instance, the branching behavior is less pronounced in AIST-LETI devices. The current dependence (Figs. 2.40c,d,e) shows the transition to steady state at the threshold current around -0.8mA with df/dI of -200/1.2mA and minimum linewidth around 50MHz at peak power of 1nW.

For a final comparison, the power versus linewidth of different devices is plotted as given in Fig. 2.41. From that plot, it can be concluded that the RF performances of Mosaic devices, RFL741 (blue dotted), are comparable with the reference Hitachi devices (blue dotted). However it is still lower compared to the state of the art of STNOs, reported by AIST, for an out-of-plane free layer configuration (violet star) with the linewidth of 4MHz and the power of 2.5µW at 50% TMR [17]. This is the best RF performances for homogeneous devices reported so far.

However, considerable advancements have been made by RFL741. The use of composite free layer CoFeB/Ta/FeNi in RFL741 improves the RF performances and reduces the threshold currents, leading to low power consumption. Further nanofabrication to obtain the straightness of the pillar will contribute to improve the dynamic excitation spectra of RFL741. Hence, the presence of multimode and branching behavior can be minimized. Besides the optimization of standard homogeneous device, different STNO configurations, i.e. out of plane free layer, vortex, and nanocontact NC-MTJ, are also explored within Mosaic to improve the RF performance of STNOs. The results of different STNO configurations are not discussed here since this thesis is focused on the demonstration of FSK-based wireless communication scheme using standard homogeneous MTJ, i.e. in-plane magnetized free layer and polarizing layer.

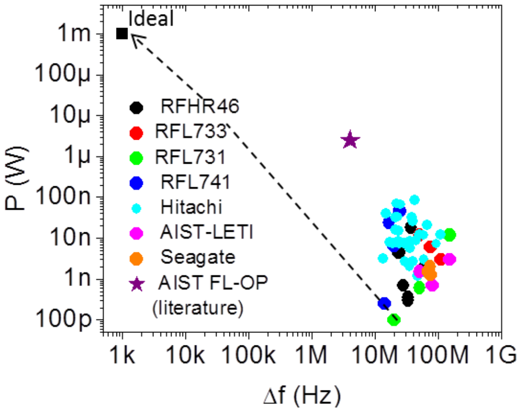

Fig. 2.41-Illustration of the performances power vs linewidth for different devices. Orange dashed box is Mosaic devices, green dashed box is other devices (outside Mosaic project)

2.4.2 Time domain characterizations

For characterization of the signal stability, single shot time traces of the magneto-resistance output signal are needed, showing the signal stability over time. Another important parameter that can be extracted from time domain measurements is the amplitude and phase noise which determines the quality of STNOs. In this Section, the signal stability and phase noise of different STNO devices will be investigated and compared for further device optimization

2.4.2.1 Amplitude stability and extinctions

In the previous Section, the RF performances were investigated by analyzing the PSD spectra as a function of current at a fixed field value. It was shown that the steady state oscillation is characterized by a minimum linewidth accompanied by a strong increase in the emitted power (precession amplitude) for all devices as investigated in Section 2.4.1. In this section, the signal stability of steady state oscillation of different devices is investigated by analyzing the single shot time traces given at a fixed current and field value. The results are shown in Fig. 2.42 for a reference Hitachi device (Fig. 2.42a) and for Mosaic devices (Fig. 2.42b). In the first column, the PSD spectra of steady state oscillations at optimum current and field value (minimum linewidth) are shown. These PSD spectra are obtained from frequency domain measurements of different devices investigated in Section 2.4.1, see Table 2.4 (RFL733, RFL731, and RFL741) and Table 2.9 (for Hitachi). The corresponding amplified time traces of 42µs long (measured via oscilloscope) of each PSD spectra is shown in the second column, revealing the long-time stability of the signal.

(a)Hitachi GST				
Device	PSD	Time traces	Histogram of extinction	Instantaneous frequency
Hitachi Ø135nm	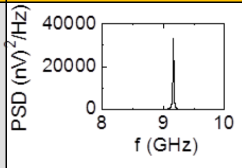 Δf=18MHz f=9.1GHz	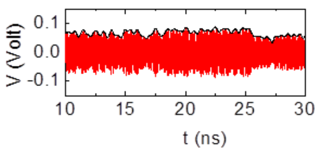	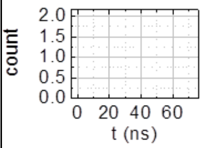	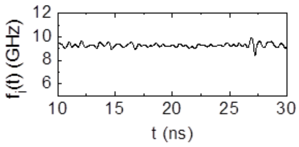
(b) Mosaic devices				
Device	PSD	Time traces	Histogram of extinction	Instantaneous frequency
RFL733	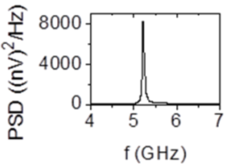 Δf=54MHz f=5.2GHz	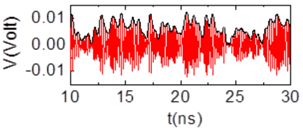	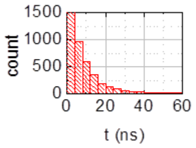	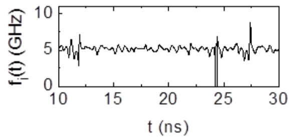
RFL731	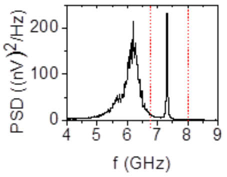 Δf=20MHz f=7.3GHz	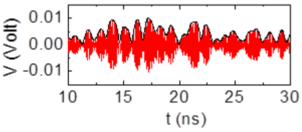	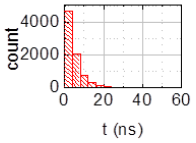	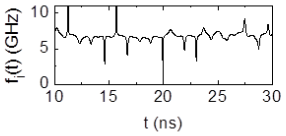
RFL741	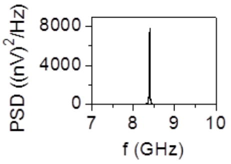 Δf=15MHz f=8.4GHz	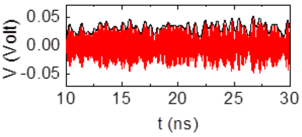	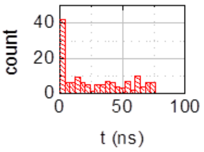	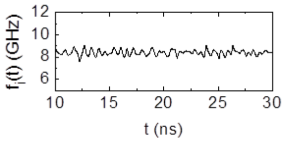

Fig. 2.42-Comparison of amplitude stability and extinctions of (a) the Hitachi device and (b) Mosaic devices. First column corresponds to PSD spectra of the excitation at given current and field. The corresponding time traces are shown in the second column. The analog HPF filter with cutoff

frequency of 3GHz was used during the measurements and a numerical bandpass filter of ±2GHz around the main peak was applied to reduce the noise. The histogram of time between extinctions extracted from time traces is shown in the third column. The last column is the instantaneous frequency extracted from the time traces via Hilbert transform.

Comparing now the time traces of Hitachi and Mosaic devices, two comments can be made. First, the amplitude of the Hitachi device is ten times larger than the one of Mosaic devices, i.e. measured using the same setup and the same amplification. This is consistent with the output power extracted from frequency domain measurements which shows that Hitachi devices have relatively higher output power on the order of ≈0.1μW, while the Mosaic devices investigated here emit only the power in the range of ≈0.1nW to ≈10nW. Second comment is that there is different signal amplitude stabilities observed in Hitachi and Mosaic devices. For the case of the Hitachi device, the signal amplitude oscillation is stable on the time scale of measurement which is 40μs (besides smaller fluctuations of amplitude due to thermal fluctuations), i.e. in this plot the signal is shown only for 20ns. Instead, in most of Mosaic devices, the signal amplitude is reduced many times to the noise level for several periods of oscillations, called ‘extinctions’. These extinctions mean that the signal oscillation is only sustained over a short time scale. There are thus two different fluctuation mechanisms with different coherencies: thermal fluctuation of the amplitude and phase (intrinsic contribution) and extinctions.

The time between extinctions is counted every time the amplitude of the signal reduced by 85% (close to the noise level) and the corresponding histogram is shown in the third column of Fig. 2.42. For the Hitachi device there is no extinction found in the 42μs long traces which indicates that the amplitude oscillation is sustained, as already mentioned. For Mosaic devices, the number of extinctions varies from one device to the other. For example in RFL733 and RFL731, the amplitude is sustained only for 20ns maximum. While for RFL741, the signal stability improves with the longest time of sustained amplitude is around 80ns and the extinction is not often compared to RFL733 and RFL741. Surprisingly, RFL731 and RFL741 have almost the same linewidth as Hitachi, which is around 20 MHz but different signal amplitude stabilities. The output power might influence on the existence of extinction. The origins of the extinctions are not yet well understood and are still under investigation. The extinction might come from the inhomogeneous tunnel junction barrier, the branching behavior (non-continuous frequency-field dispersion due to mode interaction) and the existence of multimodes, which are characteristics of RF performances of most Mosaic devices, see Section 2.4.1.

The signal extinctions need to be avoided for RF applications such as for the demonstration of operation within a phase locked loop and the demonstration of the FSK communication scheme. The existence of the signal amplitude extinction influences the frequency coherency as can be seen in Fig. 2.42-in the last column. This is because the frequency of the STNOs is nonlinearly coupled with the amplitude. The amplitude fluctuation is thus translated into frequency fluctuation via nonlinear coupling. As can be seen in the last column for the case of the Hitachi device, long time signal amplitude stability over 42μs is achieved, and thus the instantaneous frequency ≈9GHz is stable over time (besides smaller fluctuations of frequency due to thermal fluctuation). While for the case of Mosaic devices (RFL733 and RFL731), the amplitude extinction leads to the presence of the spikes in the instantaneous frequency. This is not good for the demonstration of FSK modulation especially at high modulation rates, on the order of few ns, since high frequency fluctuations will hinder the observation of the frequency shift.

2.4.2.2 Amplitude and phase noise

In this Section, the extraction of the amplitude relaxation frequency f_p from the amplitude noise plot and the phase noise at 100 kHz offset frequency $PSD_{\phi,1MHz}$ of different STNO devices will be shown and compared with the phase noise of existing oscillators. A typical example of the PSD of amplitude and phase noise for a Hitachi device is given in Fig. 2.43, plotted as double logarithmic plots.

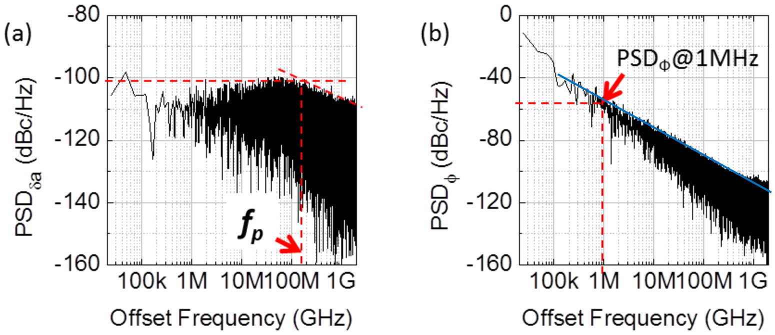

Fig. 2.43-PSD of amplitude and phase noise for Hitachi device as double logarithmic plots

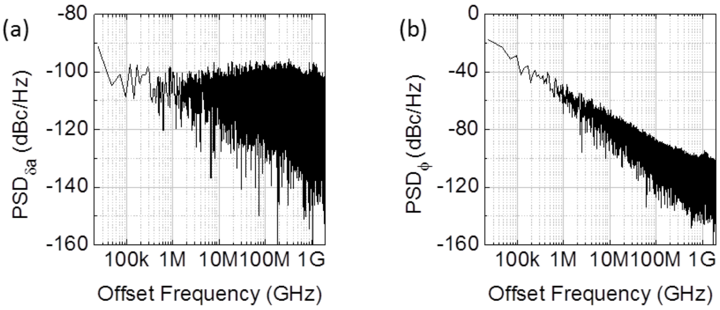

Fig. 2.44-PSD of amplitude and phase noise for RFL741 device as double logarithmic plots.

Fig. 2.43a shows the amplitude noise and the extraction of amplitude relaxation frequency f_p which is defined as the frequency at which the PSD amplitude drops by 3dB. The corresponding f_p is around 160MHz which is a typical f_p value obtained for standard homogeneous MTJ. This means that amplitude fluctuations are damped out on a time of $1/f_p$. When the perturbation is faster than $1/f_p$ the STNO does not have time to follow perturbations and accumulate. The response is then that of a random walk, characterized by a $1/f^2$ dependence. Table 2.10 gives the values of f_p for devices studied within Mosaic. The f_p varies from one device to the other. The highest f_p is achieved by RFL741, the one with a composite free layer. The amplitude noise plot actually does not show clear roll of frequency as shown in Fig. 2.44a. The other devices have f_p value of standard homogeneous MTJ devices, few hundred of MHz. For the FSK communication schemes, the amplitude relaxation frequency f_p is important because it limits the modulation bandwidth or modulation rates (discussed in Chapter 4). Hence large value of f_p is needed to achieve large modulation bandwidth and high modulation data rate which is desirable for wireless communication applications.

Table 2.10-Comparison of the linewidth, amplitude relaxation frequency, and phase noise of different STNO devices

Device	f (GHz)	Δf (MHz)	f_p (MHz)	PSD_ϕ (dBc) @100kHz	Phase noise type
RFL733	5.2	54	90	-20	$1/f^2$
RFL731	7.3	20	150	-10	$1/f^2$
RFL741	8.4	15	400	-40	$1/f^2$
Hitachi	9.1	18	160	-40	$1/f^2$

The phase noise shown in Fig. 2.43b behaves almost like $1/f^2$ (green line) over the full range of frequencies measured, i.e. over 4-5 decades. This corresponds to random walk noise of the phase. In fact, due to the amplitude-phase coupling, the amplitude noise contributes to phase noise and should lead to an enhanced phase noise level below f_p. Table 2.10-last column summarizes the phase noise values, measured at 100 kHz offset frequency for the different devices studied in Mosaic. The ones with larger linewidth (RFL733) and small linewidth but strong multimode (RFL731) have larger phase noise values of –10dBc/Hz and -20dBc/Hz, respectively. The device of RFL741 and Hitachi have lower phase noise -40dBc/Hz, the factor of 20, reflecting that linewidths are lower and high signal stability compared to two first devices. The phase noise of measured devices behaves random walk noise $1/f^2$, see Fig. 2.44-b for the PSD of phase noise of RFL741. Comparing to the phase noise value of conventional oscillators, Voltage Controlled Oscillator (VCO), the phase noise of the device investigated here is still much higher, where VCOs have -110dBc/Hz at the same offset frequency (100 kHz) [18].

To conclude, the studies of time domain measurement permits to compare the performances of STNO devices studied within Mosaic to existing technologies, showing that further reduction of phase noise is needed. Some of the strategies to achieve this are by exploiting coupling phenomena, where one can distinguish two different couplings, either between different layers within the magnetic stack, or between oscillators (synchronization). These strategies have been extensively studied via numerous experiments (and simulations) to better understand the mechanisms of coupling for the non-linear oscillations, to define routes of improving the phase noise characteristics and to gain control over the phase.

2.5 Summary and Outlook

The use of different magnetic stacks and the variation of the RA value (MgO barrier thickness), as well as different optimization in the nanofabrication process, have been explored in order to optimize the RF performances of standard homogeneous MTJ devices. Considerable advancements have been achieved within Mosaic as compared to the available standard devices used at the start of this thesis (Hitachi devices).

From the static characterization, Mosaic devices show robust barriers with much enhanced breakdown and degradation thresholds (500-800mV) as compared to Hitachi devices (300mV-400mV). However, the dynamic yield of Mosaic devices is much lower than Hitachi devices, i.e. only few of Mosaic devices show the transition to steady state oscillation. In addition, the steady state oscillations reveal that most of Mosaic devices are characterized by the multimodes and branching behavior, even for slightly larger RA value (RFL731 and RFL741). Hence, the RA value does not seem to play a significant role on the dynamic results. The best dynamic performances with a clean single mode and less branching behavior for instance can be achieved by Hitachi devices. A clean single mode and less branching behavior are of interest for FSK modulation in STNOs.

In terms of the dynamic performances such as the threshold current, power, and linewidth, considerable improvements have been obtained in RFL741 with the use of a composite free layer CoFeB/Ta/FeNi. This composite free layer leads to a slight reduction of the threshold current, three times smaller than those devices use CoFeB/CoFe free layer. This leads to low power consumption which is important for wireless sensor network applications. In addition, linewidth as low as 15MHz at output power of 45nW has been achieved in RFL741, which is comparable with the linewidth and output power observed in most of Hitachi devices. Further improvement in nanofabrication process, which seems to be related with the straightness of nanopillars, is needed to improve the static and dynamic yield of the devices and to obtain a clean single mode oscillation.

In terms of the signal stability, most of Mosaic devices are characterized by poor signal stability, showing by the large number of extinctions which reveal that the amplitude oscillation is sustained only in few ns (RFL731, and RFL733). However, a great improvement of signal stability is achieved for RFL741, the one with a composite free layer, with less number of extinction. Hitachi device, owning almost the same linewidth as RFL741 ≈20MHz reveals different amplitude stabilities. Long time amplitude oscillations over 42μs without extinction are achieved. This results in stable instantaneous frequency over long time scale. For RF applications such as FSK modulation using STNOs, long time signal stability is required. The origins of the extinctions are not yet well understood and are still under investigation. The origins of extinction are might from the inhomogeneous tunnel junction barrier, the branching behavior (non-continuous frequency-field dispersion due to mode interaction) and the existence of multimodes.

The last aspect which determines the RF performances is the phase noise. The phase noise of Hitachi and RFL741 are comparable since they own the same linewidth, which is around -60dBc/Hz. The other Mosaic devices have higher phase noise at the same offset frequency. Compared to the existing oscillator, VCO, the phase noise of STNOs is still much higher, where VCOs have -110dBc/Hz at the same offset frequency. Hence further reduction of phase noise is required.

To summarize, the change in the magnetic stack, i.e. the use of a composite free layer, realized within Mosaic does improve the RF performances such as a strong reduction in the threshold current, low linewidth, less extinction (good signal stability), and less branching behavior. This makes Mosaic devices comparable to Hitachi devices. Even though, the multimode behavior remains essential problem. Different aspects thus need to be explored for avoiding the multimode structure. The first is improving the nanofabrication process, by better defining the nanopillar shape (straighter edges). The second is the optimization of the magnetic stack deposition as well as configuration.

Chapter III

Numerical simulation: Enhanced modulation rates via field modulation in STNOs

The study of frequency shift keying (FSK) based wireless communication schemes needs to address the maximum data rate up to which a signal can be modulated or the frequency be shifted between two discrete levels. Previous studies on frequency modulation of STNOs under sinusoidal RF current reveal that the maximum data rate is limited by the relaxation frequency f_p of the STNO [22,24]. This is due to the fact that the frequency modulation occurs via the amplitude modulation through the non-linear amplitude-frequency coupling within STNOs. For homogeneous in-plane magnetized STNOs characterized in this thesis, the relaxation frequency f_p lies on the order of a few hundred MHz (see table 2.10 Chapter 2 Section 2.4.2.2). This means that the maximum data rate is limited to a few hundred Mbps. This limit remains suitable for the data rates targeted in this thesis for low to moderate data rate wireless communication used in sensor networks (10 to 100 Mbps), but will be too low when high data rates up to Gbps and more are needed. Here, frequency modulation by an RF field (field modulation) provides a solution.

This chapter focuses on the study of the frequency modulation in the STNO under the application of a sinusoidal RF field (field modulation) via numerical macrospin simulation. Here the maximum achievable data rate of the field modulation will be characterized. In this simulation, the field modulation was analyzed for homogeneous in-plane magnetized STNOs which are characterized by an in-plane precession mode. Two cases were considered here which are for longitudinal RF field modulation (the RF field is applied parallel to the easy axis of the free layer) and transverse RF field (the RF field is applied in-plane and perpendicularly to the easy axis of the free layer). For the extraction of the maximum achievable data rate, the amplitude and phase noise technique used in Ref. 24 (see Chapter 1 Section 1.4.2) was applied. This technique provides direct extraction of the maximum achievable data rate. As additional studies, the maximum achievable data rate as a function of the RF field angle with respect to the easy axis of the free layer and the modulation strength dependence on the modulation signal were considered here.

This chapter is divided into several sections. In the first Section, the analytical model for the current modulation discussed in Ref. 22 will be reviewed to remind the mechanism behind the current modulation and the kind of predictions that can be generated from the model. The second Section discusses the derivation of the analytical model for RF field modulation. This model is important to understand the numerical simulation results. It was developed by Liliana Prejbeanu. In the third Section, the numerical simulation parameters, analysis technique (amplitude and phase noise technique), and the simulation results of RF field modulation are discussed.

3.1 Review of the Analytical Model for Current Modulation

Before coming to the derivation of the analytical model and the numerical results of longitudinal RF field modulation, the analytical model for frequency modulation of the STNO via current modulation will be briefly reviewed in this Section to remind the mechanism behind the current modulation and the kind of predictions that can be generated from the model. The details of the derivation can be seen in Chapter 1 Section 1.3.4.

The following equation shows the instantaneous modulation of the power $\delta p(t)$ and the instantaneous frequency $f(t)$ of the STNO via current modulation.

$$\delta p(t) = \varepsilon \frac{2\Gamma_{-}(p_0)p_0}{\sqrt{\omega_m^2+4\Gamma_p^2}} \cos(\omega_m t + \psi) \tag{3.1a}$$

$$2\pi f(t) = \omega_g + N\varepsilon \frac{2\Gamma_{-}(p_0)p_0}{\sqrt{\omega_m^2+4\Gamma_p^2}} \cos(\omega_m t + \psi) \text{ with } \omega_g = \omega_0 + Np_0 \tag{3.1b}$$

Here, ε is the ratio of the RF current to the DC current, p_0 is the free running power of the unmodulated STNO ($\varepsilon = 0$), $\Gamma_{-}(p_0)$ is the negative damping (spin transfer torque) depending on p_0, N is the coefficient of the non-linear frequency shift, $f_m = \omega_m/2\pi$ is the modulation frequency, Γ_p is the amplitude relaxation rate, ψ is a phase shift between the external RF current and the STNO-generated signal, and ω_g is the free running frequency of the unmodulated STNO.

The equation for $\delta p(t)$ shows that the modulated amplitude cuts off at the relaxation frequency $f_p=\Gamma_p/\pi$, and, therefore, f_p determines the maximum modulation rate and also the frequency bandwidth of the amplitude (power) modulation. Due to the nonlinear coupling N between frequency and amplitude, the same cut-off appears for frequency modulation. Hence, the bandwidth of the frequency modulation is also given by the relaxation frequency f_p. This becomes evident when taking the Fast Fourier Transform (FFT) of Eq. 3.1b, as shown in Eq. 3.2. (Note that the PSD is the magnitude squared of its Fourier transform).

$$PSD\ (f) \propto A(f_m)\delta(f - f_m) \tag{3.2}$$

Where $A(f_m) = \varepsilon^2 \frac{(2N\Gamma_{-}(p_0)p_0)^2}{4\pi^2} \times \frac{1}{f_m^2+f_p^2}$

Here δ is the Dirac function and $A(f_m)$ is the frequency response of the STNO as a function of the modulation frequency, f_m. Thus there are two limiting behaviors of the frequency response of the STNO. For slow modulation frequencies, $f_m \ll f_p$, the contribution of f_m in Eq. 4.2 can be neglected such that the response of $A(f_m)$ is constant. For this case, the amplitude in the frequency response is modulated in white Gaussian manner, i.e. the same strength at all frequencies below f_p at the same time. This means that under slow modulation frequencies (slow perturbation) compared to the STNO precession period, the STNO has time to follow the perturbation such that the STNO can respond and follow the modulating RF current. In contrast, for faster modulation frequencies, $f_m \gg f_p$, the frequency response of the amplitude $A(f_m)$ is inversely proportional to the square of f_m. This means that under a faster perturbation (faster than its relaxation rate f_p), the STNO does not have enough time to follow the modulating RF current. This results in amplitude attenuation. The higher f_m with respect to f_p, the larger the amplitude attenuation. This response of the system for small ε (modulation strength) has actually a similar meaning to the solution of an autonomous (free running) oscillator with thermal noise as discussed in Chapter 1, Section 1.3.5. This analytical model, hence, predicts the behavior of the amplitude and frequency modulation of the STNO via current modulation and it is shown that the maximum achievable data rate and the modulation bandwidth of amplitude and frequency modulation of the STNO are given by its relaxation frequency f_p. These predictions have been confirmed experimentally in Ref. 24, for the case of in-plane magnetized STNOs. The STNO was modulated by a sinusoidal RF current at constant modulation strength ε and different modulation frequency f_m. The results were analyzed by using the amplitude and frequency noise technique, see Fig. 1.20 in Chapter 1, Section 1.4.2, and show that the modulated amplitude and frequency of the STNO cut off at frequency given by f_p. Hence, the results coincide with the predictions of the analytical model.

3.2 Analytical Model for Longitudinal RF Field Modulation

The frequency modulation of an STNO via field modulation is based on the fact that the precession frequency of the magnetization of the STNO is coupled with the effective field, H_{eff}, (the conservative term in the LLGS equation, see Eq. 1.19). This effective field determines the equilibrium position around which the magnetization precesses. Modulating the effective field via an RF field, will result in a modulation of the STNO frequency.

In this thesis, the analytical model for the case of longitudinal RF field modulation (RF field is applied along the equilibrium position or the easy axis direction) has been developed by Liliana Prejbeanu. Other RF field modulation schemes, i.e. the RF field is applied with and angle respect to the easy axis direction, are not considered here since this leads to much complex derivations. The developed model for longitudinal RF field modulation is based on the KTS model (see Chapter 1, Section 1.3.2). Hereafter the model is presented and the predictions are discussed.

3.2.1 Transformation to complex c-variables

To be consistent with the previous studies on current modulation [24], the in-plane magnetized STNO configuration, i.e. both free layer and polarizing layer are in plane magnetized, is considered in this model as shown in Fig. 3.1. The in plane rotation is characterized by the spherical angle β and the out plane rotation is characterized by the spherical angle θ. A static magnetic field of amplitude, H_{app}, is applied in the plane along the x-axis direction. A uniaxial magnetocrystalline (MCA) anisotropy field $\boldsymbol{H_u}$ along x-axis direction is considered of amplitude K_u (K_u>0). The demagnetizing effect are included by the demagnetizing tensor **N**=(N_X, N_Y, N_Z). To perform the field modulation, an RF magnetic field is applied to the system in the x-y plane $\boldsymbol{H_{RF}} = (H_{RFx} \quad H_{RFy} \quad 0)$.

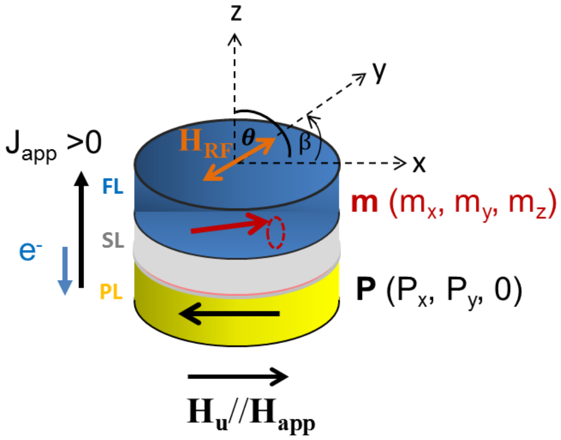

Fig. 3.1. The schematic of the field modulation for in-plane magnetized STNO

The magnetization inside the free layer FL is supposed to be uniform, thus the free energy associated of the ferromagnetic free layer of the nanopillar is:

$$E(\boldsymbol{m}) = K_u(1 - m_x^2)V + \frac{1}{2}\mu_0 M_s^2(N_x m_x^2 + N_y m_y^2 + N_z m_z^2)V \\ -\mu_0 M_s(H_{app} + H_{RFx})m_x V - \mu_0 M_s H_{RFy} m_y V \tag{3.3}$$

Here **m**=**M**/M_s is unitary magnetization vector, V the volume of the sample, M_s the spontaneous magnetization.

The effective field is given by the functional derivative of the free energy with respect to the magnetization: $\boldsymbol{H_{eff}} = -\frac{1}{\mu_0 M_s V}\frac{\delta E}{\delta \boldsymbol{m}}$.

Following the Holstein-Primakoff transformation the variables m_x, m_y, m_z are replaced by the canonical variables (a, a^*) defined such as: $a = \frac{m_y - jm_z}{\sqrt{2(1+m_x)}}$. It is convenient to express the reduced free energy as follows:

$$\frac{\gamma_0'}{\mu_0 M_s V} E(a, a^*) = (A + \omega_{RFx})a, a^* + \frac{1}{2}B\left(a^2 + a^{*2}\right) \\ + \mathcal{V}\left(aa^{*3} + a^3 a^*\right) + \mathcal{U}a^2 a^{*2} + \omega_{RFy}(a + a^*)\sqrt{1 - aa^*} \tag{3.4}$$

Here $\gamma_0' = \frac{\gamma_0}{1+\alpha^2}$ with α is the damping constant, $\gamma_0 = \mu_0 \gamma$ is the gyromagnetic ratio of the free electron multiplied by the vacuum permeability μ_0.The notations are similar to that of Ref. [87].

$$A = \omega_A + \omega_H + \frac{\omega_M}{2} \qquad \omega_M = \gamma_0' M_s (N_Z - N_Y)$$

$$\omega_H = \gamma_0' H_{app}$$

$$B = -\frac{\omega_M}{2} \qquad \text{With} \qquad \omega_A = \gamma_0' \left[\frac{2K_u}{\mu_0 M_s} + M_s(N_Y - N_X)\right]$$

$$\mathcal{V} = -\left(\omega_A + \frac{\omega_M}{2}\right) \qquad \omega_{RFx} = \gamma_0' H_{RFx}$$

$$\mathcal{U} = +\frac{\omega_M}{4} \qquad \omega_{RFy} = \gamma_0' H_{RFy}$$

Where ω_A is the frequency due to anisotropy field H_u, ω_H is the frequency given by the a static magnetic field H_{app}, ω_M is the frequency due to the demagnetization field, ω_{RFx} and ω_{RFy} are the frequency induced by the longitudinal and transverse component of the RF field, respectively.

A second transformation is used for the diagonalization of the quadratic part of the reduced free energy: $b = ua + va^*$ where $u = \sqrt{\frac{A+\omega_0}{2\omega_0}}$, $v = -\sqrt{\frac{A-\omega_0}{2\omega_0}}$ with $\omega_0 = \sqrt{A^2 - B^2}$ is ferromagnetic resonance (FMR) frequency. The last transformation is a normalization: $b = \sqrt{\frac{\omega_0}{A}}c$.

3.2.2 Complex equation for modulation under longitudinal RF fields

Applying the three transformations presented above $m \rightarrow (a, a^*) \rightarrow (b, b^*) \rightarrow (c, c^*)$ and keeping only potential resonant terms (weakly nonconservative system), the extended Landau-Lifshitz equation (see Eq. 1.19, Chapter 1, Section 1.3.2) is transformed to an equation in “complex c-variable”:

$$\frac{dc}{dt} = -j[\omega_0 + N|c|^2]c - j\left[\frac{A}{\omega_0}\omega_{RFx}c + \frac{|B|}{\omega_0}\omega_{RFx}c^*\right] - j\frac{1}{2}(u - v)\omega_{RFy} \\ -\Gamma_0[1 + Q_1|c|^2 + Q_2|c|^4]c + \alpha\omega_{RFx}\left[-1 + |c|^2 + \frac{|B|}{2A}\left(c^2 + c^{*2}\right)\right]c + \alpha\omega_{RFy}\frac{1}{2}\sqrt{\frac{A}{\omega_0}}(u + v) \\ -\Gamma_J P_x\left[1 - |c|^2 - \frac{\|B\|}{2A}\left(c^2 + c^{*2}\right)\right]c + \Gamma_J P_y \frac{1}{2}\sqrt{\frac{A}{\omega_0}}(u + v) \tag{3.5}$$

The first line of eq. 3.5 corresponds to the precession term, $\omega(|c^2|)$, the second line is the positive damping term, $\Gamma_+(|c^2|)$, and the third line is the negative damping term, $\Gamma_-(|c^2|)$. The expressions for the coefficients are the following:

$$N = -[3\omega_M uv(u^2+v^2) + (2\omega_A + \omega_M)(u^4+v^4+4u^2v^2)]\frac{\omega_0}{A}$$
$$\Gamma_0 = \alpha A$$
$$Q_1 = -\left[3uv\omega_M + (u^2+v^2)\left(\omega_H + 3\omega_A + \frac{3}{2}\omega_M)\right)\right]\frac{\omega_0}{A^2}$$
$$Q_2 = [3uv(u^2+v^2)\omega_M + (u^4+v^4+4u^2v^2)(2\omega_A+\omega_M)]\left(\frac{\omega_0}{A}\right)^2\frac{1}{A}$$
$$\Gamma_J = \gamma_0' a_{j,0} J_{app}$$

Where, $a_{j,0} = \frac{\hbar}{2e}\frac{\eta}{\mu_0 M_s t}$ is the spin–torque amplitude coefficient, t is the thickness of the free layer and η is the spin-polarization of the charge current J_{app}.

The Eq. 3.5 represents the extension of the KTS model (Eq. 1.20, Section 1.3.2) for the case of RF field and it will be used to describe the spectral proprieties of the STNO with the RF field modulation.

3.2.3 Amplitude and frequency equations for longitudinal RF field modulation

To find the stationary solution of Eq. 3.5, it is rewritten as a system of two real equations for power $p = |c|^2$ and phase ϕ of oscillations ($c = \sqrt{p}e^{-j\phi}$). For the case of the longitudinal RF field, $\omega_{RFx} = \gamma_0' H_{RFx}\cos(\omega_m t)$, two coupled equations are obtained:

$$\frac{dp}{dt} = -2\Gamma_0[1 + Q_1 p + Q_2 p^2]p - 2\Gamma_J \mathrm{P}_x[1-p]p - 2\alpha\gamma_0' H_{RFx}\cos(\omega_m t)[1-p]p \tag{3.6a}$$

$$\frac{d\Phi}{dt} = [\omega_0 + Np] + \frac{A}{\omega_0}\gamma_0' H_{RFx}\cos(\omega_m t) \tag{3.6b}$$

In the free running regime (no RF magnetic field, $\mathbf{H_{RF}}$), these generic equations allow one to extract the free running power p_0 and the free running frequency f_g as already mentioned in Chapter 1, Section 1.3.3):

$$p_0 = -\frac{\Gamma_0 + \mathrm{P}_x\Gamma_J}{\Gamma_0 Q_1 - \mathrm{P}_x\Gamma_J} \tag{3.7a}$$

$$2\pi f_g = \omega_0 + Np_0 \tag{3.7b}$$

and to define the amplitude relaxation rate Γ_p and the nonlinear frequency shift parameter ν:

$$\Gamma_p = (\Gamma_0 Q_1 - \mathrm{P}_x\Gamma_J)p_0 \tag{3.8}$$

$$\nu = \frac{Np_0}{\Gamma_p} \tag{3.9}$$

Assuming that the amplitude of longitudinal RF magnetic field, H_{RFx}, is small (neglecting high order term), the oscillation power $p(t)$ can be represented as $p(t) = p_0 + \delta p(t)$. Doing the linearization of Eq. 3.6a for small modulation $\delta p(t)$ around the free running power p_0, one obtains a system of equations for the power modulation δp of the STNO under the application of longitudinal RF field.

$$\frac{d\delta p}{dt} = -2\Gamma_p \delta p - 2\alpha\gamma_0' H_{RFx} p_0 \cos(\omega_m t) \tag{3.10a}$$

From the stationary condition, the power modulation is derived:

$$\delta p(t) = \varepsilon\alpha \frac{-2\gamma_0' H_{app} p_0}{\sqrt{\omega_m^2 + 4\Gamma_p^2}} \cos(\omega_m t - \psi) \tag{3.10b}$$

with the phase $cot\psi = \frac{2\Gamma_p}{\omega_m}$ and ε is the modulation strength defined as $\varepsilon = \frac{H_{RFx}}{H_{DC}}$. Whereas, the instantaneous frequency $f_i(t)$ of the STNO for longitudinal RF field modulation is:

$$\frac{d\phi}{dt} = 2\pi f_i(t) = \omega_g + N\delta p(t) + \frac{A}{\omega_0}\gamma_0' H_{RFx} \cos(\omega_m t) \tag{3.10c}$$

At this point, few conclusions might be drawn from the analytical model:

a) The power modulation δp is proportional to the modulation strength ε (or the modulating field amplitude H_{RFx}) and the damping parameter, α. Since the damping constant α in ferromagnetic material is usually small ~0.01 and for small ε, the resulting power modulation δp is also small and can be neglected. This power modulation δp is smaller compared to the one of current modulation (see eq. 3.1a) since in current δp is proportional with ε but independent on the damping α.

b) The instantaneous frequency $f_i(t)$ is given by eq. 3.10c similar to the eq. 3.1b. One might notice there is one additional term $\frac{A}{\omega_0}\gamma_0' H_{RFx} \cos(\omega_m t)$ directly related to the RF field. Consequently there are two ways to act on the frequency: via the term $\frac{A}{\omega_0}\gamma_0' H_{RFx} \cos(\omega_m t)$ and indirectly through the non-linear term proportional to $N\delta p$. However since $N\delta p$ is very small, the direct term is dominating the frequency modulation.

In contrast to the current modulation case, the analytical model of longitudinal RF field modulation predicts that the frequency modulation by an RF longitudinal field is not mediated by the non-linear amplitude-coupling but it is given directly by the RF field. Hence, the amplitude relaxation rate does not set the upper limit of the modulation rate and the modulation bandwidth.

To confirm this analytical prediction and check the limits of the above model, numerical simulation via macrospin approach will be discussed in the next section. The confrontation between numerical and analytical models is one of the objectives of this chapter.

3.3 Numerical Simulation of the Field Modulation in STNOs

To confirm the predictions given by the analytical model discussed in the previous Section and to check the limits of the model, numerical simulations of field modulation in STNOs have been carried out in this thesis and will be presented in this Section. The modulation concept is similar to what has been performed previously by Quinsat et. al for the case of current modulation [24]. The difference is that in this work the external modulating signal is a sinusoidal RF field instead of a sinusoidal RF current. The amplitude and frequency noise technique developed in Ref. 24 provides a direct way of the extraction of the maximum modulation rate and thus will be used in this work to extract this parameter for the case of field modulation, whether this parameter limits the modulation rate as for the case of current modulation.

This Section is divided into three parts. The first part is devoted to the description of the simulation parameters and to check the limits of the analytical model. The second part is focused on the analysis method which is the amplitude and frequency noise technique. Finally, the numerical results and the discussion will be presented in the last part.

3.3.1 Simulation parameters

The field modulation in STNOs was studied in the frame of a macrospin approach. The numerical analysis is carried out for the extended Landau-Lifshitz equation of the free layer (see Eq. 1.19, Chapter 1, Section 1.3.2) in which the damping-like spin transfer torque was included. A white Gaussian noise field with a variance proportional to the temperature T is accounted for thermal fluctuations (discussed in Section 3.3.1.2).

An in-plane magnetized STNO configuration, i.e. both free layer FL and polarizing layer PL are in-plane magnetized, was considered in this simulation. The schematic of this configuration and the corresponding magnetization precession trajectory (in-plane precession (IPP) trajectory) around its equilibrium position, x-axis, is illustrated in Fig. 3.2. A static magnetic field of amplitude H_{app}, is applied parallel to the free layer easy axis (//X). The polarizer is aligned in-plane at β=165° from the free layer easy axis such that the system is slightly non-collinear. The negative current density means that the electrons flow from the polarizer to the free layer which destabilizes the magnetization of the free layer. The simulation material parameters, such as the spontaneous magnetization (M_s), magneto-crystalline anisotropy (K_u), the demagnetizing factors (N_x, N_y, N_z), the damping parameter (α), the size of the free layer (FL), and the polarization value (η), are given in table 3.1.

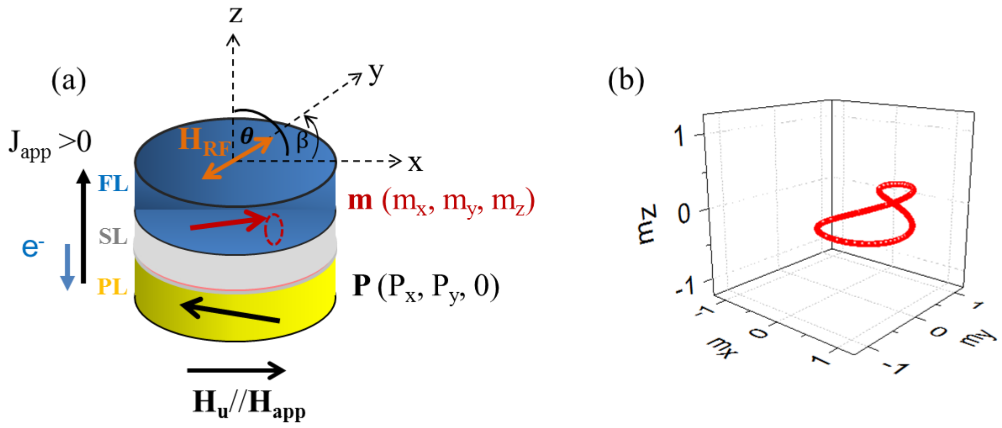

Fig. 3.2-(a) Schematics of the STNO configuration with an in-plane magnetized free layer and an in-plane polarizing layer. The polarizing layer is aligned in-plane at 165° from the free layer easy

axis. (b) The in-plane precession (IPP) trajectory of the free layer magnetization in the free running state (H_{RF}=0).

Table 3.1-The simulation material parameters

Parameter	Value
M_s (kA/m)	1000
K_u (J/m^3)	0
N_x N_y N_z	0.052553 0.059408 0.888038
FL size (nm^3)	90x80x3.9
α	0.02
η	0.30
P_x P_y	-0.965925 0.258819 Tilted φ=165°

Using the simulation material parameters and specific STNO configuration discussed above, the limits (range of validity) of analytical model will be firstly investigated. This step is important so that the simulation operational parameters used in this work, such as the free running parameters (the static magnetic field H_{app} and the current density J_{app}) and the modulation parameter (the modulation strength $\varepsilon=H_{RF}/H_{app}$) are in the range of model validity. Hence, a comparison between numerical results and analytical calculations can be performed.

3.3.1.1 Free running STNO (T=0K): comparison between analytical and numerical

In order to check the limits of the analytical model of the STNO in the free running state, the output power p_0 of STNO calculated via the analytical model is compared with the one extracted from numerical simulation.

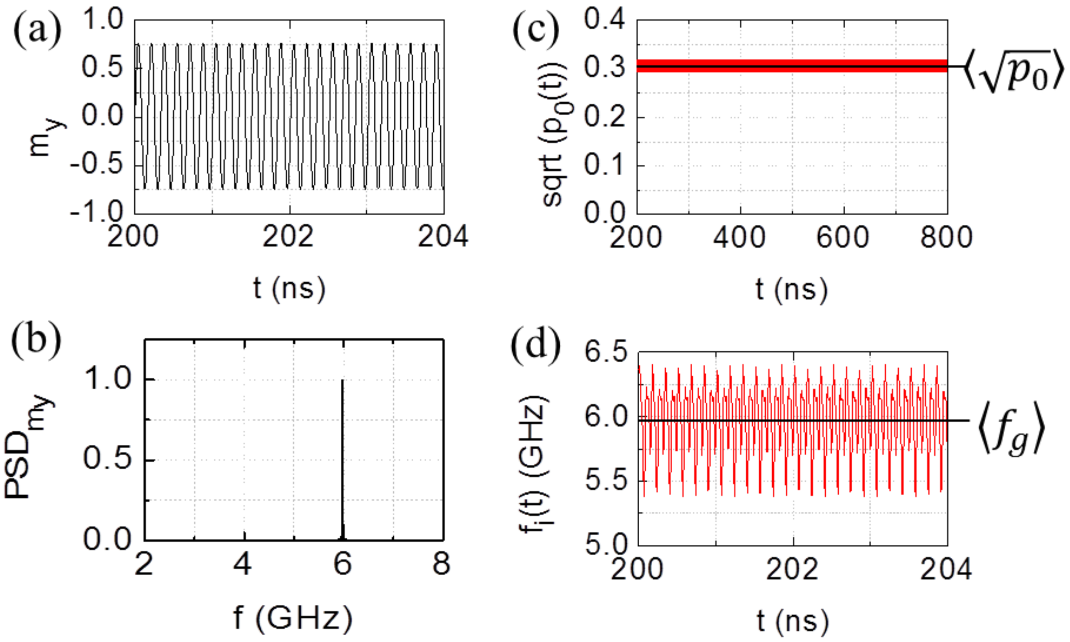

Fig. 3.3-Numerical simulation of free running STNO obtained from the full Landau-Lifshitz integration, using the complex oscillator variable c-transformation: (a) time varying components of $m_y(t)$ (b) the PSD of $m_y(t)$ showing the excitation frequency around 6 GHz (c) the instantaneous power (d) the instantaneous frequency obtained from the first derivation of the instantaneous phase. The

simulation was performed at magnetic field of 40 mT and current density of -50x10^{10} A/m^2 and at T=0K.

The analytical power p_0 of the free running STNO is calculated using eq. 3.7a (see Section 3.2.3) and the numerical power p_0 is obtained based on the full Landau-Lifshitz integration (containing all contributions) as shown in Fig. 3.3. From numerical simulation, the time varying components of $m_x(t)$, $m_y(t)$, and $m_z(t)$ were obtained and then transformed into the complex variable c-transformation. The time varying components of $m_y(t)$ is given in Fig. 3.3a. Since the simulation was taken at zero temperature, the amplitude oscillation is constant and the phase is supposed to be coherent in time. Thus the corresponding power spectral density (PSD) results in a dirac peak as shown in Fig. 3.3b. The instantaneous power $p_0(t)$ and instantaneous frequency $f_i(t)$ are given in fig. 3.3c and fig. 3.3d respectively. Taking the average value of the instantaneous power $\langle p_0 \rangle$ and the instantaneous frequency $\langle f_g \rangle$, one can obtain the numerical power p_0 and frequency f_g of the STNO.

In Fig. 4.4, the free running power (Fig. 3.4a) extracted from the analytical model (black line) and from the numerical simulation (red dotted line) as a function of current density J_{app} at a fixed magnetic field (H_{app}= 40mT) are shown. It can be seen that the analytical value of the free running power fits well with the ones extracted from numerical simulation for the current density applied between -37x10^{10}A/m^2 $\leq J_{app} \leq$ -50x10^{10}A/m^2, i.e. J_{app} -37x10^{10}A/m^2 is the threshold current at which the steady state precession is induced. Above J_{app}=-50x10^{10}A/m^2, the analytical calculation of the free running power slightly differs from the one extracted via numerical simulation. From this comparison, it can be seen that the limit of the analytical model is at J_{app}=-50x10^{10}A/m^2. This limit can also be seen by looking at the IPP mode precession trajectory as a function of current density, as shown in Fig. 4.4c (3D trajectory) and Fig. 4.4d (2D trajectory). The amplitude of the precession trajectory increases with the increase of the current density. Increasing the current density from -37x10^{10}A/m^2 $\leq J_{app} \leq$ -50x10^{10}A/m^2, the amplitude of the precession of m_x component is not crossing 0, $0 \leq m_x < 1$, so that the precession amplitude is considered small, see Fig. 4.4d. In this current range, the analytical model is valid, since the model was developed for small precession amplitudes around the equilibrium point. For large precession amplitudes induced above -50x10^{10}A/m^2, i.e when the m_x component varies from -1 to 1 ($-1 \leq m_x < 1$), the analytical model is no more valid. In this case, one needs to take into account the higher order terms neglected in the model.

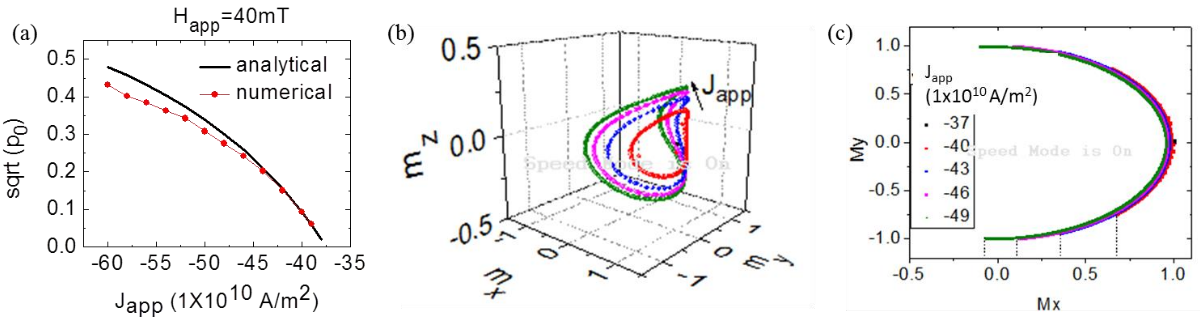

Fig. 3.4-(a) The free running power extracted from analytical calculation and numerical simulation. The bias field is 40 mT and the temperature is 0K. The analytical model is valid only for current density which is from -37x10^{10} A/m^2 to -46x10^{10} A/m^2 (the threshold current density is -37x10^{10} A/m^2). (c) The IPP precession trajectory in 3D plot as a function of current density, from -37x10^{10} A/m^2 (red curve) to -49x10^{10} A/m^2 (green curve). The amplitude precession increases upon increasing the current density. (d) The X-Y projection (2D) of the IPP trajectory.

From this investigation, it can be concluded that the analytical model developed in this thesis is valid within the current range of -37x10^{10} A/m^2 $\leq$ J_{app} $\leq$ -50x10^{10} A/m^2 for the chosen magnetic field amplitude of 40 mT. This magnetic field amplitude was chosen in order to induce the IPP mode precession and also to stay close to the situation of interest for experiments.

3.3.1.2 Free running STNO: thermal fluctuations

The simulation and calculation in the previous part was carried out at zero temperature, neglecting the influence of thermal fluctuations. It has been discussed in Chapter 1, Section 1.3.5, that thermal fluctuations determine the generation linewidth of the STNO which is one of the most important parameters from the practical point of view. In this part, the generation linewidth of the STNO as a function of external control parameters, i.e magnetic field and current density, and temperature will be investigated. The aim is to choose the operational conditions (magnetic field, current density, and the temperature) for numerical simulation for which the linewidth is small. The small linewidth is required for the observation of the sidebands under modulation. The amplitude of the sidebands as a function of the modulation frequency f_m, will be of interest.

➢ White Gaussian noise and linewidth extraction

To simulate this generation linewidth, the thermal fluctuations in the STNO magnetic structures are taken into account by adding a thermal noise field [83] to the effective field $\mathbf{H}_{\mathbf{eff}}$ in the Landau-Lifshitz equation of the free layer.

$$\langle \mathbf{H}_{\mathbf{th}}^{\mathbf{i}}(t)\mathbf{H}_{\mathbf{th}}^{\mathbf{j}}(t')\rangle = \frac{2\alpha k_B T}{\gamma_0 V \mu_0 M_S}\delta_{\mathbf{i},\mathbf{j}}\delta(t-t') \qquad (3.11)$$

The i,j representing Cartesian coordinates and the brackets are the time average. The $\mathbf{H}_{\mathbf{th}}$ is a magnetic random field with zero mean and its autocorrelation function is given by Eq. 3.11, which corresponds to a white Gaussian noise with a variance proportional to the temperature T and the damping factor $\boldsymbol{\alpha}$, and inversely proportional to the magnetic volume V. Since $\mathbf{H}_{\mathbf{th}}$ is a random field, it accounts for non-deterministic (stochastic) processes. Therefore, running the same simulation several times at finite temperature leads to a distribution of magnetization trajectories shown in Fig. 3.5a. This distribution is translated into magnetization oscillations whose amplitude as well as the phase fluctuates in time around its average value, as can be seen in the time traces of the m_y-component in Fig. 3.5b. The corresponding PSD of time traces results in the broadening of the peak (Fig. 3.5c). The Lorentzian function is used to fit the PSD and to extract the center frequency, f_g, and the linewidht, Δf. However, the Lorentzian function cannot fit successfully because the PSD distribution is too dense or noisy. To further reduce noise in the PSD, the welch averaging method [x] is applied on the time traces of the m_y-component. In this method, the time trace is split up into overlapping segments which are then windowed. The windowed segments are converted in the frequency domain by computing its Fourier Transform (periodogram). The ensemble averaged periodogram is shown in Fig. 3.5d (black curve), which results in a less noisy PSD. The Lorentzian function now fits successfully the center frequency and the linewidth of the averaged PSD.

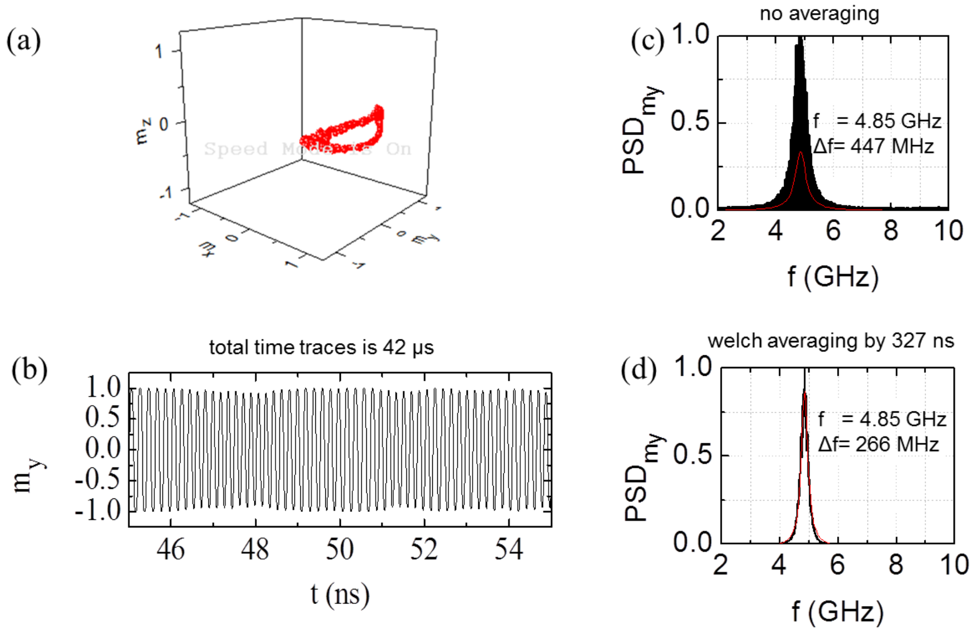

Fig. 3.5 -Numerical simulation at magnetic field of 40mT, current density of $-50x10^{10}A/m^2$ and temperature of 50K (a) The 3D trajectory of IPP mode shows that the precession fluctuates around the average value (b) The precession fluctuation is translated into the magnetization oscillations (time traces). The total time traces was 42µs (c) The corresponding PSD of 42µs time traces (with no averaging treatment) leads to the broadening of the peak (d) The averaged PSD by welch averaging method with averaging window is 327ns. Red curve in (c)(d) corresponds to Lorentzian fitting, which permits to extract the center frequency and the linewidth broadening of the peak.

➢ Linewidth as a function of external control parameters and temperature

Using the welch averaging method and Lorentzian fitting introduced previously, the frequency and the linewidth of the free running STNO as a function of external control parameters, i.e. current density, J_{app}, and magnetic field, H_{app}, and temperature, T, are shown in Fig. 3.6. In Fig. 3.6a, the center frequency f_g as a function of current density J_{app} at a fixed magnetic field (H_{app}=40mT) for different temperature, T, is shown. The center frequency does not change with temperature. The transition from a damped mode into a steady state IPP precession mode is observed at threshold current, J_{th}. Below the threshold current the frequency is constant and above the threshold current the frequency decreases upon increasing current density (redshift), which is the normal behavior of an in-plane magnetized STNO. The corresponding linewdith is shown in Fig. 3.6b. As predicted in Ref. 87, the thermal fluctuations (temperature) lead to the blurring of the generation threshold. Below the threshold current J_{th} (damped regime), the linewidth decreases linearly with the current and it is independent of the temperature. In the transition regime, the linewidth increases due to strong thermal fluctuations in the transition from a damped mode to a steady state mode. The influence of temperature on the linewidth is seen in this transition regime. Above the transition regime (steady state regime), the linewidth decreases upon increasing the current and increases upon increasing the temperature. Fig. 4.6c shows the linewidth dependence on the magnetic field. It is shown that the linewidth is smaller at low magnetic field.

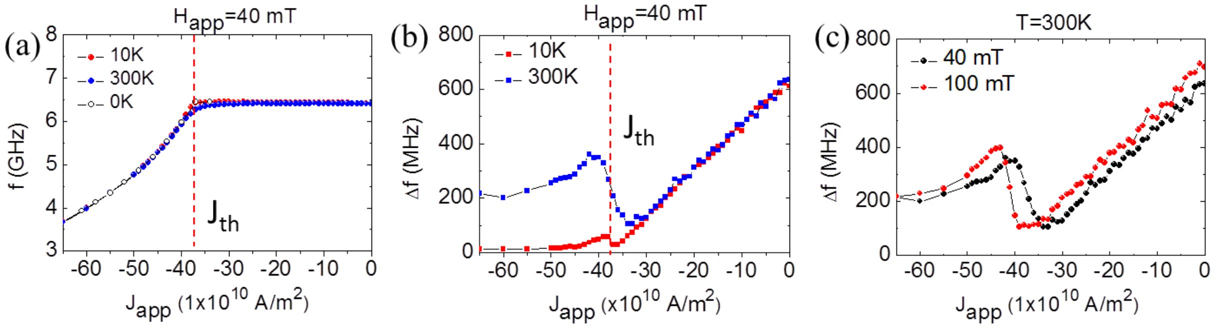

Fig. 3.6-Numerical simulation of the free running STNO as a function of external control parameters and temperature, T. (a) the frequency and (b) the linewidth of the free running STNO as a function of current density, J_{app}, at a fixed magnetic field (H_{app}=40mT) for different temperatures. J_{th} is the threshold current, showing the transition from a damped mode to a steady state IPP precession mode. (c) The linewidth as a function of current density, J_{app}, at a fixed temperature (300K) for different magnetic fields, H_{app}.

➢ The importance of linewidth for sideband observation

The linewidth of the free running STNO has to be smaller such that the sideband observation around the carrier frequency is possible, especially at low modulation frequency f_m (below the relaxation frequency, f_p). It is important to note that besides analyzing the amplitude and the frequency noise response of the modulated STNO, the PSD of the modulated STNO containing sidebands will be also analyzed. The aim is to investigate the dependence of amplitude of the sidebands on the modulation frequency f_m, especially at slow modulation frequency ($f_m<f_p$) and fast modulation frequency ($f_m>f_p$) with respect to the STNO relaxation frequency f_p, i.e. whether the sidebands amplitude is attenuated or not for the case of the presence or absence of the cut-off frequency given by the relaxation frequency f_p.

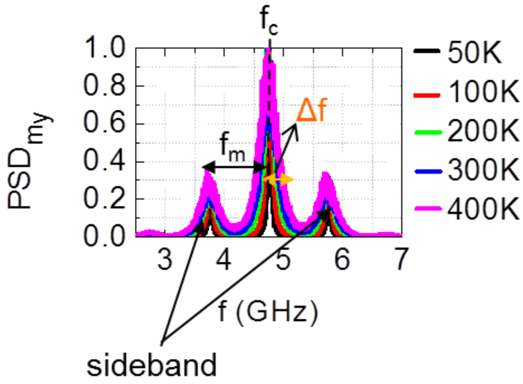

Fig. 3.7-The PSD of the modulated STNO as a function of finite temperature. The linewidth, Δf, of the carrier peak as well as the sidebands are broadening as the temperature increases. The upper and lower sideband around the carrier frequency, f_c, are separated by the modulation frequency, f_m.

Based on the modulation theory (see Chapter 1, Section 1.4.1), the modulation spectrum contains the carrier frequency and the sidebands around it (upper and lower sidebands). The sidebands are separated by f_m from the carrier frequency, f_c, as illustrated in Fig. 3.7. If the linewidth of carrier frequency, Δf, is larger than f_m, the sidebands will be hidden so that the sideband observation is impossible. In order to observe sidebands at low modulation frequency ($f_m<f_p$) with respect to the STNO relaxation frequency f_p, one should consider that the linewidth of the carrier frequency, Δf, has to be much smaller than f_p. Table 3.2 summarizes the f_p value for constant H_{app}=40mT and varied current density (within the range

of validity of the analytical model, see Section 3.3.1.1). The f_p was calculated from the analytical model Eq. 3.8, which is independent of temperature, T. The corresponding linewidth, Δf, given at finite temperature, i.e. 50K and 300K, is also shown in table 4.2. It can be seen that there are two set of parameters to fulfill the condition of $\Delta f<f_p$ shown in the dashed box. The operational condition at current J_{app}=-50x10^{10} A/m^2 and T=50K lead to a much smaller linewidth, Δf, compared with the corresponding f_p value. Hence, at this operational condition, the sidebands are expected to be clearly observed. These parameters are chosen for the modulation simulation discussed in Section 3.4.

Table 3.2-Comparison of the linewidth, Δf, and the relaxation rate, f_p, at given parameters.

Happ (mT)	J_{app} (A/m^2)	f_p (MHz)	T (K)	Δf (MHz)
40	-40x10^{10}	42.36	50	106
40	-40x10^{10}	42.36	300	350
40	-45x10^{10}	127.33	50	85
40	-45x10^{10}	127.33	300	300
40	-50x10^{10}	212.24	50	60
40	-50x10^{10}	212.24	300	250

3.3.1.3 Summary: Free running parameters

To summarize, the free running STNO parameters used in the simulation are summarized as follow:

(a) The magnetic field, H_{app}, is 40 mT: to induce the IPP mode precession, to stay close with situations and experiments, and small linewidth

(b) The current density is J_{app}=-50x10^{10} A/m^2: to induce the IPP mode with small amplitude precession ($0<m_x<1$) and to stay within the validity range of analytical model

(c) The temperature, accounted for thermal fluctuations, is 50K. The free running parameters, i.e. H_{app}=40 mT and J_{app}=-50x10^{10} A/m^2, give rise to the STNO relaxation frequency f_p of 212.24 MHz. The temperature of 50K leads to a broadening of the PSD with the corresponding linewidth around 60 MHz, which is much smaller than the STNO relaxation frequency f_p. This allows the investigation of the sidebands amplitude dependence on the modulation frequency f_m, especially at slow modulation frequency ($f_m<f_p$) and fast modulation frequency ($f_m>f_p$) with respect to the STNO relaxation frequency f_p.

3.3.1.4 Modulation parameter: modulation strength ($\varepsilon=H_{RF}/H_{app}$)

In the field modulation in STNOs, the modulation strength ε is defined as the ratio between the RF field amplitude, H_{RF}, and the bias field amplitude, H_{app}, ($\varepsilon=H_{RF}/H_{app}$). The choice of the modulation strength is motivated by several factors. On the one hand, considering the application of an STNO for wireless communication within an FSK scheme, the induced shifts in the instantaneous frequency due to shifts in the magnetic field (given by the RF field amplitude) should be sufficiently large to reach required signal to noise levels. This has been reported in Ref. [29-33], designing the use of an STNO for dynamic read head application based on the FSK modulation concept. The modulation fields (arising from the stray fields of the magnetic bits) can have a considerable value of a few hundred Oe (see table I of Ref. 29) in order to induce a modulation of the instantaneous frequency that is sufficiently large (few hundreds of MHz) for a good signal to noise ratio.

The modulation strength should not be too small, while too large modulation strength will lead to an over-modulation phenomenon. This over-modulation leads to periodic extinctions in the modulated time traces, i.e on-off modulation, which is not considered in the analytical model. This over-modulation can be observed by increasing the the modulation strength at a constant modulation frequency as shown in Figs. 3.8 (red dashed box). For the case of longitudinal RF field modulation (Fig. 3.8a), the modulated time traces shows the pure frequency modulation, i.e no amplitude variation (modulation) for moderate modulation strength ε=0.1-0.5. At high modulation strength, ε=1, the over-modulation occurs. In Fig. 3.8b, the modulated time traces for the case of transverse RF field modulation as a function of the modulation strength is shown. The amplitude variation (modulation) is observed at medium modulation strength ε=0.3 and ε=0.5 and the over-modulation occurs at ε=1. The modulation strength restriction for current modulation ($\varepsilon=J_{RF}/J_{app}$) is also investigated here (Fig. 3.8c), since the current modulation will be also performed in the simulation to compare with the field modulation results, for the same parameters such as current density, magnetic field, temperature, simulation material parameters, etc. For current modulation, the modulated time traces show strong amplitude modulation and the over-modulation occurs at modulation strength of ε=0.5.

For the case of longitudinal RF field modulation, it is also shown (Fig. 3.8) that for large modulation strength (ε=0.6) at high modulation frequency f_m, this can induce non-linear effects such as a change in the trajectory (Out of Plane trajectory), see Fig. 3.9, that is not taken into account in the analytical model.

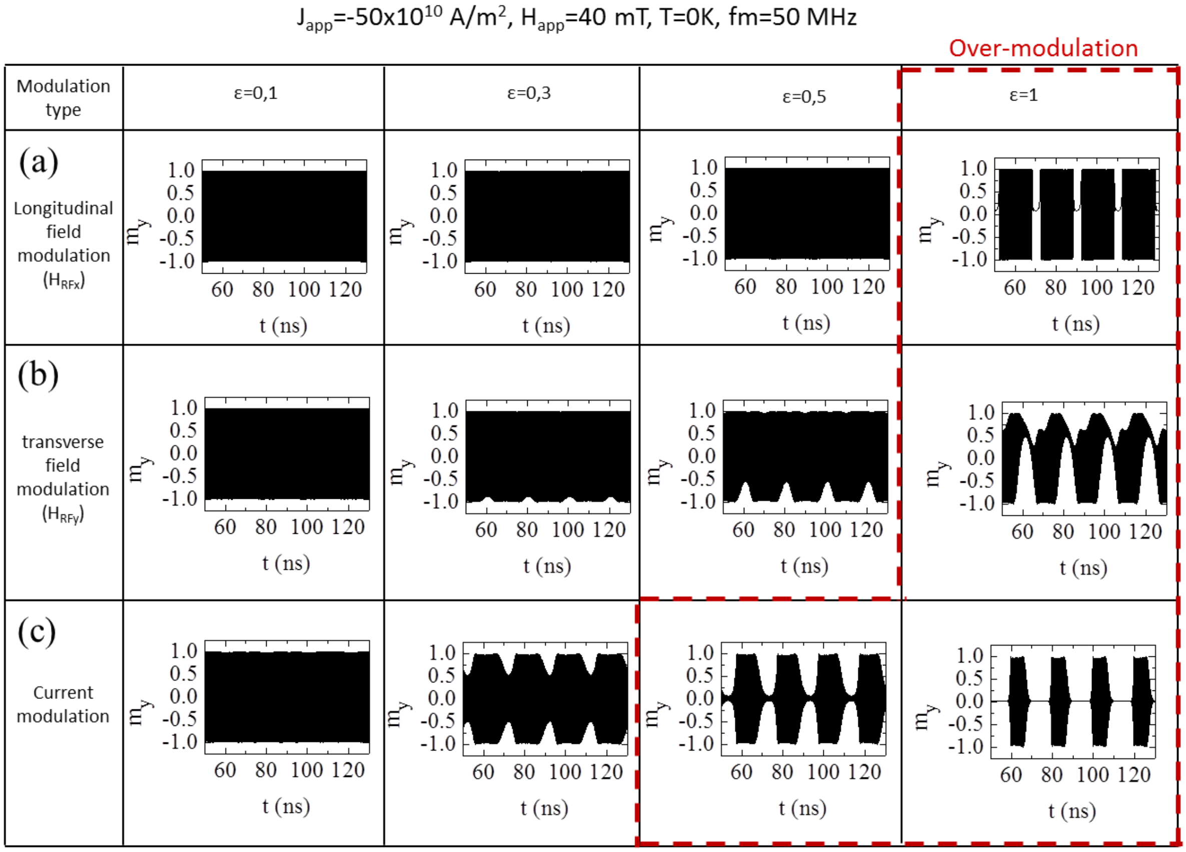

Fig. 3.8-The modulated time traces of m_y-component for different modulation strength values for the case of: (a) current modulation (b) longitudinal RF field modulation (c) tranverse RF field modulation.

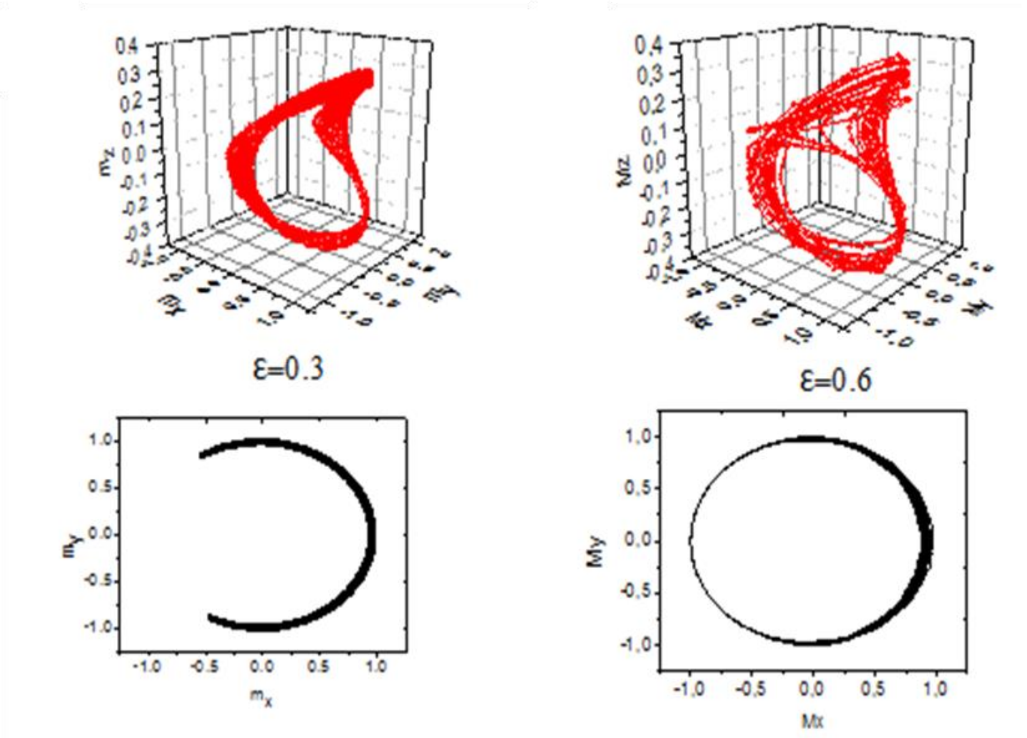

Fig. 3.9-The 3D trajectories (top) and X-Y projection (bottom) of modulated STNO for different modulation strength, ε=0.3 and ε=0.6, at fm=1GHz for the case of longitudinal RF field modulation. The free running parameters are in the range of validity of analytical model with J_{app}=-50x10^{10} A/m^2, H_{app}=40 mT, and T=50K.

To summarize, in order to avoid the over-modulation (on-off modulation) and the change in the precession trajectory, the simulation will be restricted to moderate values of ε=0.1-0.3 (varying H_{RF} at constant H_{app}). In order for modulation to occur there is no lower cut-off of H_{RF}, only the modulated amplitude will decrease as H_{RF}^2. Hence smaller H_{RF} means smaller signal to noise ratio (discussed later in the next Section). This is independent of H_{app} as long as H_{app} does not induce a modification of the type of the trajectory. To make a comparison with RF field modulation, the current modulation which is performed using the same parameters as used for field modulation simulation will be also demonstrated. The modulation strength is also restricted to moderate values of ε=0.1-0.3 (varying J_{RF} at constant J_{app}) to avoid over-modulation or on-off modulation.

3.3.2 Analysis method: Amplitude and phase noise technique

The details of the amplitude and phase noise technique of the free running STNO has been discussed in Chapter 1 and Chapter 2. In this Section, the amplitude and phase noise technique will be briefly discussed to highlight the difference between the amplitude and phase noise response of the STNO in the free running state and in the modulation state. An appropriate way of the extraction of the amplitude and phase noise of the STNO in the modulation state will be also investigated, i.e. the effect of the filtering and the welch's averaging method on the amplitude and phase noise of the modulated STNO. Finally, the extraction of the maximum modulation rate from this technique will be shown.

3.3.2.1 Free running and modulated STNO at T=0K

As has been mentioned previously, in the absence of noise (zero temperature), the magnetization of the free running STNO precesses on a constant energy trajectory around the static equilibrium point (in-plane energy minimum), as shown in Fig. 3.10a. This constant trajectory means that the magnetic component m_x, m_y, and m_z oscillate in time forever with a constant amplitude and phase (Fig. 3.10b: the m_y-component). This stable oscillation can be expressed as a function of time: $m_y(t)=m_y^0\cos(\omega_0 t)$. The m_y^0 is the amplitude and the $\omega_0=2\pi f_0$ is the angular frequency of the free running STNO.

On the contrary, in the modulation state, i.e. modulation by an RF current, at given modulation strength ε and modulation frequency f_m, the magnetization precession trajectory is modulated around the average trajectory, as can be seen in Fig. 3.10c. The corresponding magnetization oscillation of the m_y-component is given in Fig. 3.10d. It shows the amplitude modulation of the magnetization oscillation at the time period given by $T_m=1/f_m$, i.e. $T_m=20$ns.

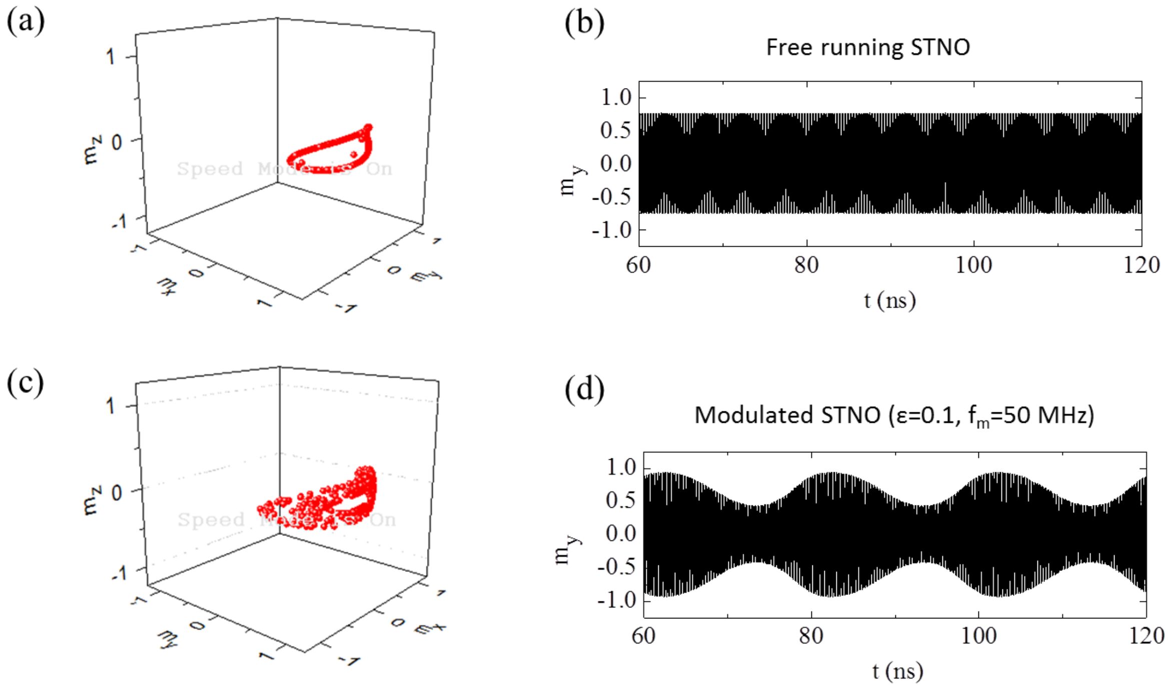

Fig. 3.10-(a) The IPP precessions trajectory (3D trajectory) of the free running STNO around the static equilibrium point (X-axis). (b) The corresponding time traces of m_y-component of the free running STNO. Modulation state: (c) The IPP precession in 3D trajectory of the modulated STNO. (d) The time traces of m_y-component of modulated STNO with modulation strength, $\varepsilon=0.1$, at slow modulation frequency, f_m=50MHz. The simulations were performed for $J_{app}=-40\times10^{10}$ A/m^2 and H_{app}=40 mT at zero temperature (T=0K). The total time traces is 42 µs, which corresponds to a frequency resolution of 23.8 kHz.

3.3.2.2 Free running and modulated STNO at finite temperature

In this part, thermal fluctuations (represented with T=50K) are added in the free running state and the modulation state of the STNO. The magnetization oscillations of m_y-component of the free running STNO and the modulated STNO under the application of thermal fluctuations are shown in Fig. 3.11a and Fig. 3.11b, respectively.

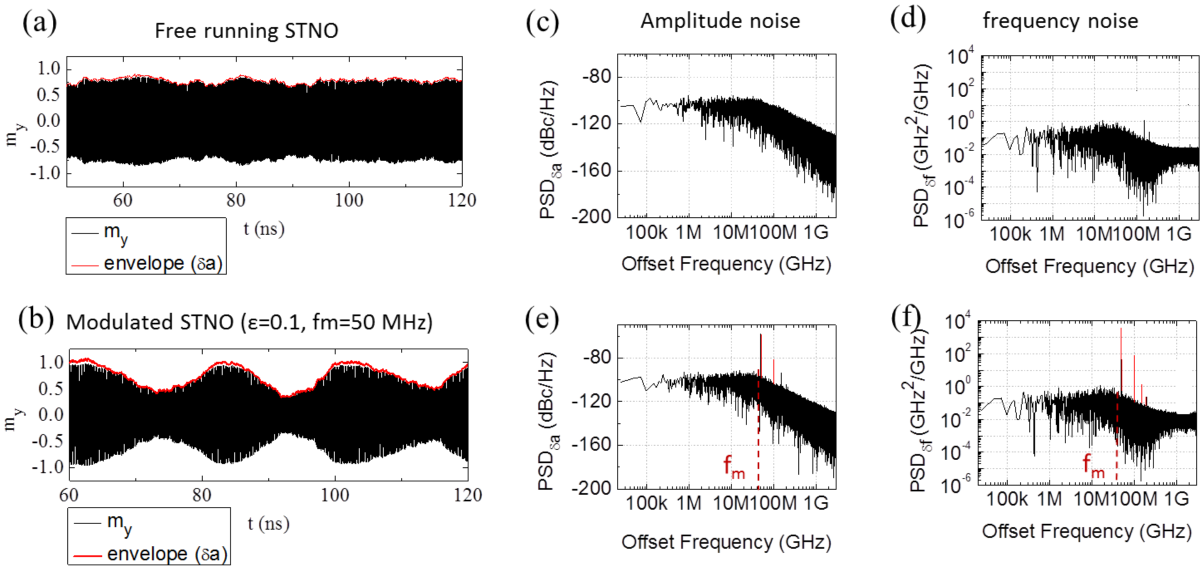

Fig. 3.11-The time traces of the m_y-component of: (a) free running STNO (black) and (b) modulated STNO (black) under thermal fluctuations (T=50K). The amplitude oscillations are fluctuating around its average value whose envelope δa(t) is shown in red curve. (c) The PSD of the amplitude noise and (d) the PSD of the frequency noise of the free running STNO at T=50K (background noise). (e) The PSD of the amplitude noise and (f) the frequency noise of the modulated STNO at T=50K. Sharp peaks (red plots) above the background noise level show the peak (and its harmonics) of the amplitude and frequency modulation. The simulations were performed for J_{app}=-40x10^{10} A/m^2 and H_{app}=40 mT.

It is shown that the magnetization oscillations are fluctuating around the average value (see red curve). These magnetization fluctuations around the average value can be expressed as a function of time: $m_y(t)=m_y^0[1+\delta a(t)]\cos(\omega_0 t+\varphi(t))$, with δa the amplitude deviations around the mean amplitude m_y^0 and φ(t) (frequency deviations, $\delta f(\mathrm{t}) = \frac{1}{2\pi}\frac{d\varphi(\mathrm{t})}{dt}$) the phase (frequency) deviations around the average phase (frequency).

3.3.2.3 Extraction of amplitude and frequency noise of STNO

The amplitude and frequency of the STNO in both state, i.e. free running and modulation states, are extracted using the technique developed in Ref. [24] and has been discussed in detail in Chapter 1 (Section 1.3.5) and Chapter 2 (Section 2.1.3). In the following, the procedure of this technique will be summarized.

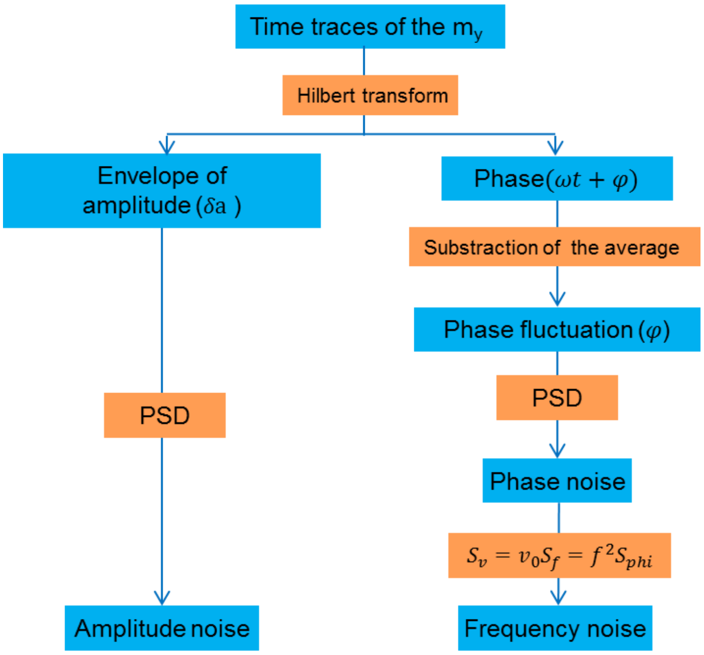

Fig. 3.12-The diagram of the amplitude and phase (frequency) noise extraction procedure

Fig. 3.12 shows the procedure of the extraction of amplitude and phase noise of the STNO, which is valid not only for the free running state but also for the modulation state. As illustrated in the diagram in Fig. 3.12, the amplitude δa(t) and the phase deviations (fluctuations) ωt+φ(t) around the average amplitude m_y^0 are extracted using the Hilbert transform (see Chapter 2, Section 2.1.3). The phase fluctuations φ(t) are extracted by subtracting the average of the phase. The corresponding power spectral densities for the amplitude fluctuations $PSD_{\delta a}$ and phase fluctuations PSD_{φ} are calculated from the Fourier transform. The phase noise is converted into frequency noise using the relation $PSD_{\delta f}=f^2PSD_{\varphi}$ [85]. Typical amplitude and frequency noise plots are shown in Figs. 3.11c,d for the free running STNO and Figs. 3.11e,f for the modulated STNO. From the plots, one can see the difference between the amplitude and frequency noise response of the STNO in the free running state and the modulation state. This difference will be discussed in the following.

In the case of the free running STNO (applying only the current density J_{app} to the STNO), the background contribution due to noise in the amplitude $PSD_{\delta a}$ and frequency noise $PSD_{\delta f}$ is shown in Figs. 3.11c,d, respectively. This background noise enables one to extract the amplitude relaxation frequency f_p from the transition from the constant (white Gaussian noise) to the $1/f^2$ dependence of the noise. For example in Fig. 3.11c, this gives an f_p value of around 42 MHz as indicated by the vertical dashed line. This is consistent with the value extracted from the analytical model, f_p=42.36MHz, as shown in table 3.2, for the same parameters: J_{app}=-40x10^{10} A/m^2 and H_{app}=40 mT.

In the presence of the modulating RF signal with a modulation strength ε and a modulation frequency f_m, an additional sharp peak and its harmonics (in red) becomes visible at the frequency f_m in the amplitude noise $PSD_{\delta a}$ and the frequency noise $PSD_{\delta f}$ above the background noise level (black) in Figs. 4.12e,f. This sharp peak corresponds to a modulated signal (modulated amplitude and frequency) whose position depends on the modulation frequency, f_m. For example, for a modulation frequency, f_m, of 1 MHz, the modulated peak will appear at f_m =1 MHz, etc. Keeping the amplitude of the modulating RF signal constant (constant modulation strength, ε) and varying the modulation frequency, f_m, then superposing the corresponding amplitude and frequency noise (for different f_m) plots together in one plot, permits the extraction of the maximum modulation rate for the modulation of an STNO. The extraction of the maximum modulation rate for field modulation in STNOs is the main purpose of this chapter.

3.3.3 Numerical simulation results and discussion

In this part, the results of numerical simulation will be shown and discussed. The discussion is divided into several parts. The first part is focused on the extraction of the maximum modulation rate of field modulation using the amplitude and frequency noise technique discussed previously. The results are compared with current modulation that is also simulated in this simulation by using the same parameters as used for field modulation. Additional studies on field modulation were also performed in this simulation:

(i) The field modulation response as a function of the angle β of the applied RF field direction with respect to the easy axis (see fig. 4.2a), which will be discussed in the second part of this Section,

(ii) The PSD modulation level dependence on the modulation strength, ε, which is important since within an FSK scheme the shifts in the instantaneous frequency depend on the amplitude of applied field H_{RF}. This will be discussed in the last part.

3.3.3.1 Enhanced modulation rates via longitudinal field modulation in STNOs

The parameters used in the simulation have been discussed in the previous Section. The magnetic field, H_{app}, is 40 mT and the current density, J_{app}, is $50x10^{10}$ A/m^2. These parameters induce the in-plane magnetization oscillations (IPP mode) around the static equilibrium point at a frequency around 5 GHz. The corresponding amplitude relaxation rate, Γ_p, of these parameters is 666.77 Mrad/s, giving rise to an amplitude relaxation frequency f_p of 212.24 MHz (see table 3.2). The temperature of 50K is taken into account as thermal fluctuations. Such temperature generates the linewidth broadening of 60 MHz around the frequency oscillations (5 GHz). To perform the field modulation, a sinusoidal RF field is added to the effective bias field whose orientation can be adjusted with respect to the easy axis (X-axis): longitudinal and transverse RF field, see Fig. 3.2a. For longitudinal RF field modulation, the modulating RF field is applied along the easy axis direction ($H_{RF}//H_{app}$). Instead, for transverse RF field, the modulating RF field is applied in-plane and perpendicularly with respect to the easy axis ($H_{RF}\perp H_{app}$). The RF field amplitude for both, longitudinal and transverse RF field, H_{RF}, is 12mT. This corresponds to a modulation strength, $\varepsilon=H_{RF}/H_{app}$, of 0.3. The RF field frequency is varied from 1 MHz to 1 GHz. For the case of current modulation, an RF current is added to the applied current density, J_{app}. The RF current amplitude J_{RF} is $-15x10^{10}$ A/m^2, corresponding to modulation strength, $\varepsilon=J_{RF}/J_{app}$, of 0.3 and its frequency is also varied from 1 MHz to 1GHz.

The simulations were performed for 42 μs time interval and the sampling frequency of $100x10^9$ point/seconds to have small enough frequency resolution (23 kHz). The amplitude and frequency noise of the modulated time traces (m_y-component) extracted according to the procedure described in the section 3.3.2. The amplitude and frequency noise response of different modulation frequency, f_m, from different simulations are superposed together in one plot as shown in Fig. 3.13. Figs. 3.13a,b show the amplitude $PSD_{\delta a}$ and frequency noise $PSD_{\delta f}$ response for current modulation, Figs. 3.13c,d shows the amplitude $PSD_{\delta a}$ and frequency noise $PSD_{\delta f}$ response for longitudinal RF field modulation, and Figs. 3.13e,f depict the amplitude $PSD_{\delta a}$ and frequency noise $PSD_{\delta f}$ response for transverse RF field modulation. The background noise is indicated by the dotted red line and the envelope of modulation peaks for all modulation frequencies is indicated by the dotted blue line as a guide to the eye.

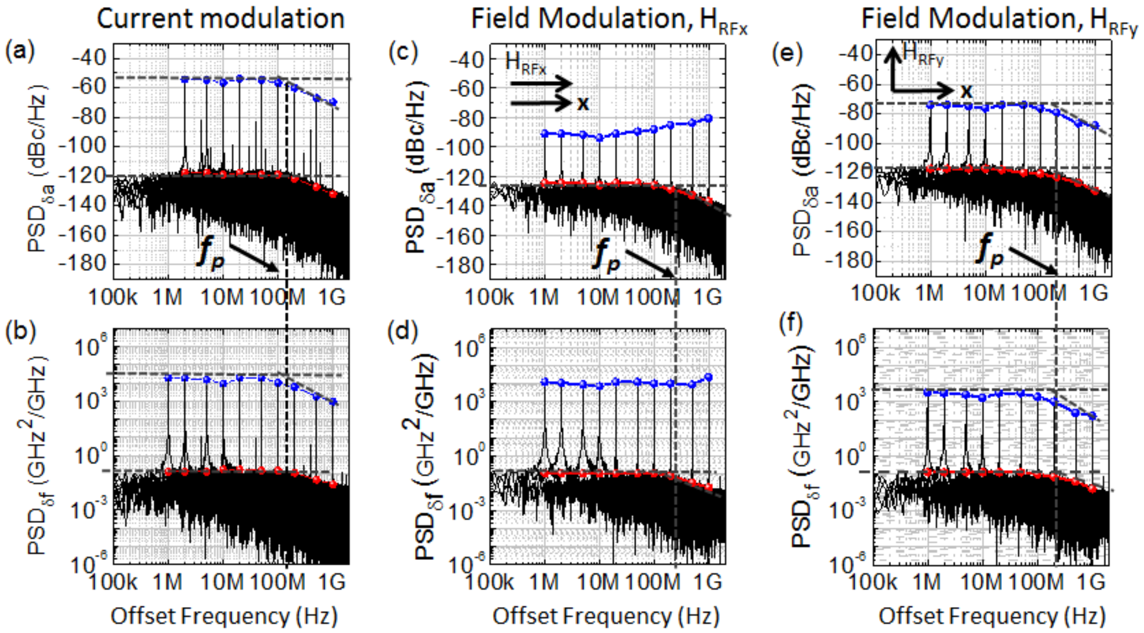

Fig. 3.13-Time traces of 42µs long was analyzed in double logarithmic plots of the amplitude noise PSD$_{δa}$ and frequency noise PSD$_{δf}$ of the modulated signal for (a,b) current modulation (c,d) longitudinal H$_{RF}$//x and (e,f) transverse H$_{RF}$//y RF fields. The current and field modulation simulation was performed with the same parameters of field modulation: H$_{app}$=40mT, J$_{app}$=-50x10^{10} A/m^2, T=50K, f$_m$=1MHz to 1GHz, and ε=0.3. The envelope of the background level due to thermal noise is indicated by the red dotted line and the envelope due to the modulation signal is indicated by the blue dotted line.

Focusing on the envelope of the modulation peaks (see the dotted blue line), different modulation responses on the amplitude noise PSD$_{δa}$ are observed for longitudinal and transverse RF modulation fields. The latter has a similar amplitude response as observed in current modulation (Fig. 3.13a), which shows a clear cut-off at f$_p$, which is on the order of a few hundred MHz (Fig. 3.13e). The consequences of the presence of this cut-off frequency can be seen in Fig. 3.14a (PSD$_{my}$ of the modulation spectrum). At modulation frequency f$_m$<f$_p$, the sidebands around the main peak (≈5 GHz) can be clearly seen. Above this cut-off f$_m$>f$_p$, the signal amplitude of the sidebands is attenuated gradually and it vanishes at high modulation frequency, i.e. f$_m$=1GHz. Since the sidebands contain the message or information carried by the carrier oscillator (STNO) that will be transferred to a receiver, the sidebands attenuation thus means loss of message or information. This is undesirable for practical applications. In contrast to this, the amplitude longitudinal RF field modulation (Fig. 3.13b) does not roll-off and even increases slightly above f$_{p.}$ Consistent with this, the frequency modulation spectrum (Fig. 3.14b, left figure) shows the sidebands are still observable even at a high modulation frequency, f$_m$=1 GHz.

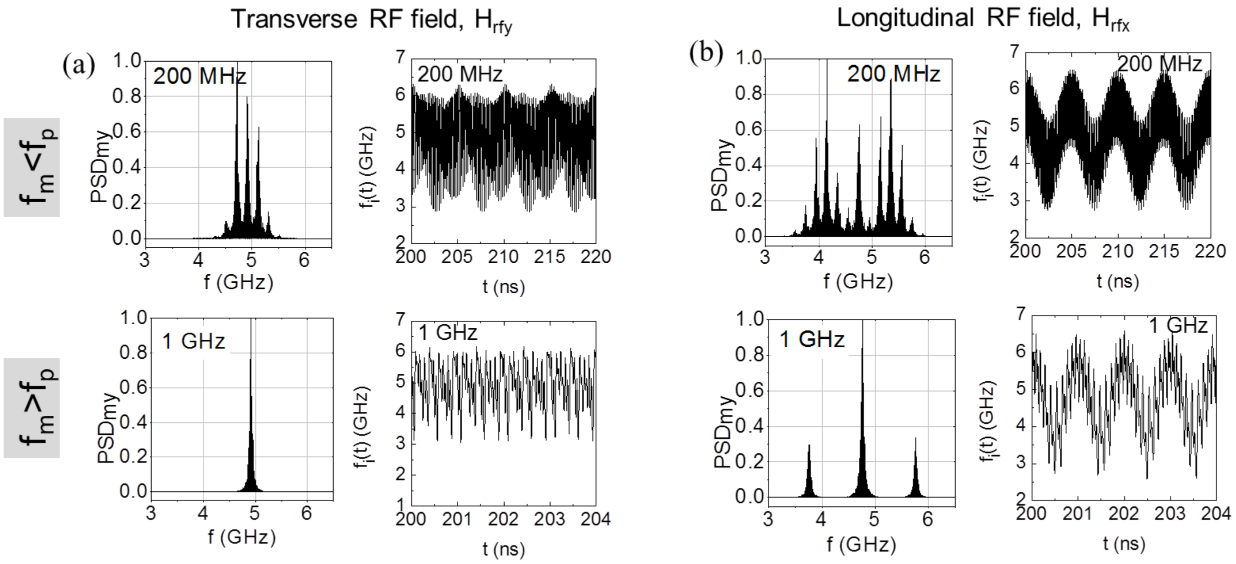

Fig. 3.14-Normalized PSD of modulated time traces of m_y-component (left) and the modulated instantaneous frequency (right) for: (a) longitudinal RF field modulation (b) transverse RF field modulation. The PSD_{my} and the modulated instantaneous frequency $f_i(t)$ of longitudinal and transverse field modulation are compared for the modulation frequency slower than the STNO relaxation frequency ($f_m<f_p$) and for the modulation frequency faster than the STNO relaxation frequency ($f_m>f_p$). It is noted that the multiple sidebands at low modulation frequencies f_m (200 MHz) arise due to high modulation index which is proportional to the ratio of the modulation strength ε and inversely proportional to the modulation frequency f_m (see Chapter 1 Section 1.4.1).

A similar observation as for the amplitude noise can be made for the frequency noise $PSD_{\delta f}$, Figs. 3.13b,d,f. First it is noted that due to the non-linear property of STNOs, amplitude and frequency are coupled. This is characterized by the coupling parameter ν. As a consequence of this coupling, the background noise level of the frequency noise $PSD_{\delta f}$ is enhanced by a factor of $(1+\nu^2)$ for low frequencies $f<f_p$ as shown by the dotted red lines in Figs. 3.13b,d,f and then cuts off for $f>f_p$. Focusing now on the envelope of the additional modulation peaks (dotted blue lines) upon field modulation, it can be seen that for transverse field modulation, Fig. 3.13f, there exists a cut-off frequency at f_p~200 MHz while for longitudinal field modulation, Fig. 3.13d, the cut-off frequency is absent. The response of the modulation in frequency is thus the same as the modulation in amplitude. As can be seen in Fig. 3.14b (right figure) for frequency modulation in longitudinal RF field modulation, a full frequency deviation can be achieved even at high modulation frequency $f_m>f_p$ (no attenuation in the modulated instantaneous frequency). In contrast to this, for transverse field modulation (Fig. 3.14a, right figure), a full frequency deviation can be achieved only at low modulation frequency $f_m<f_p$. However, the modulation frequency signal is not pure sinusoidal anymore (complex signal modulation). For a fast frequency modulation $f_m>f_p$, i.e. f_m=1GHz, the instantaneous frequency does not follow the RF field modulation and leads to the attenuation of the frequency deviation. This indicates that the maximum modulation rate of transverse RF field modulation is given by the cut-off frequency, f_p.

The absence of the cut-off frequency in the case of longitudinal modulation is important for applications, since higher modulation data rates above the STNO relaxation frequency f_p can be achieved. This can be understood that quite generally the frequency of STNOs can be changed in two ways. The first is the direct modulation of the frequency and the second is the modulation via the amplitude due to the non-linear amplitude-phase coupling. Since amplitude modulation is limited by the amplitude relaxation frequency f_p, frequency modulation via amplitude should reveal a cut-off at $f_m=f_p$. In contrast within a macrospin approach, direct modulation of the phase (frequency) should not be limited by the amplitude relaxation frequency f_p. From this it is concluded that frequency modulation via amplitude dominates in the case of transverse field modulation (with cut-off), while direct frequency modulation dominates in the longitudinal field modulation (no cut-off).

This conclusion can be substantiated by the derived analytical model for the case of longitudinal RF field modulation (Eq. 3.10) presented in Section 3.2.3. The corresponding T=0K equation for the instantaneous power deviation δp(t) and the instantaneous frequency $2\pi f_i(t)=d\phi(t)/dt$ are brought here and given as follow:

$$\delta p(t) = \varepsilon\alpha \frac{-2\gamma_0' H_{app} p_0}{\sqrt{\omega_m^2+4\Gamma_p^2}} \cos(\omega_m t - \psi) \quad \text{with the phase } \cot\psi = \frac{2\Gamma_p}{\omega_m} \tag{3.10b}$$

$$\frac{d\phi}{dt} = 2\pi f(t) = \omega_0 + N[p_0 + \delta p(t)] + \frac{A}{\omega_0}\gamma_0' H_{RFx}\cos(\omega_m t) \tag{3.10c}$$

The analytical instantaneous frequencies are plotted in Fig. 3.15 (red and green lines) and compared to the one extracted from the numerical simulation (black line). As can be seen from the analytical expression in Eq. 3.10c, the instantaneous frequency contains two contributions that modulate the frequency around the free running value $[\omega_0 + Np_0]$. First contribution arises due to the modulation of the amplitude Nδp(t) via the non-linear coupling N and the second one is directly proportional to ε and thus to the modulation field. From Fig. 3.15a, one can see that including only the variation due to amplitude modulation (red line) cannot reproduce the numerical results, while including also the direct contribution (green line) $f_i(t)$ is very close to the numerical result. This means that the frequency modulation occurs due to a direct coupling of the modulating field to the frequency. The fact that the contribution to frequency modulation coming from amplitude modulation is negligible can be explained from Eq. 3.10b showing that δp(t) is proportional not only to the strength ε of the modulating field but also to the damping parameter α. This is different to the case of current modulation discussed in the Section 3.1, where the instantaneous power δp(t) is proportional only to ε. Hence, in the given case of longitudinal field modulation even for moderate modulation field values, the deviations of δp(t) are expected to remain smaller than in current modulation since the damping is usually much smaller than one α<<1.

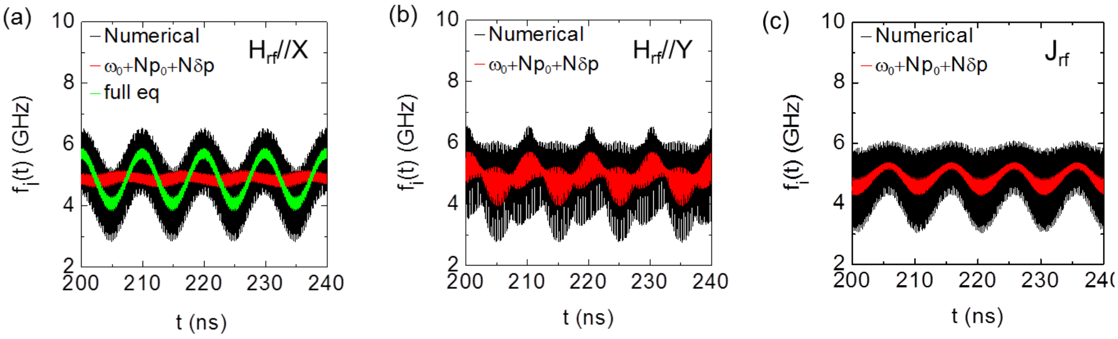

Fig. 3.15-Comparison between the numerical (black line) and analytical (red and green lines) instantaneous frequency $f_i(t)$ for: (a) longitudinal RF field (H_{RF}//X) modulation, (b) transverse RF field (H_{RF}//Y) modulation, and (c) current modulation at modulation frequency f_m=100 MHz and modulation strength ε=0.3. The red line considers only the contribution from amplitude modulation and the green line considers both amplitude and direct frequency modulation (all terms in Eq. 4.10c) for longitudinal modulation case only. The analytical evaluation was performed for H_{app}=40mT and J_{app}=-50x10^{10} A/m^2 leading to the following analytical parameters ω_0=40.5 Grad/s, N=-31.6 Grad/s and $\frac{A}{\omega_0}\varepsilon\gamma_0' H_{app} = 5.217\ \mathrm{Grad/s}$

The strength of the deviations of $\delta p(t)$ (expressed in the power spectral density of $\delta p(t)$, $PSD_{\delta a}$) can also be seen in numerical simulation results shown in Fig 3.13a and Fig. 3.13c for current modulation and longitudinal RF field modulation, respectively. It is seen that for modulation frequency below the cut-off f_p, the $PSD_{\delta a}$ of the modulated peak in longitudinal RF field modulation (30dBc/Hz above the background noise level) is much smaller than the one in current modulation (60dBc/Hz above the background noise level). This substantiates the statement from analytical expressions that the deviations of $\delta p(t)$ in longitudinal RF field modulation are indeed smaller than in current modulation. Therefore, the impact on the frequency modulation is also small for longitudinal RF field modulation. In other words modulation by a longitudinal RF field is mainly a frequency modulation rather than amplitude modulation. This explains the absence of the cut-off in the frequency noise shown in Fig. 3.13d.

The direct frequency modulation in longitudinal RF field modulation can be also understood by the fact that quite generally the precession frequency of the magnetization is given by its effective field (the conservative term in the LLGS equation) that determines the equilibrium position around which the magnetization precesses. Given the modulation field with relatively slow modulation frequency f_m as compared to the precession period, the instantaneous equilibrium is the equilibrium position determined by vector of the static bias field H_{app} and the modulation field at f_m. Modulating the effective field via an RF field parallel to the bias field, will change the conservative torque without changing the instantaneous equilibrium position and thus requires only small adaptation of the precession amplitude, see Fig. 3.16a. Consequently, the relaxation effects of the amplitude are small. This results in a direct modulation of the frequency.

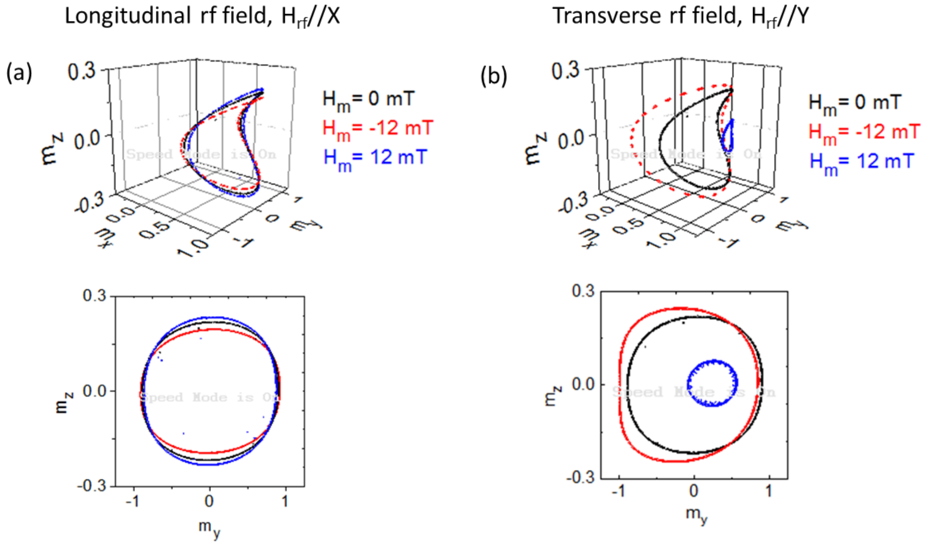

Fig. 3.16-The IPP precession trajectories in the presence of modulating RF field. The applied static field, H_{app}, is 40 mT, J_{app}=-50x10^{10} A/m^2 at T=0K. The amplitude of RF field, H_{RF}, is varied so that the changes in the trajectory can be observed for the case of (a) longitudinal RF field modulation and (b) transverse RF field modulation. The top figures are the 3D trajectories of magnetization prcessions, while the bottom figures are the corresponding Y-Z trajectory projections. The changes in the equilibrium position following by strong amplitude changes are observed in transverse RF field modulation. This is not the case for longitudinal RF field modulation in which the static equilibrium does not change and no big variation in the amplitude precession.

This is not the case for modulation by a transverse field, which will lead to a periodic motion of the instantaneous equilibrium position, since a transverse field will tilt the equilibrium. This reorientation induces much stronger changes of the amplitude as can be seen in Fig. 3.16b. Therefore the relaxation effects of the amplitude determine the dynamics much more in the transverse case than in the longitudinal case. This is why the transverse RF field case is similar to the RF current case. They share the fact that the modulation of the frequency occurs via the modulation of the amplitude which dominates. To further underline this point, one need to look back on Figs. 3.15b,c, which show similar results for respectively modulation by a transverse RF field, H_{RF}//Y and modulation by an RF current, J_{RF}. The black lines correspond to the instantaneous frequency from full numerical solution and the red lines are the contributions of the amplitude modulation through the nonlinear coupling $[\omega_0 + Np_0 + N\delta p(t)]$). In contrast to Fig. 3.15a (longitudinal RF field modulation), the results in Figs. 3.15b,c, show that the amplitude modulation via the non-linear coupling dominates in case of transverse RF field modulation and has a non-negligible contribution to the instantaneous frequency. Therefore frequency modulation will be a combination of both direct frequency modulation and amplitude modulation which have comparable strength. This explains the roll-off in this case.

3.3.3.2 RF field angle β dependence

It has been shown numerically and analytically that the modulation of the effective field in STNOs by a longitudinal RF field leads to a high modulation rate above the amplitude relaxation rate. These results provide an important strategy for applications such as in the design of FSK based communication and dynamic read head schemes. Applying this strategy means that the RF field has to be exactly collinear with the easy axis (bias field) which is difficult to realize in reality. Hence, it is important to study the field modulation in STNOs as a function of the RF field orientation, β, with respect to the easy axis, to see the limit of the β up to which the relaxation frequency f_p does not limit the modulation rate. The results are shown in Fig. 3.17. In order to make the observation easier, the envelope of modulation peak (blue dotted line in Figs. 3.17a,b) and the envelope of background noise (red dotted line in Figs. 3.17a,b) is plotted. The envelope of modulation peak and the envelope of background noise for different RF field angle, β, are shown in Fig. 3.17c and 3.17d for amplitude $PSD_{\delta a}$ and frequency noise $PSD_{\delta f}$, respectively.

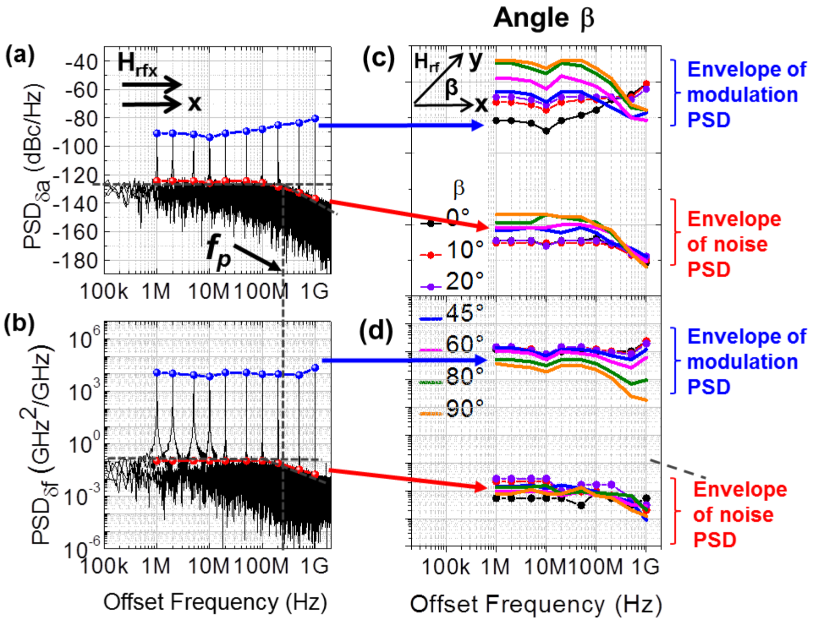

Fig. 3.17-(a,b) Double logarithmic plot of (a) amplitude $PSD_{\delta a}$ and (b) frequency noise $PSD_{\delta f}$ for longitudinal RF field modulation. The envelopes of modulation and background noise PSD of (c) amplitude noise $PSD_{\delta a}$ and (d) frequency noise $PSD_{\delta f}$ for different RF field angle β with respect to the easy axis. The group of envelopes at lower signal levels is due to thermal noise and the group of envelopes at higher signal levels is due to modulation, as indicated by the labels to the right. The full

lines with dots at β≤20° indicate modulation with absence of the roll-off, and the full lines at β>20° indicate modulation with roll-off.

The envelope of background noise PSD shows that the background noise level is independent with the variation of RF field angle. While the envelope of modulation changes with the variation of the RF field angle, i.e. the envelope level and the behavior, especially at $f_m>f_p$. The change of the envelope of modulation for different RF field angle will be discussed here:

(i) Tilting the modulating RF field up to β=20° (violet dotted lines), the amplitude and the frequency modulation have the same response (no cut-off) as observed in longitudinal RF field modulation β=0° (black dotted line).

(ii) Above β=20° (full lines), the cut-off is well pronounced.

This observation is also confirmed by investigating the dependence of the upper and lower sideband amplitude of the PSD_{my} (see Fig. 3.18a) on the RF field angle, at modulation frequency above the relaxation frequency f_m=1GHz. This dependence can be seen in Fig. 3.18b. It is shown that below β=20° the amplitude of the upper (red curve) and the lower sideband (black curve) are not changed much. Above β=20° the amplitude of both sidebands decreases sharply and vanishes above β=70°. This means that higher modulation rate due to the absence of the cut-off frequency (as observed in longitudinal RF field modulation) can be achieved for a certain range of RF field angles with respect to the easy axis direction. From this it can be concluded that within the macrospin approach high modulation rate and large modulation bandwidths (i.e. no roll-off) should be achievable even when the applied RF field is not applied exactly along the easy axis direction.

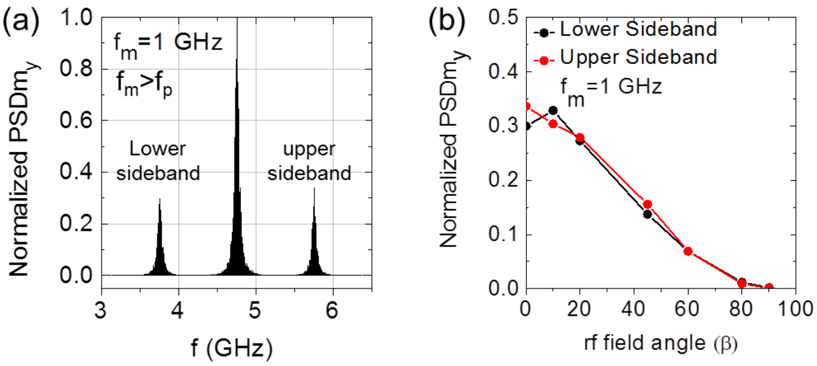

Fig. 3.18-(a) The normalized PSD of longitudinal RF field modulation with simulation parameters: ε=0.3 and f_m=1GHz. The upper and lower sideband are separated by f_m from the main peak of 4.78GHz. (b) The amplitude PSD_{my} of upper and lower sideband as a function of RF field angle.

3.3.3.3 Modulation strength ε dependence

As a final point, the dependence of the modulation peaks on the modulation strength ε, in the case of longitudinal field modulation, is considered. Figs. 3.19a,b show the envelopes for amplitude and frequency modulation peaks (upper levels) and the background noise level (lower level).

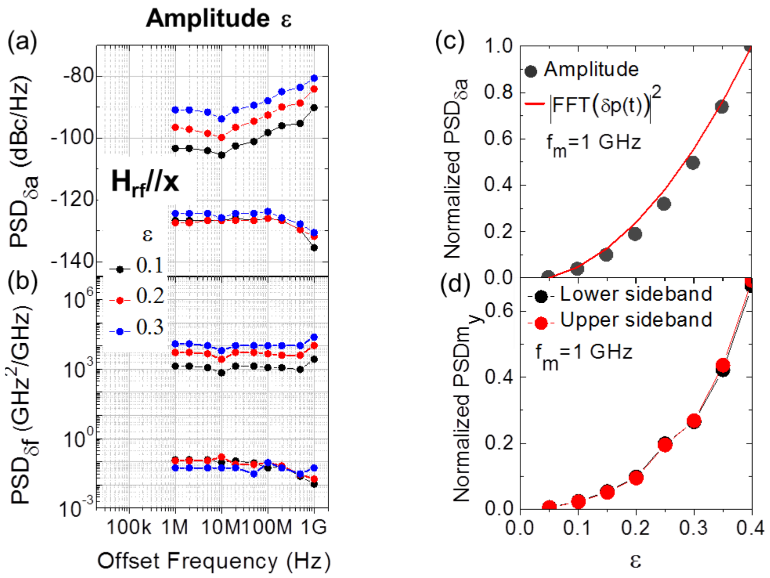

Fig. 3.19-The envelope of modulation and noise PSD of (a) amplitude $PSD_{\delta a}$ and (b) frequency $PSD_{\delta f}$ for longitudinal RF field modulation as a function of modulation strength ε. (c) The amplitude noise $PSD_{\delta a}$ at f_m=1 GHz as a function of modulation strength ε. Black dots are obtained from numerical simulation and red line is calculated from analytical model, Eq. 4.10b. (d) The amplitude PSD_{my} of upper and lower sideband as a function of modulation strength.

Increasing the modulation strength ε influences only the modulation peaks PSD while the noise backgrounds are not changed. For the case of longitudinal RF field modulation, the modulation peaks do not cut off at f_p, and even increase at higher modulation frequencies, f_m. Increasing the modulation strength ε, the amplitude and frequency modulation peak become stronger as predicted in the analytical model Eqs. 3.10b,c that both δp(t) and δf(t) are proportional to modulation strength, ε. Taking the square of the Fast Fourier transform of Eq. 3.10b at f_m=1 GHz for different modulation strength confirms that the amplitude modulation peak extracted from the amplitude noise plot is proportional to ε^2 as shown in Fig. 3.19c. The same ε^2-dependence is found for the peaks of the upper and lower sidebands of the PSD_{my} as shown in Fig. 3.19d. Increasing the modulation strength will increase the power of sidebands which means increasing the signal to noise ratio. These results are important for FSK scheme since the induced shifts in the instantaneous frequency due to shifts in the applied field (given by the RF field) should be sufficiently large to reach required signal to noise levels.

3.4 General Summary

In conclusion, the maximum achievable data rate of the frequency modulation in STNOs for different modulation configurations has been studied via macrospin simulation. This provides an important strategy for the design of FSK-based wireless communication using STNOs and how to achieve high data rates. The simulation reveals that the maximum achievable data rate of the frequency modulation by an RF current is limited by the relaxation frequency f_p of the STNO. This is due to the non-linear amplitude-frequency coupling within STNOs. For standard in-plane magnetized STNOs, this value lies on the order of a few hundred MHz and means that modulation rates of up to a few hundred Mbps should be achievable. This limit is enough for low to moderate data rate wireless communication as used in wireless sensor networks (WSNs), 10 to 100Mbps, which is targeted in this thesis. This will be explored and demonstrated in Chapter 4.

To achieve higher data rates up to Gbps for wireless communication beyond WSNs, frequency modulation by an RF field (field modulation) provides a solution. The simulation results show that the maximum data rate of the frequency modulation by an RF field is not limited by the relaxation frequency f_p of the STNO, resulting in an enhanced data rate up to Gbps. This occurs when the modulating RF field is oriented along the easy axis of the free layer (longitudinal RF field) and even for the tilted RF field angle up to $\beta=\pm20°$ with respect to the easy axis direction. The enhancement of the data rate in longitudinal RF field modulation can be understood by the fact that the frequency modulation occurs via a direct coupling of the modulating field to the frequency and not via the non-linear amplitude-frequency coupling. Other advantages of field modulation are that the frequency modulation can be performed even for zero nonlinearity, $\nu = 0$. This is not the case for current modulation that needs large nonlinearity, ν, to perform the frequency modulation since the nonlinear parameter ν is proportional to frequency tuning $N \approx df/dI$. However, the field modulation in STNOs needs an additional microstructured field placed on top of the STO device. As a consequence, the integrated chip size for wireless communication system becomes larger and potentially consumes more power. There is thus a trade-off between the data rate and the power consumption that needs to be considered when using this approach for wireless communication. The RF field modulation in STNOs is also suited for dynamic read head applications which have been proposed by Toshiba and HGST since the FSK is induced directly by the media field.

Chapter IV
FSK-based wireless communication

In this chapter, the frequency shift keying (FSK) by current in STNOs is studied and explored for wireless communication used in wireless sensor networks (WSNs). Here, the frequency shift keying is achieved by injecting the current/voltage pulse to the free running STNO such that the current experienced by the STNO varies between two discrete values, leading to a frequency shift between two discrete levels representing the two logic bits, '1' and '0'. The parameters to address are the achievable frequency shift and the maximum data rate, up to which the frequency can be shifted between two discrete levels. As discussed in Refs. 22,24 and in Chapter 3, the maximum data rate for frequency modulation via current is limited by the relaxation frequency f_p of the STNO, which is on the order of a few hundred MHz for standard in-plane magnetized STNOs investigated in this thesis (see table 2.10, Chapter 2, Section 2.4.2.2). This means that modulation rates of up to a few hundred Mbps should be achievable which is targeted here for wireless communication as used in WSNs, i.e. 10 to 100Mbps with the frequency ranging from 5-10 GHz.

To characterize the limiting data rate, numerical simulation and experimental studies of the FSK by current in standard in-plane magnetized STNOs have been performed. In the first part of this chapter, numerical simulation results of the FSK by current will be discussed. The frequency response to an abrupt change of the current pulse and the fastest data rate will be characterized by varying the rise time/fall time and the width of the current pulse. The simulation results will be used as a comparison with the FSK experimental results. In the second part, the experimental studies of the FSK on standalone STNOs for two different types of nanofabricated STNO devices, i.e. Hitachi devices and Mosaic devices, will be demonstrated. The parameters addressed here are the achievable frequency shift and the maximum achievable data rate. The results of both devices (Hitachi and Mosaic devices) will be compared and used for further optimization of Mosaic devices. In order to read back the data, the demodulation using the delay detection technique, proposed by Toshiba, was carried out numerically. In the last part of this chapter, the feasibility of STNOs within microwave systems (RF emitter) will be demonstrated. This study was performed in collaboration with the Mosaic partner, Rui Ma, from the Technische Universität Dresden (TUD). They are responsible for the design and the realization of the RF emitter. The demodulation using delay detection technique was carried out numerically to read back the data.

4.1 FSK-based Wireless Communication Concept

In wireless communication system, STNOs are potentially used as a Local Oscillator (LO) that provides the carrier frequency in GHz range. Such carrier frequency is mixed with another RF signal by using an RF mixer to obtain the intermodulation signal, i.e. frequency up and down conversion. In technical terms, the STNO has to deliver 0dBm to drive the RF mixer. However, the output power levels of the STNO are much lower than 0dBm. In addition, the phase noise of the STNO is poorer compared with those of conventional oscillators. Due to the low output power and the poor phase noise of the STNO, wireless communication by intermodulation, which uses the STNO as an LO, cannot be performed successfully. Thus, the amplitude shift keying (ASK) and frequency shift keying (FSK) for STNO-based modulation are considered, as these strategies do not require an RF mixer for wireless communication scheme. The ASK and FSK modulation can be performed directly through the same STNO devices by tuning the applied current. This leads to compact RF components and reduce the power consumption in wireless devices which is of great interest for wireless communication used in wireless sensor networks. The studies of ASK modulation of STNO by turning on and off the STNO output signal have been reported in Ref. 26-28.

In this Section, the concept of wireless communication FSK by digital current modulation in STNOs for wireless communication used in WSN will be discussed. The concept for the demodulation used here is not standard and uses an approach proposed by Toshiba for read head applications which is more suited for STNO devices characterized by a relatively large phase noise.

- **<u>FSK by digital current modulation in STNOs</u>**

The concept of FSK by digital current modulation in STNOs is shown in Fig. 4.1. In Fig. 4.1a, the STNO is employed in an emitter as a microwave source. The sequence of binary data (electrical signal) consisting of ‘1’ and ‘0’ is injected to STNO to modulate the STNO frequency, leading to a modulation of spin polarized current into two discrete levels. As a consequence, the STNO frequency f_0 is shifted between two different discrete values, higher frequency f_1 or lower frequency f_2. The mapping of binary sequence into signal waveform containing f_1 and f_2 is given in Fig. 4.1b (in time domain). This corresponds to an FSK modulated carrier signal. T is one bit period or the reciprocal of the data rate (1/T). The Power Spectral Density (PSD) of FSK modulated carrier, given in Fig. 4.1c, shows the existence of f_1 and f_2 around f_0. The frequency deviation or shift δf is defined as the difference between the higher f_1 and the lower frequency f_1. The Δf is the linewdith of the carrier frequency. The signal to noise ratio (SNR) is simply given by the ratio of the frequency shift δf to the linewidth Δf of the carrier signal f_0.

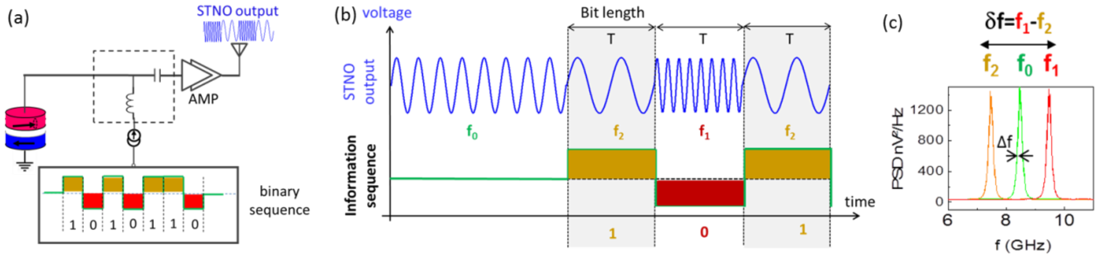

Fig. 4.1-(a) STNO emitter based on FSK modulation concept. (b) The temporal response of FSK modulated carrier waveform. The STNO frequency, f_0, is switched up, f_1, and down, f_2, depending on the data state ‘1’ or ‘0’. The data “1” corresponds to maximum pulse amplitude and the data “0” corresponds to minimum pulse amplitude at a given bit rate 1/T. (c) The Power Spectral Density (PSD) of FSK modulated carrier. The PSD contains of frequency shifts f_1 and f_2 around the carrier

frequency f_0. δf is the frequency deviation or shift (difference between f_1 and f_2). Δf is the linewidth of the carrier frequency (free running STNO).

STNO FSK demodulation

In order to read back the binary input sequence, the FSK modulation signal produced by the STNO emitter is transmitted to a receiver circuit. In this circuit, the FSK modulation signal is demodulated, allowing the frequency shift conversion into a train of voltage pulses which represents the binary sequence. For example, when the input FSK signal frequency is lower, the output voltage will be positive which corresponds to output signal '1'. When the input signal frequency is higher, the output voltage will be negative, corresponding to output signal '0'.

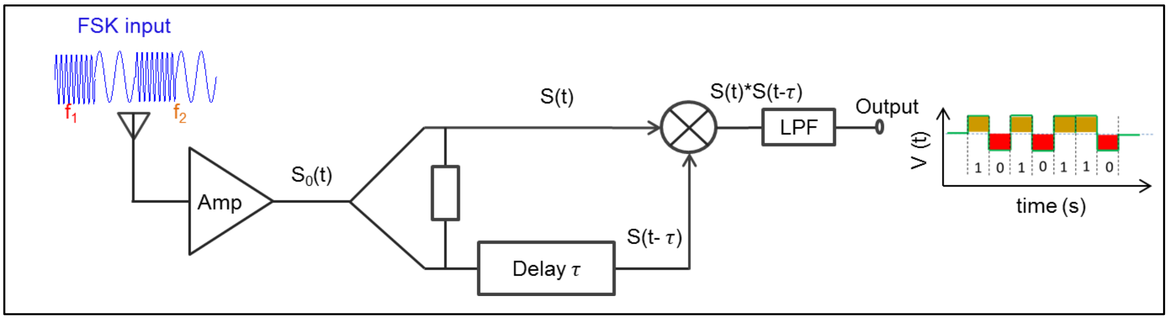

Fig. 4.2-Delay detection technique proposed by Toshiba for read head applications.

Given the poor phase noise of the signal emitted from STNOs, this would be a problem when employing the standard FSK demodulation system since long term phase noise limits the SNR and time coherency. Regarding this phase noise problem, the delay detection technique, proposed by Toshiba for read head applications provides a solution [33]. This delay detection technique does not utilize any information from the absolute phase. This means that no RF mixers with Local Oscillators are required, as can be seen in Fig. 4.2. This concept has the advantage of eliminating the problem requiring long time signal stability and less complex RF components. In this demodulation concept, the FSK signal from the emitter $S_0(t)$ is split into two parts. One part, S(t), has the same properties as $S_0(t)$, expressed in Eq. 4.1, and the other part, S(t-τ), is delayed by the time τ, expressed in Eq. 4.2. Both parts are then recombined in a mixer, S(t)*S(t-τ). The differential detection signal, S(t)*S(t-τ), involves the high frequency oscillation with the frequency of approximately $2\omega_0$. This high frequency component is then filtered out using a low pass filter (LPF). The corresponding output signal V(t) is now expressed in Eq. 4.3.

$$s(t) = s_0(t) = A\cos[\omega_0 t + \varphi(t)] \tag{4.1}$$

$$s(t-\tau) = A\cos[\omega_0(t-\tau) + \varphi(t-\tau)] \tag{4.2}$$

$$V(t) = s(t)s(t-\tau)_{LPF} = \left(\frac{A^2}{2}\right)\cos[\omega_0\tau + \varphi(t) - \varphi(t-\tau)] \tag{4.3}$$

Where:

- $\omega_0 = 2\pi f_0$ is the free running STNO frequency, i.e. no modulation.
- $\varphi(t) = \delta\omega t = 2\pi\delta f t$ is the amount of the phase (frequency) shift or change due to the presence of a current pulse modulation. The oscillation frequency shifts $+\delta\omega$ $(-\delta\omega)$ in the presence of negative (positive) pulse and the phase $\varphi(t)$ increases (decreases) linearly with time, i.e., $d\varphi = \pm\delta\omega dt$.

- $\varphi(t-\tau)$ is the delayed phase shift by the delay time of τ.
- $\varphi(t)-\varphi(t-\tau)$ is thus the phase difference over delay time τ.

Under the quadrature condition of $\omega_0\tau = 2n\pi - \pi/2$ (n is integer), the Eq. 4.3 is reduced to Eq. 4.4, such that the mixing output signal represents the sine of the change in the phase of the received signal over the delay time duration τ.

$$V(t) = \left(\frac{A^2}{2}\right)\sin[\varphi(t)-\varphi(t-\tau)] \qquad (4.4a)$$

$$V(t) = \left(\frac{A^2}{2}\right)\sin[\delta\omega\tau] \qquad (4.4b)$$

The value of delay time τ is chosen so that it satisfies the quadrature condition of $\omega_0\tau = 2n\pi - \pi/2$ and the Minimum Shift Keying (MSK) condition. In the MSK condition, which is widely used in FM communications, the phase difference $\varphi(t)-\varphi(t-\tau)$ is $\pm\pi/2$ at the boundaries of t=nτ (n:integer). This condition is imposed on the frequency difference of $\delta\omega\tau = 2\pi\delta f\tau = \pm\pi/2$. Detecting V(t) at the boundaries t=nτ, the output voltage detected at the receiver is $\pm A^2/2$ since the sine value of $\pm\frac{\pi}{2}$ is ±1. The positive or negative output voltage corresponds to the decoded bit or pulse patterns ‘1’ or ‘0’.

4.2 Numerical Analysis of FSK by Digital Current Modulation

In this Section, numerical simulations of FSK by digital current modulation in the STNO will be discussed. These simulations were performed via macrospin approach using the same material parameters as described in Chapter 3 Section 3.3.1. In chapter 3, the external source that modulating the frequency was a sinusoidal waveform (RF current or field). Here, the external source is a current pulse. The simulations were first carried out at zero temperature and for a single current pulse to observe the response of the STNO frequency to a sharp change of the pulse. The time it takes for the STNO to response the sharp change of the current pulse is investigated by varying the rise time of the current pulse while keeping constant the width and amplitude of the current pulse. The maximum data rate up to which the frequency of the STNO follows the current pulse or the frequency can be shifted between two discrete values is also characterized by varying the width of the current pulse for a constant rise time and amplitude. In order to compare with the experimental results of FSK current modulation (Section 4.3), a finite temperature was taken into account in the simulation. The frequency response to a current pulse train was also considered in this simulation to investigate its feasibility for a repetitive or periodic perturbation.

4.2.1 Numerical simulation parameters

An in plane magnetized pinned layer (PL) and free layer (FL) STNO shown in Fig 4.3a is considered in order to close with the real situations of FSK experiments. Such STNO configuration induces the in plane precession (IPP) mode around the equilibrium point given by the applied field, H_{app}. The applied current $J_{app,0}$=-45x10^{10} A/m^2 and the applied field, H_{app}=40 mT were chosen as the operating point to generate the steady state free running STNO. These parameters induce the magnetization oscillations (Fig. 4.3b) with the free running frequency of 5.25 GHz.

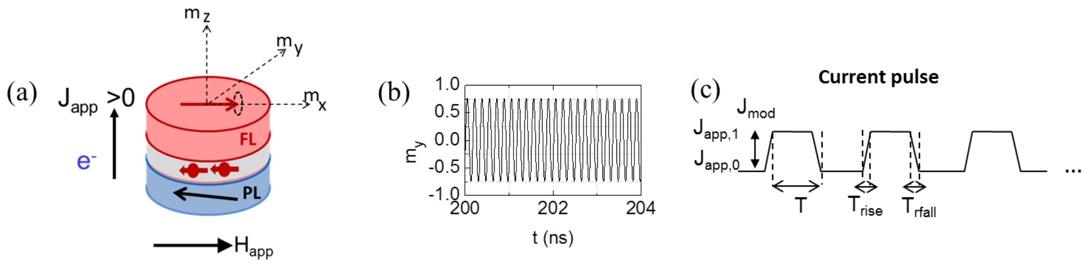

Fig. 4.3-(a) The schematic of the STNO: in-plane magnetized free layer (FL) and pinned layer (PL). (b) Time trace of the m_y component of the magnetization with a frequency of 5.25 GHz, for an applied current $J_{app,0}$=-45x10^{10} A/m^2 and an applied field H_{app}=40 mT. (c) A pulse train of the current. J_{mod} is the pulse amplitude, i.e the amplitude difference between the new state current density, $J_{app,1}$ and the initial current density, $J_{app,0}$), T is the pulse width (1/T is the pulse rate), T_{rise} is the rise time and T_{fall} is the fall time.

In order to perform the FSK modulation, a current pulse was applied to the steady state free running STNO. The amplitude, rise time, and width of the current pulse are defined as J_{mod}, T_{rise}, and T respectively, as shown in Fig. 4.3c. The application of a current pulse modulates the applied current $J_{app,0}$ into two level currents: $J_{app,0}$ and $J_{app,1}$, where $J_{app,1}$=$J_{app,0}$+J_{mod}. This leads to a frequency shift keying between the two values of f_0 to f_1 as illustrated in Fig. 4.4.

Fig. 4.4a shows the frequency current dependence of an in-plane magnetized STNO at constant applied field H_{app}=40 mT. The frequency decreases upon increasing the applied current density, J_{app}, showing normal behavior of the in-plane precession mode (redshift behavior). As can be seen in the plot, at applied current density of -45x10^{10} A/m^2 the free running frequency of the STNO is 5.25GHz. Now applying the current pulse with amplitude of J_{mod}=+5x10^{10} A/m^2, the applied current is switched down from $J_{app,0}$=-45x10^{10} A/m^2 to $J_{app,1}$=-40x10^{10} A/m^2. Consequently, the frequency of the STNO is shifted from f_0=5.25GHz (black dashed vertical line) to f_1=5.97GHz (red dashed vertical line). This frequency shift corresponds to a frequency shift keying (FSK). The corresponding power spectral density (PSD) and the magnetization trajectory are shown in Fig. 4.4b and Fig. 4.4c, respectively. The magnetization trajectory of f_0 is shown in red plot and the magnetization trajectory of f_1 is shown in black plot.

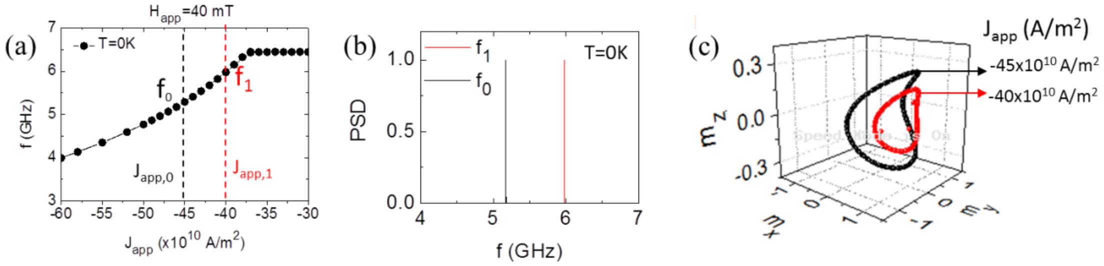

Fig. 4.4-(a) The free running frequency oscillations as a function of applied current density J_{app} at constant applied field H_{app}=40 mT. The simulation was carried out at T=0K, neglecting the thermal fluctuations in the system. In the absence of an external current pulse, the free running STNO frequency f_0 is 5.25 GHz. In the presence of an external current pulse with amplitude J_{mod}, the STNO experiences two level currents, $J_{app,0}$ and $J_{app,1}$. This leads to a frequency shift from f_0 to f_1. (b) The PSD of FSK consists of two frequencies f_0 and f_1 (c) The magnetization trajectory of the FSK.

4.2.2 Frequency response as a function of the rise and fall time of the current pulse

In this Section, the STNO frequency response to a sharp change of the current pulse will be investigated. The aim is to characterize the agility of the STNO, i.e. the time it takes for the STNO frequency to hop and stabilize to a new state given by the current pulse. To facilitate the analysis, the simulation was performed at zero temperature, neglecting the thermal fluctuations or noise in the system. The rise time and fall time of the current pulse are set to the same value, leading to a symmetric pulse. In order to study the impact of rise and fall time of the current pulse on the STNO frequency response, the rise time and fall time are varied from 2 ns to 60 ns. The pulse amplitude and the pulse width are kept constant, +5x10^{10} A/m^2 and 100 ns, respectively. The STNO response is shown in Fig. 4.5 for a rise and fall time of (a) 2ns, (b) 10ns, (c) 20ns and (d) 60ns. The graphs show the time variation of the amplitude (left) and frequency (right) of the STNO under a single positive current pulse. The time variation of the frequency is obtained from the time derrivative of the instantaneous phase extracted from the Hilbert tansform of the traces of the m_x–component (see chapter 2, section 2.1.3).

Fig. 4.5-left panels are showing the strong reduction of amplitude of the oscillation of the m_x-component (black curve) once a positive single pulse (red curve) is applied at t=50 ns for a duration of 100 ns. This amplitude reduction corresponds to a change of the applied current density from $J_{app,0}$=-45x10^{10} A/m^2 to $J_{app,1}$=-40x10^{10} A/m^2 under the application of a single positive pulse with amplitude J_{mod} is 5x10^{10} A/m^2. This amplitude oscillations reduction shows a normal behavior of STNOs since the amplitude is proportional to the applied current density. Given by the nonlinear characteristic of STNO, i.e. nonlinear amplitude-frequency coupling, the amplitude reduction induces the frequency change. Under the negative frequency-nonlinearity (df/dI< 0), the smaller the amplitude is, the higher the frequency is (see Fig. 4.4a). The reduced amplitude seen in Fig. 4.5-left panels therefore results in the

increase of the frequency (black curve) from f_0=5.25 GHz to f_1=5.97 GHz with the current pulse (red curve) as shown in Fig. 4.5-right panels.

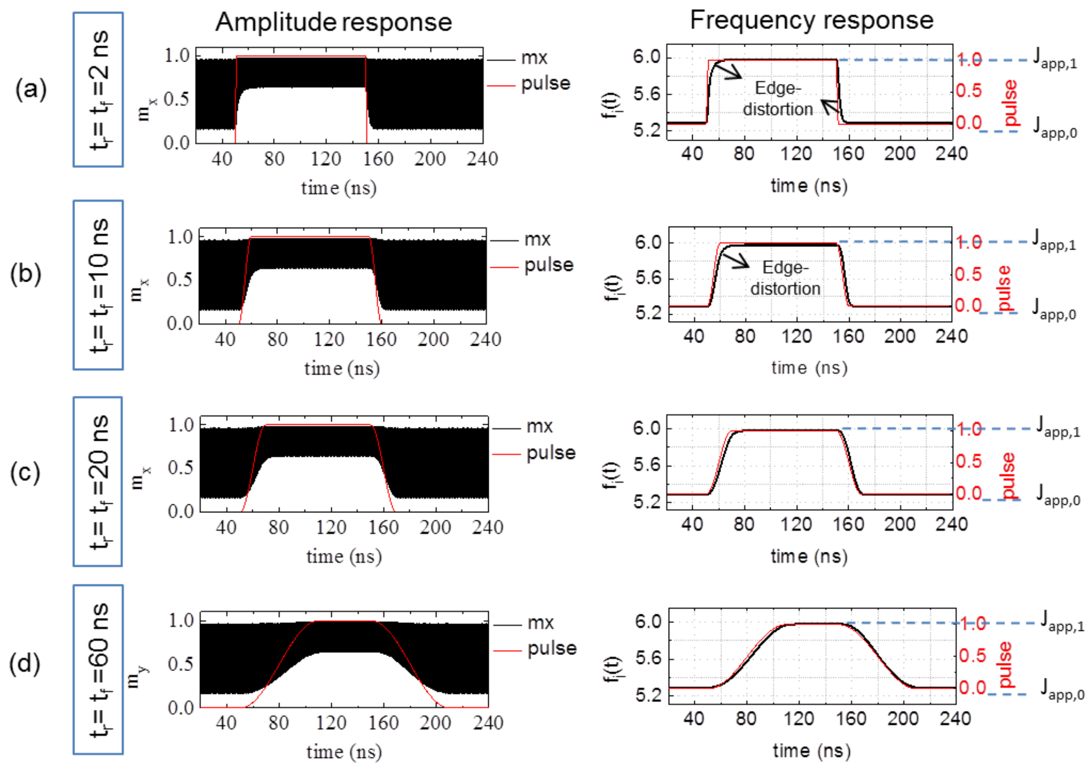

Fig. 4.5-The m_x time traces and the instantaneous frequency time variation of STNO once a pulse of current with different rise (fall) time is injected. The pulse width is kept constant at 100 ns (10 MHz). The simulation was performed at zero temperature.

As has been discussed in chapter 3, the current modulation in STNO induces simultaneously the amplitude and frequency modulation. Since the main interest of this thesis is the frequency modulation, the discussion will be concentrated in frequency response.

Now focus on the frequency response as a function of rise and fall times of the current pulse given in Fig. 4.5-right panels. For short rise and fall time shown in Fig. 4.5a, the edge distortion in the rising and falling part of the frequency response (black curve) is observed. Due to the edge distortion, the vertical edges are ‘round’ instead of ‘vertical’ (not following the rise and fall times of the current pulse). This is due to a poor high frequency response of an STNO oscillator. In other words, there is an intrinsic mechanism that limits the frequency response of an STNO toward a sharp change of an external current pulse. This limit is given by the amplitude relaxation rate of the STNO. For a larger pulse rise and fall time (Fig. 4.5b), the rise time of frequency response does not follow the rise time of the current pulse while the fall time of the frequency response nicely follows the fall time of the current pulse. This means that there is different relaxation time t_1 and t_0 of the STNO in response to a rising pulse and falling pulse, respectively. As illustrated in Fig. 4.6, the time t_1 is defined as the time it takes for the STNO to relax toward a new equilibrium state at $J_{app,1}$=-40x10^{10} A/m^2, while t_0 corresponds to the time it takes for the STNO to relax to its initial state at $J_{app,0}$=-45x10^{10} A/m^2. This different relaxation time leads to an ‘asymmetric shape’ of both amplitude and frequency response of the STNO to the current pulse. For short rise and fall times of the pulse (Figs. 4.5c,d), there is no ‘edge distortion’ in both sides of the frequency response. The STNO has time to follow the slower change of the pulse such that the time it takes for the STNO to hop from one frequency $f(J_{app,0})$ to another $f(J_{app,1})$ and vice-versa are identical (given by the rise and fall time of the current pulse). This leads to a symmetric shape of the amplitude and frequency response.

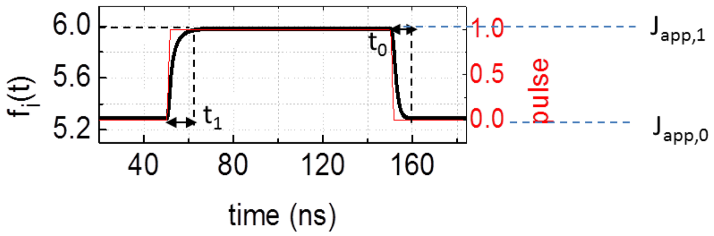

Fig. 4.6-The temporal response of STNO frequency (black curve) to a sharp single current pulse (red curve). The pulse width, amplitude, and rise time are 100 ns, $+5\text{x}10^{10}$ A/m^2, and 2 ns respectively.

From these results, it can be identified that the maximum speed of the STNO frequency in response toward a new state t_1 lies between 10 ns and 20 ns, whereas the maximum speed to relax back to its initial state t_0 lies between 2 ns and 10 ns. To extract the exact value of t_1 and t_0 (at short rise and fall time of the current pulse t_r=t_f=2 ns), the time t_1 is defined as the time window from the beginning of the modulation pulse until the steady state modulation frequency is reached. Analogously, the time t_0 is defined as the time starting from the end of the steady state modulation frequency until the initial frequency of the free running oscillator is recovered. From the calculation, the times t_1 and t_0 are 15.48 ns and 6.73 ns, respectively. This means that switching to the lower current density, $J_{app,1}$=-40x10^{10} A/m^2, (higher frequency) takes longer time than switching to the higher current density, $J_{app,0}$=-45x10^{10} A/m^2, (lower frequency). Comparing the time t_1 and t_0 with the amplitude relaxation time constant τ_p at J_{app}=-40x10^{10} A/m^2 $^{\text{and}}$ J_{app}=-45x10^{10} A/m^2 given in table 4.1, ones can see a consistency that the τ_p at lower current density J_{app}=-40x10^{10} A/m^2 is 3.75 ns which is longer than the one at higher current density J_{app}=-45x10^{10} A/m^2 (1.25 ns). From this comparison, it can be concluded that the time t_1 to switch to the lower current density $J_{app,1}$=-40x10^{10} A/m^2 (higher frequency) is characterized by the τ_p at the lower current density J_{app}=-40x10^{10} A/m^2 and vice versa. The time t_0 to switch back to its initial current density, $J_{app,0}$=-45x10^{10} A/m^2 (higher frequency) is characterized by the τ_p at the initial current density J_{app}=-45x10^{10} A/m^2. This can be understood by the fact that modulating the applied current leads to a modulation of negative damping $\Gamma\_$ (p) since the negative damping $\Gamma\_$ (p) depends on the applied current (chapter 3, section 3.1). The modulation of negative damping $\Gamma\_$ (p) thus results in the simultaneous modulation of the frequency through nonlinear amplitude-frequency coupling (Fig. 4.7a) and the amplitude relaxation rate Γ_p (Fig. 4.7b) with the corresponding relaxation time is characterized as $\tau_p = 1/2\Gamma_p$ (Fig. 4.7c). This amplitude relaxation rate Γ_p modulation explains the different relaxation times t_1 and t_0 in the amplitude and frequency response of the STNO in response to an abrupt change of the current pulse.

Table 4.1. The analytical calculation of STNO properties from Eq.1.25a and 1.25b (see chapter 1) at applied field H_{app}=40 mT for different applied current densities, J_{app}.

J_{app} (A/m^2)	F (GHz)	Γ_p (Mrad/s)	$f_p=\Gamma_p/\pi$ (GHz)	$\tau_p=1/(2\pi f_p)$ (ns)
-40x10^{10}	5.97	133.095	42.36	3.75
-45x10^{10}	5.25	399.93	127.30	1.25
-50x10^{10}	4.73	666.77	212.24	0.75

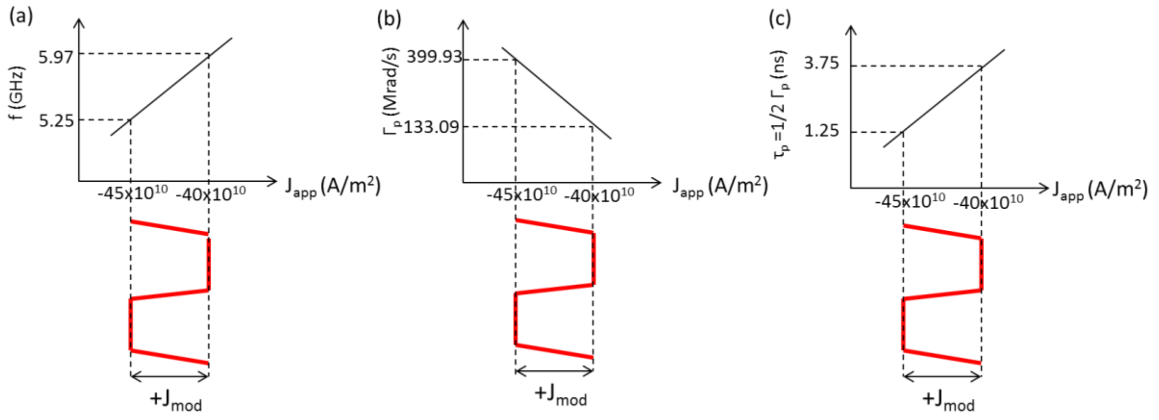

Fig. 4.7-STNO FSK modulation under a current pulse (red curve) with a positive amplitude, J_{mod}. The current pulse modulates the applied current density between two discrete values, $J_{app,0}$=-45x10^{10} A/m^2 to $J_{app,1}$=-40x10^{10} A/m^2. The current switching leads to a modulation of: (a) frequency, (b) amplitude relaxation rate Γ_p, and thus (c) amplitude relaxation time constant, τ_p.

For a further investigation of the times t_1 and t_0 and to ensure that these times are characterized by the STNO amplitude relaxation time constant τ_p, the frequency response is studied as a function of current modulation J_{mod}. The times t_1 and t_0 are calculated for different J_{mod} and compared to the relaxation time constant τ_p of the free running STNO extracted via numerical simulation for different current densities. The results are discussed in the following section.

4.2.3 Frequency response as a function of the amplitude of the current pulse

In this simulation, the parameters of the free running STNO are the same as in Section 4.2.2. The applied current density $J_{app,0}$ is -45x10^{10} A/m^2 and the applied field is 40 mT, generating the free running frequency f_0 at 5.25 GHz. The pulse width and the rise and fall time are kept constant at 100 ns and 2 ns, respectively. The pulse amplitude J_{mod} is varied from ±1x10^{10} to ±5x10^{10} A/m^2. In the presence of the current pulse, the applied current density $J_{app,0}$ is switched to a current density $J_{app,1}$. This current density $J_{app,1}$ as a function of J_{mod} is given in Fig. 4.8a. The corresponding amplitude oscillation (magnetization trajectory) is shown in Fig. 4.8b.

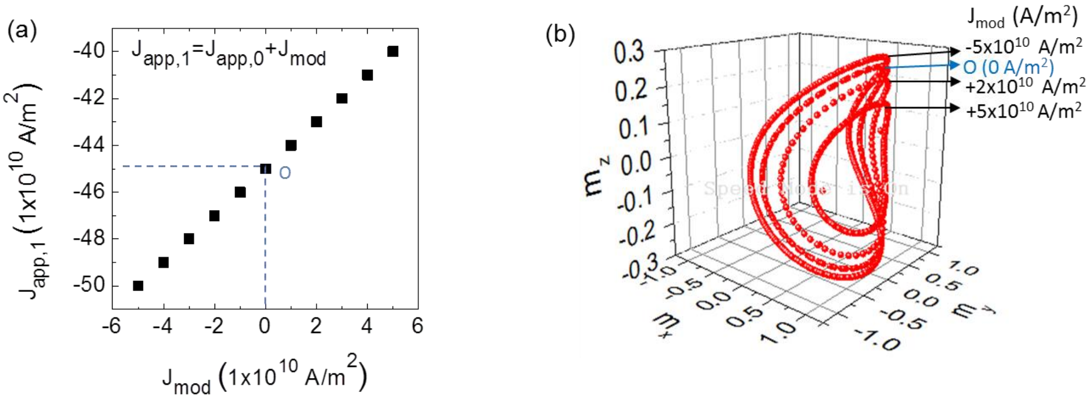

Fig. 4.8-The free running STNO is operated at applied current density $J_{app,0}$ is -45x10^{10} A/m^2 and the applied field is 40 mT. In the presence of current pulse with varying amplitude J_{mod} from ±1x10^{10} to ±5x10^{10} A/m^2, the applied current density $J_{app,0}$ is switched to a current density $J_{app,1}$. The $J_{app,1}$ is a function of J_{mod} ($J_{app,1}$= $J_{app,0}$ +J_{mod}). (a) The current density $J_{app,1}$ as a function of J_{mod} (b) The corresponding magnetization trajectory as a function of J_{mod}.

For positive current pulse, $+J_{mod}$, the initial current density $J_{app,0}$ at O point is switched to a lower current density. As a consequence, the magnetization trajectory is modulated to a lower amplitude trajectory. In contrast to this, for negative current pulse, $-J_{mod}$, the initial current density $J_{app,0}$ at O point is switched to a higher current density. This leads to a modulation of magnetization trajectory to a higher amplitude trajectory.

The modulation of current or magnetization trajectory shown in Fig. 4.8a, induces a frequency shift whose amplitude deviation depends on the pulse amplitude J_{mod}. The higher the absolute value of pulse amplitude J_{mod} is, the larger the frequency shift (the frequency deviation) is. This temporal response of frequency at different values of J_{mod} is given in Fig. 4.9a. In the absence of the pulse (J_{mod}=0), there is no variation of the instantaneous frequency as shown in black line (the free running STNO at 5.25 GHz). In the presence of the current pulse at t=50 ns for a pulse width of 100 ns, the instantaneous free running frequency f_0=5.25 GHz is shifted to a higher or lower frequency depending on the pulse amplitude J_{mod}. This frequency shift as a function of current switching $J_{app,1}$ ($J_{app,1} = J_{app,0}+J_{mod}$) is given in Fig. 4.9b with the initial frequency of free running STNO is labeled as O.

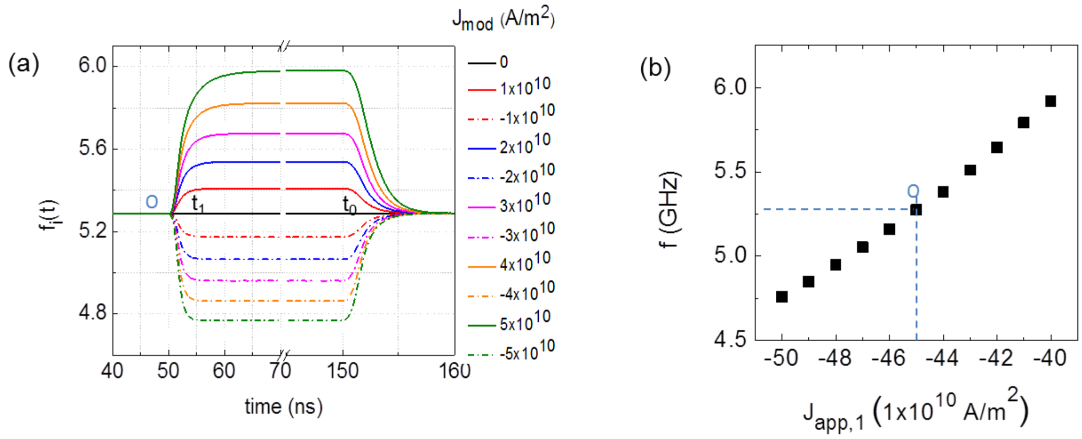

Fig. 4.9-(a) The temporal response of frequency at different values of the current modulation J_{mod}. The times t_1 and t_0 are the time window for which the STNO follows the current pulse modulation as defined in Fig. 4.6. (b) The frequency shift extracted from temporal response of frequency as a function of $J_{app,1}$ (J_{mod}). O is the free running STNO in the absence of J_{mod}. In the absence of J_{mod} (J_{mod} =0), the applied current is =-45x10^{10} A/m^2 which induces the free running frequency f_0 at 5.25 GHz.

The times t_1 and t_0 are extracted from temporal response of frequency at different pulse amplitude J_{mod}. As defined in Section 4.2.2, the time t_1 is the time it takes for the STNO to relax from its initial free running frequency f_0 toward a new steady state modulation frequency f_1 given by the corresponding current switching $J_{app,1}$ ($J_{app,0}+J_{mod}$). The time t_1 is calculated as the time window from the beginning of the modulation pulse until the steady state modulation frequency f_1 is reached. Analogously, the time t_0 corresponds to the time it takes for the STNO to relax back to its initial frequency of the free running STNO f_0=5.25 GHz. The time t_0 is calculated as the time starting from the end of the steady state modulation frequency f_1 until the initial frequency of the free running oscillator f_0 is recovered. The extracted times t_1 (blue dotted line) and t_0 (red dotted line) at different J_{mod} are compared with the amplitude relaxation time constant τ_p (black dotted line) of the free running STNO, which is extracted via numerical simulation for different current densities free running state. The comparison is shown in Fig. 4.10a.

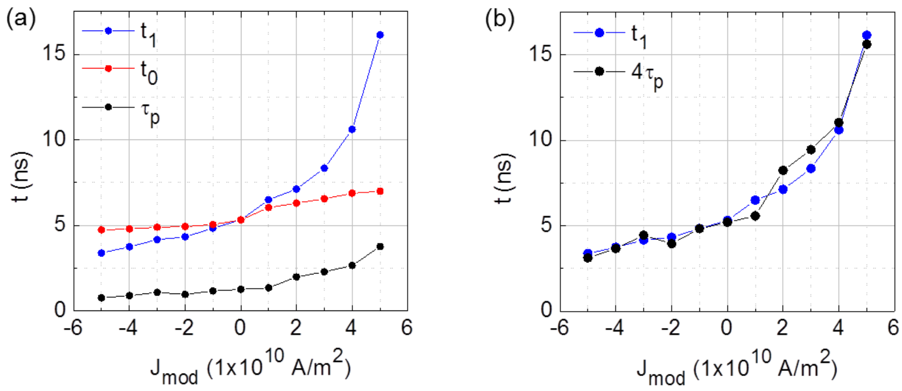

Fig. 4.10-(a) The times t_1 (blue dotted line) and t_0 (red dotted line) as a function of current pulse amplitude J_{mod} are compared with the amplitude relaxation time constant τ_p of the free running STNO at different current densities. (b) The values of time t_1 are closed to the τ_p by scaling the τ_p with a constant $(t_1 \approx 4\tau_p)$.The t_1 is calculated as the time window from the beginning of the modulation pulse until the steady state modulation frequency is reached. The time t_0 is calculated as the time starting from the end of the steady state modulation frequency until the initial frequency of the free running oscillator is recovered. The amplitude relaxation time τ_p is the time constant of exponential response of the free running STNO in response to a small perturbation. The τ_p is extracted from numerical simulation (exponential fitting of amplitude autocorrelation function) for different currents in the free running state.

From Fig. 4.10a, the time t_1 (blue dotted line) shows an exponential decrease as the J_{mod} is varied from +5x10^{10} A/m^2 to -5x10^{10} A/m^2. Such exponential decrease is also observed for the amplitude relaxation time constant τ_p (black dotted line) of the free running STNO, extracted at different current densities from J_{app}=-40x10^{10} A/m^2 to J_{app}=-50x10^{10} A/m^2. Scaling the τ_p by a constant, i.e. $t_1 \approx 4\tau_p$, one can obtain that the values of time t_1 are closed to the values of the τ_p, as shown in Fig. 4.10b. This indicates that the time t_1 for STNO to switch from its initial current density $J_{app,0}$ (initial frequency f_0) to the new current density $J_{app,1}$ (steady state modulation frequency f_1) is characterized by the τ_p at the new current density $J_{app,1}$ itself. Whereas, the time t_0 (red dotted line) to return to its initial current density $J_{app,0}$ (initial frequency f_0) is determined by the τ_p at the initial current density $J_{app,0}$. This is shown by a small variation of t_0 as a function of the pulse amplitude J_{mod}.

From the results obtained in Section 4.2.2 and 4.2.3, it can be concluded that the pulse modulation of the current in STNO leads to a modulation of the current density and thus the STNO intrinsic properties such as the amplitude relaxation rate Γ_p. The modulation of Γ_p stabilizes the amplitude or the output power of STNO between two states. Due to the non-linear amplitude-frequency coupling, the STNO frequency is also stabilized between two frequencies leading to a frequency shift keying. Under an abrupt change of the current pulse (a short rise time), the time it takes for the STNO to switch from one frequency to another and vice versa, t_1 and t_0, are different, depending on the amplitude relaxation rate Γ_p or its corresponding relaxation time τ_p at both states. Extracting the times t_1 and t_0 as a function of the amplitude of the current pulse J_{mod} one can observe that the time t_1 it takes for the STNO to switch from one frequency to another is characterized by the amplitude relaxation time τ_p at the new frequency state. While, the time t_0 for the STNO to relax back to its initial frequency is characterized by the amplitude relaxation time τ_p at its initial frequency state. These results provide an important strategy for ASK and FSK modulation of the STNO to achieve high modulation rate:

i) The higher current pulse amplitude J_{mod}, the larger amplitude and frequency shift. The maximum frequency shift can be achieved depends on the frequency tunability of the STNO, df/dI.

ii) Switching to a higher current density, the amplitude relaxation time constant τ_p of the STNO become shorter (higher amplitude relaxation rate Γ_p), leading to a faster frequency transition time or data rate.

4.2.4 Frequency response as a function of the pulse width

In this Section the impact of the pulse width, T, on the frequency response under an abrupt change of the current pulse (a short rise time) is investigated. The free running STNO induces the frequency f_0 at 5.25 GHz under the applied current density $J_{app,0}$ of -45x10^{10} A/m^2 and the applied bias field H_{app} of 40 mT. The rise (fall) time and the amplitude of current pulse are kept constant at 2 ns and 5x10^{10} A/m^2, respectively. The pulse width T is varied to be longer and shorter compared to the transition time of the frequency $t_1 \approx 4\tau_p \approx 15\,ns$ (discussed Section 4.2.2 and 4.2.3). The frequency response of the STNO at different pulse widths T is given in Fig. 4.11. The STNO frequency is shifted from its initial free running frequency f_0 at 5.25 GHz to a steady state modulation frequency f_1 at 5.97 GHz. The amplitude of the frequency shift or deviation, δf, is thus given by the difference between these two frequency levels, $\delta f = |f_1 - f_2|$.

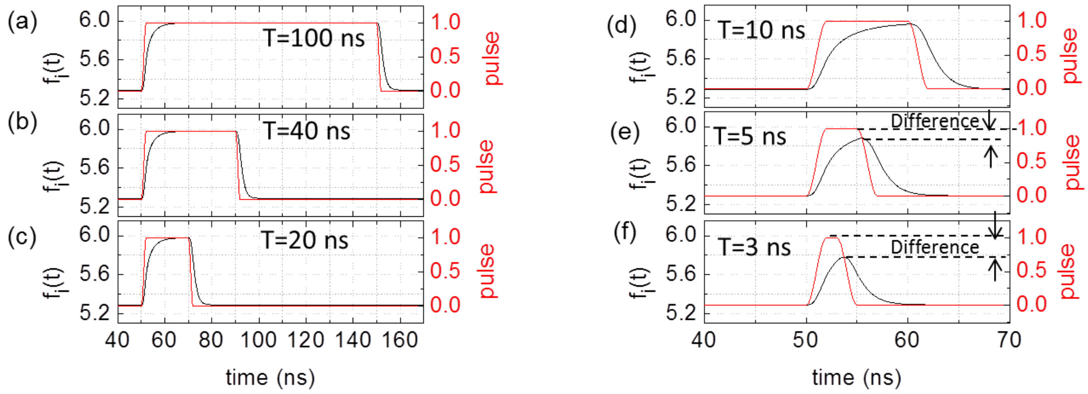

Fig. 4.11-The frequency response (black curve) to a positive current pulse (red curve) for a pulse width T of (a) 100ns, (b) 40ns, (c) 20ns, (d) 10ns, (e) 5ns, and (f) 3ns. The current pulse amplitude is J_{mod}=+5x10^{10} A/m^2, switching the initial current $J_{app,0}$=-45x10^{10} A/m^2 to a lower current $J_{app,1}$=-40x10^{10} A/m^2. The frequency is thus shifted from f_0=5.25 GHz to f_1=5.97 GHz. The simulations have been carried out at zero temperature.

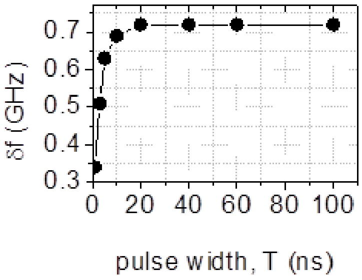

Fig. 4.12-The frequency shift δf as a function of the pulse width, T.

As given in in Figs. 4.11a,b,c. for the pulse width T longer than the frequency transition time t_1 (≈15ns), the STNO has sufficient time to reach and stabilize toward the steady state modulation frequency f_1 at 5.97GHz. This results to a full frequency shift, δf=0.72GHz. In contrast to this, when the pulse width is shorter than t_1 (15ns) as shown in Figs. 4.11d,e,f, the

STNO does not have sufficient time to reach and stabilize toward the steady state modulation frequency f_1 at 5.97 GHz. The frequency is forced to relax back to its initial state at f_0 (5.25 GHz) before reaching the steady state modulation frequency f_1 (5.97 GHz). Therefore, the resultant frequency deviation δf is less than its maximum input frequency (f_1=5.97 GHz). The shorter the pulse width, $T<t_1$, the higher the frequency difference (loss). This leads to a reduction of the amplitude of frequency shift δf. As given in Fig. 4.12, the frequency shift δf as a function of the pulse width, T, shows that the amplitude of frequency shift δf rolls off at approximately T≈15ns. This means that below 15ns a full frequency shift (δf=0.72GHz) cannot be achieved. The maximum achievable modulation rate, at which a full frequency shift δf can be achieved, is thus limited by the frequency transition time t_1 (≈15ns), with the corresponding modulation rate $1/t_1$ (≈66 Mbps).

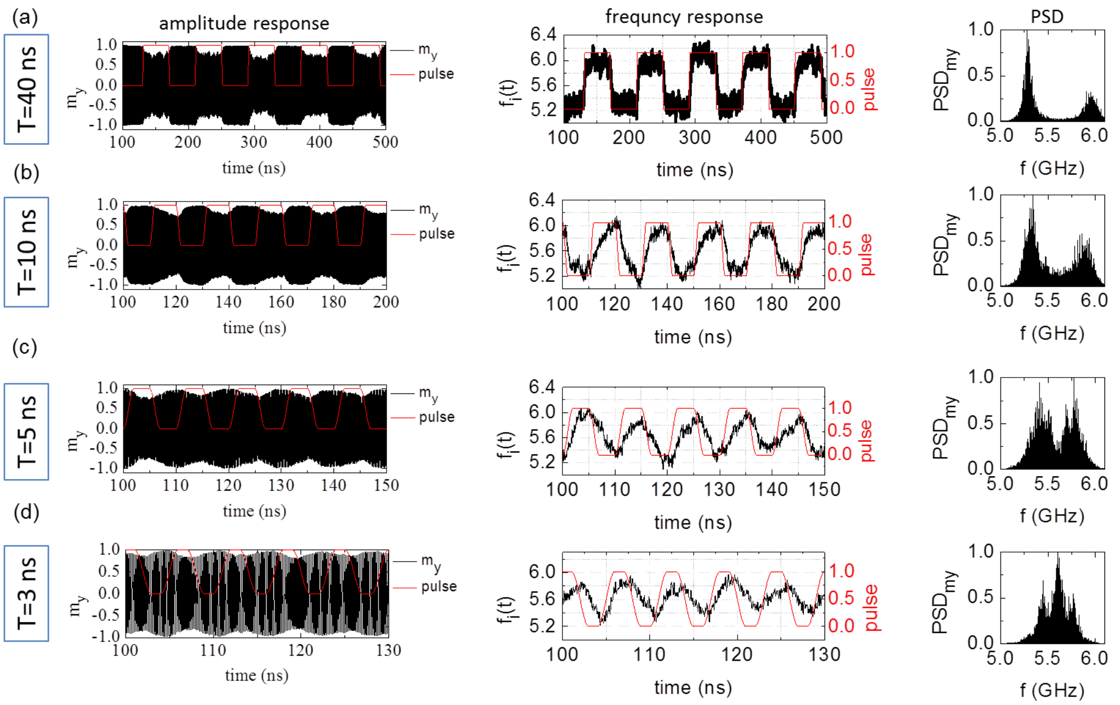

Fig. 4.13- The m_y time traces of amplitude (left), frequency response (middle) and the PSD of m_y time traces (right) for a pulse width T of (a) 40ns, (b) 10ns, (c) 5ns, and (d) 3ns. to a periodic current pulse (red curve)The free running current density is set to $J_{app,0}$=-45x10^{10} A/m^2 and the applied field is set to 40 mT. The amplitude and the rise (fall) time of periodic current pulse are set to J_{mod}=+5x10^{10} A/m^2 and 2 ns, respectively. The temperature is set to 50K.

In order to compare with the FSK measurement results, which will be discussed in Section 4.3, similar numerical calculations for different pulse widths T as the previous discussed have been carried out, but this time taking into account the thermal fluctuations (T=50K) and applying a periodic current pulse instead of a single current pulse. The results are summarized in Fig. 4.13. In the presence of noise, both amplitude (left panels) and frequency (middle panels) response fluctuate around its average value. Taking the power spectral densities (PSD) of the m_x-time traces, these amplitude and frequency fluctuations result in a finite linewidth around the center frequency (right panels). As explained previously, for a long pulse width ($T>t_1$), (see Fig. 4.11a), the STNO has sufficient time to stabilize from one frequency to another frequency periodically, which results in a clear frequency shift (with a maximum amplitude of frequency shift, δf=0.72GHz) in the instantaneous frequency time variation. The corresponding PSD contains two peaks at f_0=5.25 GHz and f_1=5.97 GHz which can be clearly distinguished. The first peak has higher amplitude than the second one because the first peak corresponds to a higher current density which is -45x10^{10} A/m^2 (larger amplitude of the magnetization trajectory). Instead, for shorter pulse widths ($T<t_1$), the STNO

does not have sufficient time to stabilize from one frequency to another periodically (Figs. 4.11a,b,c). The amplitude of the frequency shift δf becomes smaller as the pulse width T is shortened. Therefore the peaks f_0 and f_1 are approaching to each other (see the PSD of the m_x-time traces). At pulse width T=3 ns, the peaks cannot be resolved since the signal (the frequency deviation) is too small compared to the noise (linewidth of the peaks).

4.2.5 Summary

A systematic numerical simulation of the FSK current modulation has been done. The analysis was carried out by extracting the temporal response of STNO frequency to a current pulse. The important messages of the simulations are summarized as follow:

- High frequency tunability df/dI and small linewidth Δf are important criteria of STNOs to realize a successful FSK modulation, i.e. a clear frequency shift.
- The higher current pulse amplitude J_{mod}, the larger amplitude and frequency shift. This is of interest for both ASK and FSK modulation to achieve high signal (large frequency shift) to noise ratio.
- The STNO relaxation time τ_p limits the frequency transition time and thus the modulation rate. Modulating the STNO faster than its relaxation time, i.e. pulse width T shorter than the τ_p, will result on a reduction of the amplitude of the frequency shift, δf, which is not desired for applications.
- Switching to a higher current level leads to a shorter relaxation time τ_p which means that the modulation rate is higher. For the applicability of the STNOs, a high modulation rate is desired.

4.3 FSK measurements on Standalone STNOs

In this section, the experimental demonstration of the FSK measurement on standalone STNOs under digital current modulation will be discussed. The FSK measurements have been carried out for two different types of nanofabricated STNO devices:

(i) The STNO devices that were nanofabricated by Hitachi Global Storage Technologies (HGST) Inc. and which have already been discussed in Chapter 2.

(ii) The STNO devices that were realized within the Mosaic project (see Chapter 2).

The parameters addressed here are the achievable frequency shift and the maximum achievable data rate, up to which the frequency can be shifted between two discrete levels. The results of both devices (Hitachi and Mosaic devices) will be compared and used for further optimization of Mosaic devices. In order to read back the data, the demodulation using the delay detection technique, proposed by Toshiba [33], was carried out numerically. Before summarizing the FSK results of both devices, the experimental setup of the FSK measurement will be discussed.

4.3.1 Experimental setup

The experimental setup of FSK measurements is shown in Fig. 4.14. At the first step, a dynamic characterization of the STNO using standard radio frequency setup, as discussed in Chapter 2 Section 2.1.1, is necessary in order to find the optimum conditions to achieve steady state oscillations of the STNO and to ensure the FSK modulation. For this characterization, the DC current supplied by a source meter (Keithley 2401) is injected into the STNO through the inductance part of the bias-T (Marki Microwave BTN-0040). The magnetic field, H_{DC}, generated by a magnetic coil is applied in the in plane direction whose direction with respect to the pinned layer of the STNO can be adjusted to find an optimum dynamic oscillation. The output signal of the STNO is amplified by a power amplifier Miteq AMF-5D with a 43 dB gain over 100 MHz to 12 GHz, connected to a 3-10 GHz bandpass filter. A splitter or power divider is used to split the signal which is monitored by sampling oscilloscope Textronix DPO72004 with a single shot capability of 50 Gs/s and a spectrum analyzer Agilent PNAE8363B with a bandwidth of 1 MHz to 40 GHz. In order to find the operational conditions of current and field that yield steady state oscillations of the magnetization, the current and fields are swept and the output signal from the spectrum analyzer is analyzed in view of its linewidth and power. A low linewidth, large output powers and a large frequency-current tunability df/dI are desired for a successful frequency modulation.

Once the best working conditions of the STNO is determined, an additional current/voltage pulse generated by a signal generator Tektronix AWG4000 is injected into the STNO to modulate the steady state oscillation of the STNO. The signal generator Tektronix AWG4000 generates a current/voltage pulse with a relatively short rise and fall time (800 ps). The pulse frequency can be varied in the range of 1μHz to 330MHz (for 50% duty cycle). The output modulated RF signal is separated from I_{DC} by a bias-T. A 3dB attenuator is positioned between the bias-T and the 50Ω RF components to reduce the standing wave due to the impedance mismatch between the high STNO resistance, $R_{STNO}\approx100\Omega$, and the 50Ω RF components. The output signal is amplified by a 43dB amplifier and filtered by a 3GHz High Pass Filter (HPF). The purpose is to reject the low frequency noises that arise from the RF components. The filtered signal is measured and registered using both the spectrum analyzer and the oscilloscope. The spectrum analyzer and oscilloscope parameters are the same as in the dynamic characterization in Chapter 2.

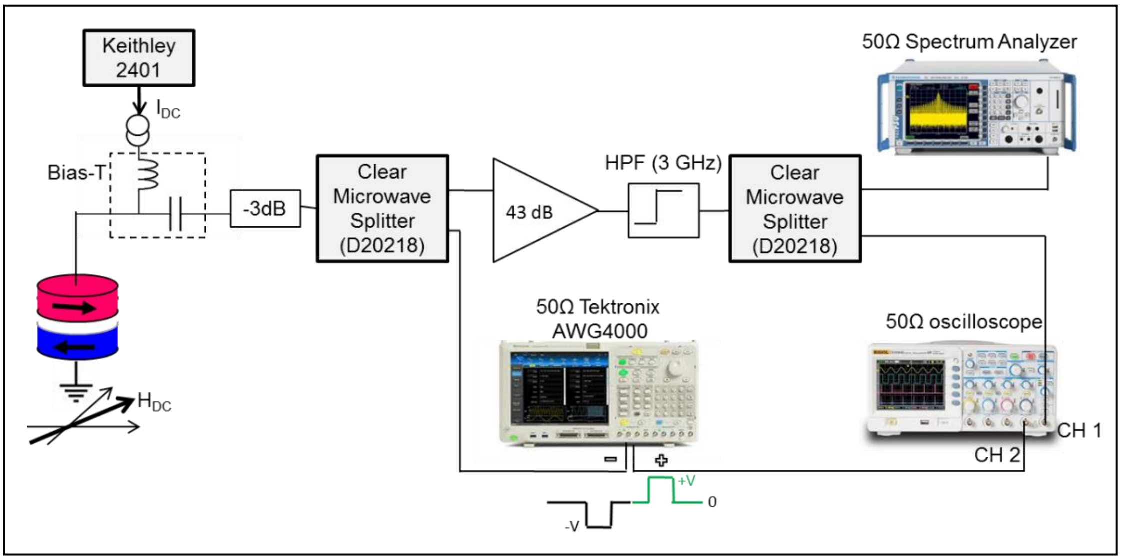

Fig. 4.14-Experimental setup for FSK modulation measurements.

Pulse characterization

As can be seen in Fig. 4.14, a digital current/voltage pulse generated by a signal generator Tektronix AWG4000 is applied to the STNO via the RF components. These lead to an attenuation or a change of the current pulse properties (rise time, amplitude, etc) due to the RF component specifications. Thus it is important to characterize the voltage pulse sent through the STNO before performing the FSK measurements. This pulse characterization provides a correction or estimation of the pulse which has to be applied to the STNO in order to achieve the optimum frequency shift keying. Following is the characterization procedure:

- **Test 1: Pulse – RF cable – oscilloscope**

In the first test, the negative and positive pulse output signal from the same channel of the pulse generator are connected to different output channels of the oscilloscope. As shown in Fig. 4.15, the negative pulse (black) is connected to the channel 3 (CH3) of the oscilloscope and the positive pulse (green) is connected to the channel 2 (CH2) of the oscilloscope. The RF cables, which are used to connect the negative and positive pulse to the output channels of the oscilloscope, have approximately the same cable length to minimize the delay (phase shift) between the negative and the positive pulse. The negative pulse (black) connected to the CH3 will correspond to the pulse felt by the STNO, while positive pulse (green) connected to CH2 will be kept as an indicator or reference of the direct output signal of the pulse generator.

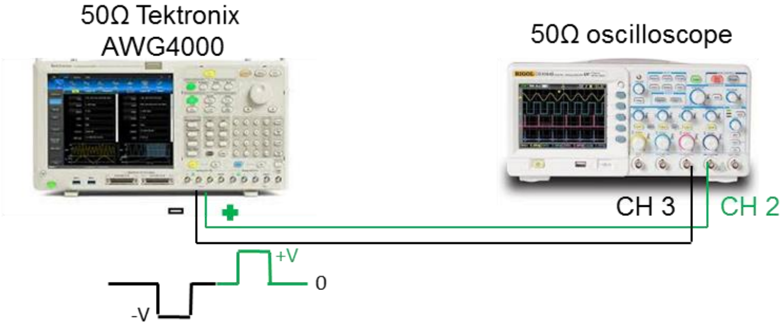

Fig. 4.15-Schematic of the first pulse characterization: Pulse - RF cable – oscilloscope. The negative (black) and positive pulse (green) from signal generator (the same channel) are connected to output channels of the oscilloscope by using the same RF cable length.

The negative (black) and positive pulse (green curve) observed in different output channels, CH3 and CH2, of the oscilloscope show the same pulse characteristics as given in Fig. 4.16. The pulse width T is 50 ns (the pulse rate 20MHz), the pulse period T_p=2T is 100 ns (the pulse frequency 10MHz), the rise time and the fall times are each 800 ps, and the pulse amplitude is ±40mV. There is no phase shift between negative and positive pulse.

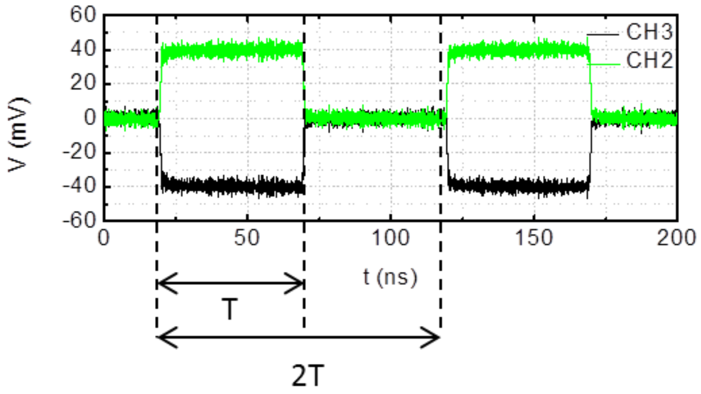

Fig. 4.16-The negative (black curve) and positive pulses (green curve) observed in different output channels of the oscilloscope. T corresponds to the pulse width (1/T is the pulse rate). 2T corresponds to the pulse period (1/2T is the pulse frequency).

- **Test 2 : Pulse – RF cable – <u>splitter (Clear Microwave D20218)</u> – oscilloscope**

In the second test, a power splitter Clear Microwave D20218 is added into the negative pulse chain as shown in Fig. 4.17. The pulse parameters are the same as used in the first test.

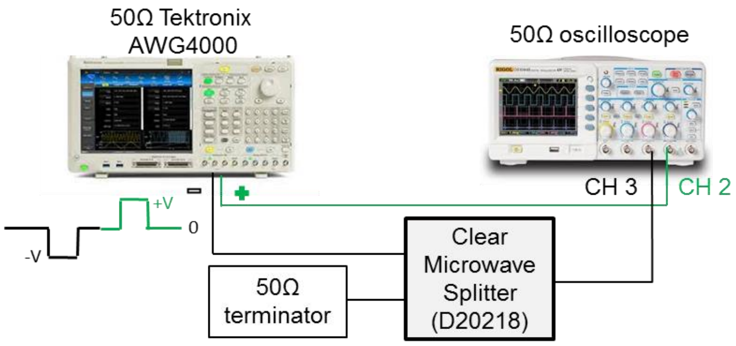

Fig. 4.17-Schematic of the second pulse characterization: a splitter Clear Microwave D20218 is added to the negative pulse chain and connected to the CH 3 of the oscilloscope. A 50Ω terminator is added into the other input port of a splitter to avoid the signal loss.

The negative (black curve) and the positive pulse (green curve) observed in the oscilloscope is shown in Fig. 4.18. Adding a splitter Clear Microwave D20218 into the negative pulse chain, the amplitude of negative pulse is reduced from -40mV to -30mV. This means an attenuation of 2.5dB. The attenuation is high because the pulse frequency is 10 MHz (the pulse period 100 ns) which is out of the splitter's frequency band characteristics. From the datasheet, the splitter Clear Microwave D20218 has an insertion loss of 0.9dB at a frequency band of 2GHz to 18GHz and a rise time of 25 ps. Zooming Fig. 4.18a in the time interval of 18 ns to 72 ns (Fig. 4.18b), one can see that the rise time of the negative pulse does not change (the rise time of both pulses remain the same t=800 ps). This is because the rise time of the splitter is fast (25ps).

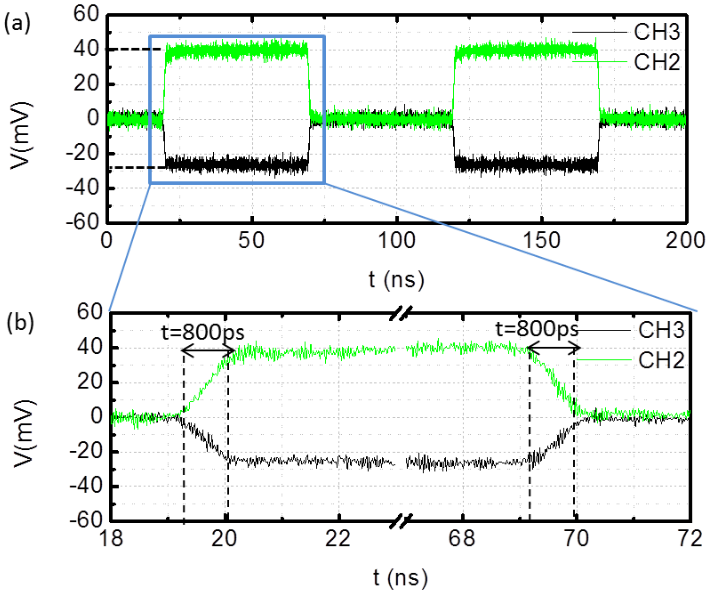

Fig. 4.18-(a) The negative (black curve) and positive pulses (green curve) observed in different output channels of the oscilloscope. A splitter Clear Microwave D20218 is added into the negative pulse chain. (b) Enlargement of the pulse waveform in the interval of t=18ns to t=72ns.

- **Test 3: Pulse – RF cable – splitter (Clear Microwave D20218) – <u>3dB attenuator – bias-T</u> – oscilloscope**

The final test is done by adding all the RF components needed for the FSK measurements into the negative pulse chain. These are the splitter Clear Microwave D20218, a 3dB attenuator and a bias-T (Marki Microwave BTN-0040). The schematic of the test can be seen in Fig. 4.19. The pulse parameters were the same as used in the previous test.

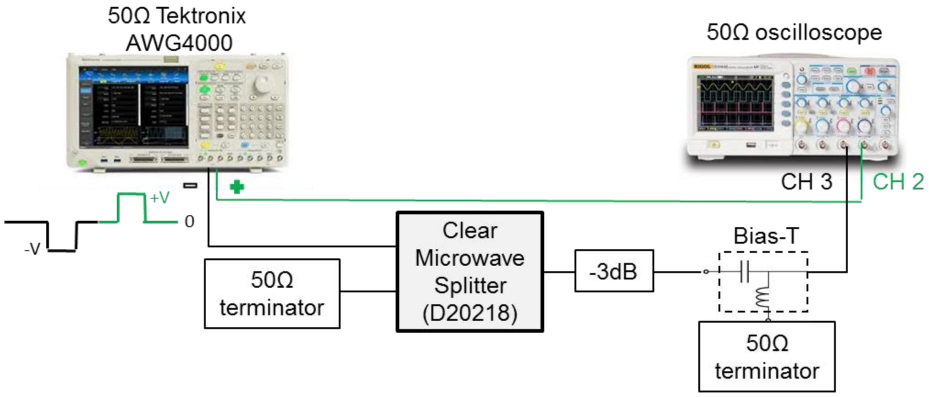

Fig. 4.19-Schematic of the final pulse characterization: all the RF components needed for the FSK measurements which are the splitter Clear Microwave D20218, a 3dB attenuator and a bias-T (Marki Microwave BTN-0040) is added to the negative pulse chain and connected to the CH 3 of the oscilloscope. A 50Ω terminator is used to avoid the signal loss.

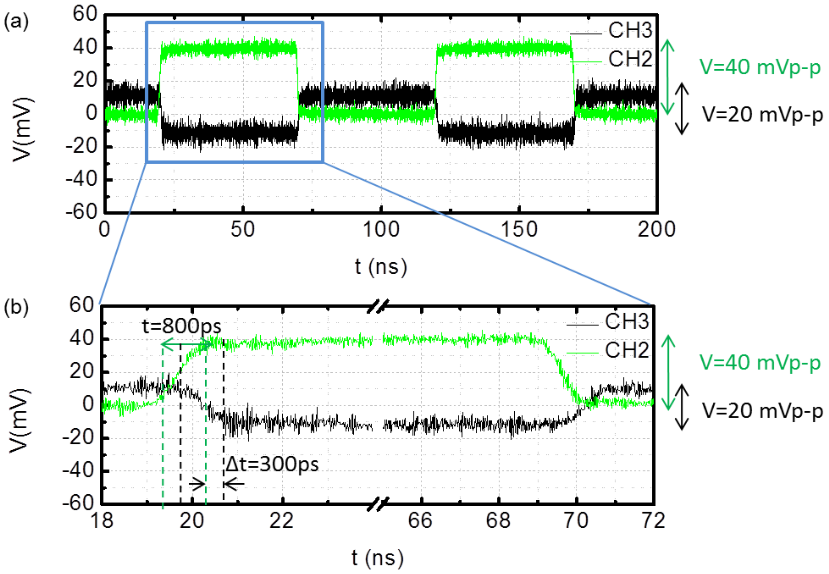

Fig. 4.20-(a) The impact of adding all the RF components into the negative pulse chain. The negative (black curve) and positive pulse (green curve) observed in different output channels of the oscilloscope. (b) Enlargement of the pulse waveform in the interval of t=18ns to t=72ns.

Connecting the negative pulse chain to the oscilloscope (CH3), one can see in Fig. 4.20a, the impact of adding all the RF components into the negative pulse (black) chain:

(i) The peak-to-peak amplitude of negative pulse (black curve) reduces from $40mV_{p-p}$ to $20mV_{p-p}$. This corresponds to an amplitude attenuation of around 6 dB, which is half of its initial amplitude (Fig. 4.16-black curve). This amplitude attenuation is given by the total attenuation of the RF components.

(ii) The amplitude of the negative pulse (black curve) shifts up by about half of its original peak-to-peak value (centered about the 0 values), i.e. oscillating between +10mV to -10mV. This is because the negative pulse is passed through the capacitance part (AC part) of the bias-T. The capacitance part will remove the DC part or the DC level of the pulse waveform and pass only the AC part. For the periodic pulse of 50% duty cycle (δ=0.5) the DC level is $0.5V_{pulse}$ (see Fig. 4.21). In this case, the DC level of negative pulse waveform is -10mV (0.5x-20mV). The capacitance part of the bias-T removes the DC level of -10mV. The output of the bias-T is thus the pulse waveform whose average value is zero.

(iii) Fig 4.20b shows the enlargement of the pulse waveform in the interval of t=18 ns to t=72 ns. From this Figure, one can observe that the rise and fall time remain the same, 800 ps. However, a delay between negative and positive pulse is observed. The negative pulse is retard by 300ps compared to the positive pulse. This is due to the fact that adding the attenuator and bias-T to the negative chain extends the transmission line from the input port (signal generator) to the output port (oscilloscope). From the datasheet, the bias-T Marki Microwave BTN-0040 has an insertion loss of 1.5dB at a frequency band of 40kHz to 40GHz and a rise time of 11 ps. The rise time of the bias-T is faster than the rise time of the pulse. This explains why the rise time of the negative pulse remain the same as the positive pulse (reference pulse).

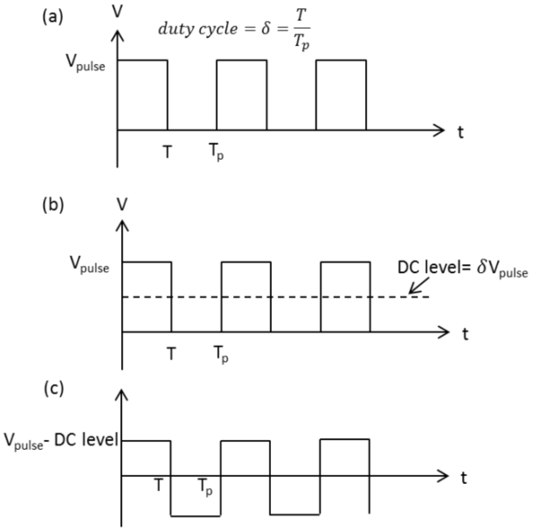

Fig. 4.21-The effect of the capacitance on a pulse train (a) The original pulse waveform, zero-to-peak amplitude, with the pulse width T and the pulse period T_p. The duty cycle δ of the pulse is the ratio between the pulse width and its period (b) The DC level calculation (c) The pulse train with DC component removed after passing the capacitance part of the bias-T.

All tests performed previously correspond to a periodic pulse with 50% duty cycle, i.e. the pulse width is half of the pulse period. Since in the FSK measurements a single pulse is also applied, the characteristics of the single pulse after passing all the RF components are also investigated. The schematic of the pulse characterization is the same as in the final test (Fig. 4.19). To perform a single pulse, the pulse period is set to be larger than the time traces of the measurement. For the FSK measurement, the time trace is 40 μs (frequency resolution 25kHz) with the oscilloscope sampling rate 50GS/s. Hence, the pulse period should be larger than 40 μs.

The pulse parameters are the same as used in the previous tests, i.e. the pulse amplitude 40mV$_{p-p}$, the pulse width 50ns, the rise and fall time 800 ps, but this time the pulse period is set to 42 μs. This means that the pulse appears every 42 μs, leading to a 0.1% duty cycle. The corresponding pulse is shown in Fig. 4.22. Adding all the RF components to the negative pulse chain will change the amplitude of the negative pulse (black curve). The amplitude reduces from -40mV$_{p-p}$ to -20mV$_{p-p}$, the same as the periodic one. The pulse offset does not change, i.e. the pulse is not centered at zero, since its duty cycle is 0.1%. As explained previously (Fig. 4.21), the DC level or offset of the pulse waveform is characterized as δV_{pulse}. For 0.1% duty cycle, the DC level/offset is thus -0.02mV (0.001x-20mV). This means that the capacitance part of the bias-T removes the DC level of -0.02mV. As a consequence, the pulse is shifted up by about 0.02mV which is too small.

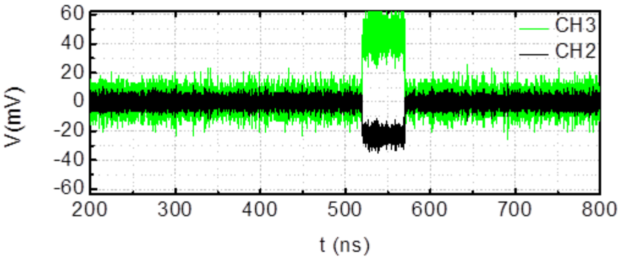

Fig. 4.22-The impact of adding all the RF components into the negative pulse chain for a single pulse. The negative (black curve) and positive pulse (green curve) observed in different output channels of the oscilloscope.

As already mentioned, all tests described above were done for a pulse frequency of 10 MHz. The attenuation of the pulse amplitude for different frequencies due to the RF components was also measured using a vector network analyzer (VNA). The measurements showed that the attenuation was around 7 dB for low frequencies in the range of 1 - 400 MHz, as seen in Fig. 4.23.

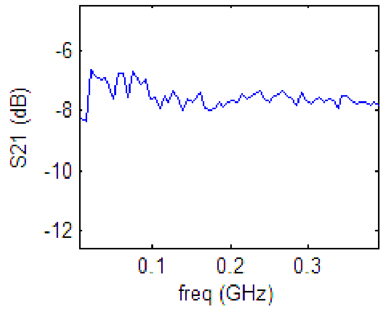

Fig. 4.23-The pulse amplitude attenuation due to the RF chain (RF cable – splitter - 3dB attenuator - bias-T) as a function of the frequency.

To summarize, the total attenuation due to the RF components (RF cable - splitter - attenuator - bias-T) needs to be considered when applying the pulse signal to the STNO. Depending on the pulse frequency, the signal attenuation varies from 6dB to 8dB (Fig. 4.23). It is also important to note that the capacitance part of the bias-T removes the DC level or offset of the pulse waveform. Hence, for the periodic pulse of 50% duty cycle with zero-to-peak amplitude, the pulse waveform will shifts by about half of its original zero-to-peak value. Consequently, the output pulse waveform will be centered at zero, oscillating between positive and negative amplitude. For the FSK measurements, modulating the DC current with a periodic pulse oscillating between positive and negative amplitude will shift the DC current into two current values $I_{DC,1}$ and $I_{DC,2}$ around its initial value $I_{DC,0}$. This result in the frequency shift between two discrete values f_1 and f_2 around its initial frequency f_0 as illustrated in Fig. 4.24a. Instead, for a single pulse with zero-to-peak amplitude, there is no change of the amplitude offset of the pulse after passing through the RF components. Modulating the DC current with a single pulse will shift the DC current from its initial value $I_{DC,0}$ to another current level $I_{DC,1}$ depending on the pulse amplitude (negative or positive). The STNO frequency is thus shifted from its initial frequency f_0 to another frequency f_1, as shown in Fig. 4.24b.

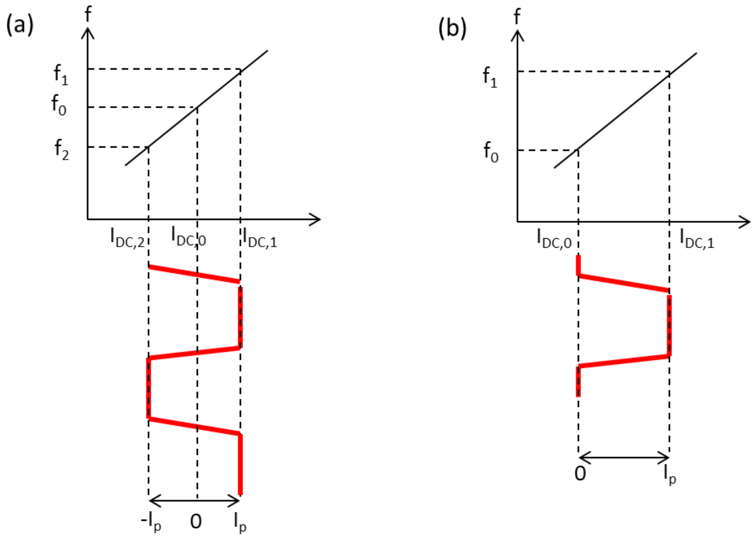

Fig. 4.24-(a) The DC current I_{DC} and frequency shift under a periodic pulse whose amplitude is alternating between positive I_p and negative value $-I_p$. (b) The DC current I_{DC} and frequency shift under a single pulse.

4.3.2 FSK measurements of Hitachi devices

In this section, the FSK measurements of Hitachi device will be discussed. Before summarizing the FSK measurement results, the RF characterization of the free running STNO Hitachi device will be discussed. This RF characterization aims to determine the best working conditions of the STNO for FSK modulation. A large frequency current tenability, df/dI, low linewidth, and large output power of the STNO are important parameters to perform a successful FSK modulation. The signal stability and the extraction of the relaxation frequency f_p of the STNO as a function of DC current and magnetic field will be also discussed.

4.3.2.1 Characterization of the free running Hitachi device

The dynamic characterization of this device has been characterized and discussed in Chapter 2, Section 2.4. Here the dynamic characterization will be reviewed and the best working conditions of the free running STNO Hitachi device for FSK modulation will be determined.

The measured magnetoresistance curve for the Hitachi device at the positive field is shown in Fig. 4.25a (white plot). The positive field stabilizes the anti-parallel (AP) state with the corresponding resistance of 125Ω and the negative field (not shown in this plot) stabilizes the parallel (P) state with the corresponding resistance of 80Ω. This gives rise to a TMR of 54%. The dynamic measurement was performed at the positive field (AP state) and the best dynamic performance was found at an in-plane magnetic field H_{DC} angle of -28° with respect to the easy axis of the free layer FL. The corresponding frequency dispersion as a function of applied magnetic field for a fixed current of I_{DC}=1.8mA is given in Fig. 4.25a. The frequency dispersion shows a clear single mode behavior with the first harmonic oscillation frequency 1f of the free layer is much powered than its second harmonic 2f. No SAF excitation observed at high frequency, showing that the SAF pinned layer is rigid upon applying high field. The frequency and the linewidth of the first harmonic 1f are extracted using Lorentzian fitting. The results are shown in Fig. 4.25b. The frequency versus field (black curve) shows that the frequency increases upon increasing the field. The linewidth field dependence, Δf vs H, (red plot) is characterized by several branches: A, B, C. For each branch, the linewidth goes to a minimum value and increases at each transition. The increase of linewidth at each transition indicates loss of temporal coherence.

Fixing the magnetic field at 750Oe (in the C-branch Fig. 4.25b), i.e. where the linewidth is minimum and the power is high, the dynamic characteristics of oscillations as a function of applied current I_{DC} is shown in Figs. 4.25c,d,e. The threshold current I_{th} marked by the green vertical dashed line is estimated to be I_{th}≈1.5mA. Below the threshold current I_{th}≈1.5mA the excitations are thermally excited (FMR mode), while above the threshold current I_{th}≈1.5mA the excitations are steady state. The steady state excitations are separated from the FMR mode by a pronounced downward frequency jump (Fig. 4.25c). Above the threshold current, the frequency shows an increase with DC current up to I_{DC}≈1.9mA. Above I_{DC}≈1.9mA the frequency does not increase with the DC current. The frequency-current tuning df/dI is positive in the range of I_{DC}=1.6mA to I_{DC}=1.9mA with a value of df/dI≈400MHz/mA. The increase in frequency as a function of the current is followed by an abrupt decrease in linewidth (Fig. 4.25d), as well as an increase in power (Fig. 4.25e). In the region where the frequency is flat, df/dI=0, the linewidth is narrower which is around 15 MHz, followed by the increase of the power of the main peak ≈70 nW for I_{DC}=1.9 mA.

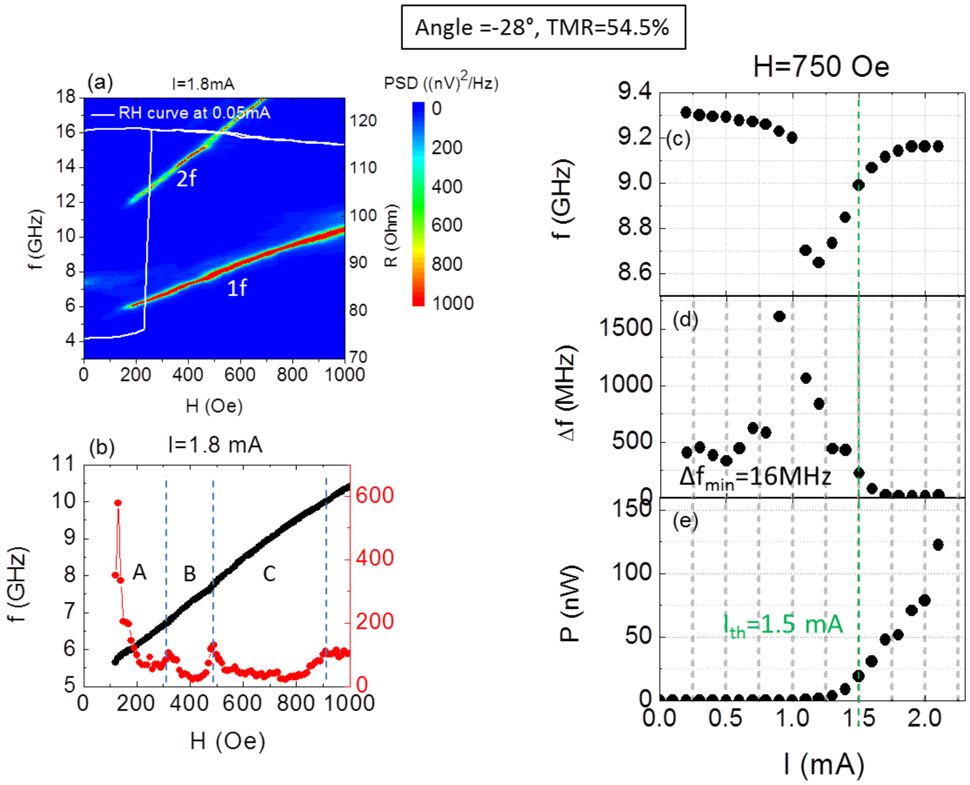

Fig. 4.25-The dynamic characterization of the Hitachi device. (a) The PSD of frequency versus field for a fixed current of I_{DC}=1.8mA. 1f is the first harmonic and 2f is the second harmonic. The white plot corresponds to the magnetoresistance curve at positive field. (b) The Lorentzian fitting of the PSD of frequency versus field. Black curve is the field dependence of the frequency dependence and red curve is the field dependence of the linewidth. The current dependence at a fixed magnetic field of 750Oe: (c) frequency versus current (d) linewidth versus current, and (e) output power versus current. The green dashed vertical line is the threshold current.

From the current dependence results, it can be determined that the working conditions of the studied STNO for FSK modulation is above the threshold current where low linewidth, large output powers and sufficient frequency tunability df/dI are achieved.

In the following the time domain characterization of the Hitachi device, characterizing the signal stability and the relaxation frequency f_p extraction, will be discussed. These parameters are also important for FSK since the relaxation frequency will determine the maximum data rate of the FSK as predicted in the simulation in Chapter 3.

The signal stability of the Hitachi device for different current values at a fixed magnetic field of 750Oe are is presented in Fig 4.26. From left to right are the 200ns and 5ns long segments of the measured time traces (40µs long), the histogram of the positive signal envelopes, and the histogram of the extinctions. For the analysis and in order to improve the signal to noise ratio, the signal presented here has been numerically filtered using a bandpass filter of 4GHz around the main oscillation peak.

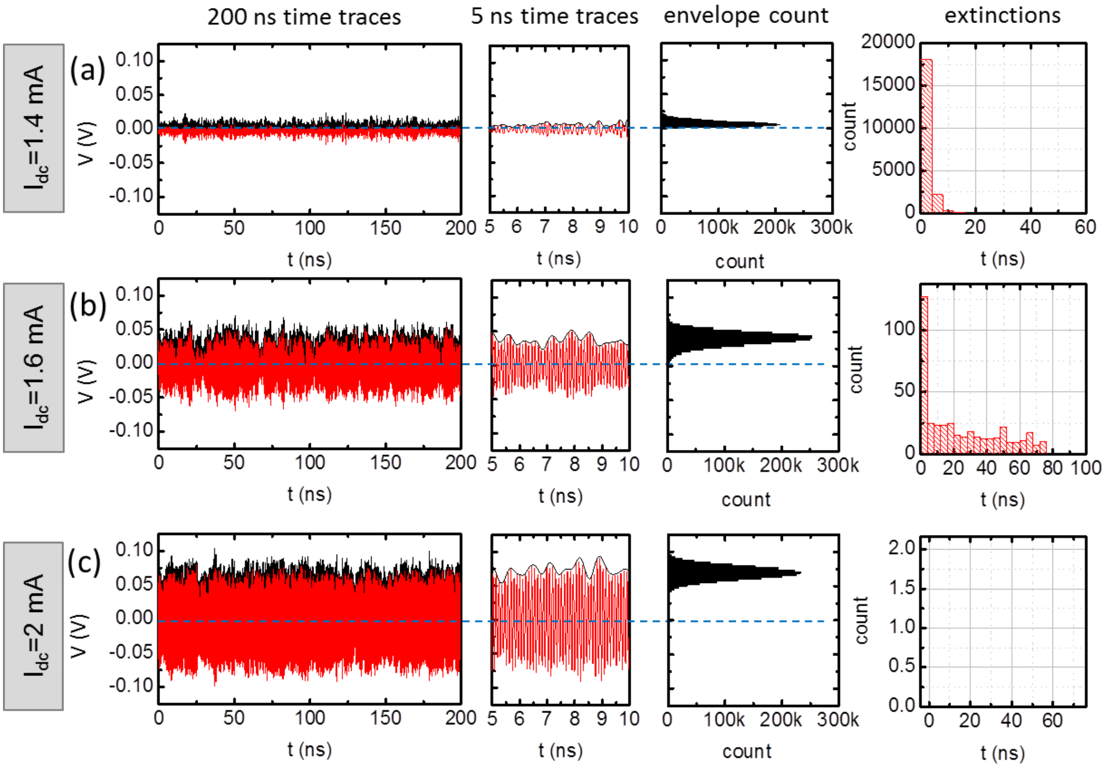

Fig. 4.26- From left to right: 200ns and 5ns long segments of the measured time traces (total length 40µs), histograms of the positive signal envelopes and the time between extinctions for: (a) I_{DC} = 1.4mA (subthreshold regime), (b) I_{DC} = 0.6mA (intermittent regime) and (c) I_{DC} = 2mA (steady state regime). A numerical filter of ±2GHz from the centered oscillation frequency was applied on the time traces during analysis to improve the signal stability.

From Fig. 4.26, the stability of the oscillation for different currents is observed. At the sub-threshold regime I_{DC}=1.4mA (Fig. 4.26a), the amplitude signal is very low which is comparable to the background noise level (0.025V). The histogram of its positive signal envelopes (black curve in time traces plot) is are distributed almost around 0V. Furthermore, the histogram of the extinctions (the amplitude reduces to the noise level) shows that the amplitude oscillations are sustained only at very short period of ~10ns. This means that the signal is dominated by the thermal noise which confirms that the oscillations are thermally excited. At the current near the threshold current I_{DC}=1.6mA (Fig. 4.26b), the amplitude signal shows an increase which is confirmed in the envelope histogram plot, showing that the distribution of the envelope of the signal is shifted a bit away from 0V. The increase in amplitude oscillations is however sustained only over short periods. The oscillations thus consist of two different fluctuation mechanisms with different coherencies: thermal magnetization fluctuation of amplitude and phase (intrinsic contribution) and extinctions. The histogram of the extinctions at this transition regime can be seen in Fig. 4.26b (right panel). This shows that there are around 20 events where the amplitude oscillations are sustained over few ns (20ns – 70ns). In contrast, for an applied current of 2mA, only the high amplitude signal peak exists, meaning that the oscillations are sustained over long (40µs) time scales without extinctions. The histogram of the envelope shows that the envelope distribution is away from 0V. This results to a narrow linewidth as can be seen in the frequency domain measurements given in Fig. 4.26c. From this, it can be conclude that above the threshold current, in the steady state regime, the signal stability increases. A sustained oscillation over long periods is obtained at higher current where the linewidth is narrow.

Since the best working condition of FSK modulation is above the threshold current (in the steady state regime), the analysis of the relaxation frequency f_p of the STNO were performed at current above the threshold current, I_{DC}=1.6mA and I_{DC}=2mA. The relaxation frequency f_p is deduced from two methods: the autocorrelation function of the amplitude fluctuations and direct extraction from the amplitude noise plot (Chapter 1 Section 1.3.5).

The amplitude and frequency noise of the STNO are obtained by taking the Power Spectral Density (PSD) of amplitude and frequency fluctuations, which are extracted from voltage time traces using the Hilbert transform, and plotting them in double logarithmic plot. The amplitude noise $PSD_{\delta a}$, the frequency noise $PSD_{\delta f}$ and the autocorrelation function of the amplitude fluctuations $K_{\delta p}$ for different current values (above the threshold current) are shown in Fig. 4.27. Now focus on the amplitude and frequency noise plot for I_{DC}=1.6mA (Fig. 4.27a) and I_{DC}=2mA (Fig. 4.27b). It can be seen that the amplitude and frequency noise level decreases with the applied current. The amplitude noise at I_{DC}=2mA is 7dB lower than the one at I_{DC}=1.6mA. Due to the nonlinear coupling of amplitude-frequency, the decrease in the amplitude noise is also observed in the frequency noise. At I_{DC}=2mA, the frequency noise is 0.28GHz^2/GHz lower than the one at I_{DC}=1.6mA. The decrease in the amplitude and frequency noise explains the reason why the oscillation at 2mA has better stability (sustained over long periods) than the one at 1.6mA which is sustained only over few tens ns. From the amplitude noise $PSD_{\delta a}$, the relaxation frequency f_p at I_{DC}=1.6mA and I_{DC}=2mA is estimated to be ≈90MHz and ≈100MHz, respectively. These f_p values correspond to the amplitude relaxation rate Γ_p of ≈282 Mrad/s at I_{DC}=1.6mA and ≈314 Mrad/s at I_{DC}=2mA. These amplitude relaxation rate values are different with those extracted via the autocorrelation function of the amplitude fluctuations, $K_{\delta p}$. From the amplitude autocorrelation plots shown in the right panel Fig. 4.27, the relaxation times obtained by fitting the amplitude autocorrelation (black curve) with the exponential fitting (red curve) are 1.28ns at I_{DC}=1.6mA and 1.06ns at I_{DC}=2mA. These correspond to f_p=124.02 MHz at I_{DC}=1.6mA and f_p=150.15 MHz at I_{DC}=2mA. The amplitude relaxation frequency f_p (amplitude relaxation rate Γ_p) from both extraction methods shows the same tendency. The amplitude relaxation frequency f_p at high current I_{DC}=2mA (good oscillation stability) is higher than the one at low current I_{DC}=1.6mA. As discussed previously in Chapter 2, this relaxation frequency f_p limits the modulation data rate. Modulating the STNO frequency above the f_p value will result on the attenuation of the modulated signal, i.e. the reduction of the amplitude of the frequency shift.

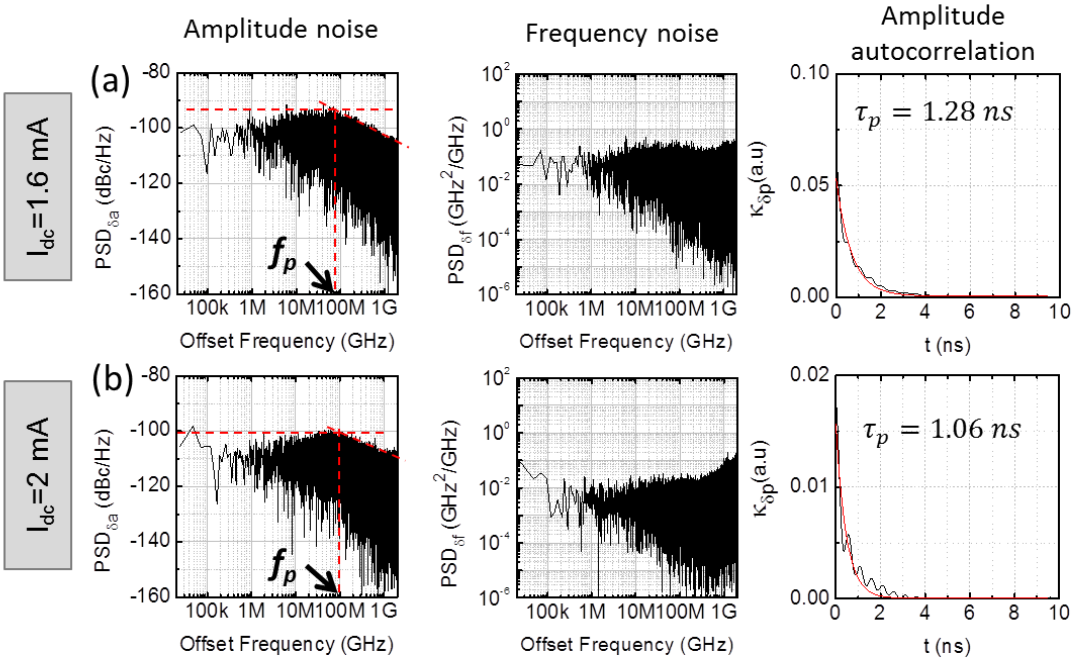

Fig. 4.27-The amplitude noise PSD$_{\delta a}$, the frequency noise PSD$_{\delta f}$, the autocorrelation function of the amplitude fluctuations $K_{\delta p}$ for different current values: (a) I_{DC}=1.6mA and (b) I_{DC}=2mA. The amplitude relaxation time of the autocorrelation function of the amplitude fluctuations $K_{\delta p}$ (black curve) is obtained by fitting the amplitude autocorrelation with the exponential function.

Conclusion

From the dynamic characterization results of the studied STNO, the working conditions of the STNO for FSK measurements are at magnetic field 750Oe applied at angle of 28° with respect to the easy axis of the free layer and for the applied DC current above the threshold current I_{th}=1.5mA. Above this threshold current, the frequency-current tuning df/dI is positive in the range of I_{dc}=1.6 mA to 1.9 mA with a value of df/dI≈400 MHz/mA. The linewidths lower than 30 MHz with output powers higher than 50 nW are achieved, making the observation of the frequency shift possible. Furthermore, it is confirmed via time domain analysis that above the threshold current I_{th}=1.5mA the signal stability increases. A sustain oscillations over long period (42μs) is achieved at I_{DC}=2mA. This is because the amplitude and frequency noise at higher current I_{DC}=2mA are lower than the noise at lower current I_{DC}=1.6mA. The relaxation frequency f_p of the STNO for different currents, I_{DC}=1.6mA and I_{DC}=2mA, have been extracted. From the autocorrelation function of the amplitude fluctuations, the relaxation frequency f_p at I_{DC}=1.6mA is 124.02 MHz and 150.15 MHz at I_{DC}=2mA. As discussed in the simulations, these relaxation frequencies f_p will limit the maximum data rate of FSK modulation, which is on the order of a few Mbps.

4.3.2.2 FSK measurement results

The FSK by current in the STNO has been carried out by injecting a current/voltage pulse, which is characterized by their rise time/fall time and pulse width T (defining the data rate), into the steady state oscillations of the STNO. The current pulse will modulate the DC current between two discrete values, leading to simultaneous modulation of amplitude (amplitude shift keying, ASK) and frequency (frequency shift keying, FSK) modulation. The FSK arises via the non-linear amplitude-frequency coupling.

To demonstrate the ASK and FSK, the steady state oscillation of the STNO at I_{DC}=2mA and H_{DC}=750Oe (applied at angle 28° with respect to the polarizing layer) was chosen as initial working conditions of the STNO while applying a voltage pulse. To achieve a maximum frequency shift δf which is characterized by the frequency-current tuning df/dI≈400MHz/mA, a single voltage pulse with amplitude of ≈-31mV was applied, accounting for the pulse amplitude attenuation due to RF components in Section 4.3.1. This corresponds to a current switching from the initial current $I_{DC,0}$=2mA to a lower current level $I_{DC,1}$=1.6mA. The frequency is expected to shift from f_0=9.18 GHz to f_1=9.05 GHz, leading to a frequency shift δf of ≈130MHz as shown in Fig. 4.28a. The linewidth remains narrower than 100 MHz within this current range such that the observation of the frequency shift possible. However, the amplitude of the peak f_1 (at $I_{DC,1}$=1.6 mA) is much lower than the amplitude of the peak f_0 (at $I_{DC,0}$=2mA), as can be seen in Fig. 4.28b.

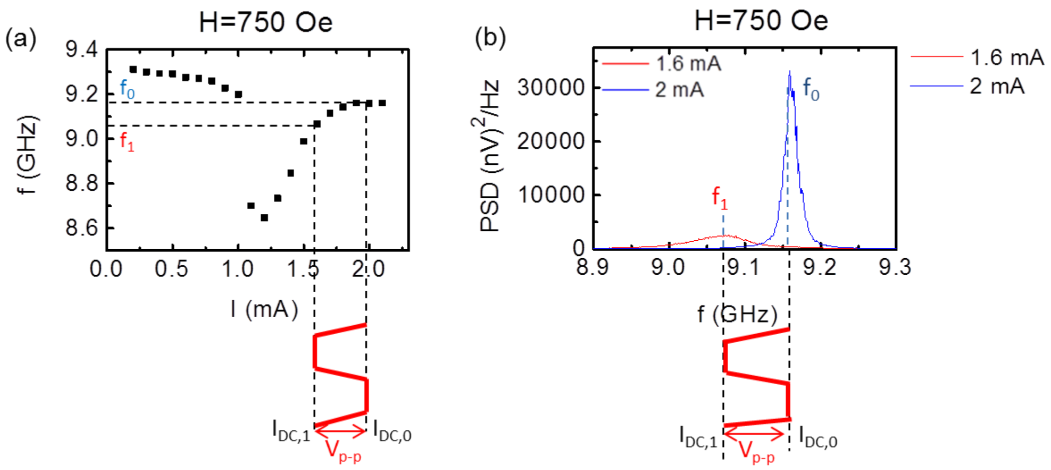

Fig. 4.28-(a) The frequency current dependence for a fixed magnetic field H_{DC}=750Oe extracted from dynamic characterizations of the studied STNO. A voltage pulse with amplitude of ≈-31mV (red curve) modulates the DC current between $I_{DC,0}$=2mA to $I_{DC,1}$=1.6mA. This current modulation will lead to a frequency modulation from f_0=9.18GHz to f_1=9.05GHz. (b) The Power Spectrum Density (PSD) of the modulated frequency (FSK signal).

The pulse amplitude was estimated by measuring the voltage of the STNO while tuning the DC current, observed on the current source meter Keithley. The corresponding voltage at H_{DC}=750Oe and I_{DC}=2mA is V_{2mA}≈227mV, while the voltage at H_{DC}=750Oe and I_{DC}=1.6mA is $V_{1.6mA}$≈196.5mV. The voltage difference is thus V_{2mA}-$V_{1.6mA}$≈31mV. Switching down the current from the initial value $I_{DC,0}$=2 mA to $I_{DC,1}$=1.6mA, one needs to apply a negative pulse with the peak-to peak amplitude of V_{p-p}≈31mV. Switching down the current is more convenient for STNO in order to avoid the heating effect on the STNO, which would lead to changes on the microwave properties, and to avoid the sample breakdown since the Hitachi devices are very sensitive to the applied DC current.

The FSK measurement results are shown in Fig. 4.29. Fig. 4.29a shows the time trace of the amplified output voltage signal registered by the oscilloscope (black curve) upon the application of the voltage pulse of -31mV (red curve). The corresponding rise time and the pulse width are 0.8ns and 500ns, respectively. As observed in the simulations Section 4.2, a slight decrease of the amplitude during the application of the current/voltage pulse can be seen clearly, revealing the amplitude modulation, i.e. amplitude switching from high to low amplitude level. Using the Hilbert transformation, the positive envelope and the phase of the output signal Φ were obtained. The positive envelope of the output signal is shown in Fig. 4.29c. The instantaneous frequency was obtained from the derivative of the phase, dΦ/dt, and it is given in Fig. 4.29c. The temporal response of the instantaneous frequency looks very noisy under current pulse modulation. This can be understood by the fact that the signal at I_{DC}=1.6mA is not very stable since this current is close to the threshold current I_{th}. In fact, as observed for the peak f_1 in Fig. 4.28b, its linewidth is very broadened. This makes the observation of the frequency shift difficult. To further reduce the noise of the resulting instantaneous frequency, a Savitzky-Golay filter algorithm [104] with a 500 points (10 ns) averaging window has been applied. The Savitzky-Golay filter is a kind of low pass filter which smoothens the noisy data based on a local least-squares polynomial approximation. The corresponding smoothened time trace of the frequency is shown in Fig. 4.29d. The frequency shift can now be clearly observed and has marked with blue dashed lines in the figure. The frequency shift is approximately from 9.18 GHz to 9.06 GHz.

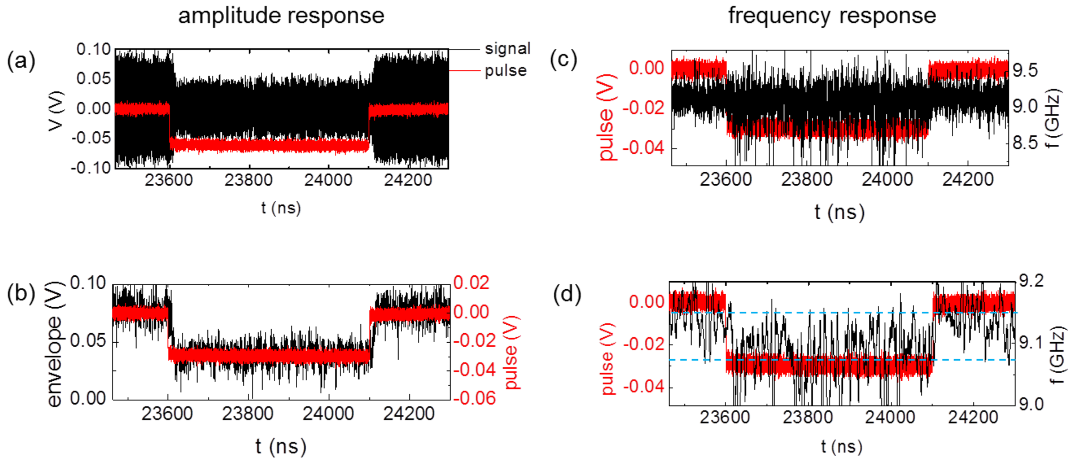

Fig. 4.29-(a) The amplified STNO output voltage signal V(t) at I_{DC}=2mA and H_{DC}=750Oe under a negative pulse V≈-31mV with a pulse width of 500ns and a sharp rise and fall time of 0.8ns. (b) The envelope and (c) the corresponding instantaneous frequency (black curves) obtained by the Hilbert transformation of the voltage time traces V(t). (d) The smoothened signal of the instantaneous frequency shown in (c). The pulse is shown in red for all plots.

Doing the same analysis as described above, further FSK measurements by varying the current pulse characteristics, such as the rise/fall time and the pulse width (T), have been conducted in order to analyze the frequency transition time and thus the maximum achievable modulation rate. The results are then compared with the numerical simulation performed in the section 4.2.

4.3.2.2.1 FSK response to a variation of the rise and fall time of the pulse

In this measurement, the rise/fall time of the pulse was varied for a constant amplitude and pulse width. This allows the investigation of the transition time it takes for the STNO to follow the pulse modulation. For this study, the same experimental parameters as the previous measurement have been used. The DC current was switched from a high DC current I_{DC}=2mA to a lower one I_{DC}=1.6mA, leading to a frequency shift from the higher frequency f_0=9.18GHz to a lower one f_0=9.06GHz.

The varying rise and fall times are 0.8ns (the shortest one), 2ns, 5ns, 10ns, 30ns, and 50ns as shown in Fig. 4.30. In the left side of the figure the time traces of the envelope of the amplified output voltage signal V(t) are displayed, while in the right side the time traces of the smoothened signal of the instantaneous frequency are displayed.

Similar results are obtained as in the simulation in Section 4.2.2. For longer rise and fall times of 30ns and 50ns (slow perturbations) as shown in Figs. 4.30a,b, the envelope of the STNO output voltage signal V(t) can follow the rise and fall time of the current pulse on the timescale given by the rise/fall time of the pulse. The same observation is obtained for the time traces of the frequency. The STNO frequency follows the pulse on the timescale given by the rise/fall time of the pulse. This frequency shift mechanism is however different when the frequency is switched from high f_0 to low frequency f_1 and from low f_1 to high frequency f_0. For the case of frequency shift from high (at I_{DC}=2mA) to low frequency (at I_{DC}=1.6mA), it take several ns of delay to response the current pulse following by a sharp frequency switching/transition. While for the case of frequency shift from low (at I_{DC}=1.6mA) to high frequency (at I_{DC}=2mA), no delay to response the current pulse and a gradual frequency switching/transition is observed. A high fluctuation in frequency is observed for low frequency f_1. This frequency f_1 corresponds to a current of I_{DC}=1.6mA which is closed to the threshold current I_{th}=1.5mA. The dynamic stability is thus poorer compared to the one of higher current I_{DC}=2mA due to a higher amplitude and frequency noise (Section 4.3.2.1).

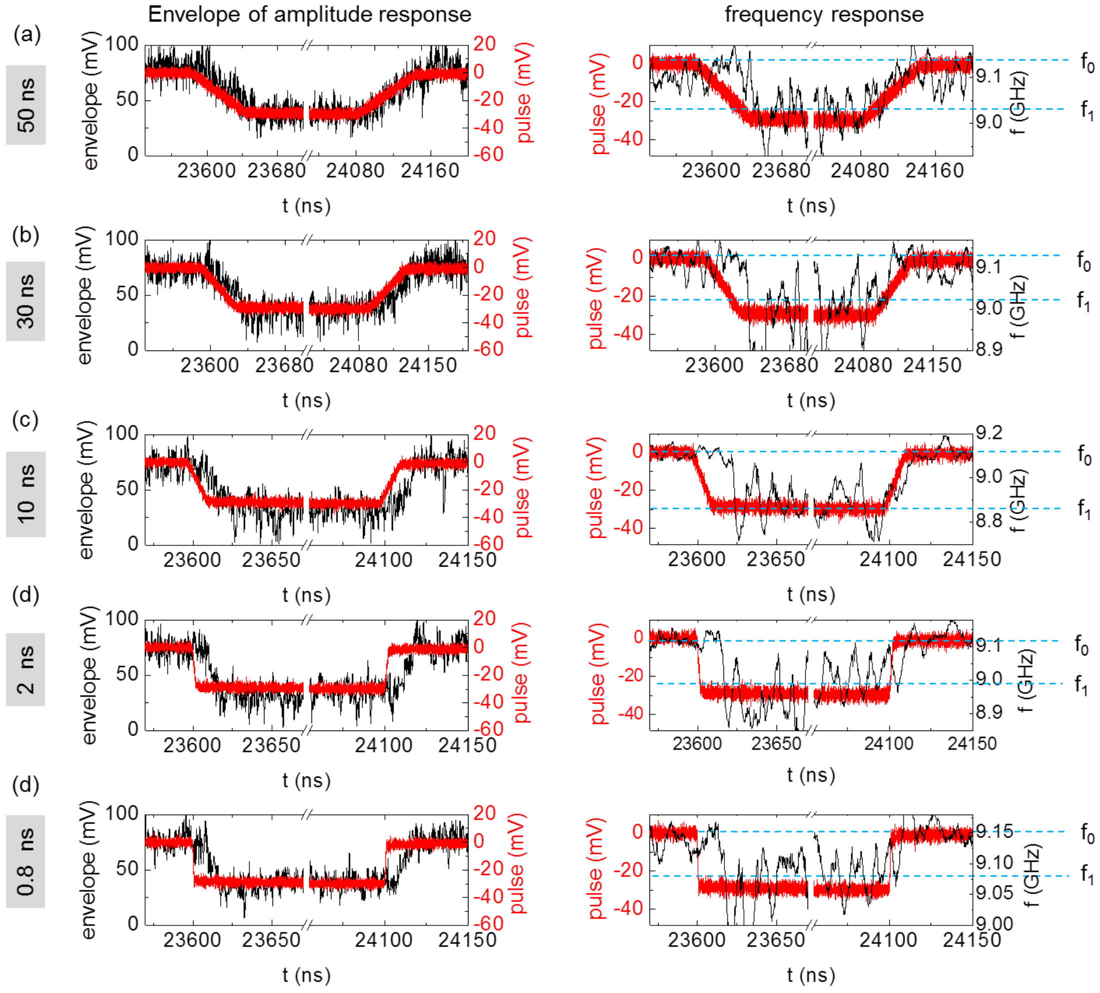

Fig. 4.30-The time traces of the envelope (left side) and the smoothened signal of the instantaneous frequency (right side) of the amplified STNO output voltage signal V(t) at I_{DC}=2mA and H_{DC}=750Oe under a negative pulse V≈-31 mV (red curve) for a constant pulse duration (500 ns) and varied rise and fall time: (a) 0.8ns (b) 2ns (c) 10ns (d) 30ns and (e) 50ns. The horizontal blue dashed line in the right plot represents the average frequency of the instantaneous frequency.

For short rise times such as 10ns, 2ns, and 0.8ns as shown in Figs. 4.30c,d,e, it is investigated that the STNO voltage signal can follow the pulse modulation, from high state (I_{DC}=2mA) to low state (I_{DC}=1.6mA) on the timescale of t_1≈14ns (1/ t_1≈70MHz) and from low state ((I_{DC}=1.6mA) to high state (I_{DC}=2mA) on the timescale of t_0≈11ns (1/t_0≈90MHz). These timescales indicate the minimum pulse width (maximum pulse rate) can be applied to the STNO in order to follow the pulse command.

In this measurement, the frequency shift from f_0 to f_1 is supposed to be constant since the pulse amplitude is constant during the measurement, only the rise and fall time are varied. However, a strong variation of the frequency shift δf is observed in this measurement as shown in Fig. 4.31. Fig. 4.31a shows the variation of the averaged frequency f_0 (black dotted line) and f_1 (red dotted line) for different rise and fall times, which are extracted from the time traces of the modulated frequency of the STNO (right side of the Fig. 4.30). From the plot, the value of frequency f_0 is more stable (smaller variation) than the value of f_1. This can be understood by the fact that the dynamic oscillation at I_{DC}=2mA, which corresponds to a frequency f_0, is more stable than the one at lower current I_{DC}=1.6mA (frequency f_1), i.e. sustained over long period and lower amplitude and frequency noise. This large variation of the frequency f_1 causes a large variation on the frequency shift, δf, as plotted in Fig. 4.31b.

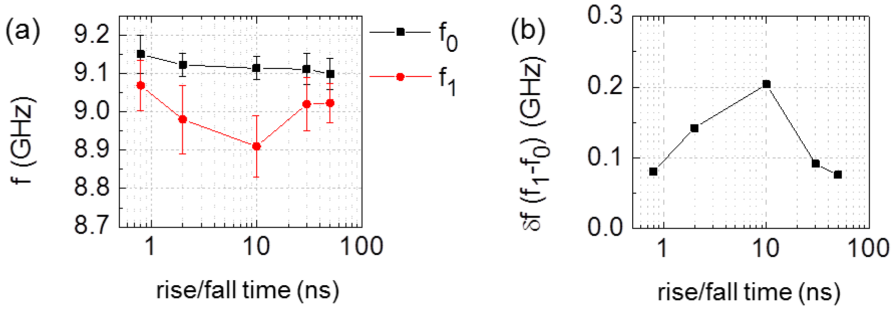

Fig. 4.31-(a) The average of the smoothened instantaneous frequency of f_0 and f_1 for different rise time values extracted from the time traces of the modulated frequency as shown in right side of Fig. 30. The frequency f_0 corresponds to the frequency at the initial steady state I_{DC}=2mA. The frequency f_1 corresponds to a steady state modulation frequency at I_{DC}=1.6 mA (b) The frequency deviation δf for different rise time values.

4.3.2.2.2 FSK response to a variation of the pulse width

In this measurement, the pulse width of the pulse was varied for a constant amplitude and rise/fall time. This allows the investigation of the achievable frequency shift and the maximum data rate of the STNO. For this study, a train of digital current pulse with amplitude oscillating alternately between positive and negative values, i.e. two levels amplitude $\pm I_{mod}$, was applied to the free running STNO to modulate the DC current between two discrete values $I_{DC,1}$ and $I_{DC,2}$ around its initial value $I_{DC,0}$. This gives rise to the amplitude and frequency shift between two discrete values of amplitude A_1 and A_2 and frequency f_1 and f_2 situated around the free running values A_0 and f_0 corresponding to $I_{DC,0}$, as illustrated in Fig. 4.24a.

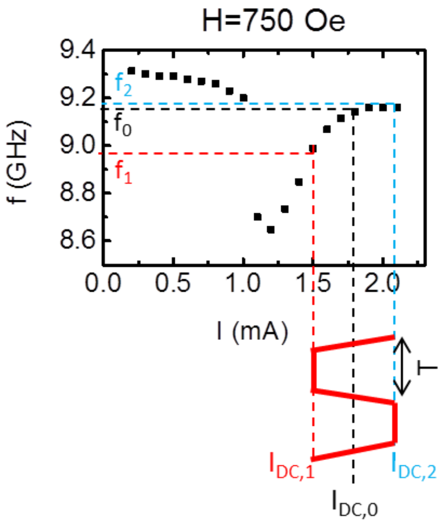

Fig. 4.32-The current and frequency modulation under the application of a train of digital current pulse whose amplitude oscillates between positive and negative amplitude $\pm I_{mod}$. The current $I_{DC,0}$ is modulated between two levels, $I_{DC,1}$ ($I_{DC,0}$-I_{mod}) and $I_{DC,2}$ ($I_{DC,0}$+I_{mod}). This leads to a frequency modulation between two discrete values, f_1 and f_2, situated around the free running value f_0.

In this case, the operation point of the free running STNO was chosen at $I_{DC,0}$=1.8 mA and H=750 Oe, while applying a train of digital current pulses. The pulse amplitude I_{mod} was ±25 mV which corresponds to a digital current modulation between two discrete values $I_{DC,1}$=1.5mA ($I_{DC,0}$-I_{mod}) and $I_{DC,2}$=2.1mA ($I_{DC,0}$+I_{mod}) as illustrated in Fig. 4.32. The rise and fall time of the pulse were equally set to 0.8ns, the shortest one, so that the STNO voltage and frequency follow the pulse modulation at the shortest timescale of t≈14ns-11ns (Section 4.3.2.2.1). The pulse width T was varied between 500ns and 10ns, i.e. the data rate 1/T was varied from 2 Mbps to 100 Mbps. The STNO response to a train of digital current pulses for different pulse width T (data rate 1/T) is shown in Fig. 4.33.

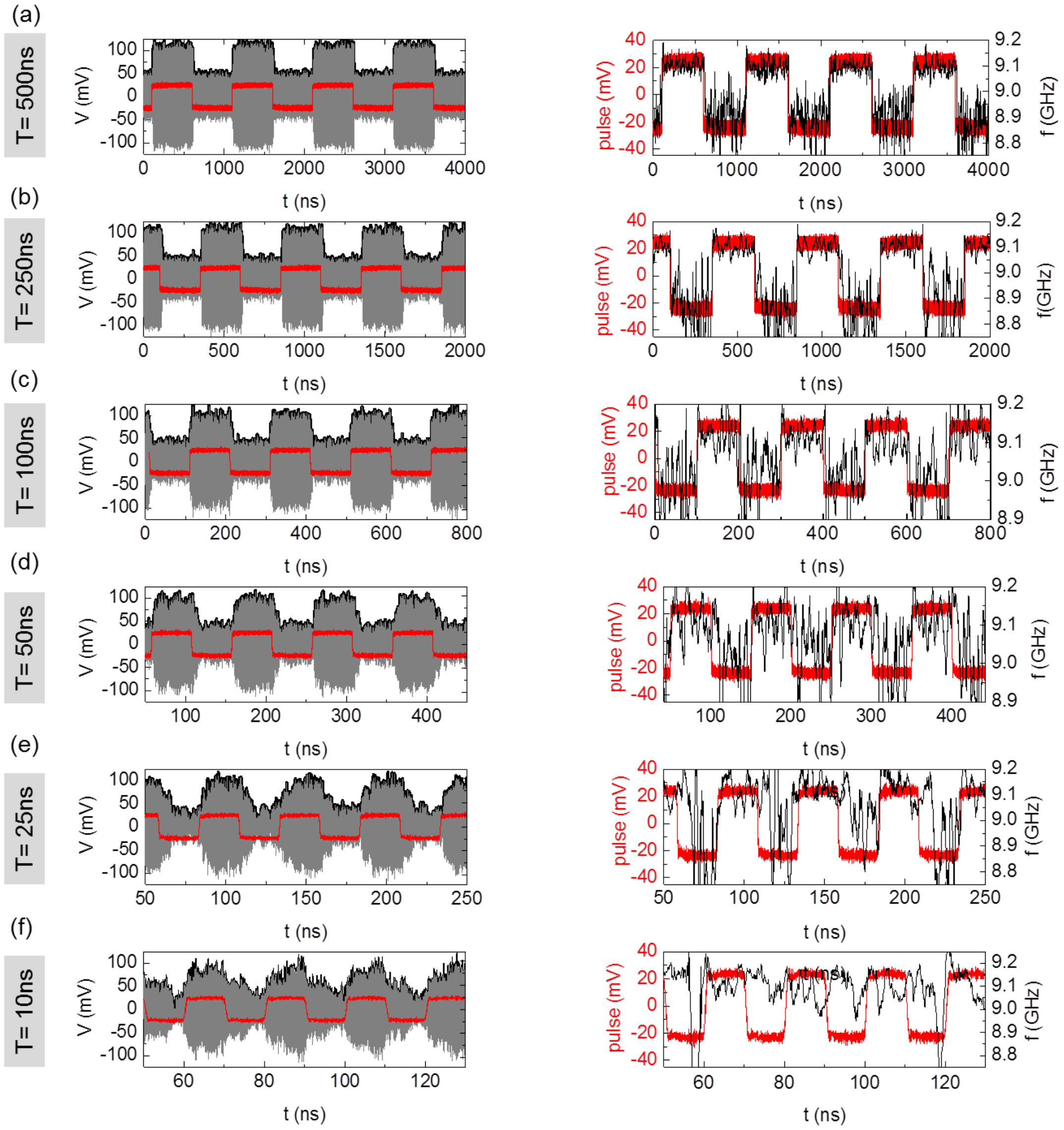

Fig. 4.33-The time domain analysis of the STNO output voltage signal at I_{DC}=2mA and H_{DC}=750Oe, under a periodic voltage pulse with a constant amplitude of V=±25mV and rise (fall) time of 0.8ns. The pulse width is ranging as follow: (a) 500ns (20ns averaging/50MHz) (b) 250ns (20ns averaging/50MHz) (c) 100ns (10ns averaging/100MHz) (d) 50ns (5ns averaging/200MHz) (e) 25ns (4ns averaging/250MHz) and (f) 10ns (3ns averaging/333MHz). The left figures show the amplified STNO output voltage signal (grey curve) and the positive envelope of the voltage signal (black curve). The right figures show the instantaneous frequency of the voltage signal (black curve). The pulse is shown in red for all plots.

In the left side of the figure, the time traces of the amplified STNO output voltage signal (grey curve) and the corresponding positive envelope (black curve) are displayed. In the right side of the figure, the time traces of the smoothened instantaneous frequency (black curve) extracted from the voltage time traces V(t) using the Hilbert transformation are displayed. The averaging window of the smoothing was adapted according on the pulse width, T, (see in the description of the Fig. 4.33).

As can be seen in the left side of Figs. 4.33a,b,c,d,e, for the pulse width T longer than the STNO transition timescales, t≈14ns-11ns, the amplitude (grey curve) or the positive envelope (black curve) of the STNO voltage time traces can periodically follow the current pulse. The amplitude is modulated between two discrete levels, high and low amplitude level, characterized by a clear plateau in both levels. The amplitude modulation between two discrete levels gives rise to the frequency modulation between two discrete values f_1 and f_2 as shown in the right side of Figs 4.33a,b,c,d,e. However, a full frequency shift from f_1≈8.9GHz to f_2≈9.1GHz, (δf≈0.2GHz) can only be achieved for the pulse widths of up to T=250ns which corresponds to data rates of up to 4Mbps (see Figs. 4.33a,b). For the pulse width of T=100ns (data rate of 10Mbps) up T=25ns (data rate of 40Mbps), the frequency shifts from f_1≈9GHz to f_2≈9.1GHz (see Figs. 4.33c,d,e), leading to a reduction of the amplitude of the frequency shift, δf≈0.1GHz. Now for the pulse width of T=10ns (data rate 100Mbps) which is shorter than the STNO transition timescales t≈14ns-11ns, the amplitude (grey curve) or the positive envelope (black curve) of the voltage time traces cannot fully follow the pulse command and the frequency shift is no longer observed, as given in Fig. 4.33f.

From the results, this can be concluded that the maximum modulation rate for amplitude modulation (ASK) of the Hitachi device is close to 100Mbps, while for frequency modulation (FSK), it is limited to 40 Mbps at reduced frequency shift and below 10Mbps at full frequency shift of 200MHz. Hence frequency shift keying is confirmed to be efficient up to ~10Mbps for a frequency shift of 100-200MHz. The reason that this is less than the limit for amplitude modulation as predicted in the simulation is seen in the relatively high phase noise of the device.

4.3.2.3 FSK demodulation: Delay detection calculation

As discussed in Section 4.1, the delay detection technique proposed by Toshiba is used for the demodulation of the STNO output voltage signal to read back the digital voltage pulse as signal information. This technique has only been developed for field modulation where there is no amplitude variation (modulation) in the output voltage time traces of the modulated STNO, leading to a pure FSK modulation. In contrast to this, the amplitude of the output voltage signal in these studies varies significantly, leading to a well-pronounced amplitude shift keying (ASK) modulation. This ASK modulation induces the FSK modulation through nonlinear coupling of the amplitude-frequency (simultaneous ASK and FSK). Since the FSK modulation is the main interest of this thesis, the demodulation of FSK modulation is important to realize. In order to see whether the delay detection technique of FSK modulation is working for such output voltage signal, i.e. mix of ASK and FSK modulation, the auto-correlation of the output voltage time traces <V(t)*V(t-τ)> with a correlation time (or signal delay time) τ has been performed. The calculation of the delay detection and the determination of the delay time τ are shown in Fig. 4.34.

Fig. 4.34a depicts the STNO output voltage signal V(t) (grey curve) and the corresponding positive envelope (black curve). The output is dominated by the ASK modulation, showing by a strong variation of the amplitude at every 500ns pulse width. The corresponding FSK modulation is extracted from the Hilbert transform of the output voltage signal as shown in Fig. 4.34b. The instantaneous frequency consists of two frequencies f_1 and f_2. The corresponding frequency deviation, $\delta f=f_2-f_1$, is ≈0.2GHz. To perform the delay detection technique, the free running oscillation f_0 is adjusted to be centered between f_1 and f_2, i.e. f_0=9 GHz (see Fig. 4.34b). The delay time τ is chosen to be 2.3ns to satisfy both the quadrature condition $\tau f_0 = n - 1/4$ with f_0=9 GHz, n=21, and the minimum shift keying condition $\tau\delta f = 0.5$ (phase shift is $\pm\pi/2$). The output of delay detection signal <V(t)*V(t-τ) is shown in Fig. 4.34c which involves the high frequency oscillation with the frequency of approximately $2f_0$. After the removal of the high frequency oscillation by 100MHz low pass filter (LPF), the output signal of delay detection shows a pulse train forms with the voltage varies from 0 to some positive value at every T=500ns as shown in Fig. 4.34d.

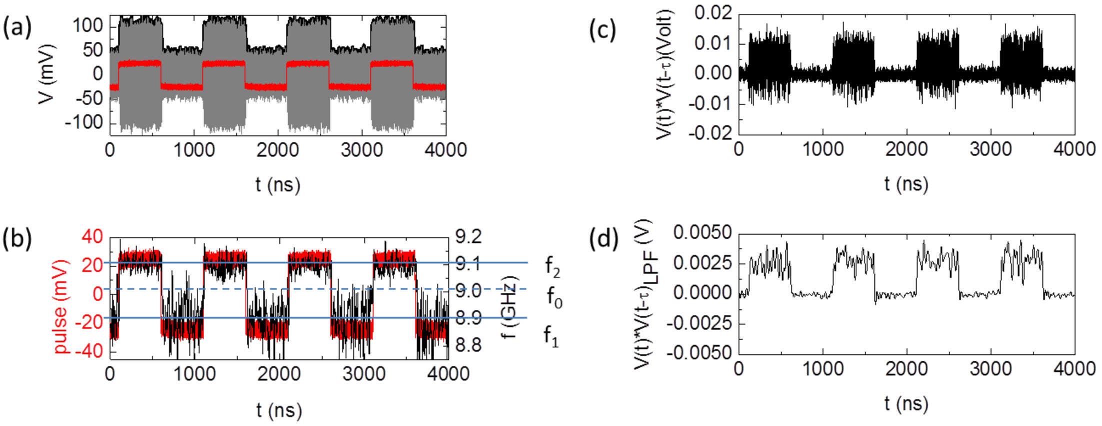

Fig. 4.34-(a) The time traces of the amplified STNO output voltage signal (grey curve) and the corresponding positive output signal envelope (black curve) at I_{DC}=2mA and H_{DC}=750Oe under a periodic voltage pulse (red curve) with amplitude of V=±25mV, rise (fall) time of 0.8ns and pulse width of 500ns (b) The time traces of the smoothened instantaneous frequency (black curve) of the output voltage signal shown in (a). (c) The output signal of delay detection V(t)*V(t-τ) of the output voltage signal shown in (a). (d) A low pass filter with a cut-off frequency of 100 MHz was applied to the output of delay detection signal, V(t)*V(t-τ), to remove high frequency parts.

Using the same calculation, the delay detection of the STNO output voltage signal for different pulse widths is shown in Fig. 4.35. In the left side of the figure, the amplitude envelope of the output voltage signal V(t) is displayed. In the right side of the figure, the output of delay detection of the output voltage signal V(t) is displayed. Looking at the output of delay detection, the demodulated signal does not have much in common with the FSK signal (right side of Fig. 4.33). The noise of the output of delay detection is high where it was low in the frequency response and vice versa. Furthermore, looking at the FSK signal in Fig. 4.33 at high modulation rates, in particular the one for 100Mbps (T=10ns), the FKS seems really poor, i.e. the frequencies cannot be separated, but the demodulation signal at this rate looks half-way good, i.e. high and the low level still can be separated. And also the amplitude of the demodulated signal varies from 0 to some positive values instead of going from some negative and positive values even though the phase shift is set to be ±π/2 (minimum shift keying condition), as explained in Section 4.1. Compared with the amplitude envelopes of the output voltage signal, the demodulation signals have so much in common with them. This means that the main factor determining the output of delay detection arises from the amplitude, revealing the ASK demodulation instead of FSK demodulation.

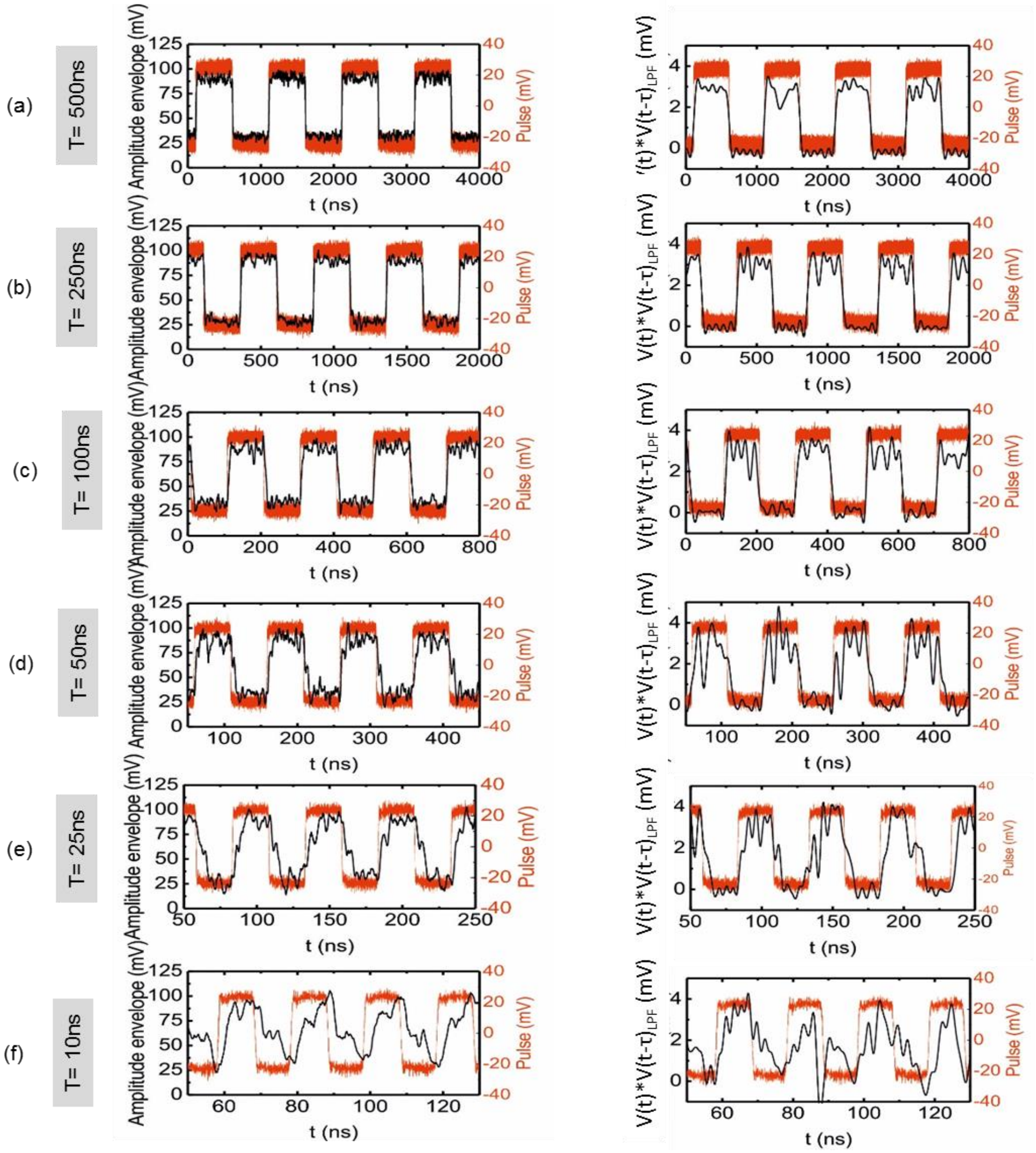

Fig. 4.35-The smoothened amplitude envelope of the STNO output voltage signal V(t) shown in Fig. 5.34 (left side) and the output of delay detection (right side) of the output voltage signal V(t), for different pulse width: (a) 500ns (LPF=10MHz) (b) 250ns (LPF=25MHz) (c) 100ns (LPF=50MHz) (d) 50ns (LPF=100MHz) (e) 25ns (LPF=250MHz) and (f) 10ns (500MHz).

To really see how the demodulation works for the pure FSK modulation, a fictive signal for pure FSK modulation (without ASK modulation) has been created by using the cosine function of the instantaneous frequency as a function of the time extracted from the Hilbert transform of the output voltage signal (the right side of Fig. 4.33), i.e. cos(2πft). The delay detection is calculated from the autocorrelation of the instantaneous frequency <(cos(2πf*(t))*cos(2πf*(t-τ))> with the correlation time τ =0.23ns. The output of delay detection for different pulse width is given in Fig. 4.36. In the left side of the figure, the instantaneous frequency of the output voltage signal for different pulse width is displayed (the same one as in Fig. 4.33-right side). In the right side of the figure, the output of delay detection, i.e. the autocorrelation of the instantaneous frequency, for different pulse width is displayed.

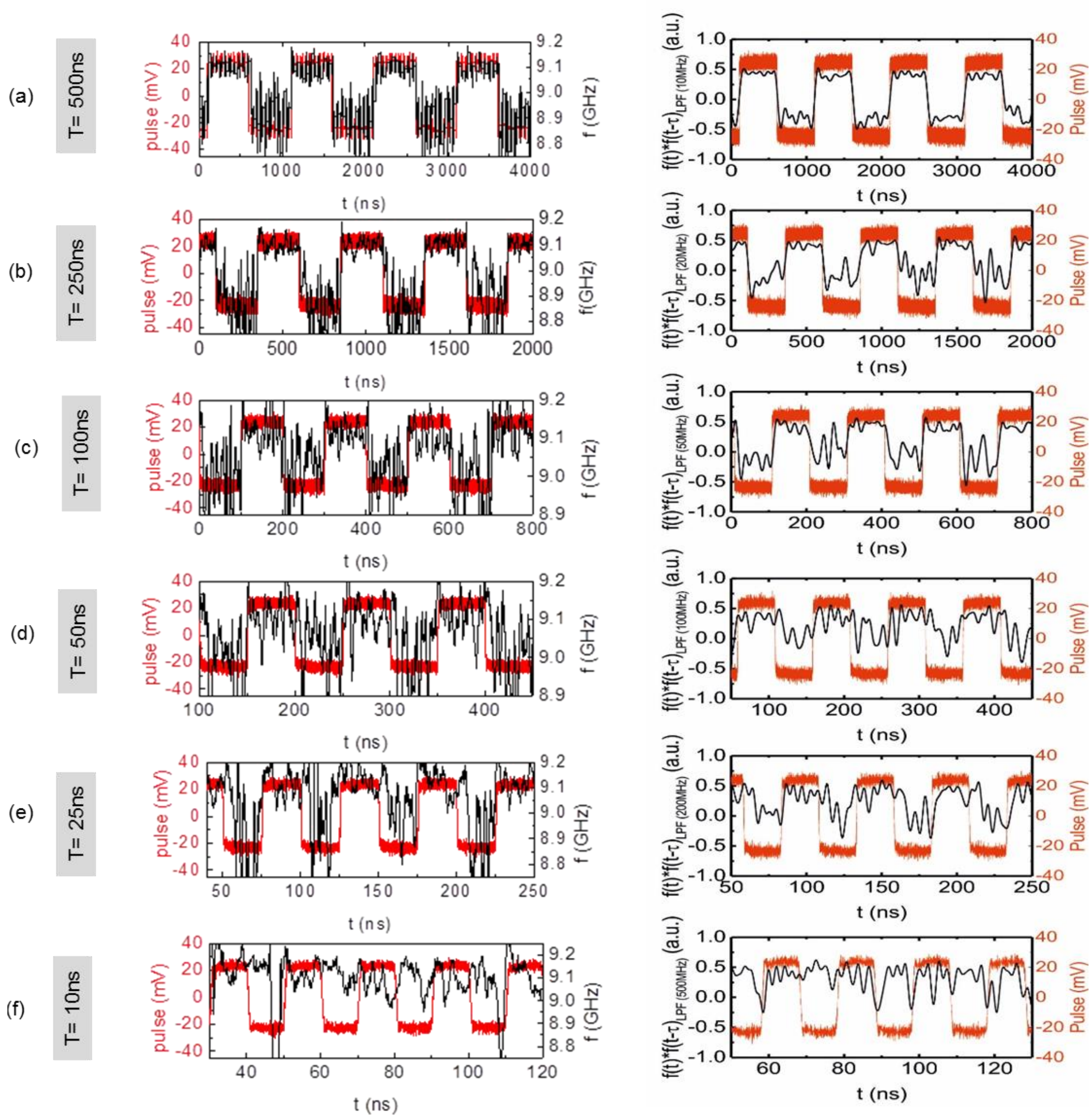

Fig. 4.36-The smoothened instantaneous frequency of the STNO output voltage signal V(t) (left side) and the output of frequency delay detection (right side) for different pulse width: (a) 500ns (LPF=10MHz) (b) 250ns (LPF=20MHz) (c) 100ns (LPF=50MHz) (d) 50ns (LPF=100MHz) (e) 25ns (LPF=200MHz) and (f) 10ns (LPF=500MHz).

Looking at the output of the delay detection for different pulse width, the demodulation signals have so much in common with the FSK signals in the left side of the figure 4.36. The output of the delay detection is less noisy than the FSK signals since the applied cut-off frequency of the low pass filter is 10 times lower than the one used in the FSK signals (smoothing frequency=1/averaging window). The amplitude of the output of the demodulation signal varies from some negative to positive values since the phase difference of the frequency shift, f_1 and f_2, is set to be ±π/2 to fulfill the minimum shift keying condition. This shows that the output of the delay detection arises only from the frequency or phase change. For modulation rate up to 10Mbps (T=100ns), the positive and negative amplitude can clearly be detected at the pulse width of T, representing the state of the digital signal ‘1’ and ‘0’ respectively. Above 10Mbps (T=100MHz), the demodulation is still possible up to 40Mbps (T=25ns) but the output voltage varies around 0 to some positive values. Furthermore, the signal fluctuation is higher at high data rate which is translated from a high frequency fluctuation in the FSK signal. This makes the separation between two states becomes smaller and more difficult to read. At 100Mbps (T=10ns), the demodulation cannot recover the voltage digital signal.

From the demodulation results, it can be concluded that for the case of current-induced FSK modulation in the STNO, the FSK demodulation cannot be achieved directly from the output voltage signal. Applying the delay detection technique directly on the output voltage signal of the STNO will correspond to the demodulation of the ASK signal as the output of delay detection arises from the amplitude variation. The ASK signal can be demodulated with a data rate below 100Mbps. The FSK demodulation can be achieved by applying the delay detection on the instantaneous frequency of the STNO without amplitude modulation. The output of delay detection arises only from the frequency or phase change from f_1 to f_2 and vice versa. This gives rise to digital signal '1' and '0' detection at the bit length (pulse width) T by detecting the output voltage of the demodulation signal, positive or negative amplitude. The demodulation of FSK signal of the studied STNO is possible up to 40Mbps (T=25ns). However the output is noisy and the separation between two levels of the digital voltage output is smaller. A clear demodulation is thus limited to 10Mbps.

4.3.2.4 Summary

The current-induced FSK modulations of the steady state oscillation of the STNO have been performed. Time domain techniques, i.e. analyzing the temporal response of frequency, have been carried out in order to evaluate the frequency response of the STNO upon the application of a current pulse. From the experimental results, it can be summarized as follows:

- The digital current modulation in the STNO induces simultaneously the amplitude shift keying ASK modulation and the frequency shift keying FSK modulation.
- The variation of the current pulse rise time shows that the STNO voltage signal can follow the pulse modulation, from on the timescale of $t\approx11$-14ns ($1/t\approx70$-90MHz). These timescales indicate the minimum pulse width (maximum modulation rate) can be applied to the STNO in order to follow the current pulse.
- The variation of the pulse width T (data rate 1/T) shows that the maximum modulation rate for amplitude modulation (ASK) of the Hitachi device is close to 100Mbps, while for frequency modulation (FSK), it is limited to 40 Mbps at reduced frequency shift and below 10Mbps at full frequency shift of 200MHz. Hence frequency shift keying is confirmed to be efficient up to ~10Mbps for a frequency shift of 100-200MHz. The reason that this is less than the limit for amplitude modulation is seen in the relatively high phase noise of the device.
- The delay detection shows that the ASK signal can be demodulated at the data rate below 100Mbps and the demodulation rate of the FSK signal is limited to 10Mbps.

4.3.3 FSK measurements of Mosaic device

In this section, the FSK measurements of the Mosaic devices will be discussed. The measurement setup, procedure, and analysis are the same with the one for Hitachi device as discussed in the previous section. The dynamic characterization of the studied STNO has been performed firstly to achieve steady state oscillations and to determine the working conditions for FSK studies. The results of the dynamic characterization of the studied STNO are summarized in the following sub-section.

4.3.3.1 Characterization of the Mosaic device (RFL741)

For Mosaic devices, RFL741 has been chosen to perform the FSK measurements. As has been discussed in Chapter 2, Section 2.4.1.1, RFL741 has the best dynamic properties compared to the other Mosaic devices. Furthermore the use of a composite free layer, CoFeB (1.5nm)/Ta(0.2nm)/FeNi(2), in RFL741 allows the reduction of the threshold current so that the transition to steady state oscillation can be achieved at low current compared to the other Mosaic devices and Hitachi devices. This is of interest for FSK-based wireless communication scheme since the FSK can be performed at low current. Low current operation means that low power consumption.

RFL741 is a homogeneously in-plane magnetized MTJ nanopillar with measured diameter circular of 115nm and a nominal resistance area (RA) product of 1.5 $\Omega\mu m^2$. The detail of the magnetic stack of the pillar can be seen in Chapter 2, Section 2.2 Table 2.1. The dynamic characterization of RFL741 has been discussed previously in Chapter 2 Section 2.4.1.1. Here, the dynamics of RFL741 will be reviewed to determine the best working conditions for FSK measurements.

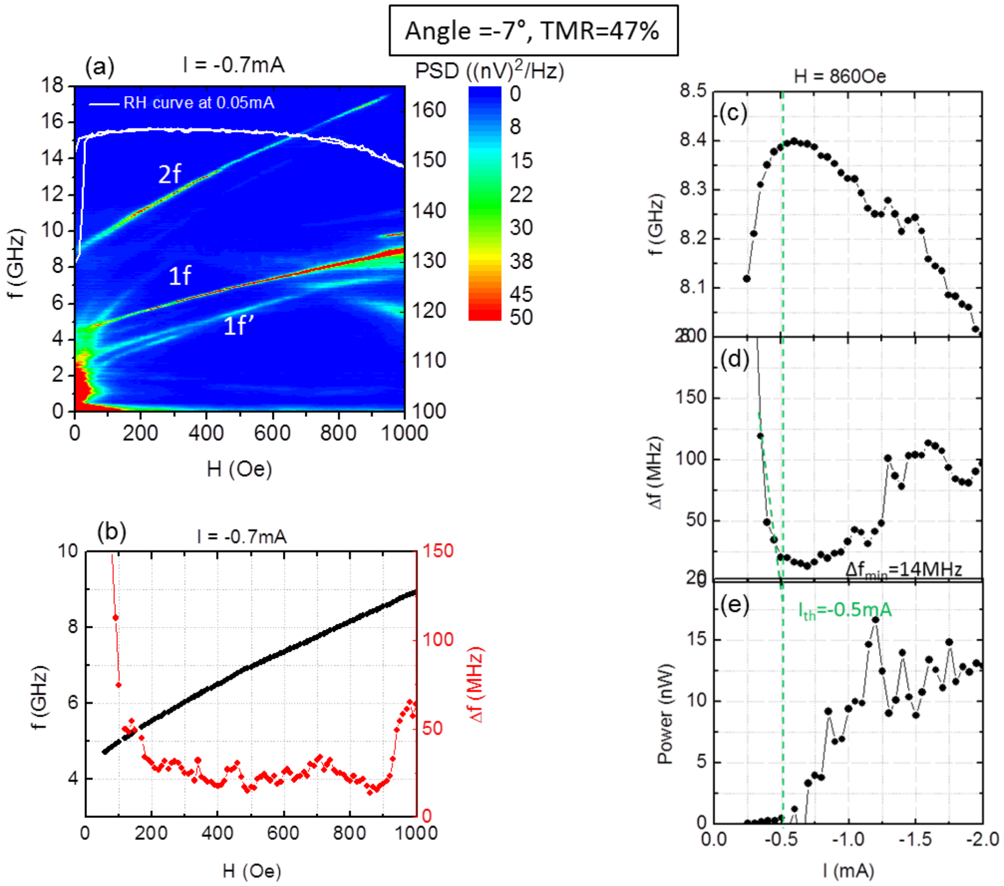

Fig. 4.37-The dynamic characterization of the Mosaic device, RFL741. (a) The PSD of frequency versus field for a fixed current of I_{DC}=-0.7mA. 1f is the first mode with the corresponding second harmonic is 2f and 1f' is the second mode. The white plot corresponds to the magnetoresistance curve at positive field. (b) The Lorentzian fitting of the PSD of frequency versus field. Black curve is the field dependence of the frequency dependence and red curve is the field dependence of the linewidth. The current dependence at a fixed magnetic field of 860Oe: (c) frequency versus current (d) linewidth versus current, and (e) output power versus current. The green dashed vertical line is the threshold current.

The dynamic performances of RFL741 are shown in Fig. 4.37. This was achieved at the positive magnetic field (AP state) and when the magnetic field is applied in-plane at angle of -7 degree with respect to the easy axis of the free layer. The corresponding magnetoresistance curve at the positive magnetic field at angle of -7 degree is shown in Fig. 4.37a (white curve) with the corresponding TMR of 47%. The PSD of the frequency versus field, H_{DC}, for a fixed DC current I_{DC}=-0.7mA is given in Fig. 4.37a. This reveals that the dynamics show weak multimode excitations 1f and 1f'. The mode 1f goes into steady state and it is much powered than its second harmonic 2f and the mode 1f'. At higher field, 700Oe to 1000Oe, SAF excitations are also weakly observed whose frequency decrease upon increasing the magnetic field and it is crossing with mode 1f' at ≈700Oe. The SAF does not cross the main mode 1f so that the branching behavior is less observed at the frequency versus field (black curve) and the linewidth versus field (red curve) shown in Fig. 4.37b. The linewidth lower than 50MHz is obtained in a wide range of the field values, from 100Oe to 950Oe, with the narrowest linewidth of 13MHz lies at H=860Oe. This minimum linewidth is comparable with the one obtained for the Hitachi device in the previous discussion. In order to confirm that the dynamic excitation is steady state, the analysis of the current dependence at a fixed magnetic field H_{DC}=860Oe where the linewidth minimum was carried out, as shown in Figs. 4.37c,d,e.

From the current dependence, one can observe that the dynamic transition from the damped mode to steady state mode at the threshold current of I_{th}=-0.5mA, (green vertical dashed line). This threshold value is much lower than the threshold current of the Hitachi device investigated previously. This is due to the use of FeNi in the free layer which is softer and has lower saturation magnetization. The transition from the damped mode to steady state mode at I_{th}=-0.5mA is characterized by the decrease of frequency upon increasing the magnitude of the applied current, i.e. in-plane precession mode, with a negative frequency, df/dI≈-258MHz/mA (Fig. 4.37c). The linewidth decreases upon increasing the applied current to I_{DC}=-1.25mA (Fig. 4.37d) following by the increase of the output power (Fig. 4.37e). Above I_{DC}=-1.25mA, the linewidth increases up to 100MHz and following by the power fluctuation around a power of ≈12nW. The output power of the RFL741 is still much lower compared to the one of Hitachi device.

From the current dependence, it can be determined that the best working conditions of the studied STNO for FSK modulation is above the threshold current of I_{th}=-0.5mA up to the current I_{DC} of -1.25mA, with frequency-current tuning df/dI≈-200MHz/mA and linewidths lower than 30MHz. The signal stability above the threshold current is shown in Fig. 4.38.

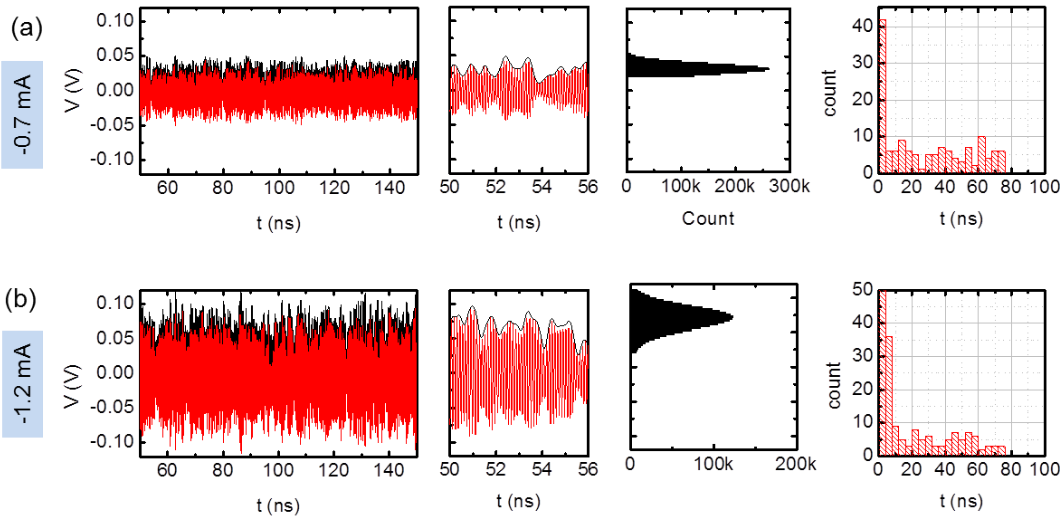

Fig. 4.38- From left to right: 100ns and 6ns long segments of the measured time traces (total length 40µs), histograms of the positive signal envelopes and the time between extinctions for: (a) I_{DC} = -0.7mA (steady state regime), (b) I_{DC} = -1.2mA (steady state regime). A numerical filter of ±2GHz from the centered oscillation frequency was applied on the time traces during analysis to improve the signal stability.

Fig. 4.38a shows the signal stability at I_{DC}=-0.7 mA and Fig. 4.38b shows the signal stability at higher DC current I_{DC}=-1.25mA. At higher current I_{DC}=-1.25mA, the amplitude of the output voltage signal increases, the distribution of the histogram of the envelope of the output signal is shifted away from 0V. The number of the extinction for both current are however the same. The both signal are sustained only over short period, i.e. 1ns to 80ns. The signal stability of this device is worse than the one observed in the Hitachi device as shown in the previous Section. As discussed in Chapter 2, Section 2.4.2.1, the extinction leads the presence of the spike in the instantaneous frequency of the STNO. The higher the number of the extinction, the higher the presence of the spike in the instantaneous frequency. For the FSK modulation, the presence of the spike in the instantaneous frequency hinders the observation of the frequency shift.

4.3.3.2 FSK measurement results

For a demonstration of the FSK modulation of the studied device, the steady state oscillation of the free running STNO at $I_{DC,0}$=-1.15mA and H_{DC}=860Oe (applied at angle -7° with respect to the polarizing layer) was chosen, while applying a current/voltage pulse. The application of the current/voltage pulse with amplitude of 57.6mV is expected to shift the DC current from $I_{DC,0}$=-1.15mA to $I_{DC,1}$=-0.7mA. Under this condition, the output power/amplitude is expected to shift from the initial power P_0=15nW to the low power P_1=4nW (Fig. 4.39a). While the frequency is expected to shift from the initial frequency f_0=8.26GHz to f_1=8.39GHz which corresponds to a frequency shift of 130MHz (Fig. 4.39b). The linewidths are lower than 50 MHz within this current range, such that the frequency shift of 130 is expected to be achieved.

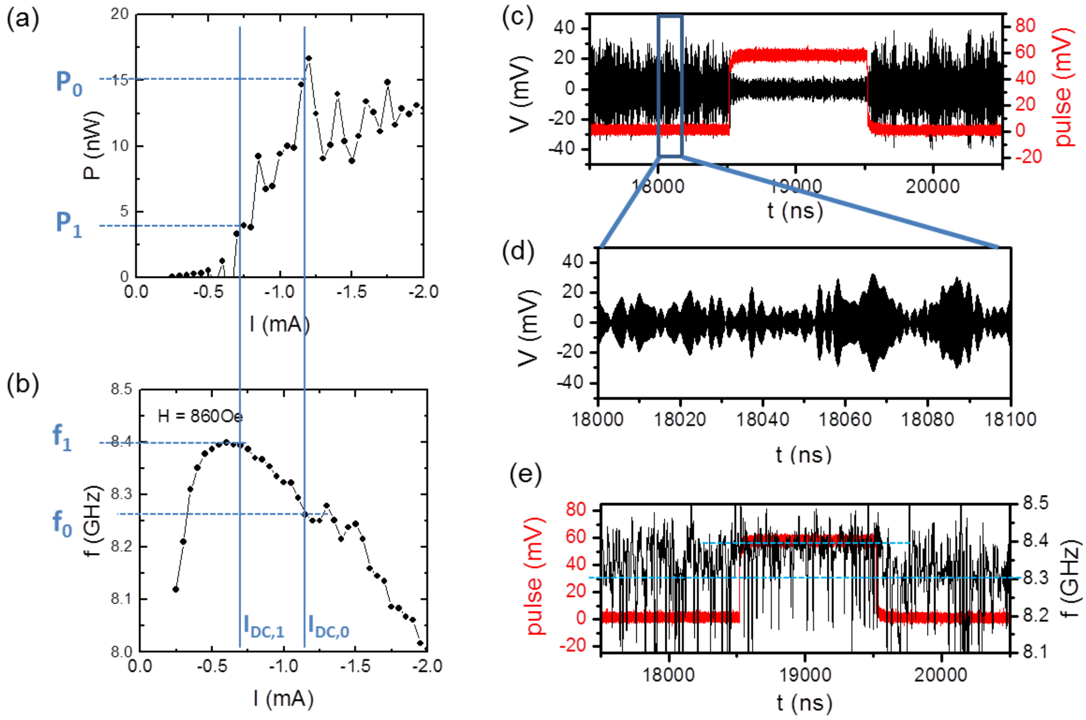

Fig. 4.39-(a) The STNO output power shift and (b) the frequency shift under the application of a positive voltage pulse of 57mV (c) The temporal response of the amplified STNO output voltage under a positive voltage pulse of 57mV, rise time and fall time are each 1.8 ns, and the pulse width is 1μs. (d) The enlargement of the output voltage signal in (c) in the interval of 100ns. (e) The smoothened instantaneous frequency (by 20ns averaging window of Savitsky Golay algorithm) extracted from the Hilbert transform of the output voltage signal.

The amplified STNO output voltage signal V(t) under a positive voltage pulse of V=57mV at 1 μs long is shown in Fig 4.39c. The amplitude of the output voltage is obviously switched from high to low amplitude level, i.e. reduction of the power, under the application of a positive current pulse. Zooming the time traces of the output voltage signal in the interval of 100ns as shown in Fig. 4.39d, one can observe that the signal stability is very poor, indicated by the amplitude extinctions (amplitude reduces to the noise level ~0V) over short periods. This amplitude extinction reduces the amplitude coherency and thus the phase coherency. This results on high frequency fluctuations (spikes) around the average frequency value as shown in Fig. 4.39e. As a consequence, the observation of the frequency shift difficult, i.e. two frequencies cannot be distinguished.

FSK response to a variation of the pulse width

In order to investigate the maximum achievable modulation rate of the studied STNO, the STNO response under a variation of the pulse width was studied. The initial operation of the free running STNO is the same as in the previous measurement, which is at $I_{DC,0}$=-1.15mA and H=860Oe. This induces the free running oscillation frequency at f_0=8.26GHz.

The FSK modulation was achieved by injecting a train of the voltage pulse with amplitude of ±30mV to the steady state free running of the STNO. This leads to a current modulation between two discrete values $I_{DC,1}$=-0.7mA and $I_{DC,2}$=-1.6mA as illustrated in Fig. 4.40. This current modulation stabilizes the power (amplitude) between two levels, P_1 and P_2, around the free running power P_0 (Fig. 4.40a). This power (amplitude) modulation results on the frequency modulation between two discrete values, f_1 and f_2, around the free running frequency f_0 (Fig. 4.40b).

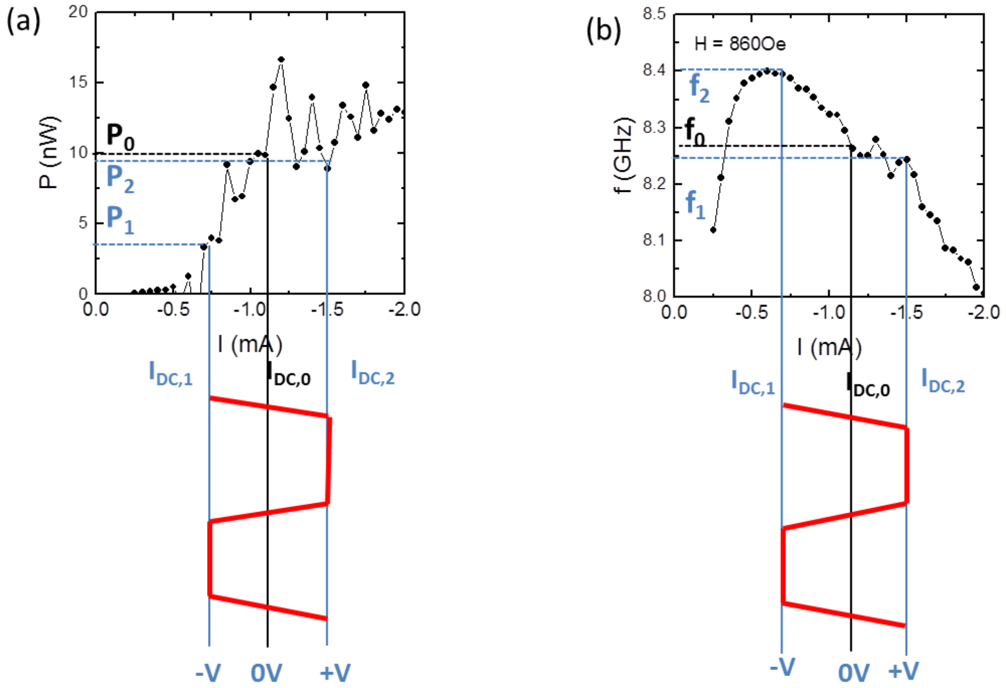

Fig. 4.40-(a) The STNO output power modulation and (b) the frequency modulation under the application of a periodic voltage pulse (red curve) whose amplitude oscillates between positive and negative voltage amplitude. The output power is modulated between two discrete values P_1 and P_2 around the free running power P_0 and the frequency is modulated between two discrete values f_1 and f_2 around the free running frequency f_0.

The STNO response to a train of the voltage pulse for different pulse width T is shown in Fig. 4.41. The pulse width, T, was varied from 500ns to 20ns which corresponds to the variation of the rate (1/T) from 2 Mbps to 50 Mbps. The rise and fall time of the pulse were equally set to 1.8ns and kept constant. In the left side of Fig. 4.41, the time traces of the amplified STNO output voltage signal (grey curve) are displayed. In the right side of the figure, the time traces of the smoothened instantaneous frequency (black curve) extracted from the voltage time traces V(t) using the Hilbert transformation are displayed. The averaging window of the smoothing was adapted according on the pulse width, T, (see in the description of the Fig. 4.41).

For long pulse widths T as shown in Figs. 4.41a,b,c, the amplitude (grey curve) of the voltage time traces can follow the a train of the current pulse. The amplitude is modulated between two discrete values, high and low amplitude level. This results in a full frequency shift, $\delta f \approx 0.15$GHz, between two discrete values, $f_1 \approx 8.25$GHz and $f_2 \approx 8.4$GHz. Above the pulse width of T=100ns, Figs. 4.41d,e, the amplitude of the voltage time traces cannot fully follow the current pulse. The high and low amplitude level cannot be distinguished due to the extinctions. The frequency modulation is no longer observed in this case.

From the results, this can be concluded that the amplitude and frequency modulation is limited to modulation rates of 10Mbps (T=100ns) and this is limited by the noise of the STNO. This maximum modulation rate is the same as obtained for the Hitachi device. The frequency shift in the Hitachi device is however larger than the one obtained in this the Mosaic device. Also, the signal stability of the Hitachi device is better than the one of the Mosaic device, leading to a clearer frequency shift.

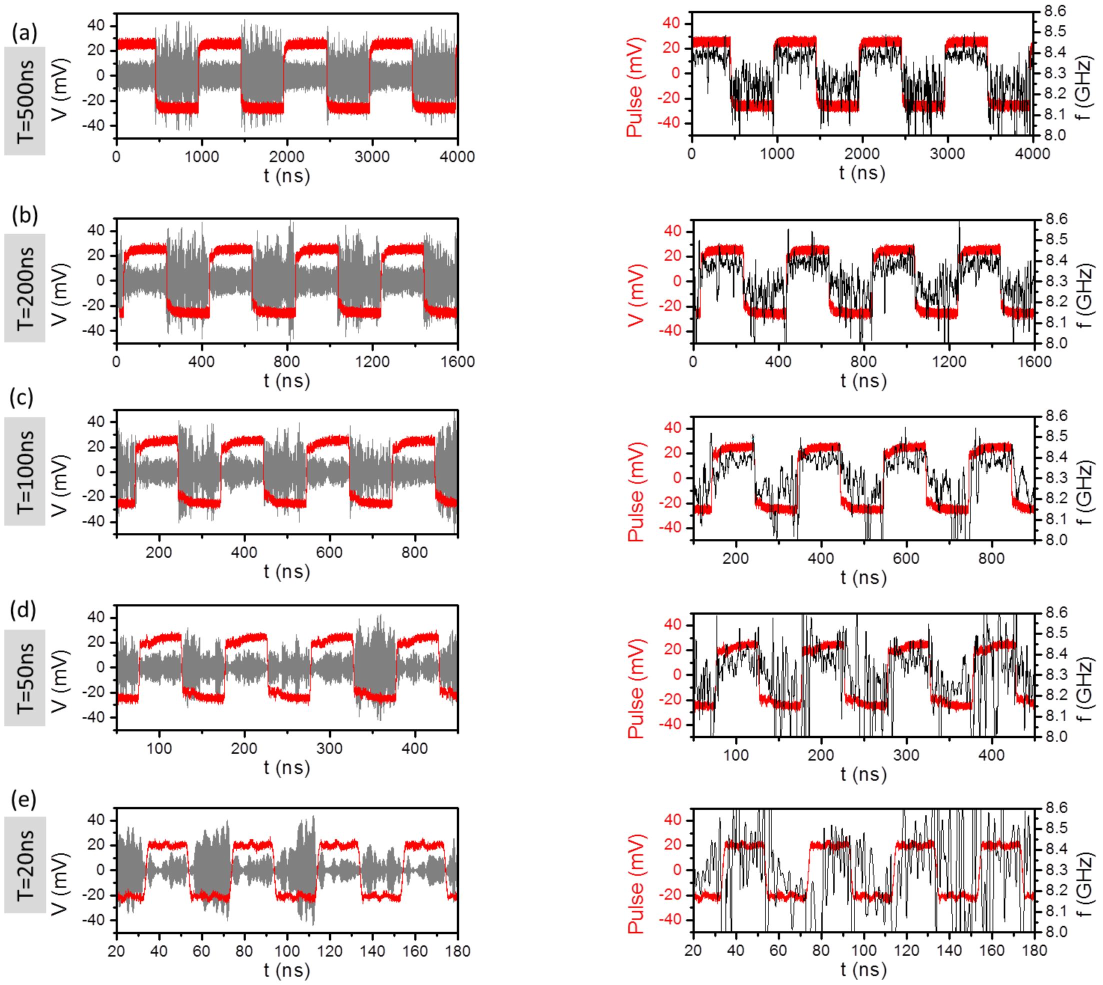

Fig. 4.41-The time domain analysis of the STNO output voltage signal at I_{DC}=-1.15mA and H_{DC}=860Oe, under a periodic voltage pulse with a constant amplitude of V=±30mV and the rise (fall) time of 1.8ns. The pulse width is ranging as follow: (a) 500ns (20ns averaging/50MHz) (b) 200ns (10ns averaging/100MHz) (c) 100ns (10ns averaging/100MHz) (d) 50ns (4ns averaging/250MHz) (e) 20ns (2ns averaging/500MHz). The left figure shows the amplified STNO output voltage signal (grey curve) and the right figure shows the instantaneous frequency of the voltage signal (black curve). The pulse is shown in red for all plots.

4.3.3.3 FSK demodulation: Delay detection calculations

In order to read back the digital voltage signal, the delay detection calculation is carried out in a similar way as for the Hitachi device, explained in the previous section. The previous discussion shows that the FSK demodulation cannot be directly achieved from the delay detection of the output voltage signal due to a strong amplitude modulation in the output voltage time traces. The delay detection of the output voltage signal corresponds to a demodulation of the ASK modulation. The FSK demodulation is achieved by applying the delay detection on the instantaneous frequency of the STNO extracted from the Hilbert transformation of the output voltage signal, i.e. no amplitude modulation. From the frequency shift characteristics, the delay time τ is chosen to be 2.5ns in order to satisfy both the quadrature condition $\tau f_0=n-1/4$ with f_0=8.3GHz, n=21, and the minimum shift keying condition $\tau\delta f=0.5$. The output of delay detection $<V(t)*V(t-\tau)>$ of the voltage signal for different pulse width T (data rate 1/T) is shown in Fig. 4.42.

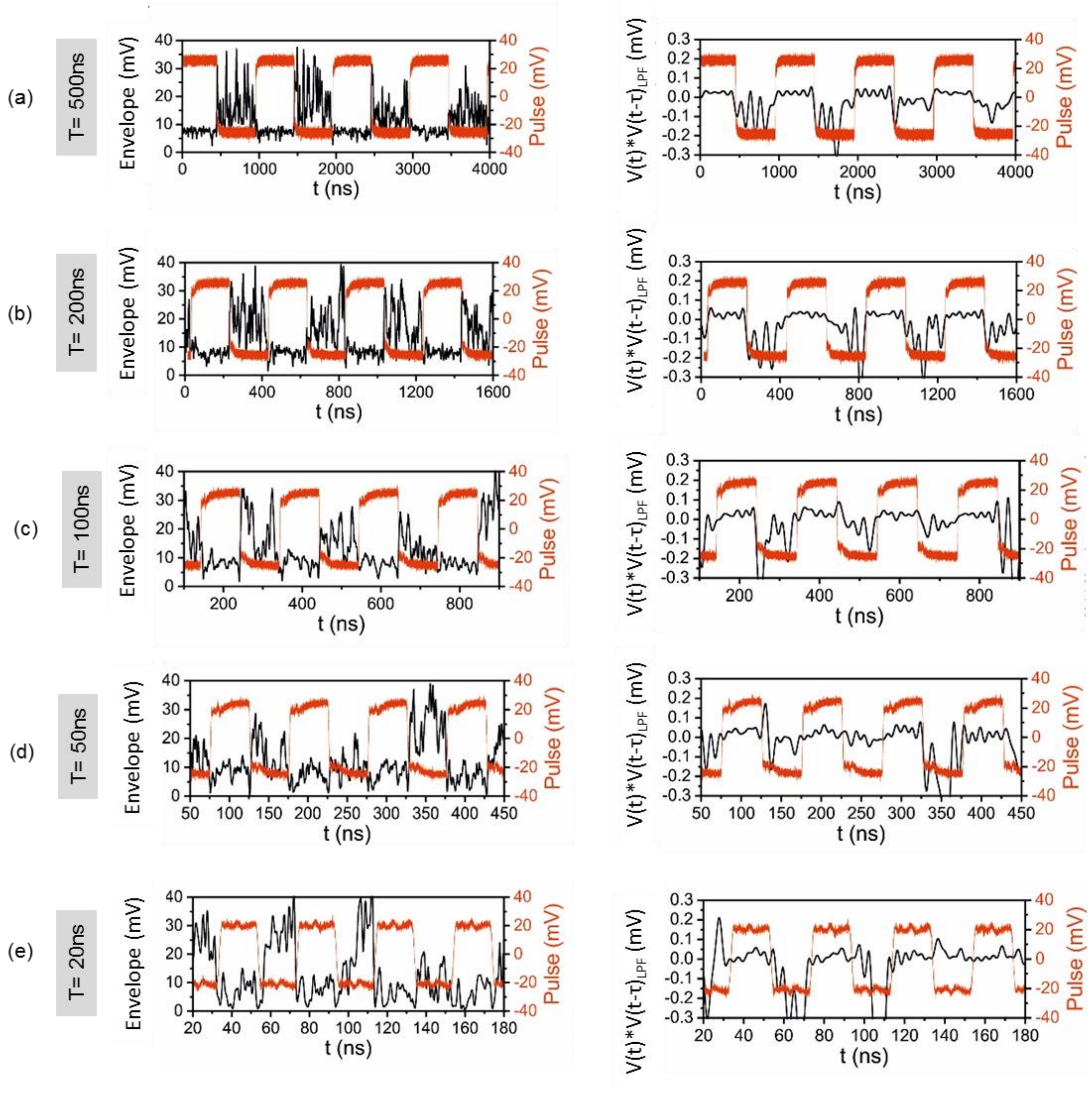

Fig. 4.42-The smoothened amplitude envelope of the STNO output voltage signal V(t) (left side) and the output of delay detection (right side) of the output voltage signal V(t), for different pulse width: (a) 500ns (LPF=10MHz) (b) 250ns (LPF=25MHz) (c) 100ns (LPF=50MHz) (d) 50ns (LPF=100MHz) and (e) 20ns (LPF=250GHz).

In the left side of the figure, the positive envelope of the output voltage signal V(t) is displayed in order to be compared with the output of delay detection of the output voltage signal V(t) given in the right side of the figure. To analyze the results, the envelope of the output voltage signal is smoothed to further reduce the noise with the average window is less than the pulse width T. The output of delay detection is filtered using LPF filter to remove the high frequency component. The amplitude demodulation demonstrates that the output of delay detection is not clearly observed at any given data rate. Indeed at long pulse width T=500ns, the two levels of the digital voltage can still be distinguished but these two levels separation is too small due to the high noise in the high level of the amplitude modulation shown in the left figure of Fig. 4.42. For short pulse widths, the high and low level of the digital voltage cannot be separated. In contrast to this, the output of the delay detection of the frequency shift shown in Fig. 4.43-right demonstrates a clear demodulation of the FSK signal. It is seen that the output of the demodulation signal varies from some negative to positive values arises from the frequency change, f_1 and f_2. At data rates from 2Mbps (T=500ns) to 20Mbps (T=50ns), the frequency shift can clearly be decoded into digital voltage signal, positive and negative voltage, which represents the state of the digital signal ‘1’ and ‘0’ respectively. Above 20Mbps (T=50MHz), the demodulation cannot be observed. The two levels of the digital output voltage cannot be distinguished.

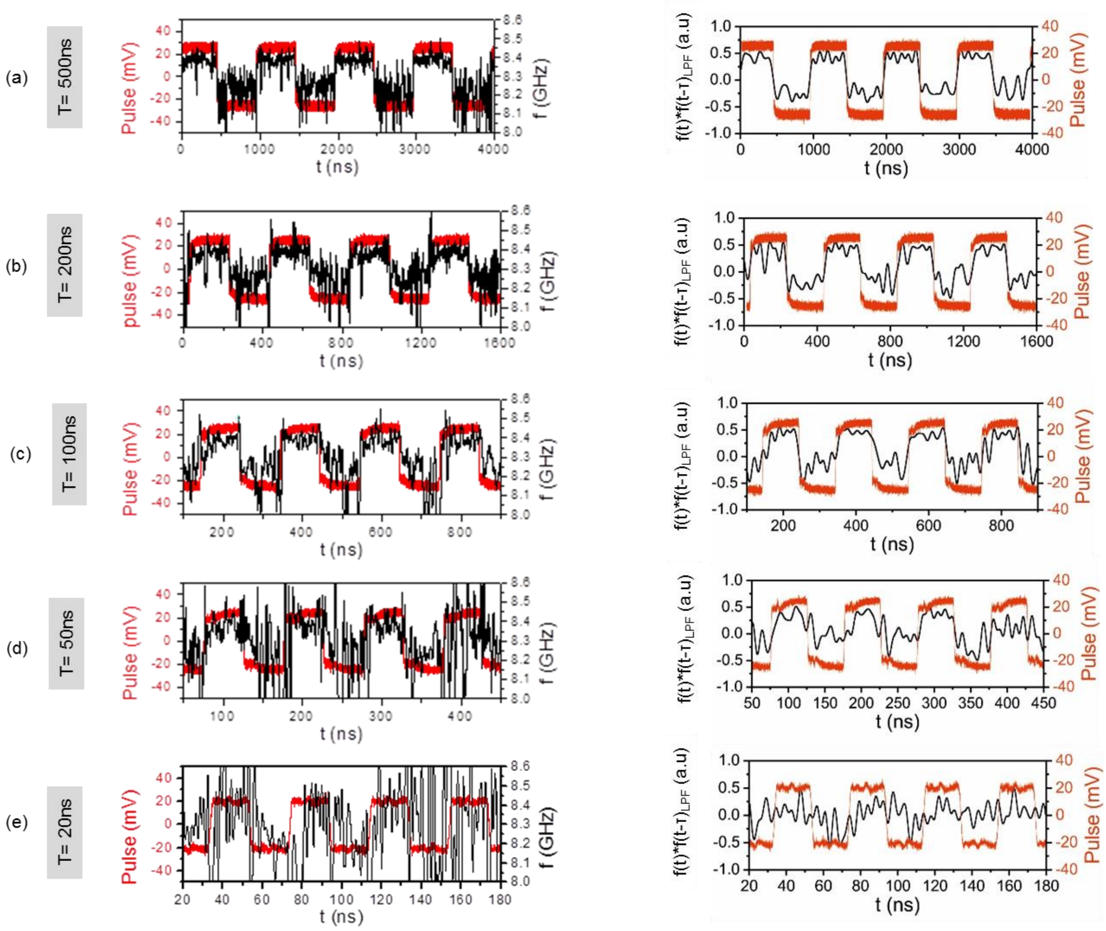

Fig. 4.43- The smoothened instantaneous frequency of the STNO output voltage signal V(t) (left side) and the output of frequency delay detection (right side) for different pulse width: (a) 500ns (LPF=10MHz) (b) 200ns (LPF=25MHz) (c) 100ns (LPF=50MHz) (d) 50ns (LPF=100MHz) and (e) 20ns (LPF=250MHz).

From the demodulation results, it can be concluded that the demodulation of ASK signal is difficult to achieve due to the high amplitude noise. Whereas, the demodulation of FSK signal up to 20Mbps is possible but it is noisy. A clear demodulation is thus limited to 10Mbps, the same as the one observed for the Hitachi device.

4.3.3.4 Conclusion

From the experimental results and analysis of the FSK modulation of the Mosaic device RFL741, it can be concluded as follows:

- The best operation of the studied Mosaic device for FSK modulation was achieved at a field value of H = 860 Oe and the field angle of -7 degree. The steady oscillations occurs at low threshold current I_{th}=-0.5mA due to the use of a composite free layer. The frequency-current tuning above the threshold current is -400 MHz/1.4mA, for the DC current varies from -0.6mA to -2 mA. Within this current range, the linewidths below 100 MHz are achieved with the output power varies from 2nW to15nW. The signal stability is worse compared to the one observed for the Hitachi device. The extinction occurs at short period of 1-80ns, i.e. no long term steady state.
- The variation of the pulse width T (pulse rate 1/T) shows that the maximum modulation rate for ASK modulation of the Mosaic device is limited to 10Mbps which is lower compared to the ASK modulation of the Hitachi device, while for FSK modulation it is limited to 10Mbps at full frequency shift of 150MHz i.e. from $f_1 \approx 8.25$GHz and $f_2 \approx 8.4$GHz, and to 20 Mbps at reduced frequency shift. The reason that this is less than the limit for amplitude modulation is seen in the relatively high phase noise of the device analysed.
- The output of delay detection calculation for ASK modulation shows that the digital voltage input can be read back at the demodulation rate of 2Mbps due to the poor signal stability. For the FSK demodulation, the digital output voltage can be read up to the demodulation rate of 10Mbps, i.e. the same data rate for the Hitachi device.

4.3.4 Summary of the FSK measurements on standalone STNOs

The experimental demonstrations of the FSK current modulation performed on standalone STNOs for two different types of nanofabricated STNO devices, i.e Hitachi and MOSAIC device, have been demonstrated. The measurement results of both devices are summarized in this section. The comparison of the dynamic performances, i.e. free running state, and the FSK measurements of both devices are given in table 4.2.

Consistent with the characterization results discussed in Chapter 2, the Hitachi devices have a clear single mode behavior and no SAF excitation which is desirable for many applications. This single mode steady state excitation is characterized by the high output power of 100nW (-40dBm) and the linewidth narrower than 20MHz. Furthermore long term signal stability over 42μs is achieved for this device. In contrast to this, the dynamics of the MOSAIC device RFL741 are weakly multimode excited with the main mode goes into steady state. The maximum output power achieved for this device is less compared to the Hitachi device, which is 15nW (-48dBm). The signal stability is achieved only in a short period, 1 to 8ns. The minimum linewidth is however comparable with the Hitachi device, lower than 20MHz. Besides that, the threshold current I_{th} of the RFL741 device is smaller than the one of Hitachi device, which is good for applications, leading to low power consumption. The signal stability and the output power however need to be improved since this is crucial for the realization of the FSK modulation.

In terms of the FSK results, the maximum data rate of ASK modulation and demodulation of the Hitachi device is limited to the data rate below 100Mbps. While the data rate of the FSK modulation and demodulation is limited to 10Mbps at a full frequency shift of δf=200MHz. This limit is given by the noise of the STNO. For RFL741, the ASK modulation is limited to 10Mbps, while the data rate of the demodulation is limited to 2 Mbps. This limit is given by the poor signal stability of RFL741 characterized by the amplitude extinctions at short periods, 1ns-80 ns. The data rate of the FSK modulation and demodulation can be achieved up to the data rate of 10Mbps, the same as for the Hitachi device, with smaller frequency shift δf=150MHz. The optimization and the development of the nanofabrication processes are of importance for the improvement of the signal stability and the output power of Mosaic devices to perform better FSK modulation.

Table 4.2. The comparison of the dynamic performance, i.e. free running state, and the FSK measurements of the Hitachi device and the MOSAIC device.

No.	Parameters	Hitachi	Mosaic RFL741
1	Device stacks	IrMn (6.1nm)/ CoFe (1.8nm)/ Ru (0.4nm)/ CoFeB (2nm)/ MgO/ CoFe (0.5nm)/ CoFeB (3.4nm)/Ru/Ta/Ru	PtMn (20nm)/ CoFe (2nm)/ Ru (0.85nm)/ CoFeB (2.2nm)/MgO/ CoFeB (1.5nm)/Ta/FeNi (2nm)/Ta/Ru
2	Nanopillar's size	Circle 90nm	Circle 115nm
Dynamic characterization			
3	RA	$1\Omega\mu m^2$	$1.5\Omega\mu m^2$
4	R_{AP}	125 Ohm	157Ohm
5	TMR	54%	49%
6	Multimode	No (clear single mode)	Very weak multimode
7	SAF excitation	No	Weak SAF excitation
8	$I_{th}/I_{DC,max}$	1.5mA/ 2.1mA	-0.5mA/ -2mA
9	df/dI	≈160MHz/0.4mA ≈400MHz/mA	≈-400/1.4mA ≈-285MHz/mA
10	I_{DC}/H_{DC}/angle	1.8mA/ 750Oe/ -28degree	1.15mA/ 860Oe/ -7degree
11	f, Δf_{min}, P_{max}	9.18GHz/ 15MHz/ 125nW	8.26GHz/ 20MHz/ 15nW
12	extinction	No extinction for 42µs long	1-80ns
FSK parameters			
13	Frequency shift	δf=200MHz, with f_1=8.9GHz andf_2=9.1GHz	δf=150MHz, with f_1=8.25GHz and f_2=8.4GHz
15	ASK modulation rate	Below 100Mbps	10Mbps
16	FSK modulation rate	10Mbps @ full δf=200MHz (possible up to 40Mbps at reduced δf)	10Mbps @ full δf=150MHz (possible up to 20Mbps but it is too noisy)
17	ASK demodulation rate	Below 100Mbps	2Mbps
18	FSK demodulation rate	10Mbps	10Mbps

4.4 FSK measurements within RF emitter

In order to investigate the feasibility of STNOs within microwave systems (RF emitter), the FSK measurement of STNOs was performed on a printed circuit board (PCB) level in collaboration with the partner of the Mosaic FP7 project, the Technische Universität Dresden (TUD). In this work, TUD was responsible for the design and the realization of the RF emitter. The author was responsible to select STNO devices of suitable RF performances and realized the RF characterization together with Rui Ma from TUD. The parameters addressed in this measurement are the achievable frequency shift and the maximum modulation rate, up to which the frequency can be shifted between two discrete values. These parameters were characterized upon varying the pulse width of the current/voltage pulse. For the demodulation part, the delay detection technique, proposed by Toshiba [33], was carried out numerically. Before summarizing the FSK measurement results, the schematic of the FSK measurement using PCB emitter card will be discussed in the following.

4.4.1 PCB emitter card

In this Section, the schematic of the PCB emitter card and the experimental setup of the FSK measurement using the PCB emitter card will be discussed. The first discussion focuses on the schematic of the PCB emitter card to understand how the FSK can be performed within the card. In the second part, the experimental setup of the FSK measurement using the PCB emitter card will be described.

4.4.1.1 Schematic of the PCB emitter

The PCB emitter was designed and realized by TUD. The schematic design of this emitter based on FSK modulation is shown in Fig. 4.44. Fig. 4.44a shows the schematic of the STNO emitter in the fabricated PCB and Fig. 4.44b shows the simplified block diagram of the STNO emitter.

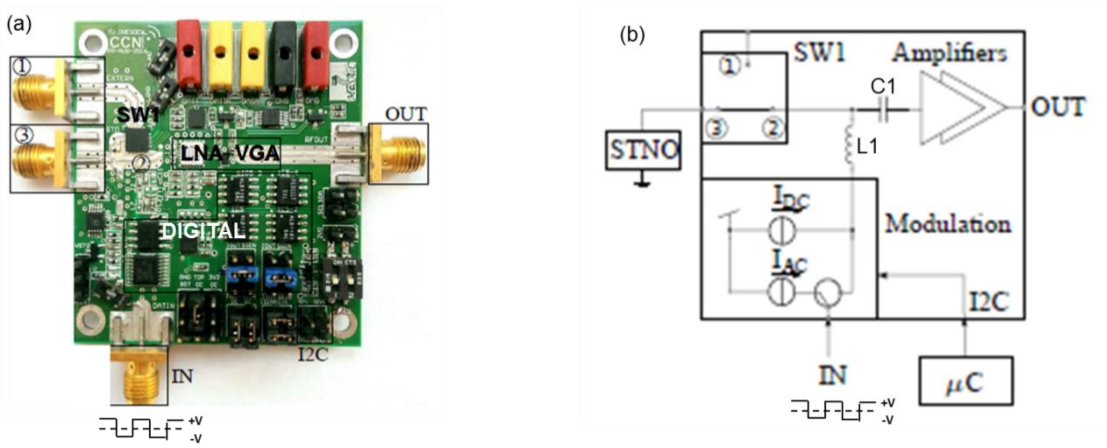

Fig. 4.44-(a) STNO emitter implemented on a PCB level. SMA connector IN, OUT, (1), (3), and jumper I2C correspond to the pin with the same name in Fig (a), which are the main interface of this PCB. (b) The simplified block diagram of the STNO emitter based FSK modulation.

Key interfaces of the emitter are (1), (3), OUT, IN and I2C. (1) is the connection to the external RF characterization setup in SPINTEC. (3) is the connection to the STNO and thus to the PCB card. IN is the connection to the data input, and OUT is the output of the FSK modulation. I2C is the interface to the microcontroller (μC) board. The STNO emitter is composed mainly of two parts, the digital modulation part which generates the two discrete current values, and the RF part which amplifies the AC signal coming from the STNO. A Bias-Tee (composed by L1=25nH and C1=100pF) is positioned between the digital and the RF part to separate the DC and AC parts, so that only the AC parts are passed to the output of the emitter (OUT). The digital part is controlled by a microcontroller (μC) board with an I2C interface and a self-developed Phyton program to send the current to the μC board.

The detail of the digital part is shown in Fig. 4.45. It consists of a differential CMOS transistor pair N1 and N2, and two current sources I_{AC} and I_{DC}. Output currents of the two current sources are controllable by the μC board via its I2C interface. The differential pair is controlled by the input binary data (a squared voltage pulse) coming into the SMA connector IN. During working, only one of the differential pair is on, and two currents flowing through the STNO are obtained: (1) $I_{STNO} = I_{DC}$ when N1 is on and N2 off, (2) $I_{STNO} = I_{DC} - I_{AC}$ when N1 is off and N2 on. Thus the current flowing through the STNO is shifted between two values I_{DC} and $I_{DC} - I_{AC}$. Both of I_{DC} and I_{AC} are tunable through the μC board in the range between 0 to 10 mA, according to the STNO characteristics (resistance, emitted frequency and etc.). An operational amplifier (OPA) with an input resistor 2.5Ω is added into the path where I_{STNO} flows to exactly monitor the modulation current or digital pulse felt by the STNO.

The RF part consists of an RF DC switch (SW1) with an insertion loss of -1.3dB over 0 to 8GHz, a low noise amplifier (LNA) with 15dB gain over 1GHz to 10GHz and a variable gain amplifier (VGA) with 10dB gain at bandwidth of 20GHz.

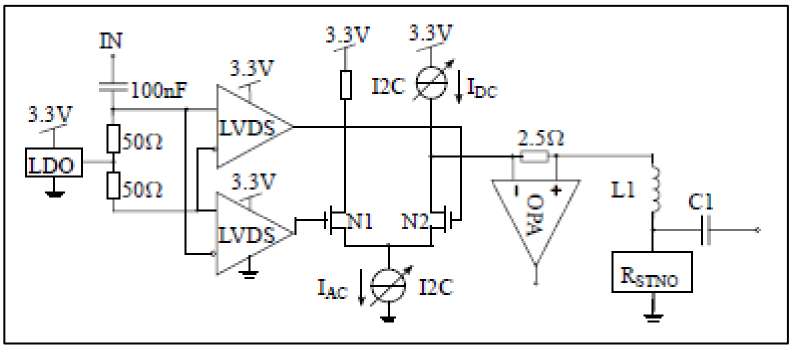

Fig. 4.45-Detail of the digital (modulation) part together with the bias-Tee and STNO.

4.4.1.2 Experimental setup

The experimental setup of the FSK measurement within emitter card is shown in Fig. 4.46. The same as in the previous FSK measurements, a previous characterization of the STNO is necessary in order to find the optimum conditions to achieve steady state oscillations to ensure the FSK modulation. For the STNO characterization, point (3) and (1) of both the switch SW1 on the modulation board and the switch SW2 were connected. This corresponds to an RF measurement using a standard RF setup. In this way, a DC current generated by Keithley 2401 source meter is injected into the STNO via the inductive part of an external bias-T, and the RF signal is extracted via the capacitive part. This signal is then amplified using an external power amplifier Miteq AMF-5D with a 43 dB gain over 100 MHz to 12 GHz, connected to a 3-10 GHz bandpass filter. A power divider is used to split the signal which is monitored by sampling oscilloscope Textronix DPO72004 with a single shot capability of 50 Gs/s and a spectrum analyzer Agilent PNAE8363B with a bandwidth of 1 MHz to 40 GHz. In order to find the operational conditions of current and field that yield steady state oscillations of the magnetization, the current and field are swept and the output signal from the spectrum analyzer is analyzed in view of its linewidth, frequency tunability df/dI, and power. A low linewidth, large df/dI and large output powers are desired for a successful FSK modulation.

In order to test the FSK modulation, ports (3) and (2) are now connected of both SW1 and SW2. Values of the DC current I_{DC} and the AC current I_{AC} are set via the µC board using a computer with the self-written Python program. The modulation of the signal is achieved in the same way as explained in the digital part (refers to Fig. 4.45). The output voltage signal was internally amplified by LNA and VGA in the RF part with the total amplification of 15dB at the bandwidth of 4GHz. Since the frequency of the STNO varies from 5-10GHz, an external amplifier of 43dB in the frequency range of 100MHz to 12GHz is used to enhance the low gain at high frequency. The amplified signal is filtered using a 3-10 GHz bandpass filter (BPF). The data measurement is displayed and registered by the spectrum analyzer and oscilloscope.

The characterization of the emitter card performed by TUD estimated that the maximum data rate of the emitter is limited to 20 Mbps due to the non-optimize RF components. Hence the maximum data rate of the FSK meausrement will be limited by the emitter card and nit to the dynamic parameters of the STNO.

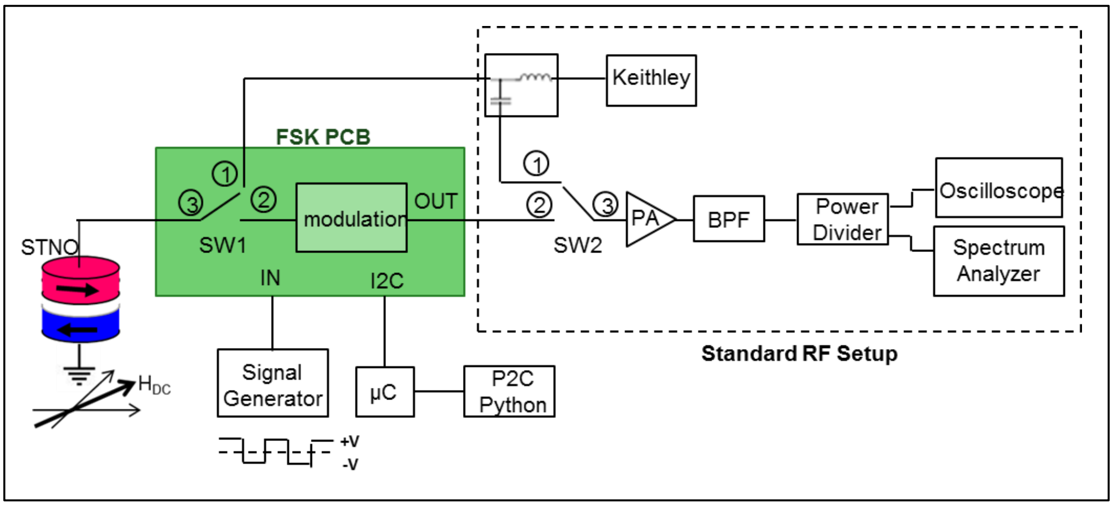

Fig. 4.46-Experimental setup for STNO based FSK modulation. For STNO characterization, point (3) of SW1 and SW2 was connected to point (1) of the corresponding switch. For FSK modulation, point (3) of SW1 and SW2 was connected to point (2).

4.4.2 Characterization of the free running Hitachi device

Before summarizing the FSK measurement results, the RF characterization of the free running STNO Hitachi device will be discussed. As already mentioned, this RF characterization aims to determine the best working conditions of the STNO for FSK modulation. A large frequency current tenability, df/dI, low linewidth, and large output power of the STNO are important parameters to perform a successful FSK modulation.

The Hitachi device measured for this measurement has an ellipse shape of 65nm x 130nm. The corresponding TMR is ≈50% with the antiparallel resistance of 215Ohm as given in Fig. 4.47a. The dynamic characterization was performed at positive field and at a magnetic angle of 15degree with respect to the easy axis direction. The corresponding PSD of the frequency versus field at a fixed DC current of 1mA is given in Fig. 4.47b. The PSD shows a clean single mode excitation of the free layer with the second harmonic appears at 2f. The SAF pinned layer is rigid enough so that there is no SAF excitation.

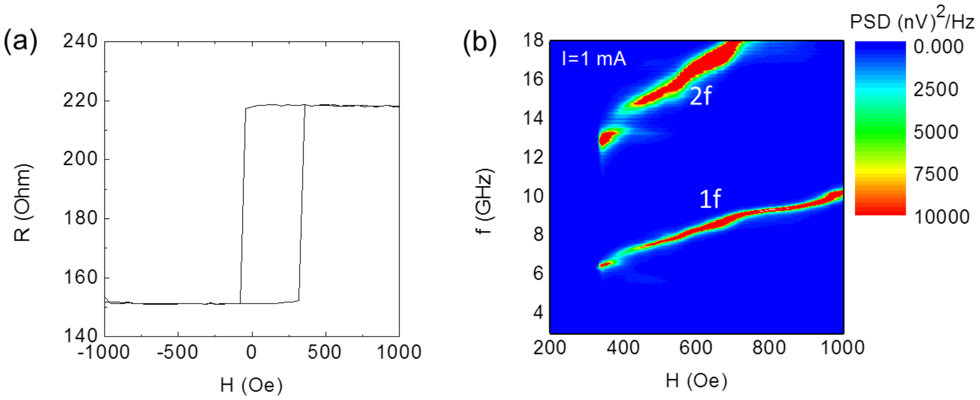

Fig. 4.47-(a) The magnetoresistance curve obtained at low applied DC current I_{DC}=0.05 mA and at applied field angle of 15degree off the polarizing layer. (b) The PSD of the frequency versus field for a fixed DC current I_{DC}=1mA.

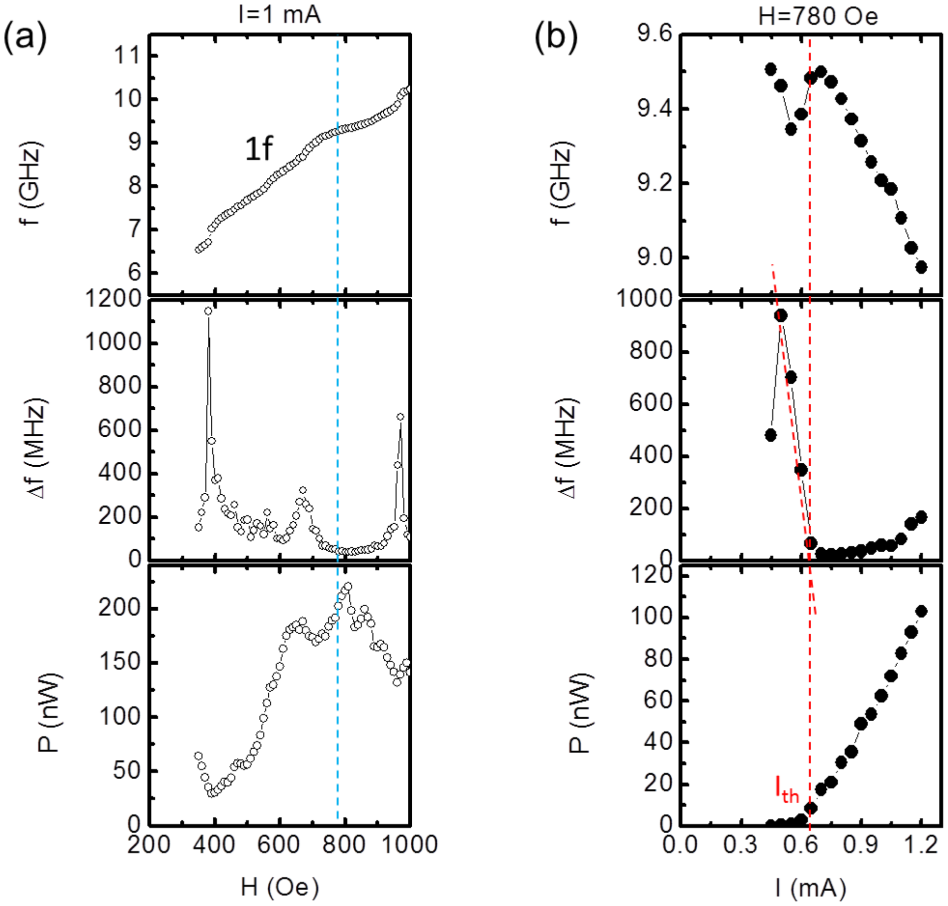

Fig. 4.48-(a) The frequency, linewidth, and the output power of the first harmonic excitation as a function of applied magnetic field for a fixed applied DC current I_{DC}=1mA. (b) The frequency, linewidth, and the output power of the first harmonic excitation as a function of applied DC current for a fixed applied magnetic field H_{DC}=780Oe.

The analysis of the frequency, linewidth and the output power of the first harmonic excitation 1f as a function of applied field for a fixed DC current of 1 mA are shown in Fig. 4.48a. The frequency increases upon increasing the field and it is bent at a field around 700Oe-900Oe. In this field range, the linewidths are narrower than 100MHz and the output powers are larger than 150nW. Fixing the field at which the linewidth minimum, i.e. 780Oe (blue dashed line), the current dependence is obtained. The analysis of the frequency, linewidth, and the output power as a function of applied current for a fixed magnetic field 780Oe is shown in Fig. 4.48b. The threshold current is 0.6mA above which the steady oscillation is obtained. The steady state oscillation is characterized by the relatively large frequency-current tuning, df/dI=-530 MHz/0.5 mA, minimum linewidths of around 13MHz, and the output powers of up to 100 nW, which are of interest for FSK modulation.

In order to investigate the signal stability of the STNO, the time domain characterization was performed for different applied current. The results are shown in Fig. 4.49. From left to the right side of the figure are the 100ns time traces, the 4ns time traces, the histogram of positive envelope of the output voltage signal, and the histogram of the extinction. The signal stability increases as the applied current increases. This is shown by the evolution of the amplitude, the distribution of the histogram of the envelope, and the less number of extinctions during 42μs long. At the threshold regime I_{DC}=0.6mA (Fig. 4.49a), the amplitude signal is very low which is comparable to the background noise level (0.025V). The histograms of its positive signal envelopes are distributed almost around 0V and many events of extinction occur at short period of 1ns-30ns, i.e. the oscillations are sustained only at very short period. Increasing the current, I_{DC}=0.7mA (Fig. 5.49b) and I_{DC}=1.1mA (Fig. 4.49c), the amplitude signal increases. This is shown by the distribution of the envelope of the signal which is shifted away from 0V. The number of extinctions at I_{DC}=0.7mA is very less compared to the one at low current. While at I_{DC}=2mA, a sustained oscillation over long (40μs) time scales is obtained, which is good for FSK demonstration.

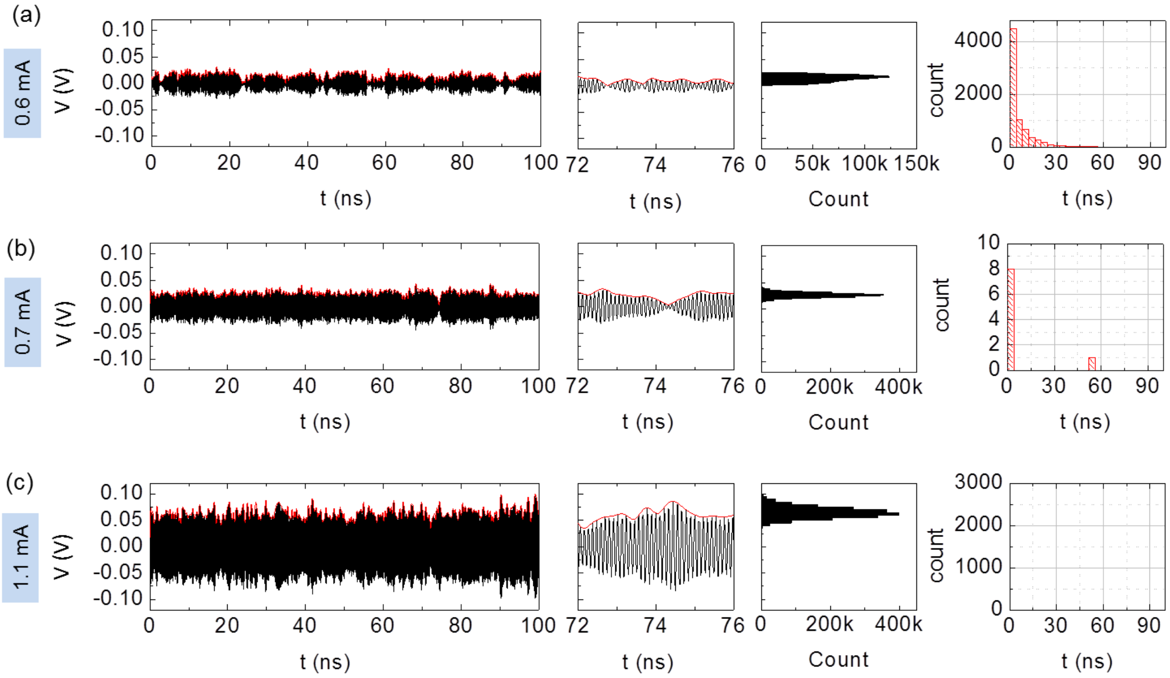

Fig. 4.49-From left to right: 100ns and 4ns long segments of the measured time traces (total length 40μs), histograms of the positive signal envelopes and the time between extinctions for: (a) I_{DC}=0.6mA (threshold current), (b) I_{DC}=0.7mA (intermittent regime) and (c) I_{DC}=1.1mA (steady state regime). A numerical filter of ±2GHz from the centered oscillation frequency was applied on the time traces during analysis to improve the signal stability.

The frequency and time domain characterization discussed above were performed using standard RF setup as discussed in Chapter 2 Section 2.1. The time domain characterization shows that a sustained oscillation over long (40μs) time scales is obtained for the applied current above the threshold current. For comparison, the same characterization was also performed using RF emitter setup discussed previously in Section 4.4.1.2. The results are shown in Fig. 4.50.

4.4.3 FSK measurement results

This section discusses the results of the FSK measurement of the integrated STNO within RF emitter. Before summarizing the results of the FSK measurement, the characterization of the RF emitter card will be discussed. This characterization is an important step to investigate the RF emitter performances and to understand the measurement results.

4.4.3.1 Characterization of the RF emitter

In order to investigate the performance of the RF emitter card, the time traces of the free running STNO was measured using RF emitter setup. The schematic of the RF emitter setup can be seen in Fig. 4.46. For the free running measurement (no modulation), the RF emitter point (3) and (2) of both the switch SW1 and SW2 were connected. The DC current of I_{DC}=1.1mA (above the threshold current) and the AC current of 0mA was injected into the STNO through the µC board and then via the I2C. The magnetic field of 780Oe and oriented at angle of 15 degree was also applied to the STNO. This induces a steady state oscillation of the free running STNO at oscillation frequency of f_0=9.1GHz since the no AC current flowing to the digital part. The time traces of the free running steady state STNO under these parameters was registered in the oscilloscope for 42µs long. This time trace is then compared to the time traces of the free running STNO measured using standard RF setup (see Chapter 2 Section 2.1.1) that has been discussed in the previous Section. The comparison is shown in Fig. 4.50.

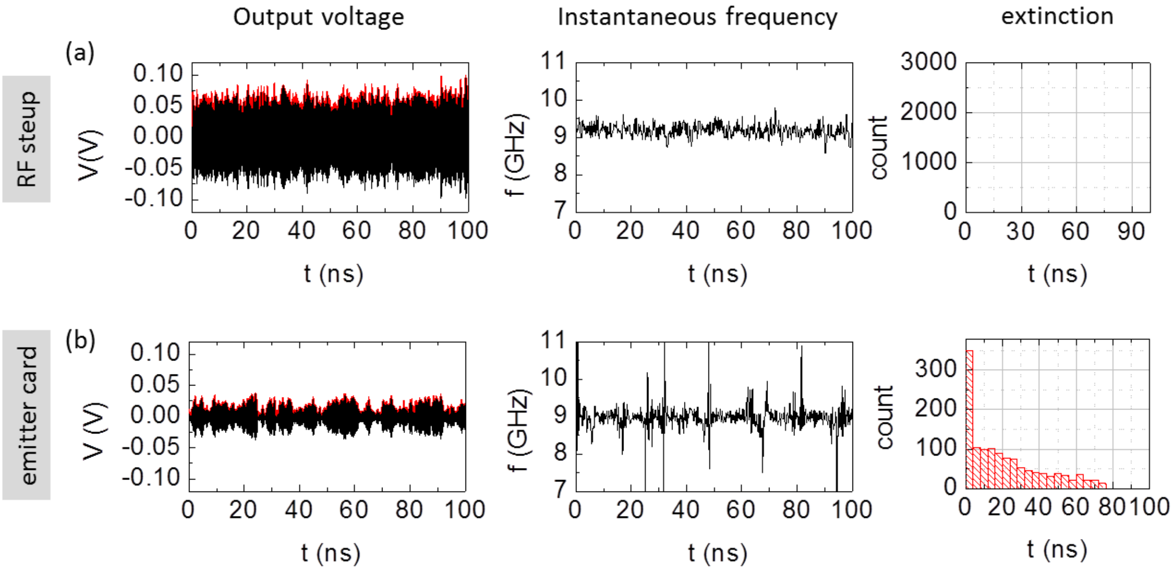

Fig. 4.50-Comparison of the time traces measurement of the free running STNO at I_{DC}=1.1mA and H_{DC}=780Oe, using (a) standard RF setup and (b) RF emitter card. A numerical filter of ±2GHz from the main oscillation frequency was applied on both time traces.

Fig 4.50a shows the time traces measured via the standard RF setup (has been shown in Fig. 4.49c, Section 4.4.2). Fig. 4.50b shows the time traces measured using the RF emitter card. A numerical filter of ±2GHz from the main oscillation frequency was applied on both time traces to improve the signal stability. A quite different output voltage signal was observed. The voltage time traces measured using the standard RF setup has very good signal stability, only the high amplitude signal peak exists, meaning that the oscillations are sustained over long (40µs) time scales without extinctions (4.50a). This results on a small fluctuation frequency around the average value f_0=9.1GHz. In contrast to this, the time traces measured using the RF emitter card has poorer signal stability as shown in Fig. 4.50b. This is shown by the lower amplitude of the output voltage signal which is close to the noise level and the large numbers of extinctions, i.e. oscillations are sustained only at very short period of 20-80ns. This extinction is responsible for the presence of the spikes in the instantaneous frequency fluctuation for example at 25ns, 31ns, 49ns, 64ns, 80ns, and 94ns. This comparison shows that the performance of the RF emitter needs to be improved. The poor time traces from RF emitter is due to the noise figure of electronics components, i.e. amplifier, in the emitter card. This noise figure is much higher than the one of standard RF setup. This noisy and low output signal would be a problem for the detection in the receiver.

4.4.3.2 FSK measurement results

For the FSK measurement, the DC current and AC current were simultaneously injected into the digital part, see Fig. 4.46. The DC current I_{DC} value was set to 1.2mA and the AC current I_{AC} was set to 0.3 mA. This corresponds to a current modulation between I_{DC}=1.2mA and I_{DC}–I_{AC}=0.9mA. This current modulation is expected to induce the frequency modulation into two frequency values f_0≈9GHz and f_1≈9.3MHz as can be seen in the frequency versus current plot in Fig. 4.48. The pulse width was varied between T=500ns to T=50ns which corresponds to a variation of the data rates, 1/T, between 2Mbps to 20Mbps. The results are shown in Fig. 4.51.

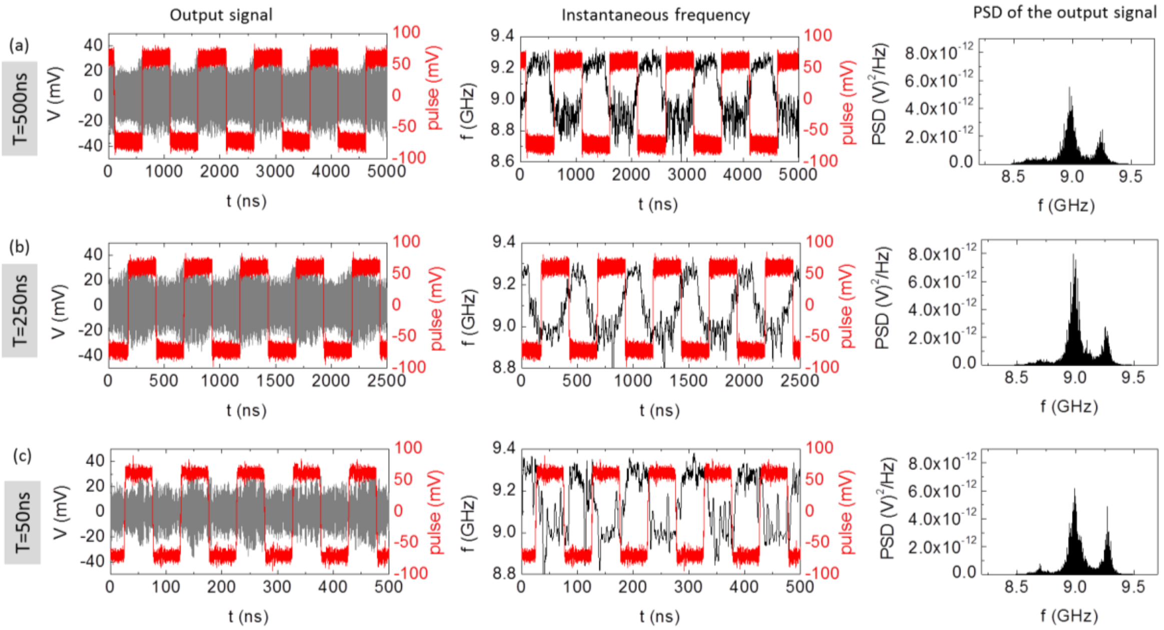

Fig. 4.51-The FSK measurement results for different bit length T (a) T=500ns, (b) T=250ns, and (c) T=50ns. The left figure shows the output voltage signal of the FSK measurement. The smoothed instantaneous frequency is shown in the middle of the figure. The averaging window of Savitzky-Golay frequency smoothing algorithm is 20 ns, 20ns, and 6ns for the bit length of 500ns, 250ns, and 50ns, respectively. The right side of the figure shows the PSD of the output voltage signal.

In the left side of Fig. 4.51, the output voltage signal for different pulse width T is shown. A modulation of the amplitude is clearly seen for long pulse widths, 500ns to 250ns. However at a short pulse width of T=50ns (Fig. 4.51c), the amplitude modulation is not clearly observed due to the noise. In order to analyze the frequency shift, the instantaneous frequency is obtained from the first derivative of the phase extracted from the Hilbert transformation of the output voltage signal. To reduce noise, the Savitzky-Golay frequency smoothing algorithm is used with an averaging window less than the pulse width T ns (see in the description of Fig. 4.51). The smoothed instantaneous frequency for different pulse width T is shown in the middle of Fig. 4.51. The frequency shift between 9GHz ($I_{STNO}=I_{DC}=1.2mA$) and 9.33GHz ($I_{STNO}=I_{DC}-I_{AC}=0.9mA$) is observed up to pulse width of 50ns (data rate of 20Mbps). This frequency shift is also clearly observed in the power spectral density of the output voltage signal as shown in the right side of Fig. 4.51. A main frequency peak at around 9GHz has higher amplitude (power) than the second peak at around 9.33GHz, which is in accordance with the dependence of the power versus current as shown in Fig. 4.48. The existence of two peaks in the PSD of the output voltage signal gives a proof that the FSK modulation for this device is successfully demonstrated.

4.4.3.3 FSK demodulation: Delay detection calculation

Since the demodulation of the FSK signal using delay detection technique within the receiver card has not been successfully demonstrated yet, the demodulation here is carried out numerically. The delay detection calculation is carried out separately for ASK modulation and FSK modulation. The delay detection for ASK modulation and FSK modulation at different pulse width T (data rate 1/T) are shown in Fig. 4.52 and Fig. 4.53, respectively. The delay time τ is chosen to be 1.51ns to satisfy both the quadrature condition $\tau f_0=n-1/4$ with $f_0=9.15GHz$, $n=15$, and the minimum shift keying condition $\tau\delta f=0.5$. In Fig. 4.52, the left figures show the smoothed envelope of the output voltage signal and the right figures show the demodulation of ASK signal, i.e. the autocorrelation of the output voltage signal and its delayed version, $<V(t)*V(t-\tau)>$. The low pass filter is applied in the output of delay detection, $V(t)*V(t-\tau)_{LPF}$, to remove the high frequency components. The output of delay detection has so much in common with the envelope of output voltage signal, i.e. the amplitude fluctuation at high level of the demodulation output is higher than the one at low level. The digital output voltage of demodulation varies from positive to negative voltage, ±0.1mV, which coincides with the digital input voltage pulse. Thus, the ASK signal can nicely be decoded into a train voltage pulse up to data rate of 20Mbps. Similar results are obtained for the demodulation of FSK signal shown in Fig. 4.53. The output of delay detection (right figures) coincides with the FSK signal (left figures). Thus, the FSK signal is able to be decoded into a train pulse with ±0.5 amplitude variation up to data rate of 20Mbps.

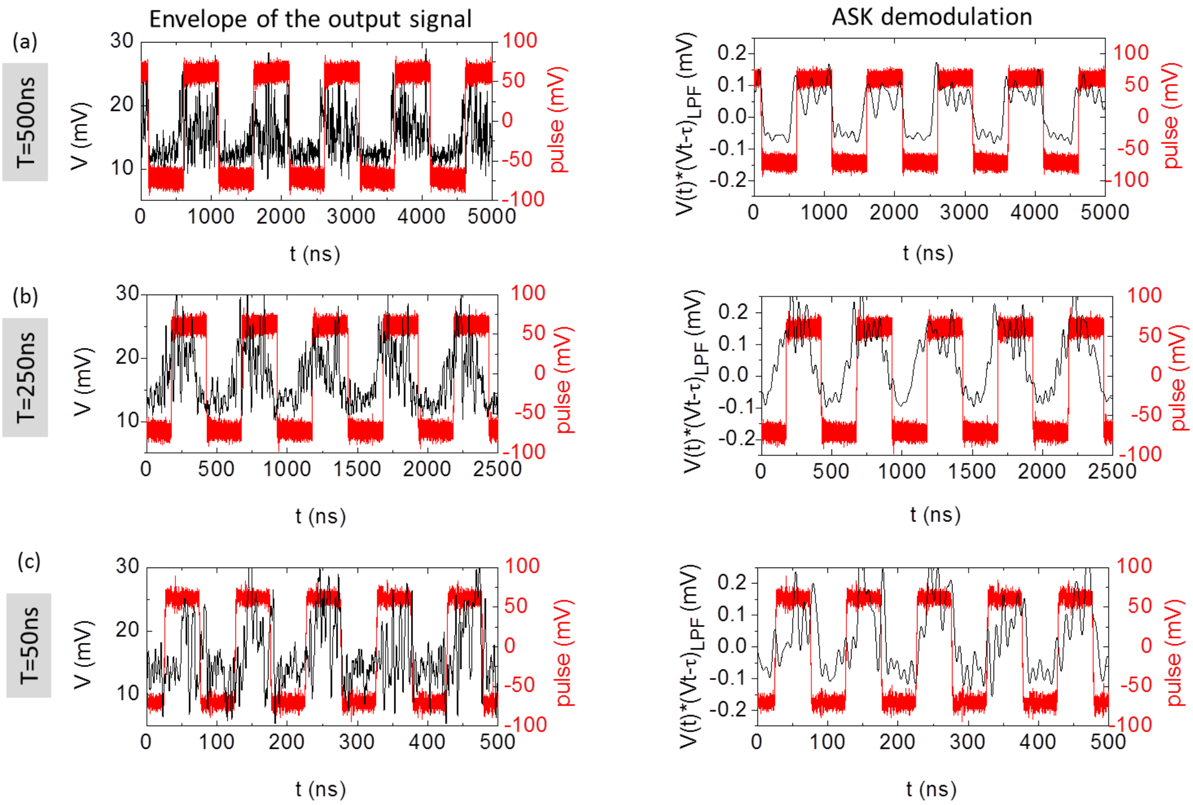

Fig. 4.52-(a) The smoothed envelope of the output voltage signal and the delay detection of the output voltage signal, <V(t)*V(t-τ)>, for different bit length T: (a) T=500ns (LPF=10MHz), (b) T=250ns (LPF=20MHz), and (c) T=50ns (LPF=100MHz).

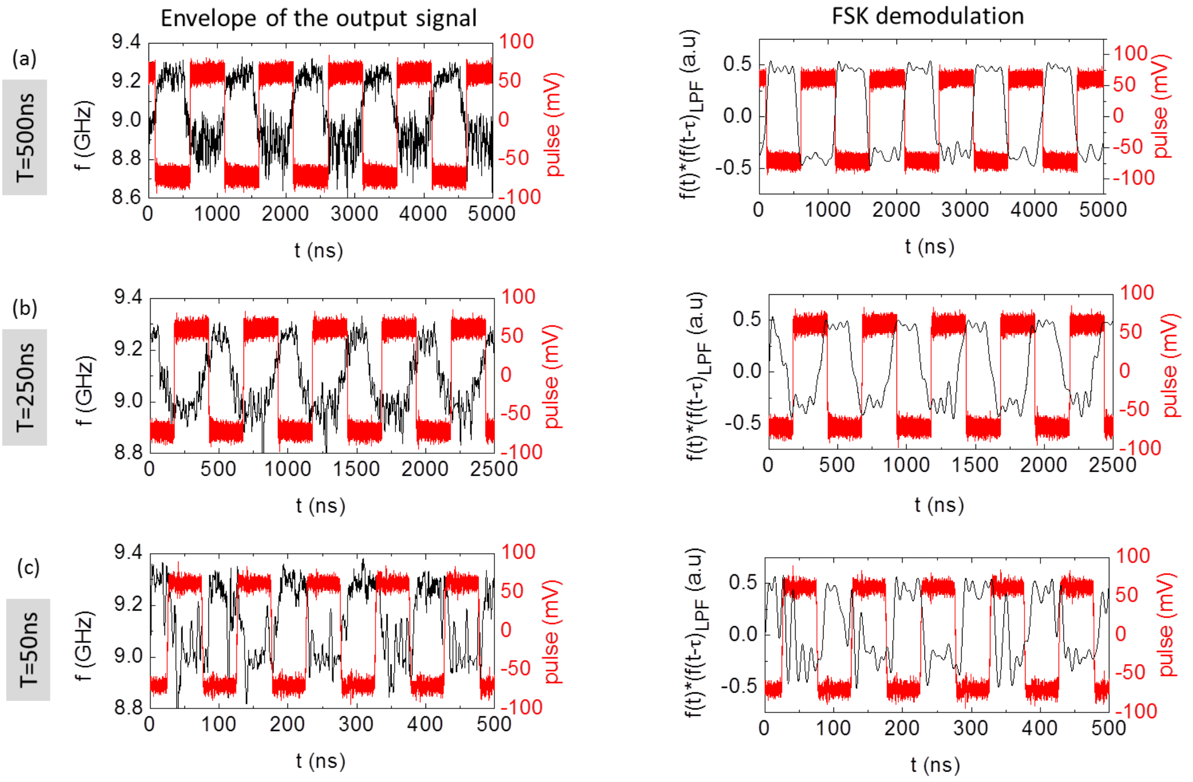

Fig. 4.53-(a) The smoothed instantaneous frequency of the output voltage signal, i.e. FSK signal, (has been shown in Fig. 4.51-middle) and the delay detection of FSK signal, <cos(2πf*(t))*cos(2πf*(t-τ))>, for different bit length T: (a) T=500ns (LPF=10MHz), (b) T=250ns (LPF=20MHz), and (c) T=50ns (LPF=100MHz).

4.4.3.4 Summary: FSK measurement within RF emitter

The feasibility of the STNO within RF emitter has been successfully demonstrated with the maximum modulation rate of 20Mbps at a full frequency shift of 330MHz. This maximum data rate is limited by the non-optimized RF components in the RF emitter and not to the intrinsic of the STNO. For the demodulation, the delay detection technique was calculated numerically and showed that the ASK and FSK signal can be decoded into a train voltage pulse up to demodulation rate of 20Mbps. Further improvement of the PCB emitter is needed to increase the maximum input data rate and to reduce the noise figure of the amplification path in the PCB emitter. Besides the improvement of the PCB emitter, further improvements in materials and nanofabrication of STNOs are needed to enable more output power and to improve the spectral characteristics of the oscillations to push the data rates to higher values with large frequency shift.

4.5 General Summary

The feasibility of the FSK scheme by current modulation has been studied for in-plane magnetized MTJ STNOs in view of wireless communications used in WSNs. The parameters addressed in this study are the achievable frequency shift and the maximum modulation rate, up to which the frequency can be shifted between two discrete values. To characterize the maximum data rate, macrospin simulation and experimental studies have been performed. The simulations reveal that the maximum data rate for FSK by current is limited by the relaxation frequency f_p of the STNO, which is on the order of a few hundred MHz for standard in-plane magnetized STNOs. This means that the data rate of up to a few hundred Mbps should be achievable, which is targeted here for moderate data rate wireless communication as used in WSNs.

Experimental studies of the FSK by digital current modulation in STNOs have been performed for standalone STNO devices and for integrated STNOs within microwave systems. The FSK measurements on standalone STNO devices have been performed for two different types of nanofabricated STNOs, which are Hitachi and Mosaic devices. The variation of the pulse width T (pulse rate 1/T) shows that the maximum modulation rate for ASK modulation of the Hitachi device is close to 100Mbps, while for FSK modulation it is limited to 40 Mbps at reduced frequency shift and to 10Mbps at full frequency shift of 200MHz. Hence frequency shift keying is confirmed to be efficient up to ~10Mbps for a frequency shift of 100-200MHz. The reason that this is less than the limit for amplitude modulation is seen in the relatively high phase noise of the device analysed. Similar results have also been achieved using Mosaic devices with smaller frequency shift around 150MHz at the data rate of 10Mbps. This shows an important achievement for Mosaic devices besides its enhancement of the device stability under DC current (enhanced degradation voltage).

The FSK measurements of STNOs on a printed circuit board (PCB) emitter have been performed using Hitachi devices in collaboration with the Mosaic partner, Rui Ma from TUD University. The results reveal that the FSK with a frequency shift around 300MHz (between ≈9 GHz and ≈9.3 GHz) was observed with a data rate of 20 Mbps. The data rate was limited by characteristics of the PCB emitter and is not intrinsic to the STNO. Hence, further improvements of the PCB emitter are needed to achieve maximum data rates given by the dynamic parameters of the STNO.

To evaluate the feasibility of the FSK-based wireless communication schemes performed in this thesis, it is important to compare the results with the state of the art of the STNO-based wireless communication. This is summarized in table 4.3. The results achieved in this thesis are shown in green. It is shown that the maximum data rate achieved in this study is comparable with the study in Ref. 25 [Manfrini et. al] which investigated the FSK by digital current modulation in vortex-based STNOs. Complete studies of MTJ-based STNO for wireless communication have been carried out in Ref [26-28] in the context of OOK concepts and using the envelope detector as for the demodulation. The STNO performances of in these references are worse compared to the STNOs measured in this thesis. The frequency current tuning df/dI is too small compared to the linewidth so that the OOK concept is more convenient for these STNO devices. The best maximum data rate detected at the demodulation is 4Mbps at a distance of 100cm and the signal to noise SNR of 6dB. The FSK modulation of STNO devices studied in this thesis is able to achieve higher data rate with the frequency shift of 330MHz at maximum data rate of 20Mbps. However the demodulations of FSK signal was carried out numerically, i.e. no experimental demonstration of delay detection of FSK signals. A complete experimental demonstration of FSK modulation and demodulation (delay detection technique) thus needs to carry out in order to compare with the results given in Ref. [26-28]. The determination and characterization of SNR are also of importance for wireless applications.

Table 4.3. Comparison of maximum data rate of STNO modulation for wireless communication applications. Here f is the oscillation frequency, Δf_{min} is the minimum linewidth, P_{out} is the maximum output power, δf is the frequency shift (for the case of FSK modulation), df/dI is the frequency-current tenability, D is the distance between transmitter and the receiver.

STNO	Concept	TMR (%)	f_0 (GHz)	Δf_{min} (MHz)	P_{max} (pW)	δf (MHz)	df/dI (MHz/mA)	Data rate (Mbps)	D (cm)	SNR (dB)
Ref.25-vortex	FSK	2.7%	0.4	8	0.9	72	250/33	20	-	-
Ref.26-MTJ	OOK	79%	2.5	200	2.7	-	50/1.5	0.2	100	12.5
Ref.28-MTJ	OOK (STNO array)	R_{AP}= 80Ω	3.5-4.2	130	79	700	220/1.5	0.4	1	-
Ref.27-MTJ	OOK	75%	3.6	101	100	-	-	4	100	6
MTJ Hitachi	FSK	54%	9.18	15	125k	200	160/0.4	10	-	-
MTJ MOSAIC	FSK	49%	8.26	20	15k	150	-400/1.4	10	-	-
MTJ Hitachi-PCB emitter	FSK	50%	9	13	100k	330	-530/0.5	20	-	-

Chapter V
Conclusion and perspective

5.1 Conclusion

The frequency shift keying (FSK) by current in standard in-plane magnetized STNOs for wireless communication used in WSNs has been studied in this thesis. For this study, the RF properties of STNOs have been characterized to identify appropriate devices for FSK measurements and for further improvements in materials and nanofabrication process. Good spectral characteristics, large frequency tuning, and large output power of STNOs are of interest for the realization of the FSK-based wireless communication used in wireless sensor networks (WSNs).

The FSK-based wireless communication scheme needs to address the achievable frequency shift and the maximum data rate (up to which a signal can be modulated or the frequency be shifted between two discrete levels). To characterize the maximum data rate, simulation and experimental studies have been performed. The simulation has been done in two studies, the first using a sinusoidal RF current modulation (Chapter 3) and the second using square current pulses (digital current) or pulse trains of varying rise time and pulse length T (Chapter 4). Both simulations reveal that the maximum data rate under current modulation is limited by the relaxation frequency f_p of the STNO, which is on the order of a few hundred MHz for standard in-plane magnetized STNOs investigated in this thesis. This means that the data rate is limited to a few hundred Mbps. This limit remains suitable for the data rates targeted in this thesis, up to 100Mbps, for low to moderate data rate wireless communication as used in WSNs.

For wireless communication applications that need higher data rate of up to Gbps, field modulation provides a solution. It has been investigated via macrospin simulation that the maximum data rate of the field modulation is not limited by the relaxation frequency f_p of the STNO. This results in an enhanced data rate up to Gbps. This occurs when the modulating RF field is oriented along the easy axis of the free layer (longitudinal RF field) and even for the tilted RF field angle up to $\beta=\pm 20°$ with respect to the easy axis direction. The enhancement of the data rate in longitudinal RF field modulation can be understood by the fact that the frequency modulation occurs via a direct coupling of the modulating field to the frequency and not via the non-linear amplitude-frequency coupling as for current modulation.

To investigate the feasibility of the FSK by digital current modulation in STNOs, experimental studies have been performed for standalone STNO devices and for integrated STNOs within microwave systems (RF emitter). Here, the square shaped pulses are used to modulate the frequency of the free running STNOs, leading to the frequency shift between two discrete values. The maximum data rate at a full frequency shift was characterized by varying the current pulse width. The FSK measurements on standalone STNO devices have been performed for two different types of nanofabricated STNOs, which are Hitachi and Mosaic devices. The FSK using Hitachi devices was successfully observed with a frequency shift around 200MHz (the frequency shift between ≈8.9 GHz and ≈9.1 GHz) at the data rate of 10Mbps. This data rate is less than the upper limit, which is given by the relaxation frequency f_p of the STNO as predicted in the numerical simulation, because of the relatively high phase noise of the device analyzed. Similar results have also been achieved using Mosaic devices with smaller frequency shift around 150MHz at the data rate of 10Mbps. This shows an important achievement for Mosaic devices besides its enhancement of the device stability under DC current (enhanced degradation voltage). However, the static and dynamic yield as well as the output power of Mosaic devices needs further improvements.

The FSK measurements of STNOs on a printed circuit board (PCB) emitter have been performed using Hitachi devices in collaboration with the Mosaic partner, Rui Ma from TUD University. The partner has realized and developed the PCB emitter card and the author has characterized the RF properties of STNOs to provide appropriate STNO devices for FSK measurements. The results reveal that the FSK with a frequency shift around 300MHz (between ≈9 GHz and ≈9.3 GHz) was observed with a data rate of 20 Mbps. The data rate was limited by characteristics of the PCB emitter and is not intrinsic to the STNO. Hence, further improvements of the PCB emitter are needed to achieve maximum data rates given by the dynamic parameters of the STNO.

Additionally to the FSK study, the demodulation of the FSK signal achieved in both measurements, standalone and integrated STNOs, were carried out numerically using the delay detection technique proposed by Toshiba which is more suited for STNO devices characterized by a relatively large phase noise (Fig. 4.2 Chapter 4 Section 4.1). The calculation showed that the FSK signal can be read or decoded at the same data rate as the modulation rates.

The experimental studies of FSK by current in STNOs demonstrate that STNOs are adequate for wireless communication used in WSNs. However, further improvements in materials and nanofabrication of STNOs are needed to improve the spectral characteristics of the oscillations to push the data rates to higher values with large frequency shift.

5.2 Perspective

The FSK study demonstrated in this thesis was only performed within an emitter, while the demodulation was carried out numerically. It will be of great interest to demonstrate a complete wireless communication scheme using STNOs based on the FSK concept. This permits the evaluation of the feasibility of the FSK such as the data rate and the SNR as a function of the distance between emitter and receiver. To achieve this functionality, improvements of the PCB emitter are required in order to increase its maximum input data rate. Besides that, it is also important to reduce the noise figure of the amplification path in the PCB emitter. The noise of the emitter adds to the STNO noise and reduces the SNR. For the STNO, the first improvement required would be an increase of its output power to -30 dBm, i.e. current STNO power is ≈-40dBm for Hitachi devices and ≈-50dBm for Mosaic devices. This will decrease the complexity of the amplification path in the PCB emitter and thus reduce the power consumption and the noise of the emitter itself. For the receiver, improvements of its sensitivity and its input data rate are required. In this thesis, the receiver has not been succesfully tested due to the lower power and high noise emitted from the STNO emitter and low sensitivity of the receiver itself (a sensitivity to signal levels of -10dBm). This low receiver sensitivity is mainly due to non-optimized components such as the RF mixer. It is expected that with the improvement of the STNO, the PCB emitter and the receiver itself, the sensitivity can be improved to -30 dBm at a high data rate of 20 Mbit/s. Figure 5.1 shows the design plan for the short term perspective for complete wireless communication scheme using STNO based on FSK concept.

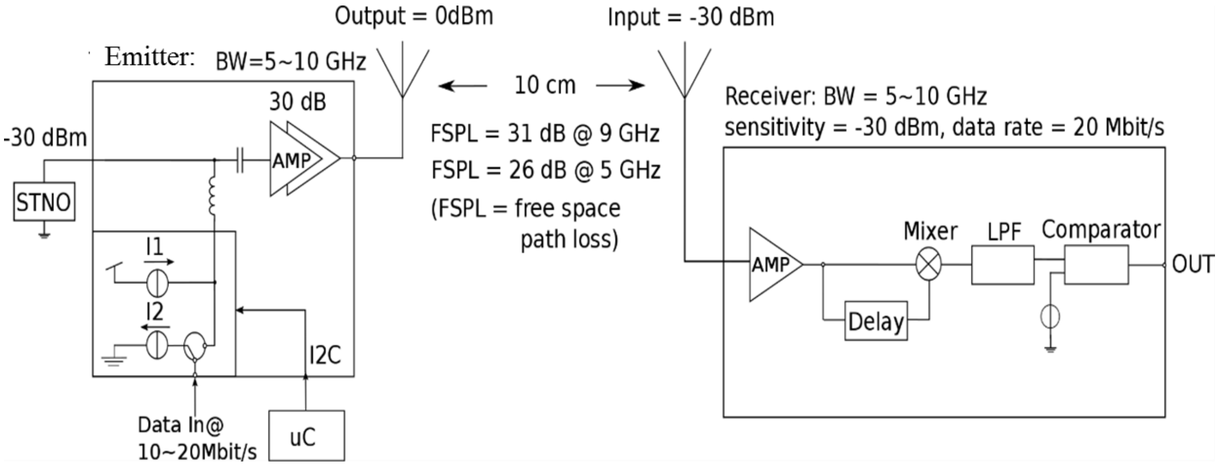

Fig. 5.1-Design and its specification of the STNO based transceiver in the short term (Designed by Rui, Ma, TUD University)

A wireless communication over a short wireless distance such as 10 cm with data rate of 20Mbps is targeted which is a good value for applications in WSNs. The free space path loss (FSPL) is proportional to the square of distance between the emitter and receiver and also proportional to the square of the STNO frequency. It is characterized to be 26dB to 31dB for the frequency band from 5 GHz to 9 GHz. The parameters that need to be characterized are the influence of the oscillator amplitude and phase noise on the achievable frequency shift and data rate, the achievable emission power and the signal to noise ratio (SNR) of the receiver that will determine the distance of communication. It is also important to characterize the total power consumed by the emitter-receiver using STNOs and to compare with the power consumed in the existing wireless communication scheme. Low power wireless communication schemes are of great importance for WSN applications as mentioned in the introduction. The long term perspective would be to demonstrate a wireless communication up to 10m distance (and potentially above) between the emitter and receiver. For this, the PCB boards need to be replaced by an integrated circuit (IC). With the IC design, the design process in terms of circuit gain, stability, noise, power consumption and etc. can be much better controlled. With all the improvement, it can be expected the STNO-based wireless communication can function in the 10m range.

As shown in numerical simulations, the FSK in STNO can be achieved not only through the modulation of the current but also through the modulation of the field. It has been predicted in the simulation that higher modulation data rates above the upper limit (the amplitude relaxation frequency of the STNO) is achievable. This is thus of great importance to demonstrate experimental studies of the field modulation in STNOs to confirm the simulation results and also as for the demonstration of FSK-based dynamic read heads.

Annexes

Nomenclature of the Mosaic device

The Mosaic's wafer (Fig. 1a) consists of chips (Fig. 1b) which contain the STNO devices (Fig. 2). The chip's nomenclature is given by the row (i.e. across) and the column (i.e. down). For example presented below, chip 2,4 means that the chip at 2nd row and 4th column. The STNO devices on each chip are labelled as A1, A2, A3, A4, A5, A6, B1, B2, B3, B4, B5, B6. While, row C and D are for MRAM devices.

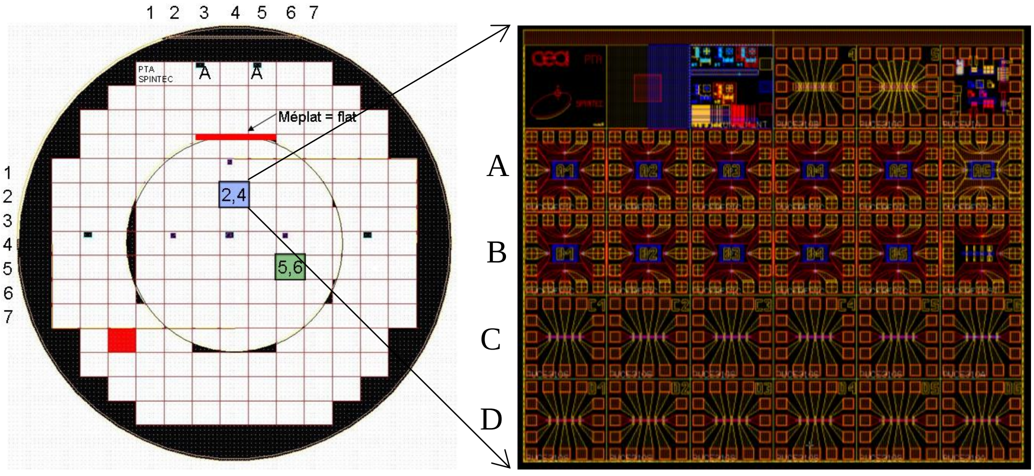

Wafer

Chip 2,4

Fig. 1-(a) RF wafer consists of several chips which are indicated by the number of row and column, for example chip 2,4 (row 2 and column 4). (b) The zooming part of the chip 2,4. Row A & B are the RF mask for STNO devices while row C & D are the RF mask designed for MRAM devices.

In Fig. 2, if we look more closely at the RF mask design (row A and B), one can see that it has both transmission (J2 and J4) and reflection devices (J1 and J3). It is important to note that the reflection devices, J1 and J3, correspond to the STNO devices measured and analyzed in this thesis due to its simple probing.

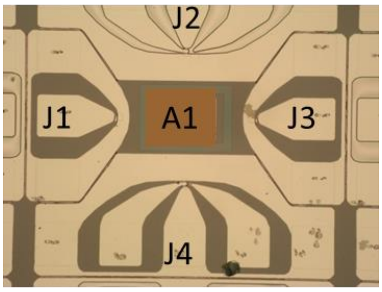

Fig. 2-Transmission ((J2 and J4) and reflection (J1 and J3) STNO devices

Bibliography

[1] Kumar, A., Shwe, H.U., Wong, K.J. and Chong, P.H.J, “Location-Based Routing Protocols for Wireless Sensor Networks: A Survey,” *Wireless Sensor Network,* 9, 25-72 (2017). http://dx.doi.org/10.4236/wsn.2017.91003

[2] D. Estrin and R. Govindan, “Next century challenges: scalable coordination in sensor networks”. *MobiCom*, Seattle, WA, pp. 263-270 (1999).

[3] Svetoslav Atanasov, “An overview of wireless communication technologies used in wireless sensor networks,” *International Scientific Conference eRA-8,* September 2009. DOI: 10.13140/2.1.4440.6720

[4] 2. J. C. Slonczewski, “Current-driven excitation of magnetic multilayers”. *J. Magn. Magn. Mater*. 159, 1–7 (1996).

[5] L. Berger, “Emission of spin waves by a magnetic multilayer traversed by a current,” *Phys. Rev. B*. 54(13), 9353–9358 (1996).

[6] S. I. Kiselev, J. C. Sankey, I. N. Krivorotov, N. C. Emley, R. J. Schoelkopf, R. A. Buhrman, and D. C. Ralph, “Microwave oscillation of a nanomagnet driven by a spin-polarized current,” *Nature*. 425, 380 (2003).

[7] M.Tsoi, A.G. M. Jansen, J. Bass, W.C. Chiang, M.Seck, V. Tsoi, and, P. Wyder, “Excitation of a magnetic multilayer by an electric current”. *Phys. Rev. Lett*., vol. 80, pp. 4281-4284, (1998).

[8] A. A. Tulapurkar, Y. Suzuki, A. Fukushima, H. Kubota, H. Mahara, K. Tsunekawa, D.D. Djayaprawira, N. Watabene, and S. Yuasa, “Spin torque diode effect in magnetic tunnel junctions,” *Nature*, vol.438, pp. 339-342, (2005).

[9] Ruotolo, A. et al., “Phase-locking of magnetic vortices mediated by antivortices,” *Nature Nanotechnology* 4, 528–532 (2009).

[10] KaKa, S. et al., “Mutual phase-locking of microwave spin torque nano-oscillators,” *Nature Letter* 437, 389–392 (2005).

[11] Z. Li, Y. C. Li, and S. Zhang, “Dynamic magnetization states of a spin valve in the presence of dc and ac currents: Synchronization, modification, and chaos,” *Phys. Rev. B,* vol. 74, p. 054417, (2006).

[12] R. Bonin, G. Bertotti, C. Serpico, I. D. Mayergoyz, and M. d’Aquino. Model of phase locking in spin-transfer-driven magnetization dynamics. *J. Appl. Phys.,* vol. 101, p. 09A506, (2007).

[13] A. N. Slavin and V. S. Tiberkevich, “Theory of mutual phase locking of spin-torque nanosized oscillators,” *Phys. Rev. B,* vol. 74, p. 104401, (2006).

[14] M. Quinsat, J. F. Sierra, I. Firastrau, V. Tiberkevich, A. Slavin, D. Gusakova, L. D. Buda-Prejbeanu, M. Zarudniev, J.-P. Michel, U. Ebels, B. Dieny, M.-C. Cyrille, J. A.

Katine, D. Mauri, and A. Zeltser, “Injection locking of tunnel junction oscillators to a microwave current,” *App. Phys. Lett*. 98, 182503 (2011).

[15] W. H. Rippard, M. R. Pufall, S. Kaka, S. E. Russek, and T. J. Silva, “Direct current induced dynamics in $Co_{90}Fe_{10}/Ni_{80}Fe_{20}$ point contacts”, *Phys. Rev. Lett*. 92(2), 027201– (2004).

[16] Y. Masugata, S. Ishibashi, H. Tomita, T. Seki, T. Nozaki, Y. Suzuki, H. Kubota, A. Fukushima, S. Yuasa. “Spin-torque induced rf oscillation in magnetic tunnel junctions with an Fe-rich CoFeB free layer,” *Journal of Physics:* Conference Series 266, 012098, (2011). DOI:10.1088/1742-6596/266/1/012098

[17] Mistral, Q. et al., “Current-driven microwave oscillations in current perpendicular to-plane spin-valve nanopillars,” *Appl. Phys. Lett*. 88, 192507–192507-3 (2006).

[18] Houssameddine, D. et al., “Spin-torque oscillator using a perpendicular polarizer and a planar free layer,” *Nature Materials* 6, 447–453 (2007).

[19] Pribiag, V. S. et al., “Magnetic vortex oscillator driven by DC spin-polarized current,” *Nature Physics* 3, p. 498–503 (2007).

[20] Gusakova, D. et al., “Spin-polarized current-driven excitations in spin-valve nanopillars with a synthetic antiferromagnetic pinned layer,” *The 53rd Annual Conf. Magnetism and Magnetic Materials proceedings*, (2008).

[21] Houssameddine, D. et al., “Spin transfer induced coherent microwave emission with large power from nanoscale MgO tunnel junctions,” *Appl. Phys. Lett.* 93, 022505 (2008).

[22] A. N. Slavin and V. Tiberkevich, “Nonlinear Auto-Oscillator Theory of Microwave Generation by Spin-Polarized Current,” *IEEE Transactions on Magnetics*, vol. 45, no. 4, p. 1889-1890 (2009).

[23] M. Manfrini, T. Devolder, Joo-Von Kim, P. Crozat, N. Zerounian et al, “Agility of vortex-based nanocontact spin torque oscillators,” *Appl. Phys. Lett*. 95, 192507 (2009). Doi: 10.1063/1.3263727.

[24] M. Quinsat, F. Garcia-Sanchez, A.S. Jenkins, A. Zeltser and J.A. Katine, A.N. Slavin, L.D. Buda-Prejbeanu, B. Dieny, M.-C. Cyrille, U.Ebels, “Modulation bandwidth of spin torque oscillators under current modulation,” *Appl. Phys. Lett*. 105, 152401 (2014).

[25] M. Manfrini, T. Devolder, Joo-Von Kim, P. Crozat, C. Chappert et al., “Frequency shift keying in vortex-based spin torque oscillators,” *J. Appl. Phys*. 109, 083940 (2011).

[26] Hyun Seok Choi, Sun Yool Kang, Seong Jun Cho, Inn-Yeal Oh, Mincheol Shin, Hyuncheol Park, Chaun Jang, Byoung-Chul Min, Sang-Il Kim, Seung-Young Park & Chul Soon Park, “Spin nano–oscillator–based wireless communication,” *Sci. Rep*. 4, 5486. DOI: 10.1038/srep05486 (2014).

[27] R. Sharma, et al., “Modulation Rate Study in A Spin Torque Oscillator Based Wireless Communication System,” *IEEE Transactions on Magnetics*. 51, 1401304 (2015). DOI: 10.1109/TMAG.2015.2438033.

[28] Inn-Yeal Oh, et al., “Wireless Spintronics Modulation With a Spin Torque Nano-Oscillator (STNO) Array,” *IEEE Microwave And Wireless Components Letters*. 24, 502 (2014).

[29] K. Mizushima, K. Kudo, T. Nagasawa, and R. Sato, “Signal-to-noise ratios in high-signal-transfer-rate read heads composed of spin-torque oscillators,” *J. Appl. Phys*. 107, 063904 (2010).

[30] Kiwamu Kud, Tazumi Nagasawa, Koichi Mizushima, Hirofumi Suto, and Rie Sato, “Numerical Simulation on Temporal Response of Spin-Torque Oscillator to Magnetic Pulses,” *Applied Physics Express* 3 (2010) 043002.

[31] Hirofumi Suto, Tazumi Nagasawa, Kiwamu Kudo, Koichi Mizushima, and Rie Sato, “Real-Time Measurement of Temporal Response of a Spin-Torque Oscillator to Magnetic Pulses,” *Applied Physics Express* 4 (2011) 013003. DOI: 10.1143/APEX.4.013003.

[32] Tazumi Nagasawa, Hirofumi Suto, Kiwamu Kudo, Koichi Mizushima, and Rie Sato, “Frequency transition of spin-torque oscillator under the magnetic field pulse in nanosecond range,” *J. Appl. Phys*. 109, 07C907 (2011); doi: 10.1063/1.3549592.

[33] Tazumi Nagasawa, Hirofumi Suto, Kiwamu Kudo, Tao Yang, Koichi Mizushima, and Rie Sato, “Delay detection of frequency modulation signal from a spin-torque oscillator under a nanosecond-pulsed magnetic field,” *Journal of Applied Physics* 111, 07C908 (2012); doi: 10.1063/1.3673836.

[34] Jyotsana Tewari, Hari Mohan Singh, “Performance Comparison of Digital Modulation Techniques used in Wireless Communication System,” *International Journal of Innovative Research in Computer and Communication Engineering*. Vol. 4, Issue 7, (2016).

[35] M. N. Baibich, J. M. Broto, A. Fert, F. N. Van Dau, F. Petroff, P. Etienne, G. Creuzet, A. Friederich, J. Chazelas, “Giant magnetoresistance of (001)Fe/(001)Cr magnetic superlattices,” *Phys. Rev. Lett*. 61, 2472 (1988).

[36] G. Binasch, P. Grunberg, F. Saurenbach, W. Zinn, “Enhanced magnetoresistance in layered magnetic structures with antiferromagnetic interlayer exchange,” *Phys. Rev. B.*, 39, 4828 (1989).

[37] “The nobel prize in physics 2007,” Nobelprize.org. [Online]. Available: http:// www.nobelprize.org/nobel_prizes/physics/laureates/2007/

[38] H. Kubota, A. Fukushima, Y. Ootani, S. Yuasa, K. Ando, H. Maehara, K. Tsunekawa, D. D. Djayaprawira, N. Watanabe, and Y. Suzuki, “Evaluation of Spin-Transfer Switching in CoFeB/MgO/CoFeB Magnetic Tunnel Junctions,” *Jpn. J. Appl. Phys*. 44 (40), L1237-L1240 (2005).

[39] G. Bertotti, C. Serpico, I. D. Mayergoyz, A. Magni, M. d'Aquino, and R. Bonin, “Magnetization Switching and Microwave Oscillations in Nanomagnets Driven by Spin-Polarized Currents,” *Phys. Rev. Lett.* 94, 127206- (2005).

[40] Everspin, “Everspin Technologies takes MRAM to higher densities with 16 megabit product introduction”, Press release (2010), http://www.everspin.com/PDF/press/2010 april 19 16mb mram.pdf.

[41] Freescale, “Freescale leads industry in commercializing MRAM technology”, Press release (2006), http://ir.freescale.com/investor-relations/press-releases/press-releases-archive/2006/ 07102006.aspx.

[42] E. B. Myers, D. C. Ralph, J. A. Katine, R. N. Louie and R. A. Buhrman, “Current-induced switching of domains in magnetic multilayer devices,” *Science,* 285, 867-870 (1999).

[43] J. A. Katine, F. J. Albert, R. A. Buhrman, E. B. Myers and D. C. Ralph, “Current-Driven Magnetization Reversal and Spin-Wave Excitations in CoCuCo Pillars,” *Phys. Rev. Lett.,* 84, 3149-3152 (2000).

[44] M. Tsoi, A. G. M. Jansen, J. Bass, W. –C. Chiang, V. Tsoi and P. Wyder, “Generation and detection of phase-coherent current-driven magnons in magnetic multilayers,” Nature, 406, 46-48 (2000).

[45] Everspin, “Everspin debuts first Spin-Torque MRAM for high performance storage systems,” Press release (2012), http://www.everspin.com/PDF/ST-MRAM Press Release.pdf.

[46] Toshiba, “Toshiba’s new STT-MRAM memory element promises world’s best power consumption and to outperform SRAM,” Press release (2012), http://www.toshiba.co.jp/about/press/2012 12/pr1001.htm.

[47] MRAM-Info, “TDK to present a 8-Mbit STT-MRAM prototype, plans to commercialize the technology in 3-5 years,” Press release (2014), http://www.mram-info.com/tdk-present-8-mbit-stt-mram-prototype-plans-commercializetechnology-3-5-years.

[48] N. Locatelli, V. Cros, and J. Grollier, “Spin-torque building blocks,” *Nature Materials*, 13(1):11–20, (2014).

[49] W. Zhao and G. Prenat, “Spintronics-based computing,” *Springer International Publishing*, (2015).

[50] K. Muller, “Theory of Magnetism,” Technische Universitat Dresden, Institute for Theoretical Physics, (2015).

[51] Stoner, E. C., “Collective electron ferromagnetism,” *Proc. R. Soc. London Ser. A* 165, 372–414, (1938).

[52] P. M. Tedrow, “Spin-Dependent Tunneling into Ferromagnetic Nickel,” *Physical Review Letters*, 26(4), (1971).

[53] M. Julliere, "Tunneling between ferromagnetic films," *Phys. Lett. A* 54, 225 (1975).

[54] J. C. Slonczewski, "Conductance and exchange coupling of two ferromagnets separated by a tunneling barrier," Phys. Rev. B 39, 6995 (1989).

[55] T. Miyazaki and N. Tezuka, "Giant magnetic tunneling effect in Fe/Al_2O_3/Fe junction," J. Magn. Magn. Mater. 139, L231 (1995).

[56] J. S. Moodera, L. R. Kinder, T. M. Wong, and R. Meservey, "Large Magnetoresistance at Room Temperature in Ferromagnetic Thin Film Tunnel Junctions," Phys. Rev. Lett. 74, 3273 (1995).

[57] P. LeClair, J. T. Kohlhepp, C. H. van de Vin, H. Wieldraaijer, H. J. M. Swagten, W. J. M. de Jonge, A. H. Davis, J. M. MacLaren, J. S. Moodera, and R. Jansen, "Band Structure and Density of States Effects in Co-Based Magnetic Tunnel Junctions," Phys. Rev. Lett. 88, 107201 (2002).

[58] J. S. Moodera, J. Nowak, and R. J. M. van de Veerdonk, "Interface Magnetism and Spin Wave Scattering in Ferromagnet-Insulator-Ferromagnet Tunnel Junctions," Phys. Rev. Lett. 80, 2941 (1998).

[59] S. Yuasa, T. Nagahama, and Y. Suzuki, "Spin-Polarized Resonant Tunneling in Magnetic Tunnel Junctions," Science 297, 234 (2002).

[60] D. Wang, C. Nordman, J. M. Daughton, Z. Qian, and J. Fink, "70% TMR at Room Temperature for SDT Sandwich Junctions With CoFeB as Free and Reference Layers," IEEE Trans. Magn. 40, 2269 (2004).

[61] J. J. Yang, C. Ji, Y. A. Chang, X. Ke, and M. S. Rzchowski, "Over 70% tunneling magnetoresistance at room temperature for a CoFe and AlOx based magnetic tunnel junction," Appl. Phys. Lett. 89, 202502 (2006).

[62] W. H. Butler, X.-G. Zhang, T. C. Schulthess, and J. M. MacLaren, "Spin-dependent tunneling conductance of Fe|MgO|Fe sandwiches," Phys. Rev. B 63, 054416 (2001).

[63] J. Mathon and A. Umerski, "Theory of tunneling magnetoresistance of an epitaxial Fe/MgO/Fe(001) junction," Phys. Rev. B 63, 220403 (2001).

[64] Yuasa, S. and Djayaprawira, D. D., "Giant tunnel magnetoresistance in magnetic tunnel junctions with a crystalline MgO(0,0,1) barrier," *Journal of Physics D: Applied Physics*, 40(21):R337-R354 (2007).

[65] S. S. P. Parkin, C. Kaiser, A. F. Panchula, P. Rice, M. G. Samant, S.-H. Yang, and B. Hughes, "Giant tunneling magnetoresistance at room temperature with MgO (100) tunnel barriers," *Nature Materials* 3, 862 (2004).

[66] S. Yuasa, T. Nagahama, A. Fukushima, Y. Suzuki, and K. Ando, "Giant room-temperature magnetoresistance in single-crystal Fe/MgO/Fe magnetic tunnel junctions," *Nature Materials* 3, 868 (2004).

[67] S. Ikeda, J. Hayakawa, Y. Ashizawa, Y. M. Lee, K. Miura, H. Hasegawa, M. Tsunoda, F. Matsukura, and H. Ohno, "Tunnel magnetoresistance of 604% at 300K by

suppression of Ta diffusion in CoFeB/MgO/CoFeB pseudo-spin-valves annealed at high temperature," *Appl. Phys. Lett.* 93, 082508 (2008).

[68] Komagaki, K., Hattori, M., Noma, K., Kanai, H., Kobayashi, K., Uehara, Y., Tsunoda, M., and Takahashi, M., "Influence of Diffused Boron Into MgO Barrier on Pinhole Creation in CoFeB/MgO/CoFeB Magnetic Tunnel Junctions, *IEEE Transactions on Magnetics*, 45(10):345-3456 (2009).

[69] Schreiber, D. K., Choi, Y.-S., Liu, Y., Chiaramonti, A. N., Seidman, D. N., and Petford-Long, a. K., "Enhanced magnetoresistance in naturally oxidized MgO-based magnetic tunnel junctions with ferromagnetic CoFe/CoFeB bilayers," *Applied Physics Letters*, 98(23):232506 (2011).

[70] M. Stiles and J. Miltat, "Spin transfer torque and dynamics". vol. Spin Dynamics in Confined Magnetic Structures III,, (Springer Berlin / Heidelberg, 2006).

[71] D. Ralph and M. Stiles, "Spin transfer torques," *J. Magn. Magn. Mater.* 320, 1190 (2008).

[72] C. Baraduc, M. Chshiev, and U. Ebels, "Introduction to spin transfer torque," *World Scientific Review*, Volume - 9in x 6in, Chapter 1 (2008).

[73] D. Gusakova, D. Houssameddine, U. Ebels, B. Dieny, L. Buda-Prejbeanu, M. C. Cyrille, and B. Delaët, "Spin-polarized current-induced excitations in a coupled magnetic layer system," *Physical Review B* 79, 104406 (2009).

[74] B. Lacoste, L. D. Buda-Prejbeanu, U. Ebels, and B. Dieny, "Magnetization dynamics of an in-plane magnetized synthetic ferrimagnetic free layer submitted to spin-transfer torques and applied field," *Physical Review B* 89, 064408 (2014).

[75] M. Romera, E. Monteblanco, F. Garcia-Sanchez, B. Delaët, L. D. Buda-Prejbeanu, and U. Ebels, "Non-linear mode interaction between spin torque driven and damped modes in spin torque nano-oscillators," *Applied Physics Letters* 106, 192405 (2015).

[76] Dimitri Houssameddine, "Dynamique de l'aimantation de nano-oscillateurs micro-ondes a transfert de spin, " PhD thesis, UMR SPINTEC, 2009.

[77] A. N. Slavin and V. S. Tiberkevich, "Current-induced bistability and dynamic range of microwave generation in magnetic nanostructures," *Phys. Rev. B.* 72 (9), 094428–5 (2005).

[78] S. I. Kiselev, J. C. Sankey, I. N. Krivorotov, N. C. Emley, A. G. F. Garcis, R. A. Buhrman, D. C. Ralph, D. C., "Spin-transfer excitations of permalloy nanopillars for large applied currents," *Phys.Rev. B* 72, 64430-64439 (2005).

[79] D. Houssameddine, U. Ebels, B. Delae T, B. Rodmacq, I. Firastrau, F. Ponthenier, M. Brunet, C. Thirion, J.-P. Michel, L. Prejbeanu-Buda, M.-C. Cyrille, O. Redon And B. Dieny, "Spin-torque oscillator using a perpendicular polarizer and a planar free layer," *nature materials* Vol 6 (2007).

[80] U. Ebels,D. Houssameddine, I. Firastrau, D. Gusakova,C. Thirion, B. Dieny, and L. D. Buda-Prejbeanu, “Macrospin description of the perpendicular polarizer-planar free-layer spin-torque oscillator,” *Phys. Rev. B* 78, 024436 (2008).

[81] Redon, O., Dieny, B. & Rodmacq, B. “Magnetic spin polarization and magnetization rotation device with memory and writing process using such a device,” US patent 6,532,164 B2 (2003).

[82] Lee, K. J., Redon, O. & Dieny, B. Analytical investigation of spin-transfer dynamics using a perpendicular-to-plane polarizer. *Appl. Phys. Lett.* 86, 22505–22507 (2005).

[83] W. F. Brown, “Thermal Fluctuations of a Single-Domain Particle,” *Physcial Review*, 130(5):1677-1686, (1963).

[84] J. Xiao, A. Zangwill, and M. D. Stiles, “Macrospin models of spin transfer dynamics,” *Physical Review B*, 72(014446), (2005).

[85] Michal Quinsat, “Etude d’un oscillateur non-isochrone: Application à la dynamique non-linear de l’aimantation induite par transfert de spin,” PhD thesis. UMR SPINTEC, 2012.

[86] Joo-von Kim, “Stochastic theory of spin-transfer oscillator linewidths,” *Physical Review B*, 73(174412), 2006.

[87] A. N. Slavin and V. S. Tiberkevich, “Nonlinear Auto-Oscillator Theory of Microwave Generation by Spin-Polarized Current,” *IEEE Transactions on Magnetics*, Vol. 45, No. 4, (2009).

[88] V. S. L’vov, “Wave Turbulence Under Parametric Excitation,” New York: Springer-Verlag, (1994).

[89] V. S Tiberkevich and A. N. Slavin, J.-V. Kim, “Microwave power generated by a spin transfer oscillator in the presence of noise,” *IEEE Transations on Magnetics*, 44(7):1916-1927, (2008).

[90] L. Bianchini, S. Cornelissen, J.-V. Kim, T. Devolder, W. van Roy, L. Lagae, and C. Chappert, “Direct experimental measurement of phase-amplitude coupling in spin torque oscillators,” *Applied Physics Letters*, 97(032502), (2010).

[91] M. Quinsat, D. Gusakova, J. F. Sierra, J. P. Michel, D. Houssameddine, B. Delaet, M.-C. Cyrille, U. Ebels, B. Dieny, L. D. Buda-Prejbeanu, J. A. Katine, D. Mauri, A. Zeltser, M. Prigent, J.-C. Nallatamby, and R. Sommet, “Amplitude and phase noise of magnetic tunnel junction oscillators,” *Applied Physics Letters* 97, 182507 (2010).

[92] S. Haykin, “Communication Systems,” 5th ed. New York:Wiley, (2009).

[93] Agilent Technology, “Agilent Spectrum Analysis Amplitude and Frequency Modulation: Application Note 150-1”. *Printed in USA*, 5954-9130, October 8, 2001.

[94] M. R. Pufall, W. H. Rippard, S. Kaka, T. J. Silva, and S. E. Russek. “Frequency modulation of spin-transfer oscillators”. *Applied Physics Letters*, 86(082506), (2005).

[95] P. K. Muduli, Ye. Pogoryelov, S. Bonetti, G. Consolo, Fred Mancof, and Johan Akerman. “Nonlinear frequency and amplitude modulation of a nanocontact-based spin-torque oscillator”. *Physical Review B*(R), 81(140408), April 2010.

[96] G. Consolo, V. Puliafito, G. Finocchio, L. Lopez-diaz, R. Zivieri, L. Giovannini, F. Nizzoli, G. Valenti, and B. Azzerboni. “Combined Frequency-Amplitude Nonlinear Modulation: Theory and Applications”. *IEEE Transactions on Magnetics*, 46(9):3629-3634, (2010).

[97] Ezio Iacocca, and Johan Akerman, “Analytical investigation of modulated spin-torque oscillators in the framework of coupled differential equations with variable coefficients,” *Physical Review B* 85, 184420 (2012).

[98] Agilent Technologies, Inc., “Spectrum Analysis Basics: Application note 150,” USA. 2014.

[99] Tektronix, Inc., “Digital and Mixed Signal Oscilloscopes: DPO/DSA/MSO70000 Series Datasheet,” 2011.

[100] D. Houssameddine, U. Ebels, and B. Dieny, “Temporal Coherence of MgO Based Magnetic Tunnel Junction Spin Torque Oscillators,” *PRL* **102**, 257202 (2009).

[101] H. Maehara, K. Nishimura, Y. Nagamine, K. Tsunekawa, T. Seki, H. Kubota, A. Fukushima, K. Yakushiji, K. Ando, and S. Yuasa, “Tunnel Magnetoresistance above 170% and Resistance-Area Product of 1 $(\mu m)^2$ Attained by In situ Annealing of Ultra-Thin MgO Tunnel Barrier,” *Applied Physics Express*, **4** (033002), 2011.

[102] K. Tsunekawa, D. D. Djayaprawira, M. Nagai, H. Maehara, S. Yamagata, N. Watanabe, S. Yuasa, Y. Suzuki, and K. Ando, “Giant tunneling magnetoresistance effect in low-resistance CoFeB/ MgO (001)/ CoFeB magnetic tunnel junctions for read-head applications,” *Applied Physics Letters*, **87** (072503), 2005.

[103] E. Monteblanco, D. Gusakova, J. F. Sierra, L. D. Buda-Prejbeanu, and U. Ebels, “Redshift and Blueshift Regimes in Spin-Transfer-Torque Nano-Oscillator Based on Synthetic Antiferromagnetic Layer,” IEEE Magnetics Letters, Volume 4, 2013.

[104] Abraham. Savitzky and M. J. E. Golay, “Smoothing and Differentiation of Data by Simplified Least Squares Procedures”. *Analytical Chemistry*. Vol. 36 No. 8: 1627–39,1964.

Publications and Conferences

Publication

A. Purbawati, F. Garcia-Sanchez, L.D. Buda-Prejbeanu, U. Ebels, *Enhanced modulation rates via field modulation in spin torque nano-oscillators*, Appl. Phys. Lett. **108**, 122402 (2016)

R. Ma, M. Kreissig, A. Purbawati, J. Hem, A. Ruiz-Calaforra, U. Ebels, F. Ellinger, *BFSK Modulation based on spintronic technology*, submitted (2017)

A. Ruiz-Calaforra, A. Purbawati, T. Brächer, J. Hem, C. Murapaka, E. Jiménez, D. Mauri, A. Zeltser, J. A. Katine,M.-C. Cyrille, L. D. Buda-Prejbeanu, *and* U. Ebels, *Frequency shift keying by current modulation in a MTJ-based STNO with high data rate*, Appl. Phys. Lett. **111**, 082401 (2017)

Conferences

XVIème Colloque Louis Néel, Autrans, France, Septembre 2014
Poster: *Characterization of Spin Torque Nano Oscillators (STNOs) based on magnetic tunnel junctions*
A. Purbawati, K.J.Merazzo, R. Hida, J. Hem, M. Tortarolo, C. Dieudonné, R. Ferreira, L. Vila, U. Ebels, M.T. Delaye, M.-C. Cyrille

LANEF, Spintronics and Nanomagnetism, Grenoble, France, November 2015
Poster: *Frequency modulation of spin torque nano-oscillators*
A. Purbawati, F. Garcia-Sanchez, L.D. Buda-Prejbeanu, U. Ebels

MMM-Intermag 2016, San Diego, California, January 2016
Poster: *Frequency modulation of spin torque nano-oscillators without cutoff frequencies*
A. Purbawati, F. Garcia-Sanchez, L.D. Buda-Prejbeanu, U. Ebels

Colloque Louis Néel 2016, Saint-Dié-des-Vosges, France, March 2016
Poster: *Frequency modulation of spin torque nano-oscillators*
A. Purbawati, F. Garcia-Sanchez, L.D. Buda-Prejbeanu, U. Ebels